Non-Invasive metabolic profiling in tissue engineering and innate immunology by 2P-FLIM

Trinity College Dublin
Coláiste na Tríonóide, Baile Átha Cliath
The University of Dublin

A thesis submitted to the University of Dublin in partial fulfilment of the requirements for the degree of

Doctor in Philosophy

Nuno G. B. Neto, B.Sc., M.Sc.

January 2023

Supervisor:

Prof. Michael G. Monaghan

Declaration

I declare that this thesis has not been submitted as an exercise for a degree at this or any other university and it is entirely my own work.

I agree to deposit this thesis in the University's open access institutional repository or allow the Library to do so on my behalf, subject to Irish Copyright Legislation and Trinity College Library conditions of use and acknowledgement.

I consent to the examiner retaining a copy of the thesis beyond the examining period, should they so wish (EU GDPR May 2018).

_____

Nuno G. B. Neto

Summary

During the golden age of biochemistry from 1920s to 1960s, many of the metabolic pathways responsible for nutrient usage and energy production in humans and other organisms was defined. During this period, glycolysis, Krebs cycle, urea cycle, oxidative phosphorylation pathways and the role of ATP were uncovered. Research in this field lost momentum due to the rise of new cellular and molecular technologies in conjugation with an overall belief that most of the intermediary metabolism has already been unravelled. Interestingly, it was the ongoing exploration of cellular biology and diseases that propelled a renewed interest in cellular metabolism. Nowadays, metabolites and metabolic pathways have several functions ranging from homeostatic regulation, biosynthesis to fuel phenotypic changes and cellular functions. In addition, cellular metabolism is also becoming a promising therapeutic target of health conditions such as cancer.

With this renewed interest in cellular metabolism, new technologies and methods are also being developed to infer on specific parts of cellular metabolism. Most metabolic probing methods are invasive, require large numbers of cells or are technically challenging requiring sample pre-processing. Two-photon fluorescence lifetime imaging microscopy is a technique which uses a lower number of cells, is non-invasive and is able to follow metabolic changes occurring in real-time. This microscopy technique uses cellular autofluorescence emission and fluorescence lifetime from NAD(P)H and FAD^+ to determine the metabolic profile of cells, tissues and organoids.

The overall goal of this thesis is to characterise the metabolic profile of human stem cells and macrophages using two photon fluorescence lifetime imaging microscopy (2P-FLIM) concomitant with advanced data and image analysis tools. The specific aims pursued to achieve this goal are: (i) modulate human stem cell metabolism using different flow velocities in a bioreactor and biochemically validate the spatial distribution of the metabolic profile; (ii) to

modulate human stem cell metabolism by promoting anaplerotic metabolic pathways to trigger higher levels of osteogenic differentiation, and (iii) to metabolically profile human macrophages using a series of metabolic chemical inhibitors in order to classify human macrophages polarisation state using machine learning models.

In chapter 3 of this thesis, it is demonstrated that flow velocity in bioreactors can be tuned to modulate complex tissue environments such as the perivascular stem cell niche. Here it was observed that lower flow velocities can promote an oxygen gradient from the inlet to the outlet regions of the bioreactor due to cellular respiration. Due to this oxygen gradient, cellular metabolism is restricted and thus generates a metabolic gradient from oxidative phosphorylation to glycolysis from the inlet to the outlet regions. In chapter 4, osteogenic differentiation of human stem cells promoted by osteogenic media was profiled using 2P-FLIM. It was observed that osteogenic-differentiated stem cells rely on oxidative phosphorylation and anaplerotic pathways as a source of energy and metabolite supply to fuel biosynthetic pathways. By adding lactate as an extracellular metabolite, osteogenic differentiation was upregulated, concomitant with higher dependence on anabolic pathways such as glutaminolysis. Chapter 5 details human macrophages classification using machine learning methods trained on 2P-FLIM extracted fluorescence variables. By using 2P-FLIM, fluorescence lifetime variables were measured during on-going inhibition of metabolic pathways of polarised human macrophages using metabolic enzyme chemical inhibitors. In addition, based on 2P-FLIM predictors, machine learning models were trained and used to classify human macrophages based on its polarisation state. High classification efficiency was achieved for full field-of-view images. This methodology was also applied to classify single-cell human macrophages.

Overall, the results of this thesis shows that 2P-FLIM is a powerful non-invasive tool to explore cellular metabolism. Taking in account the metabolic profile of the cells imaged with 2P-FLIM, it is possible to tailor cellular metabolism by adding metabolites, inhibitors or controlling

flow velocities in bioreactors. In addition, 2P-FLIM allows real-time continuous monitoring of cellular metabolism during cell culture in cells, tissues or organoids due to its non-invasive features. This allows long term undisturbed probing of cellular metabolism during longer periods of cell culture. Furthermore, 2P-FLIM fluorescence lifetime variables can then be used as predictors for machine learning algorithms.

Acknowledgements

I would like to start by thanking Trinity College Dublin for allowing me to pursue my PhD studies by establishing the PhD funding program “Provost Award” in 2018. I want to thank my PhD supervisor, Michael Monaghan for the support during these studies and for allowing some degree of intellectual and research freedom. I believe, I enjoyed some freedom to establish multidisciplinary collaborations and pursue interesting research avenues such as applying machine learning algorithms to FLIM data. This way, we were able to learn a lot about cell metabolism, immunology and other scientific fields, while developing novel FLIM analysis techniques.

I would also like to thank to all my collaborators and friends that I made while exploring FLIM and for learning all about the exciting research happening in Trinity College Dublin and Ireland. It was truly inspirational and I learned immensely; not only about science, but also about life in Ireland.

I would like to thank my family, my in-laws and my fiancé for all of the support during these 4 + years of PhD. We celebrated the good things and they were able to pick me back up when things weren’t as great. In particular, thanks to my fiancé for motivating me on my last stretch of PhD work – writing the PhD thesis - and making sure I was prepared for the Viva.

Finally, thanks to all my friends back in Portugal and my hometown for all the support during these years, I hope I made all of you proud.

List of publications, conference proceedings and awards

First-author publications

Neto G.B.N., Suku M., Hoey D., Monaghan M.G. (2022). 2P-FLIM unveils time-dependent metabolic shifts during osteogenic differentiation – Manuscript in Preparation

Neto G.B.N., O'Rourke S.A., Zhang M., Fitzgerald H.K., Dunne A. and Monaghan M.G. (2022). Non-Invasive classification of macrophage polarisation by 2P-FLIM and machine learning. eLife 11:e77373

Perottoni. S.*, **Neto G.B.N.***, Di Nitto C., Dmitriev R.I., Raimondi M.T. and Monaghan M.G. (2021). Intracellular label-free detection of mesenchymal stem cell metabolism within a perivascular niche on-a-chip . Lab on a Chip, 21, 1395-1408

Neto, N., Dmitriev, R.I., Monaghan, M.G. (2020). Seeing Is Believing: Non-invasive Microscopic Imaging Modalities for Tissue Engineering and Regenerative Medicine. In: Gimble, J., Marolt Presen, D., Oreffo, R., Wolbank, S., Redl, H. (eds) Cell Engineering and Regeneration. Reference Series in Biomedical Engineering(). Springer, Cham.

*Both authors contributed equally

Co-author publications

Leikeim A., Wußmann M., Schmidt F.F., **Neto N.G.B.**, Benz F., Tiltmann K., Junger C., Monaghan M.G., Schilling B and Groeber-Becker F. K. (2022). A Preclinical Model of Cutaneous Melanoma Based on Reconstructed Human Epidermis. Scientific Reports 12, 16269

Shanley L.C., Mahon O.R., O'Rourke S.A., **Neto N.G.B.**, Monaghan M.G., Kelly D.J. and Dunne A. (2022). Hydroxyapatite particle size differentially alters macrophage metabolism. Manuscript submitted to Acta Biomaterialia

Chariyev-Prinz F., Szojka A., **Neto N.**, Burdis R., Monaghan M.G. and Kelly D.J. (2022). An assessment of the response of human MSCs to hydrostatic pressure in environments supportive of differential chondrogenesis. Submitted to Journal of Biomechanics

Floudas A., Gorman A., **Neto N.**, Monaghan M.G., Elliott Z., Fearon U. and Marzaioli V. (2022). Inside the Joint of Inflammatory Arthritis Patients: Handling and Processing of Synovial Tissue Biopsies for High Throughput Analysis. Frontiers in Medicine 9:830998.

Fitzgerald, H.K., O'Rourke, S.A., Desmond, E., **Neto, N.G.B**., Monaghan, M.G., Tosetto, M., Doherty, J., Ryan, E.J., Doherty, G.A., Nolan, D.P., Fletcher, J.M. and Dunne, A. (2022). The Trypanosoma brucei-Derived Ketoacids, Indole Pyruvate and Hydroxyphenylpyruvate, Induce HO-1 Expression and Suppress Inflammatory Responses in Human Dendritic Cells. Antioxidants 11, 164.

O'Rourke S.A., **Neto N.G.B.**, Devilly E., Shanley L.C., Fitzgerald H.K., Monaghan M.G. and Dunne A. (2022) Cholesterol crystals drive metabolic reprogramming and M1 macrophage polarisation in primary human macrophages. Atherosclerosis 352, 35-45

Floudas A., **Neto N**., Orr C., Canavan M., Gallagher P., Hurson C., Monaghan M.G., Nagpar S., Mullan R.H., Veale D.J. and Fearon U. (2022). Loss of balance between protective and pro-inflammatory synovial tissue T-cell polyfunctionality predates clinical onset of rheumatoid arthritis. Annals of the Rheumatic Diseases 81:193-205

Floudas A., Smith C.M., Tynan O., **Neto N.**, Krishna V., Wade S.M., Hanlon M., Cunningham C., Marzaioli V., Canavan M., Fletcher J.M., Mullan R. H., Cole S., Hao L., Monaghan M.G., Nagpal S., Veale D.J. and Fearon U. (2022). Distinct stromal and immune cell interactions shape the pathogenesis of rheumatoid and psoriatic arthritis. Annals of the Rheumatic Diseases 81:1224-1242

Rooney M.F., **Neto N.**, Monaghan M., Hill E., Porter R. (2021). Conditionally Immortalised Equine Skeletal Muscle Cell Lines for in Vitro Analysis. Manuscript in preparation

Okkelman I.A., **Neto N.**, Papkovsky D.B., Monaghan M.G. and Dmitriev R.I. (2020). A deeper understanding of intestinal organoid metabolism revealed by combining fluorescence lifetime imaging microscopy (FLIM) and extracellular flux analyses. Redox Biology 30, 101420. 2213-2317

Floudas A., **Neto N.**, Marzaioli V., Murray K., Moran B., Monaghan M.G., Low C., Mullan R.H., Rao N., Krishna V., Nagpal S., Veale D.J. and Fearon U. (2020) Pathogenic, glycolytic PD-1+ B cells accumulate in the hypoxic RA joint. JCI Insight. Nov 5;5(21):e139032.

Ozaki E., Gibbons L., **Neto N.G.B**., Kenna P., Carty M., Humphries M., Humphries P., Campbell M., Monaghan M., Bowie A. and Doyle S.L., (2020). SARM1 deficiency promotes rod and cone photoreceptor cell survival in a model of retinal degeneration. Life Science Alliance Apr 2020, 3 (5) e201900618.

Conference proceedings

Neto N.*, O'Rourke S., Zhang M., Fitzgerald H., Dunne A., Monaghan M.G., Non-Invasive classification of macrophage polarisation by 2P-FLIM and machine learning. 2nd Joint Symposium of microscopy society Ireland and Scottish Microscopy Society. Galway, Ireland 6th-8th April 2022. Oral and Poster Presentation

Neto N.*, O'Rourke S., Zhang M., Dunne A., Monaghan M. G., Single-cell metabolic profiling of macrophage polarization by fluorescence lifetime imaging microscopy (FLIM). 6th European Congress for Immunology Meeting. Virtual conference 1- 4th September 2021. Oral presentation.

Neto N.*, Perottoni S., di Nitto C., Dmitriev R., Raimondi M.T., Monaghan M. G., Intracellular label-free detection of mesenchymal stem cell metabolism within a perivascular niche-on-a-chip. TERMIS Workshop 2021, Virtual conference, Brno 10-11th June 2021. Oral presentation.

Neto N*., Dmitriev R., Monaghan M. G., Metabolic profiling and imaging of 2D and 3D cell cultures by fluorescence lifetime imaging. Microscopy Society Ireland Symposium 2020, 8-10th January 2020, Dublin, Ireland. Poster Presentation.

Neto N.*, O'Rourke S., Mahon O., Dunne A., O'Farrelly C., Monaghan M., Metabolic profiling of macrophage polarization by fluorescence lifetime imaging microscopy. Irish Society for Immunology Meeting 2019. Dublin, Ireland. 19th - 20th September 2019. Poster Presentation.

Neto N.*, O'Rourke S., Mahon O., Dunne A., O'Farrelly C., Monaghan M., Metabolic profiling of macrophage polarization by fluorescence lifetime imaging microscopy. TBSI Research Symposium 2019, Dublin, 4th of September 2019. Poster presentation.

Neto N.*, O'Rourke S., Vishwanathan A., Dunne A., O'Farrelly C., Monaghan M. G., Metabolic profiling of Macrophage Polarization by Fluorescence Lifetime Imaging Microscopy. Immunometabolism Symposium, Dublin, Ireland. 5th of April 2019. Oral Presentation.

Neto N.*, Greaney C., Olvera D., Duffy C., Hoey D., Monaghan M.G., Discerning the Effect of Substrate directed differentiation on Mesenchymal Stromal Cell Metabolic Activity using FLIM. 25th Bioengineering in Ireland 2019, Limerick. 18-19 January 2019. Oral presentation.

Neto N.*, Greaney C., Olvera D., Duffy C., Hoey D., Monaghan M.G., Discerning the Effect of Substrate directed differentiation on Mesenchymal Stromal Cell Metabolic Activity using FLIM. Matrix Biology Ireland, Galway, Ireland. 21st November 2018. Oral Presentation.

Awards

1st place best poster presentation, Microscopy Society Ireland Symposium (2020). Dublin, Ireland, 8th-10th January 2020

1st place in Early Research Career ("Other Bioengineering"), 25th Bioengineering in Ireland conference (2019). Limerick, Ireland, 18th-19th January, 2019

Contents

List of figures

List of tables

List of equations

Nomenclature

2D	Two dimensions
2-DG	2-Deoxy-d-glucose
2-NBDG	2-(N-(7-Nitrobenz-2-oxa-1,3-diazol-4-yl)Amino)-2-Deoxyglucose
3D	Three dimensions
AA	Antimycin A
Acetyl-CoA	Acetil coenxyme A
ADP	Adenosine di-phosphate
α_n	Fraction of fluorescence lifetime
ANOVA	Analysis of variance
AUC	Area under the curve
c	Speed of light
CFD	Computational fluid dynamics
Cm	Centimeter
Dyn	Dyne (unit of force)
E	Energy
ECAR	Extracellular acidification ratio
ECM	Extracellular matrix
ETC	Electron transport chain
FAD	Flavin adenine dinucleotide
FAO	Fatty acid oxidation
FAS	Fatty acid synthesis
FBS	Foetal bovine serum
FBGC	Foreign body giant cells
FCCP	Carbonyl cyanide-p-trifluoromethoxyphenylhydrazone
FLIM	Fluorescence lifetime imaging microscopy
FRET	Förster resonance energy transfer
fs	Femtosecond
GFP	Green fluorescence protein
h	Planck's constant
HIF1	Hypoxia inducible factor 1
hMSCs	Human mesenchymal stem cells
IFNγ	Interferon gamma
iNOS	Inducible nitric oxide synthase

iPSCs	Induced pluripotent stem cells
Laser	Light amplification by stimulated emission of radiation
LPS	Lipopolysaccharide
MHz	Megahertz
MOAB	Miniaturised optically accessible bioreactor
MPM	Multiphoton Microscopy
NAD(P)H	NADH + NADPH
NADH	Nicotinamide adeninine dinucletodide
NADPH	Nicotinamide adenine phosphate dinucleotide
NIR	Near infrared radiation
nm	Nanometre
NOC	Niche on a chip
ns	Nanosecond
OCR	Oxygen consumption ratio
Oligo	Oligomycin
ORR	Optical redox ratio
Osteo +	Osteogenic cell culture medium
Osteo + Lact	Osteogenic medium supplemented with lactate
OxPhos	Oxidative phosphorylation
PCL	Polycaprolactone
PCA	Principal component analysis
PCR	Polymerase chain reaction
Pen/Strep	Penicillin and streptomycin
PLIM	Phosphorescence lifetime imaging microscopy
PMT	Photomultiplier tube
PPP	Pentose phosphate pathway
ps	Picosecond
qPCR	Quantitative PCR
ROC	Receiver operator characteristic
ROS	Reactive oxygen species
Rot	Rotenone
RT-PCR	Realt time PCR
s	Second
S	Singlet state of energy

SHG	Second harmonic generation
T	Triplet state of energy
TCA	Tricarboxylic acid cycle
TCSPC	Time-correlated single photon counting
TMRM	Tetramethylrhodamine, methyl ester
TNFα	Tumor necrosis factor alpha
t-SNE	t-distributed stochastic neighbour embedding
µm	Micrometer
UMAP	Uniform Manifold Approximation and Projection
UV	Ultraviolet
Vis	Visible electromagnetic radiation
χ^2	Chi-squared
Xpan	Expansion/growth cell culture medium
λ (nm)	Wavelength
τ_n	Fluorescence lifetime

Chapter 1 – Introduction

1.1. Research motivation

Ongoing cell biology and disease research has recently renewed an interest in cellular metabolism [1]. Cellular metabolism is no longer a self-regulating network of biochemical reactions independent detached other biological processes. Instead, metabolism impacts and regulates almost every cellular process [2]. As a consequence, fundamental steps of energy metabolism are highly conserved throughout species, cell type and complexity of the organism of study [3].

The proper functioning of metabolic pathways that are involved in the sensing and management of nutrients is essential to metabolic homeostasis and its fundamental requirements for survival. Stem cells and macrophages are dependent on cellular metabolism for cellular division and differentiation or immune responses, polarisation and pathogen-sensing, respectively. In addition, these processes are evolutionarily conserved [4, 5]. However, cellular metabolism is not limited to be a scientific field used to understand complex cellular and systemic functions. With the growth of the immunometabolism field and the altered metabolic pathways responsible for a wide variety of diseases, cellular metabolism has also become an important target of therapeutics [6, 7]

Cancer, diabetes and autoimmune complications can be traced to impaired metabolic pathways [8-10]. In 2020 alone, around 20 million people have been diagnosed with cancer and 10 million registered deaths due to cancer [11]. In addition, it is estimated that more than 24 million people have an auto-immune disease in the United States of America alone and, the incidence rate of auto-immune diseases is increasing in Europe by 3-7% each year [12, 13]. Therefore, there is a need to progress research in these areas to develop new methods of treatment and diagnosis. Disease-oriented metabolic research interest is high and since it pervades every area of cellular biology there is a huge potential as a therapeutic target.

Cancer research has described various metabolic alteration events that enable cancer cells to proliferate and survive, suggesting that metabolic pathways are a good target for therapeutics [6]. Pharmaceutical components such as phloretin and lonidamine target in tumour cells glucose transport across plasma membranes and inhibit hexokinase activity, respectively, with both chemical components showings promising results in treating cancer in preclinical and clinical patient tissues [14-16]. In addition, pharmaceutical compounds that modulate cellular metabolism can be used to increase sensitivity to clinical tumour treatments such as radiotherapy one such example being metformin, an antidiabetic drug used to treat type II diabetes whereby the combination of metformin with radiotherapy increased tumour cell apoptosis and limited tumour growth in oesophageal, lung and colorectal cancer [17-19]

1.2. Role of metabolism in human stem cells and immunology

Human mesenchymal stem cells (hMSCs) are one cell type with self-renewing and multipotent capabilities [20]. In the biomedical and tissue engineering fields, hMSCs are widely used for their potential to generate differentiated cells in the adipogenic, osteogenic and chondrogenic lineages [21].

The differentiation process of hMSCs encompasses phenotypic and biochemical changes. These changes are related with an arrest of cell cycle, protein, fatty acids and nucleotide synthesis. In addition, there are metabolic changes that occur to be able to trigger and sustain the differentiation process [4, 22]. Albeit being a less efficient source of ATP, hMSCs rely on glycolysis to be able to keep up with the cellular division process by producing more metabolic precursors needed for cell division [4]. After stem cell maturation, osteogenic and adipogenic differentiated stems cells are reliant on oxidative phosphorylation as a main metabolic pathway, albeit oxidative phosphorylation dependence is not clear for chondrogenic differentiation. [23-25]. Interestingly, induced pluripotent stem cells (iPSCs) have their cellular metabolism revert back to glycolysis upon cellular reprogramming. This shift in cellular

metabolism from oxidative phosphorylation when cells are mature to glycolysis when cells re-acquire pluripotency demonstrates that cellular metabolic rewiring is an important feature in both hMSCs and iPSCs [26].

Within the field of immunology there has been a renewed on the interest in cellular metabolism due to the rise in the field of immunometabolism. Several studies regarding the metabolism of immune cells has demonstrated that immune cells functions such as pathogen-related activation and inflammatory or anti-inflammatory responses, are directly correlated with changes in metabolic pathways [27-29].

One particular immune cell where cellular metabolism is strongly linked to cellular phenotype and function is the macrophage. Macrophages adapt their immunologic function and behaviour in response to intrinsic or extrinsic stimuli such as tissue environment shifts, cytokines, growth factors, fatty acids, prostaglandins and pathogen-derived molecules [30]. Initially, this macrophage adaptation of function was defined as two polar opposites: M1 macrophages as having a pro-inflammatory phenotype; M2 considered as anti-inflammatory macrophages [31, 32]. However, studies using human macrophages have shown that the polarisation route and associated phenotypic changes of macrophages are not restricted to only two phenotypes [33, 34].

Macrophages are known to be the first line of defence of the innate immune system. M1 macrophage polarisation occurs in an inflammatory environment characterised by increased signalling of Toll-like receptors (TLR) and interferon (IFN). M1-like macrophages have high levels of phagocytic activity, can promote acute inflammatory response by producing pro-inflammatory cytokines and chemokines which induce T-cell response activation and facilitate further phagocytosis [35, 36]. M1-like macrophages are also characterised by elevated antigen presentation capacity and, microorganism and matrix debris phagocytosis in the early stages of healing [30, 37]. Furthermore, M1-like macrophages are the dominant infiltrating cells that

respond to biomaterial implantation[38]. During such an event, macrophages respond by triggering an inflammatory response. Depending on the size of the implanted biomaterials, macrophages can phagocytize the biomaterial particles or form foreign body giant cells (FBGCs) at the biomaterial-tissue interface [39]. In addition, macrophage response to biomaterials is also dependent on the biodegradability and surface chemistry of the implant. Degradable biomaterials are eroded by extracellular resorption, with or without the involvement of FBGCs and phagocytosed within phagosomes. After total resorption of the biomaterial, any associated inflammation is resolved. For non-degradable biomaterials, macrophages continue to infiltrate the tissue and fuse into FBGCs, remaining on the interface of the implanted biomaterials [40]. M1-like macrophages activity takes place in hours or day and therefore require rapid energy and reducing molecules required for bacterial activity. Glycolysis is therefore induced upon macrophage activation towards a M1-state to achieve rapidly high levels of energy.

M2-like macrophages have a role in the resolution phase of the inflammatory response. Here, M2-like macrophages damp the inflammation processes and promote tissue repair by stimulating angiogenesis and tissue remodelling, due to the release of molecules such as endothelial growth factor, TGF-β or fibroblast growth factor [37, 41]. M2-like macrophages due to their prolonged role on tissue repair, require a long-term sustained energy supply. Oxidative phosphorylation pathway is upregulated in M2-macrophages since it provides longer and stable amounts of energy. Interestingly, forcing glycolysis in M2-macrophages drives the macrophage into a M1-like state. Additionally, forcing oxidative phosphorylation in a M1-macrophage drives the macrophage into a M2-like state [42, 43]

For both stem cell biology and immunology fields there is a clear anchor in cellular metabolism in which metabolic shifts occur to meet the energetic and biosynthetic demands of cell maturation, phenotype activation or cellular function [27, 44]. Therefore, there is a huge interest in exploring cellular metabolism in order to fully understand cellular and molecular

processes underpinning cellular biology. This interest is also extended to biomedical research and medical research for prevention, detection and treatment of ailments [45, 46]. Furthermore, research in cellular metabolism opens the possibility for metabolic engineering in which cellular metabolism can be tailored based on metabolic chemical inhibitors or extracellular metabolites to modulate cellular metabolism and cellular function [47].

For this thesis, two-photon lifetime imaging microscopy (2P-FLIM) was used to probe cellular metabolism in a non-invasive manner. 2P-FLIM can map and quantify cellular autofluorescence emitted by metabolic co-factors such as nicotinamide adenine dinucleotide (NAD(P)H) and flavin adenine dinucleotide (FAD^+); which can be used to infer a dominating state of oxidative phosphorylation or glycolysis. In addition, 2P-FLIM as a microscopy technique complements cellular imaging with spatial resolution. The spatial resolution of 2P-FLIM opens the possibility to image different regions of biological samples as well as within different areas of a bioreactor. Furthermore, using 2P-FLIM provides the opportunity to measure cellular metabolic responses to treatments or metabolic inhibitors in real-time. 2P-FLIM will allow to determine the metabolic profile of stem cells and macrophages in response to cell culture environmental modifications and chemically-induced treatments as well to measure 2P-FLIM fluorescence variables for use in advanced data analysis methods such as predictors for machine learning models.

1.3. 2P-FLIM as a tool for metabolic profiling

Two-photon fluorescence lifetime imaging microscopy (2P-FLIM) is a technique which measures and maps the lifetime property of fluorescence emission. The lifetime of the fluorescence emission is the time it takes for an excited fluorescence molecule to emit fluorescence and return to the ground state [48]. 2P-FLIM encompasses the use of multiphoton excitation which reduces photobleaching, photodamage and increase tissue penetration when compared with single-photon lasers [49].

2P-FLIM has been mostly used in autofluorescence molecular imaging to study cellular metabolism [50]. This technique has gained track due to its high sensitivity to evaluate the molecular environment and shifts of molecular conformation of fluorescent molecules. 2P-FLIM of metabolic co-factors such as NAD(P)H and FAD^+ provides unique observations of cellular metabolism in a non-destructive manner with spatiotemporal resolution [51, 52]. 2P-FLIM has been applied to several cell types, tissues and 3D cell culture systems providing metabolic insights not observed with conventional metabolomics techniques [51, 53-55]. 2P-FLIM of NAD(P)H discerns between the fraction of protein-bound NAD(P)H and free NAD(P)H. The interaction of metabolic enzymes with NAD(P)H promotes a conformational change in the NAD(P)H molecule which results in longer fluorescence lifetimes when compared with free NAD(P)H [52, 56]. It has been established that higher ratios of protein-bound NAD(P)H are associated with a higher metabolic reliance in oxidative phosphorylation as a source of energy. For lower protein-bound NAD(P)H ratios, there is a higher reliance in glycolysis [52]. In addition, the ratios and fluorescence lifetimes of NAD(P)H can be combined to calculate the average fluorescence lifetime. The average fluorescence lifetime allows for a quicker understanding of the metabolic profile being measured with 2P-FLIM [57]. Another parameter extracted from 2P-FLIM measurements is the fluorescence intensity of NAD(P)H.

The fluorescence intensity of NAD(P)H has been shown to correlate with the cellular concentration of NAD(P)H however fluorescence intensity does not provide information regarding the conformational changes of NAD(P)H and therefore is a more limited approach to study cellular metabolism [58, 59]. However, to overcome the limitations of fluorescence intensity measurements of NAD(P)H, the fluorescence intensity of NAD(P)H and the fluorescence intensity of FAD^+ can be combined to calculate the optical redox ratio (ORR) [60, 61]. There are multiple applications of this parameter and some studies utilise different equations to calculate the ORR values [61-63]. Therefore, interpretation of ORR results is not always straightforward and highly depends on the mathematical equation being applied to the

experimental data. Throughout this thesis, ORR will be calculated used a ratio of FAD^+ fluorescence intensity divided by NAD(P)H fluorescence intensity. When higher values of ORR are measured, there is a decrease in the concentration of NAD(P)H and/or a higher concentration of FAD^+. Therefore, higher ORR values can be associated with a higher activity of the electron transport chain or NAD(P)H consuming pathways such as the late stage of glycolysis. Whereas, smaller values of ORR are associated with higher Krebs cycle activity or NAD(P)H regenerating pathways such as the early stage of glycolysis [64]. However, any metabolic pathway utilising either NAD(P)H and FAD^+ as a metabolic co-factor can impact the ORR ratios.

2P-FLIM microscopy technique generates a large number of variables. Fluorescence lifetime, fluorescence intensity, average fluorescence lifetime and ORR are variables collected using only 2P-FLIM. When analysing 2P-FLIM data, all of these variables can be used to characterise metabolically a sample or a response to a microenvironmental cues or treatments. To fully analyse 2P-FLIM data without compromising trends or significance between variables, there is a need to use multivariate statistical analysis methods. These multivariate analysis methods such as principal component analysis (PCA) or uniform manifold approximation and projection (UMAP) reduce the dimensionality of the data to allow for a quicker visual analysis and identification of experimental trends [65, 66] . The use of PCA and UMAP has been establish for life sciences and biomedical research with the increase of large datasets generated by experimental “omics” setups such as genomics, transcriptomics and metabolomics [67-69]. In addition, 2P-FLIM variables can analysed using supervised advanced statistical such as machine learning [70]. During the machine learning approach, a subset of 2P-FLIM data, established as a training dataset, is used to train a machine learning model such as random forests [71]. After training and tuning the machine learning model, this model can be used as a tool to classify 2P-FLIM experimental groups or predict trends. In particular, random forests allows to determine the feature importance of each 2P-FLIM variable used to train the initial random forest model

[72, 73]. By determining the feature importance using random forests models, it is possibly to uncover or highlight a metabolic shift by understanding the importance of a single 2P-FLIM variability for classification of an experimental group.

1.4. Objectives

The fundamental goal of this thesis is to experimentally expand the repertoire of information acquired by 2P-FLIM and subsequent methods of analysis such as machine learning. In addition, another goal is to showcase the usage of 2P-FLIM as a non-invasive spatiotemporal tool to probe cellular metabolism of stem cell growth, differentiation and polarisation of immune cells (Figure 1.1). 2P-FLIM will be used to metabolically characterise cells during various experimental conditions and in response to metabolic modulators. Furthermore, metabolic shifts measured with 2P-FLIM will be validated using biochemical assays such as quantification of glucose uptake and consumption, mitochondrial morphology, mitochondrial membrane potential, extracellular metabolite secretion and uptake and qPCR of metabolic-related genes. Furthermore, machine learning approaches such as random forests are used to both classify and infer on the metabolic properties of cells as well to identify the importance of each relative 2P-FLIM variable.

These studies enable the characterisation of cellular metabolic profiles in response to environmental conditions and during cell behaviour. In the 1st study, there is a modulation of cellular metabolism from oxidative phosphorylation towards glycolysis due to decreased availability of oxygen and nutrients, quantified using 2P-FLIM. For the 2nd and 3rd study, cellular differentiation and polarisation dictated shifts in cellular metabolism. During these studies, metabolic changes were measured using 2P-FLIM and validated using biochemical assays. In addition, these studies will uncover new approaches of the 2P-FLIM technique to probe cellular metabolism and cellular behaviour whilst applying novel data analysis techniques such as 2P-FLIM integration with machine learning models.

Specific Aim 1: Use 2P-FLIM to probe cellular metabolism non-invasively and in real-time within a miniaturised bioreactor chamber while tuning hMSCs metabolism to achieve an oxygen and a metabolic gradient using different flow velocities, validated using standard fluorescence staining.

Specific Aim 2: Unravelling the time-dependence of stem cell differentiation and link metabolic pathways used during osteogenesis using 2P-FLIM. Then using this information to metabolically promote osteogenic differentiation, uncovering a potential therapeutic or metabolic trigger of hMSCs osteogenic differentiation.

Specific Aim 3: Evaluate the metabolic profile of human macrophage polarisation towards M1-like and M2-like state using 2P-FLIM. Use 2P-FLIM data to train random forests models for classification of human macrophages polarisation in both full field-of-view and single cell approach.

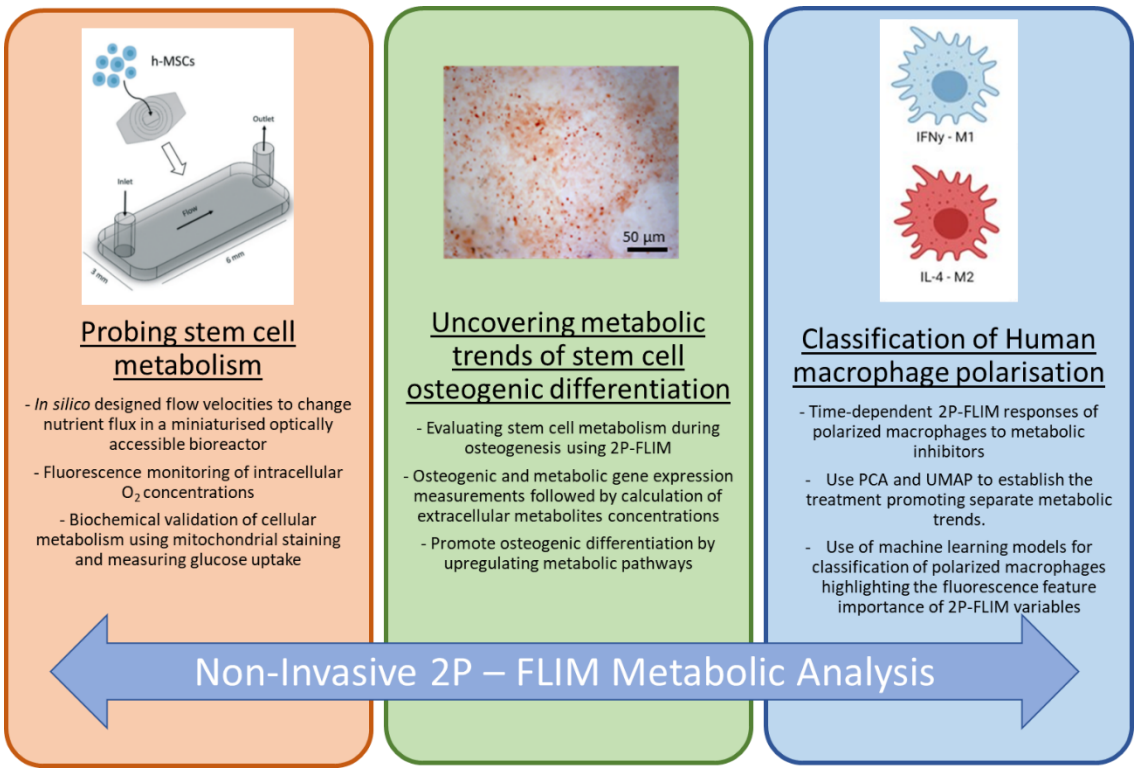

Figure 1.1 - Graphic summary of research objectives

1.5. References

[1] S.L. McKnight, On getting there from here, Science. 330(6009) (2010) 1338-1339.
[2] R.J. DeBerardinis, C.B. Thompson, Cellular metabolism and disease: what do metabolic outliers teach us?, Cell. 148(6) (2012) 1132-1144.
[3] J.M. Peregrin-Alvarez, C. Sanford, J. Parkinson, The conservation and evolutionary modularity of metabolism, Genome Biology. 10(6) (2009) 1-17.
[4] M. Agathocleous, W.A. Harris, Metabolism in physiological cell proliferation and differentiation, Trends in Cell Biology. 23(10) (2013) 484-492.
[5] G.S. Hotamisligil, E. Erbay, Nutrient sensing and inflammation in metabolic diseases, Nature Reviews Immunology. 8(12) (2008) 923-934.
[6] Y. Zhao, E.B. Butler, M. Tan, Targeting cellular metabolism to improve cancer therapeutics, Cell Death and Disease. 4 (2013) e532.
[7] N. Huang, A. Perl, Metabolism as a target for modulation in autoimmune diseases, Trends in Immunology. 39(7) (2018) 562-576.
[8] R.R. Kalyani, J.M. Egan, Diabetes and altered glucose metabolism with aging, Endocrinology and Metabolism Clinics of North America. 42(2) (2013) 333-347.
[9] Z. Yang, E.L. Matteson, J.J. Goronzy, C.M. Weyand, T-cell metabolism in autoimmune disease, Arthritis Research and Therapy. 17 (2015) 29-39.
[10] R.J. DeBerardinis, N.S. Chandel, Fundamentals of cancer metabolism, Science Advances. 2(5) (2016) e1600200.
[11] J. Ferlay, M. Colombet, I. Soerjomataram, D.M. Parkin, M. Pineros, A. Znaor, F. Bray, Cancer statistics for the year 2020: An overview, International Journal of Cancer. (2021).
[12] N.A.D.C. Committee, Progress in autoimmune diseases research, 2005.
[13] A. Lerner, P. Jeremias, T. Matthias, The world incidence and prevalence of autoimmune diseases is increasing, International Journal of Celiac Disease. 3(4) (2016) 151-155.
[14] X. Cao, L. Fang, S. Gibbs, Y. Huang, Z. Dai, P. Wen, X. Zheng, W. Sadee, D. Sun, Glucose uptake inhibitor sensitizes cancer cells to daunorubicin and overcomes drug resistance in hypoxia, Cancer Chemotherapy and Pharmacology. 59(4) (2007) 495-505.
[15] M. De Lena, V. Lorusso, A. Latorre, G. Fanizza, G. Gargano, L. Caporusso, M. Guida, A. Catino, E. Crucitta, D. Sambiasi, A. Mazzei, Paclitaxel, cisplatin and lonidamine in advanced ovarian cancer. A phase II study, European Journal of Cancer. 37(3) (2001) 364-368.
[16] A. Bokil, P. Sancho, Mitochondrial determinants of chemoresistance, Cancer Drug Resistance. 2(3) (2019) 634-646.
[17] Y. Storozhuk, S.N. Hopmans, T. Sanli, C. Barron, E. Tsiani, J.C. Cutz, G. Pond, J. Wright, G. Singh, T. Tsakiridis, Metformin inhibits growth and enhances radiation response of non-small cell lung cancer (NSCLC) through ATM and AMPK, British Journal of Cancer. 108(10) (2013) 2021-2032.
[18] T. Feng, L. Li, S. Ling, N. Fan, M. Fang, H. Zhang, X. Fang, W. Lan, Z. Hou, Q. Meng, D. Jin, F. Xu, Y. Li, Metformin enhances radiation response of ECa109 cells through activation of ATM and AMPK, Biomedicine and Pharmacotherapy. 69 (2015) 260-266.
[19] H. Jin, S. Gao, H. Guo, S. Ren, F. Ji, Z. Liu, X. Chen, Re-sensitization of radiation resistant colorectal cancer cells to radiation through inhibition of AMPK pathway, Oncology Letters. 11(5) (2016) 3197-3201.
[20] J.J. Minguell, A. Erices, P. Conget, Mesenchymal stem cells, Experimental Biology and Medicine. 226(6) (2001) 507-520.
[21] S.E. Haynesworth, D. Reuben, A.I. Caplan, Cell-based tissue engineering therapies: the influence of whole body physiology, Advanced Drug Delivery Reviews. 33(1-2) (1998) 3-14.
[22] O. Yanes, J. Clark, D.M. Wong, G.J. Patti, A. Sanchez-Ruiz, H.P. Benton, S.A. Trauger, C. Desponts, S. Ding, G. Siuzdak, Metabolic oxidation regulates embryonic stem cell differentiation, Nature Chemical Biology. 6(6) (2010) 411-417.

[23] A.D. Hofmann, M. Beyer, U. Krause-Buchholz, M. Wobus, M. Bornhauser, G. Rodel, OXPHOS supercomplexes as a hallmark of the mitochondrial phenotype of adipogenic differentiated human MSCs, PloS One. 7(4) (2012) e35160.
[24] D.W. Wang, B. Fermor, J.M. Gimble, H.A. Awad, F. Guilak, Influence of oxygen on the proliferation and metabolism of adipose derived adult stem cells, Journal of Cell Physiology. 204(1) (2005) 184-191.
[25] Q. Li, Z. Gao, Y. Chen, M.X. Guan, The role of mitochondria in osteogenic, adipogenic and chondrogenic differentiation of mesenchymal stem cells, Protein Cell. 8(6) (2017) 439-445.
[26] J. Wu, A. Ocampo, J.C.I. Belmonte, Cellular metabolism and induced pluripotency, Cell. 166(6) (2016) 1371-1385.
[27] L.A. O'Neill, R.J. Kishton, J. Rathmell, A guide to immunometabolism for immunologists, Nature Reviews Immunology. 16(9) (2016) 553-565.
[28] J. Van den Bossche, L.A. O'Neill, D. Menon, Macrophage immunometabolism: where are we (Going)?, Trends in Immunology. 38(6) (2017) 395-406.
[29] S. Galvan-Pena, L.A. O'Neill, Metabolic reprograming in macrophage polarization, Frontiers in Immunology. 5 (2014) 420-426.
[30] C. Atri, F.Z. Guerfali, D. Laouini, Role of human macrophage polarization in inflammation during infectious diseases, International Journal Molecular Sciences. 19(6) (2018) 1801-1816.
[31] S. Goerdt, O. Politz, K. Schledzewski, R. Birk, A. Gratchev, P. Guillot, N. Hakiy, C.D. Klemke, E. Dippel, V. Kodelja, C.E. Orfanos, Alternative versus classical activation of macrophages, Pathobiology. 67(5-6) (1999) 222-226.
[32] F.O. Martinez, A. Sica, A. Mantovani, M. Locati, Macrophage activation and polarization, Frontiers in Bioscience. 13 (2008) 453-461.
[33] A.A. Tarique, J. Logan, E. Thomas, P.G. Holt, P.D. Sly, E. Fantino, Phenotypic, functional, and plasticity features of classical and alternatively activated human macrophages, American Journal of Respiratory Cell and Molecular Biology. 53(5) (2015) 676-688.
[34] D.Y. Vogel, J.E. Glim, A.W. Stavenuiter, M. Breur, P. Heijnen, S. Amor, C.D. Dijkstra, R.H. Beelen, Human macrophage polarization in vitro: maturation and activation methods compared, Immunobiology. 219(9) (2014) 695-703.
[35] P. Italiani, E.M. Mazza, D. Lucchesi, I. Cifola, C. Gemelli, A. Grande, C. Battaglia, S. Bicciato, D. Boraschi, Transcriptomic profiling of the development of the inflammatory response in human monocytes in vitro, PloS One. 9(2) (2014) e87680.
[36] F.O. Martinez, S. Gordon, M. Locati, A. Mantovani, Transcriptional profiling of the human monocyte-to-macrophage differentiation and polarization: new molecules and patterns of gene expression, Journal of Immunology. 177(10) (2006) 7303-7311.
[37] P. Krzyszczyk, R. Schloss, A. Palmer, F. Berthiaume, The role of macrophages in acute and chronic wound healing and interventions to promote pro-wound healing phenotypes, Frontiers in Physiology. 9 (2018) 419-441.
[38] Z. Sheikh, P.J. Brooks, O. Barzilay, N. Fine, M. Glogauer, Macrophages, foreign body giant cells and their response to implantable biomaterials, Materials. 8(9) (2015) 5671-5701.
[39] Z. Xia, J.T. Triffitt, A review on macrophage responses to biomaterials, Biomedical Materials. 1(1) (2006) 1-9.
[40] J.M. Anderson, Multinucleated giant cells, Current Opinion in Hematology. 7(1) (2000) 40-47.
[41] T.A. Wynn, K.M. Vannella, Macrophages in tissue repair, regeneration, and fibrosis, Immunity. 44(3) (2016) 450-462.
[42] J.C. Rodriguez-Prados, P.G. Traves, J. Cuenca, D. Rico, J. Aragones, P. Martin-Sanz, M. Cascante, L. Bosca, Substrate fate in activated macrophages: a comparison between innate, classic, and alternative activation, Journal of Immunology. 185(1) (2010) 605-614.

[43] D. Vats, L. Mukundan, J.I. Odegaard, L. Zhang, K.L. Smith, C.R. Morel, R.A. Wagner, D.R. Greaves, P.J. Murray, A. Chawla, Oxidative metabolism and PGC-1beta attenuate macrophage-mediated inflammation, Cell Metabolism. 4(1) (2006) 13-24.
[44] M.G. Vander Heiden, L.C. Cantley, C.B. Thompson, Understanding the warburg effect: the metabolic requirements of cell proliferation, Science. 324(5930) (2009) 1029-1033.
[45] X. Geeraerts, E. Bolli, S.M. Fendt, J.A. Van Ginderachter, Macrophage metabolism as therapeutic target for cancer, atherosclerosis, and obesity, Frontiers in Immunology. 8 (2017) 289-302.
[46] C.J. Zuurbier, L. Bertrand, C.R. Beauloye, I. Andreadou, M. Ruiz-Meana, N.R. Jespersen, D. Kula-Alwar, H.A. Prag, H. Eric Botker, M. Dambrova, C. Montessuit, T. Kaambre, E. Liepinsh, P.S. Brookes, T. Krieg, Cardiac metabolism as a driver and therapeutic target of myocardial infarction, Journal of Cellular and Molecular Medicine. 24(11) (2020) 5937-5954.
[47] B.M. Woolston, S. Edgar, G. Stephanopoulos, Metabolic engineering: past and future, Annual Review of Chemical and Biomolecular Engineering. 4 (2013) 259-288.
[48] J.R. Lakowicz, Principles of fluorescence spectroscopy, 2006.
[49] W. Denk, J.H. Strickler, W.W. Webb, Two-photon laser scanning fluorescence microscopy, Science. 248(4951) (1990) 73-76.
[50] J.V. Chacko, K.W. Eliceiri, Autofluorescence lifetime imaging of cellular metabolism: Sensitivity toward cell density, pH, intracellular, and intercellular heterogeneity, Cytometry A. 95(1) (2019) 56-69.
[51] M.C. Skala, K.M. Riching, A. Gendron-Fitzpatrick, J. Eickhoff, K.W. Eliceiri, J.G. White, N. Ramanujam, In vivo multiphoton microscopy of NADH and FAD redox states, fluorescence lifetimes, and cellular morphology in precancerous epithelia, Proceedings of the National Academy of Sciences of the United States of America. 104(49) (2007) 19494-19499.
[52] J.R. Lakowicz, H. Szmacinski, K. Nowaczyk, M.L. Johnson, Fluorescence lifetime imaging of free and protein-bound NADH, Proceedings of the National Academy of Sciences of the United States of America. 89(4) (1992) 1271-1275.
[53] I.A. Okkelman, N. Neto, D.B. Papkovsky, M.G. Monaghan, R.I. Dmitriev, A deeper understanding of intestinal organoid metabolism revealed by combining fluorescence lifetime imaging microscopy (FLIM) and extracellular flux analyses, Redox Biology. 30 (2020) 101420.
[54] K. Konig, A. Uchugonova, E. Gorjup, Multiphoton fluorescence lifetime imaging of 3D-stem cell spheroids during differentiation, Microscopy Research Technology. 74(1) (2011) 9-17.
[55] S. Chakraborty, F.S. Nian, J.W. Tsai, A. Karmenyan, A. Chiou, Quantification of the metabolic state in cell-model of parkinson's disease by fluorescence lifetime imaging microscopy, Scientific Reports. 6(19145) (2016) 1-9.
[56] T.S. Blacker, M.R. Duchen, Investigating mitochondrial redox state using NADH and NADPH autofluorescence, Free Radical Biology and Medicine. 100 (2016) 53-65.
[57] M.Y. Berezin, S. Achilefu, Fluorescence lifetime measurements and biological imaging, Chemistry Review. 110(5) (2010) 2641-2684.
[58] A. Uppal, P.K. Gupta, Measurement of NADH concentration in normal and malignant human tissues from breast and oral cavity, Biotechnology and Applied Biochemistry. 37(Pt 1) (2003) 45-50.
[59] N. Ma, M.A. Digman, L. Malacrida, E. Gratton, Measurements of absolute concentrations of NADH in cells using the phasor FLIM method, Biomedical Optics Express. 7(7) (2016) 2441-2452.
[60] A. Varone, J. Xylas, K.P. Quinn, D. Pouli, G. Sridharan, M.E. McLaughlin-Drubin, C. Alonzo, K. Lee, K. Munger, I. Georgakoudi, Endogenous two-photon fluorescence imaging elucidates metabolic changes related to enhanced glycolysis and glutamine consumption in precancerous epithelial tissues, Cancer Research. 74(11) (2014) 3067-3075.
[61] A.J. Walsh, R.S. Cook, H.C. Manning, D.J. Hicks, A. Lafontant, C.L. Arteaga, M.C. Skala, Optical metabolic imaging identifies glycolytic levels, subtypes, and early-treatment response in breast cancer, Cancer Research. 73(20) (2013) 6164-6174.

[62] K.P. Quinn, E. Bellas, N. Fourligas, K. Lee, D.L. Kaplan, I. Georgakoudi, Characterization of metabolic changes associated with the functional development of 3D engineered tissues by non-invasive, dynamic measurement of individual cell redox ratios, Biomaterials. 33(21) (2012) 5341-5348.
[63] J.H. Ostrander, C.M. McMahon, S. Lem, S.R. Millon, J.Q. Brown, V.L. Seewaldt, N. Ramanujam, Optical redox ratio differentiates breast cancer cell lines based on estrogen receptor status, Cancer Research. 70(11) (2010) 4759-4766.
[64] W. Ying, NAD+/NADH and NADP+/NADPH in cellular functions and cell death: regulation and biological consequences, Antioxidants & redox signaling. 10(2) (2008) 179-206.
[65] L. McInnes, J. Healy, N. Saul, L. Großberger, UMAP: uniform manifold approximation and projection, Journal of Open Source Software. 3(29) (2018).
[66] K.Y. Yeung, W.L. Ruzzo, Principal component analysis for clustering gene expression data, Bioinformatics. 17(9) (2001) 763-774.
[67] E. Becht, L. McInnes, J. Healy, C.A. Dutertre, I.W.H. Kwok, L.G. Ng, F. Ginhoux, E.W. Newell, Dimensionality reduction for visualizing single-cell data using UMAP, Nature Biotechnology. (2018).
[68] M. Oide, Y. Sugita, Protein folding intermediates on the dimensionality reduced landscape with UMAP and native contact likelihood, Journal of Chemical Physics. 157(075101) (2022) 1-12.
[69] J. Alonso-Gutierrez, E.M. Kim, T.S. Batth, N. Cho, Q. Hu, L.J.G. Chan, C.J. Petzold, N.J. Hillson, P.D. Adams, J.D. Keasling, H. Garcia Martin, T.S. Lee, Principal component analysis of proteomics (PCAP) as a tool to direct metabolic engineering, Metabolism Engineering. 28 (2015) 123-133.
[70] M. Mohri, Rostamizadeh, A. & Talwalkar, Foundations of machine learning, MIT press2012.
[71] L. Breiman, Random forests, Machine Learning. 45(1) (2001) 5-32.
[72] K.L. Lunetta, L.B. Hayward, J. Segal, P. Van Eerdewegh, Screening large-scale association study data: exploiting interactions using random forests, BMC Genetics. 5 (2004) 32-45.
[73] A. Verikas, A. Gelzinis, M. Bacauskiene, Mining data with random forests: A survey and results of new tests, Pattern Recognition. 44(2) (2011) 330-349.

Chapter 2 - Literature review

The majority of the work in this chapter has been peer reviewed and published in: Neto, N., Dmitriev, R.I., Monaghan, M.G. (2020). Seeing Is Believing: Non-invasive Microscopic Imaging Modalities for Tissue Engineering and Regenerative Medicine. In: Gimble, J., Marolt Presen, D., Oreffo, R., Wolbank, S., Redl, H. (eds) Cell Engineering and Regeneration. Reference Series in Biomedical Engineering(). Springer, Cham.

2.1. Introduction

Since its development in the 16th century by Hans and Zacharias Janseen, microscopy rapidly found applications in imaging, and soon works by Robert Hooke and Anton van Leeuwenhoek were published describing the first visualization of cells [1]. Nowadays, microscopic imaging remains a steadfast tool in the life sciences with microscopy techniques routinely applied in the biosciences and tissue engineering research fields. Transmission light, confocal and fluorescence microscopy are the most commonly used microscopic techniques for cell identification, analysis and evaluation of cell response to chemical and mechanical stimuli. However, transmission light microscopy gives generic detail of cell responses and is predominantly employed to evaluate cell division and proliferation [2]. Confocal and fluorescence microscopy often require cell or tissue staining using external fluorophores, either alone or bound to antibodies; rendering it an invasive technique as stained cells are not usually compatible for further assays [3]. The use of invasive techniques can require pre-treatments or fixation regimes which affect cell and tissue physiology, and protein conformation; rendering it a destructive end-point technique [4]. Such necessities have generated an increasing demand for non-invasive methods of fluorescence microscopy in order to diagnose diseases and optimize tissue engineering approaches [5]. The use of non-invasive fluorescent-based microscopic techniques can allow real-time analysis of living cells without the requirement cell fixation, reducing sample manipulation and interference; while decreasing costs. This literature review will discuss emerging non-invasive fluorescent-based imaging technologies in particular multiphoton microscopy (MPM) and its applications in fluorescence lifetime imaging microscopy (FLIM) for evaluation of cell and tissue behavior. These applications enable high-resolution *in vitro*, *in situ* and *in vivo* imaging of cells in intact and engineered tissues. Uncovering the full potential of non-invasive imaging can provide more accurate results and reduce sample manipulation, while avoiding the pitfalls of complex and invasive staining protocols.

2.2. Principle of fluorescence

The interaction of light with matter is underpinned by quantum theory which is the basis of most microscopy techniques. Due to the higher mass of protons and their strong electromagnetic interaction in the nucleus of an atom, light interacts preferably with electrons, characterized by their lower mass; existing at the periphery of atoms. The electron of an atom or molecule can absorb the energy of an incident photon of light, promoting a transition to a higher energy state – this energy transfer process is called absorption. The energy associated with a photon is described by the Einstein-Planck equation (1), with *h* being Planck's constant, *c* the speed of light and λ the photon wavelength. The energy gap that the electron must overcome in order to jump to the increasing energy state depends on the position of the electron, the atom, and the molecular structure of a compound. This is the basis of all fluorescence microscopy, whereby excitation light of a defined wavelength generates fluorescence emission from an excited fluorophore at an emission wavelength.

$$E = \frac{hc}{\lambda}$$

Equation 2.1 – Einstein-Planck Equation

Prior to the 1930's a belief was held that this quantic jump could only occur if the energy of the photon is equal or above the energy gap of the electron transition [6]. In 1931 this dogma was revised. Marie Goeppert-Mayer described an alternative process in her doctoral

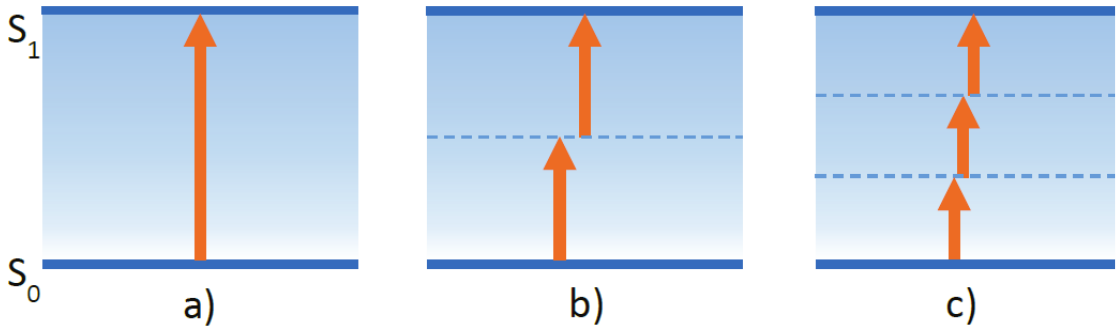

Figure 2.1 - Energy transitions due to light absorption. This transition occurs from ground-state (S_0) to a higher energy state (S_1) and can be promoted by a) one-photon, b) two-photon or c) three-photon excitation.

dissertation which hypothesized that in specific conditions, such an excitation process could be achieved in two-steps [7]. Specifically, two photons whose combined energy would be equal or higher to the energy gap could be enough to achieve an electronic transition. According to quantum mechanics, a single photon excites the molecule to a virtual intermediate state that by recombination with a second photon brings the molecule to the final excited state and higher energy level. Only in 1961 was this process first confirmed by Wolfgang Kaiser using a CaF_2:Eu^{2+} crystal laser [8]. This quantum process is the basis of MPM (Figure 2.1).

2.3. Multiphoton microscopy (MPM)

MPM can be modelled further in a time-dependent Schrödinger equation in which the hamiltonian contains an electric dipole moment$\vec{E}_\gamma \cdot \vec{r}$, where $\vec{E}_\gamma$ is the electric field vector of the photons and $\vec{r}$ is the position operator. ε_γ is the photonic energy associated with the electric field vector and ε_m is the energy difference between the state *m* and the ground state. The first order solution corresponds to the one-photon excitation and multiphoton transitions are represented by higher order solutions. Here, the transition probability between the molecular initial state$|i\rangle$, the virtual intermediate state $|m\rangle$ and the final state $|f\rangle$ is given by:

$$P \sim \left| \sum_m \frac{\langle f|\vec{E}_\gamma \cdot \vec{r}|m\rangle\langle m|\vec{E}_\gamma \cdot \vec{r}|i\rangle}{\varepsilon_\gamma - \varepsilon_m} \right|^2$$

Equation 2.2 – Transition probability equation.

After excitation of a molecule, by a single or multiphoton approach to S_1 energy level; the molecule undergoes internal conversion and reaches the lowest vibrational level of the S_1 state. From here the energy can be dispersed in a radiative or non-radiative way followed by a return to its ground state. A radiative decay is associated with light emission phenomena while non-radiative decay is related to the losing of energy by particle vibration and by heat.

Radiative decay can be decomposed further into fluorescence or phosphorescence processes. In detail, fluorescence is characterized by short decay time durations (picoseconds to nanoseconds) and occurs from S_1 to S_0 energy level (Figure 2.2). Phosphorescence has a longer decay time (micro- to milliseconds) due to intersystem crossing that the molecule must undergo to reach the energy state T1 and then convert back to S_0.

The radiative decays of an electron are dependent on the molecular structure, and its local environment such as solvent, pH and temperature. The rate of these decays is measured

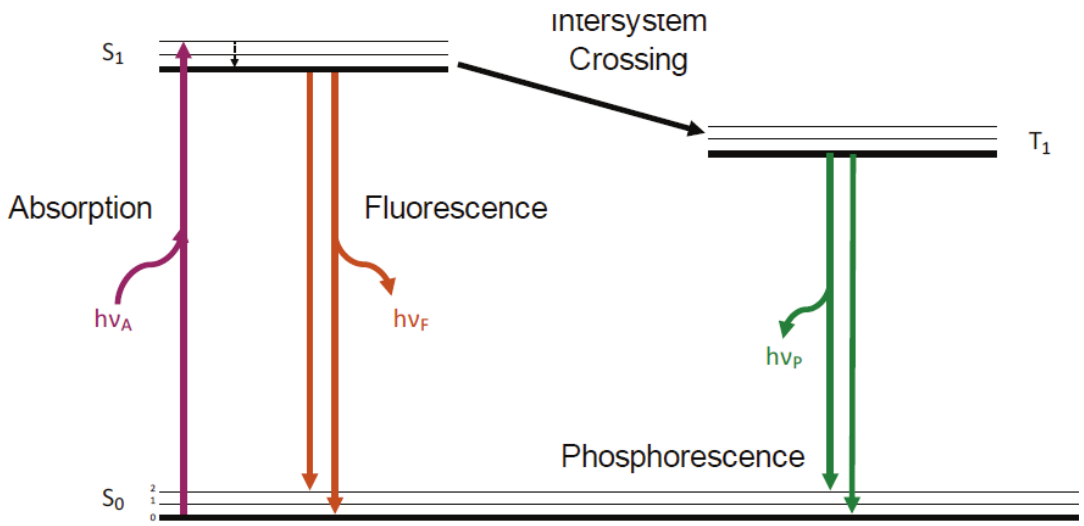

Figure 2.2 - Simplified Jabloski diagram. Higher vibrational levels are represented by thin lines. hvA/F/P is the energy associated to each photon described by Einstein-Planck's equation (1). h is related to the Planck's constant and vA/F/P with the wave frequency of each transition process.

by quantum yields whereby a high fluorescence quantum yield results in a higher percentage of energy being released by light subsequently rendering a brighter emission and higher number of photons being radiated. The absorption and decay pathways that an electron or molecule can undergo are graphically represented in a Jabloski Diagram (Figure 2.2).

In MPM the absorption step in the Jabloski diagram (Figure 2.2) is achieved using light amplification by stimulated emission of radiation (LASER). Wavelengths on the ultraviolet (UV), visible and near infrared (NIR) range are commonly used as excitation sources in microscopy. When going deeper inside of a sample, light scattering dominates the attenuation of light

propagation. However, with the use of non-linear optical processes such as two-photon excitation, the effects of emission scattering are mitigated. In addition, longer wavelengths can be used which increase light penetration and reduce photobleaching due to the confinement of the excitation volume in a tissue due to the quantic nature of the multiphoton recombination. To accomplish this, intense ultrashort-pulsed lasers in the femtosecond range (~80-250 fs) are used [9, 10].

Therefore, wavelengths applied in MPM have lower energies and less scattering of photons occurs when imaging deep inside biological tissues whilst less damage to the samples is produced in comparison to conventional confocal/fluorescence microscopy with higher photostability and higher laser penetration potential.

2.4. FLIM microscopy

Another advanced non-invasive imaging technology facilitated by multiphoton microscopy is Fluorescence Lifetime Imaging Microscopy: an advanced microscopy technique that generates an image based on the fluorescence intensity and on the spatial distribution of excited energy states lifetimes of an endogenous or exogenous molecule of interest on fresh or fixed cells, and tissue. FLIM microscopes are designed to measure lifetimes from the nanosecond to microsecond (μs-FLIM or PLIM) range. Within cells there are molecules present with chemical configurations which enable them to undergo fluorescence emission after excitation with a specific UV/Vis wavelength. These components have within their molecular structure an aromatic group and a high number of π-bonds which increases fluorescence quantum yield and the probability of emitting light of higher intensity [6]. The presence of fluorescent residues (tyrosine and tryptophan) in proteins is standardly measured in both enzymatic or biochemical assays for protein quantification. [11]

Since the dawn of multiphoton technology, it has been possible to excite a cell's endogenous fluorophores in order to obtain fluorescence light emission by means of low energy

wavelengths that avoid phototoxic properties characteristic of higher energy wavelengths [12]. This emission is normally designated as cell autofluorescence. The molecules responsible for the autofluorescence emission are aromatic amino acids (tryptophan, tyrosine), serotonin, lipo-pigments (keratin, melanin), NAD(P)H and FAD (Table 2.1). In tissues, ECM molecules also contribute for the overall fluorescence of the sample mostly due to the presence of elastin and collagen and their high quantum yield which can be excited to perform SHG.

As described previously the excitation of a fluorophore can be followed by emission of a photon and, depending on the radiative quantum yield of the fluorophore; this process can occur by fluorescence, phosphorescence or delayed fluorescence. The predominant emission phenomenon measured in FLIM is fluorescence. The fluorescence lifetime of a molecule is the time – normally pico- to nanoseconds – that a fluorophore remains in an excited state before decaying and emitting a photon. Therefore, fluorophores can be characterized not only by their excitation and emission spectra but also by their unique lifetime. Fluorescence lifetime can be described by Equation 2.3:

$$I_f = \alpha_1 exp^{\frac{-t}{\tau_1}} + \alpha_2 exp^{\frac{-t}{\tau_2}} + \ldots + \alpha_n exp^{\frac{-t}{\tau_n}}$$

Equation 2.3 – Fluorescence lifetime exponential decay

where $If(t)$ is the fluorescence intensity at a given time t, α_n is the fraction of the fluorophore that is responsible for a specific τ_n fluorescence lifetime. The fluorescence lifetime decay of a fluorophore can be decomposed in several fractions depending on the molecule and its environment – mono-exponential or multi-exponential decay. If the fluorophore has a mono-exponential decay, α_n value is 1 whereas in a multi-exponential decay the sum of the various fractions α_n is 1.

Fluorescence microscopy has been one of the most used tools in biological science and it is mostly based on the fluorescent intensity of the specific fluorophores being analyzed. This

technique is dependent on the light detection efficiency of the system and concentration of fluorophores and can result in variable levels of photobleaching and phototoxicity. Contrary to fluorescence microscopy, fluorescence lifetime is minimally affected by the aforementioned variables, although it is sensitive to fluorophore microenvironment such as changes in pH, temperature or presence of FRET donors/acceptors. Therefore, fluorescence lifetime measurements provide a more focused and profound analysis than measuring the fluorescence intensity [13-15]

2.4.1. Frequency-Domain and Time-Domain FLIM

Acquisition of FLIM data can be performed in the frequency- or time- domain. Briefly, in frequency-domain FLIM; a high frequency modulated laser is used to excite the specimen and the fluorescence lifetime is determined by the demodulation and phase shift of the fluorescence signal [16]. Consequently, it is possible to determine the lifetime τ, from the measured phase shift and from the decrease in modulation from the emitted fluorescence compared with the excitation pulse. This will originate two separated lifetimes: τω, lifetime calculated from the phase shift and τA, the lifetime obtained from the modulation difference. If the fluorophore has a mono-exponential decay, τω = τA. For the analysis of more complex fluorescence lifetime decay patterns, measurements can be repeated using multiple modulation frequencies [17]. To appropriately apply frequency-domain FLIM it is required to have a modulated light source and to be able to extract both the phase and modulation signal from the excitation light and emitted light.

In time-domain FLIM, a short pulse of light is used to excite the sample after which the emitted fluorescence is measured in time resulting in curves described by equation 3 [18]. These measurements are acquired using a time correlated single photon counting (TCSPC) detector where after each excitation pulse, the arrival time of the first photon is monitored at a very high resolution [19]. A representative curve of the fluorescence lifetime decay is then obtained by

recording the arrival time of the large number of photons being emitted by the sample. This time-domain technique is dependent on the detection sensitivity of the TCSPC unit so to avoid bias toward photons with shorter lifetimes. Time-gated FLIM is another time-domain FLIM technique in which photons are collected at a fixed number in discrete intervals of time using a time-gated camera. The sample is excited with a short pulse of light and the emission light is measured at two (or more) intervals of time during the fluorescence decay opposite to the previous technique where all the photons during a decay are measured. This way, the acquired lifetime is independent of laser intensity fluctuations. Increasing the number of time-gates can provide more accurate results for multi-exponential decays [20].

FLIM measurements can be done in a non-spatially-resolved fluorescence spectroscopy by exciting a sample or solution in a cuvette [21]. Although, for biomedical and tissue engineering fields it is far more interesting to be able to use FLIM coupled with a microscope allowing morphological analysis, decomposition of complex samples by focusing the excitation volume or having the possibility to 3D reconstruct a sample. Therefore, FLIM has been connected to wide-field [22, 23], confocal [24, 25], multiphoton microscopes [26, 27] and light-sheet microscopy [28, 29]

Typically, the choice for the most adequate FLIM microscopy instrument are dependent on the specific application and spatial-time resolution besides financial consideration, equipment and expertise available. Most of FL/IM systems used in research have been custom-built by their users. Still, there are some considerations to be made between the different FLIM systems: wide-field and confocal microscopy are limited to one-photon excitation while only confocal and multiphoton microscopy capable of performing 3D FLIM z-stacks.

2.4.2. Fluorescence lifetime imaging microscopy (FLIM) to monitor cellular metabolism

All cells require a source of energy to maintain homeostasis and feed energy-consuming processes such as cytoskeletal dynamics, transcription, translation and DNA repair. Cell metabolism also provides the building blocks for production of nucleotides, phospholipids and amino acids [30]. Metabolism in cells has evolved to sense locally available nutrient required to supply the cell to fulfil their biomass needs. When nutrients are scarce, cells halt biomolecular precursor production (amino acids, nucleotides and acetyl-CoA) and adapt to extract maximum free energy from available resources to survive. Differences in metabolic pathways are dictated by distinct regulatory mechanisms that can control and adjust the cellular metabolism in differentiated and proliferative cells [31]. In most mammalian cells, glucose and glutamine are predominantly catabolized and used as sources of carbon, nitrogen and energy. The breakdown of glucose follows two major pathways: Glycolysis and Oxidative Phosphorylation (OxPhos) to ensure efficient production of functional biomolecules and adenonise 5'- triphosphate (ATP) which is the main component of cellular energy and as fuel for important homeostatic reactions happening in the cell (Figure 2.3). Glutamine undergoes glutaminolysis which generates biomolecules and helps fuel the Krebs cycle. [32, 33].

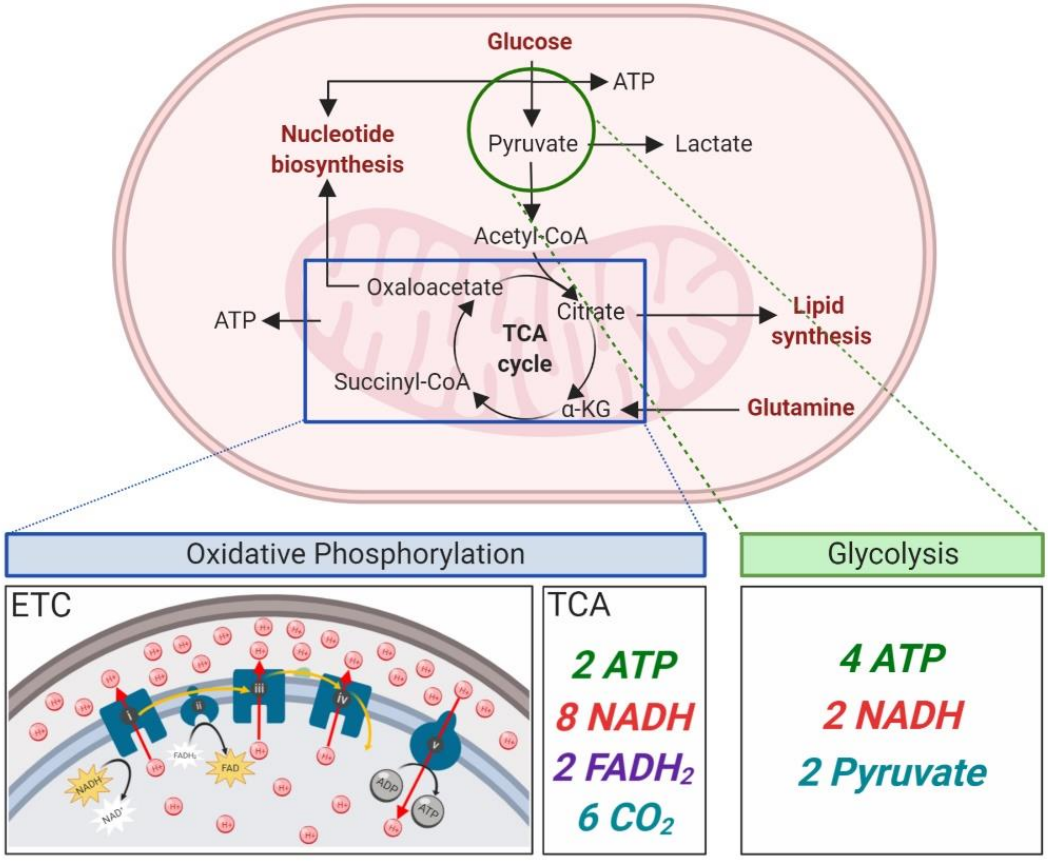

Figure 2.3 –Overview of glycolysis and oxidative phosphorylation. OxPhos was divided in two major pathways: tricarboxylic acid cycle (TCA) and the electron transport chain (ETC). Major by-products of glycolysis and TCA are highlighted as well as a schematic for the ETC process. Figure was created with BioRender.com

Glycolysis is the starting point for the breakdown of glucose. It occurs in cell cytoplasm and culminates in the formation of pyruvate. From here, pyruvate is shuttled inside the mitochondria, aided by mitochondrial pyruvate carriers or, can be used as a substrate to produce lactate. In the mitochondria, the starting point of the OxPhos pathway; pyruvate is converted to acetyl-CoA which is used to feed the Krebs cycle by producing two electron carrier species (NADH and $FADH_2$) and important biomolecules for lipid, amino acid and nucleotide synthesis, such as citrate, malate, oxaloacetate and α-ketoglutarate. Afterwards, both NADH and $FADH_2$ react with enzymes on the electron transport chain (ETC), specifically, NADH:ubiquinone oxidoreductase (complex I) and succinate:ubiquinone reductase (complex II), respectively. Here, the passage of electrons between the different protein complexes releases energy which is stored as a proton gradient across the mitochondrial inner membrane ending

in the formation of adenonise 5'- triphosphate (ATP) from adenosine 5'-diphosphate (ADP) at complex V or F1F0-ATPase. Overall, the OxPhos pathway yields 36 mol of ATP per mol of glucose consumed and, in addition; it produces CO_2 and reactive oxygen species (ROS) while consuming O_2 (Figure 2.3). In the cytoplasm, pyruvate conversion to lactate occurs without the consumption of O_2 and with only 4 mol of ATP produced per mol of glucose consumed [31, 34-36].

Glutamine is imported to the cell and used for the production of glucosamine (in conjugation with glucose), nucleotides and proteins. Furthermore, it undergoes glutaminolysis and is lysed by glutaminase into glutamate and ammonia. Glutamate is then imported into the mitochondria where glutamate dehydrogenase converts glutamate into α-ketoglutarate generating nicotinamide adenine dinucleotide phosphate (NADPH) while replenishing the Krebs cycle (Figure 2.3). The last step of glutamine metabolism makes it an anaplerotic pathway which can be used to feed oxidative phosphorylation if glucose concentration is low [32, 33].

Aside from the availability of nutrients in the microenvironment, cellular metabolism can also be affected by other intrinsic or extrinsic factors such as genetic mutations [37], viral/bacterial infection [38], hormone or cytokine response [39], cell density (inhibition by contact) [40] or chemical metabolic challengers [41]. Interestingly, cell metabolism can be more than just a response to a stimuli or a microenvironment condition. An emerging field, known as immunometabolism, has established a definitive relationship between immune cell function and metabolism. It is widely acknowledged that M1 polarized macrophages with pro-inflammatory responses are glycolytic, whilst anti-inflammatory M2 activated macrophages are characterized by an oxidative phosphorylation dependent metabolism [42]. The relationship between immune cell function and metabolism is also observed in activated effector T-cells and activated natural killer (NK) cells [9]. Activated T-cells have a higher dependence on glycolysis

compared with naïve T-cells [43]. In addition, activated NK-cells are more reliant in both glycolysis and OxPhos when comparing compared with their resting state [44].

In addition to immune cells, stem cells and differentiated cells possess distinct metabolic phenotypes. Stem cells are majorly glycolytic whereas their differentiated counterpart is more OxPhos. Remarkably, when pluripotency is induced, their metabolic features revert back to a glycolytic state present in native stem cells [45].

The coupling of FLIM measurements with multiphoton microscopy has opened a new modality to probe cellular metabolism in a non-invasive manner. Lakowicz et al. were the first to measure the fluorescence lifetime of free and protein-bound nicotinamide adenine dinucleotide (NADH) uncovering the potential of gauging this endogenous fluorophore and its impact on metabolism [46]. Since NADH has a single-photon excitation wavelength of 360 nm it requires powerful and cell damaging excitation sources. With the use of multiphoton microscopes this problem is resolved by exciting NADH with 740-760 nm and allowing in vitro and in vivo metabolic profiling [47-50]. Following this, Huang et al. reported fluorescence spectroscopy and multiphoton microscopy of both NADH and FAD which are spectrally distinct at 750 nm and 900 nm excitation wavelengths. In addition, it is possible to separate both light emitting species by their emission wavelength provided an adequate 410-490 nm bandpass filter for NADH and 510-560 nm bandpass filter for FAD [51].

With FLIM it is possible to uncover the role of these factors on the major cellular metabolic pathways (Figure 2.3). Therefore, FLIM microscopy opens a pathway for non-invasive metabolic imaging and analysis that allows deeper understanding of the connections between metabolism and cell function or phenotype, while enabling metabolic probing in real-time. Furthermore, it can unveil distinctive metabolic features present in diseases (eg. cancer), consequences of external and infer on their impact and improve treatments, immune cell function or stem cell differentiation while uncovering cell dependence on a specific metabolic

profile. Using a multiphoton microscope (MPM) coupled with a fluorescence lifetime imaging microscopy (FLIM) or phosphorescence lifetime imaging microscopy (PLIM) detector, it is possible to evaluate NADH and FAD [47, 52, 53], and O_2 concentrations using exogenous probes

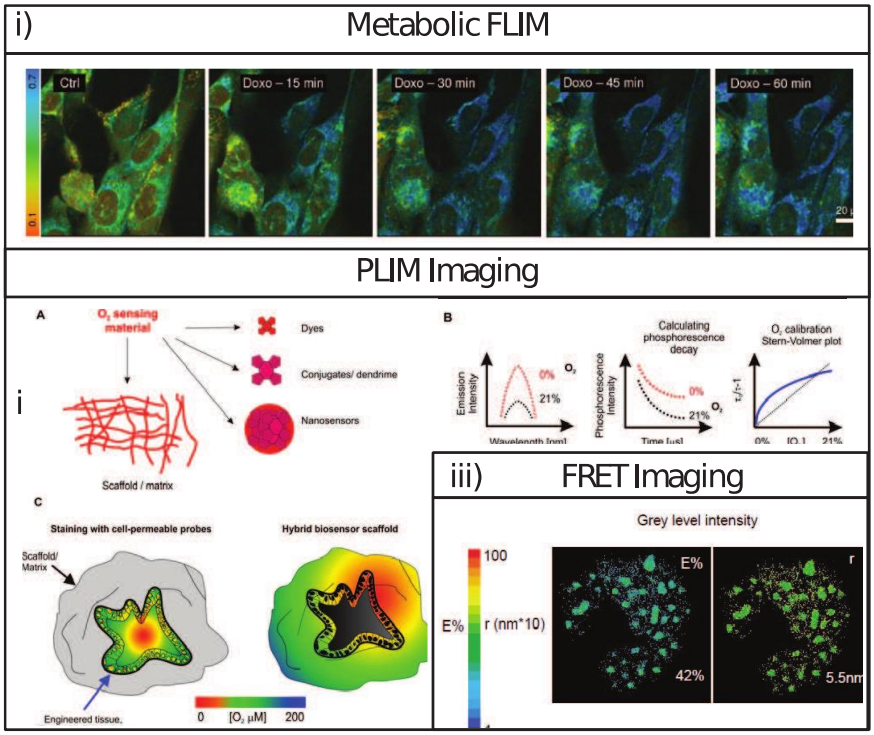

Figure 2.4 - Overview of FLIM, PLIM and FRET imaging. i) in vivo multiphoton FLIM images representing the continuous effect of doxorubicin on the optical redox ratio of human prostate cancer cell line. Reproduced from Wallrabe et al. (2018) with permission from Springer Nature. ii) functionalization strategies for scaffolds/matrixes (a,c) and dynamics of O_2 concentration measurements by PLIM (b). iii) intensity-based FRET with estimation of energy transfer efficiency (E%) and distance between probes ® used to identify C/EBPa (CCAAT/enhancer binding protein a) dimerization. Reproduced from Wallrabe et al. (2005) with permission from Elsevier.

[54] (Figure 2.4). An emerging application of such non-invasive microscopy is cell-specific metabolic analysis which has found application in tumor biology, immunology and organoid research fields [47, 55].

NADH fluorescence lifetime typically exhibits a double-exponential decay which is decomposed in a short lifetime related with free NADH in the cytoplasm, and a long lifetime reflective of enzyme-bound NADH [46]. Following equation 5 is possible to calculate the fraction respective to each of them. In a single cell type, the enzymes in which NADH reacts are well conserved regions in a cell, meaning that the majority of the shifts in fluorescence lifetime

fractions are connected with the free-NADH fraction. Generally, when this fraction increases the cell metabolic profile is tending towards glycolysis. Conversely, when this fraction decreases, the cell is less dependent on glycolysis [56]. Regarding NADH fluorescence intensity, it was been shown that increasing glucose concentration in the cell culture medium or adding glycolysis inhibitors increases NADH autofluorescence revealing a higher usage of the OxPhos pathway [50]. However, NADH fluorescence intensity and lifetime have limited capacity for fully grasping the cell metabolic profile, nonetheless, they are well suited for separating distinct cellular populations or following disease progression [57].

The coenzyme nicotinamide adenine dinucleotide phosphate (NADPH) possesses an overlapping excitation and emission spectra with NADH and hard to be separated [58]. Although the NADPH contribution is 10 times lower than NADH, NADPH still contributes significantly to cell autofluorescence [59]. Fluctuations of NADPH levels are intertwined with the long-lived component of the fluorescence lifetime decay – protein-bound NADH. NADPH processes two major biological functions: acting as an electron source for synthesis of fatty acids, steroids and DNA, and a key component in cellular antioxidation systems intertwined with the production of reactive oxygen species [60, 61]. Although, it is still important to understand how the metabolic profile is being affected in the experimental conditions or to perform a biochemical assay to fully understand the impact of NADPH on the cell metabolism.

Assessing other metabolic co-factors besides NADH can add additional information to metabolic profiling. The endogenous molecule flavin adenine dinucleotide (FAD) is commonly used due its autofluorescence. After measuring the fluorescence intensity of both co-factors, is possible to calculate the redox ratio by following Equation 2.4:

$$Redox\ Ratio = \frac{FAD_{photons}}{NADH_{photons}}$$

Equation 2.4 – Redox Ratio Equation

This redox ratio has been associated qualitatively with metabolic profiling after challenging of the glycolytic or oxidative phosphorylation pathway [27]. During both these metabolic pathways, there is a regeneration of fluorescent NADH and during OxPhos; the formation of non-fluorescent $FADH_2$. Following Figure 2.3, NADH is converted to non-fluorescent NAD^+ by complex I and $FADH_2$ to fluorescent FAD^+ by complex II of the electron transport chain. When OxPhos is more active there is more production of $FADH_2$ and therefore more FAD^+ production leading to a rise of FAD^+ fluorescent intensity culminating in an increase of the redox ratio. On the contrary, when glycolysis is majorly used to obtain energy, NADH is produced increasing its fluorescence emission and FAD^+ regeneration has been hindered resulting in an decrease of the redox ratio [62]. Furthermore, is possible to combine both fluorescence intensity measurements and lifetimes to originate the optical redox ratio (ORR) which confirms and better describes the shifts in cellular metabolism (Figure 2.4i) [63].

While measuring endogenous FAD/ NADH (redox or optical metabolic imaging) is highly informative, frequently there is a need in assessing additional parameters of cell metabolism, such as analysis of mitochondrial polarization, oxygen consumption, extracellular acidification, lipid droplets production and others. The majority of these additional parameters are measured via exogenously introduced or genetically encoded fluoro- and phosphores [64].

For example, a number of genetically encoded fluorescent protein biosensors (which require transfection to be introduced into eukaryotic cells) can serve as indicators of redox, peroxide production or NADH:NAD^+ ratio [65, 66]. Mitochondrial membrane potential can be assessed by intensity- or FLIM-based measurement, with the help of tetramethylrhodamine methyl ester dye (TMRM) [67, 68]. TMRM is a membrane permeable molecule which accumulates mainly in both the inner mitochondrial membrane and matrix space of live cells due to its charge and solubility. The change in TMRM uptake is linked to shifts in the mitochondria membrane potential which results in variations of the fluorescence intensity. By

measuring the fluorescence intensity at 573 nm and 546 nm, it is possible to estimate the mitochondria membrane potential [69]. This molecule, also has the possibility to be used as an exogenous multiphoton FLIM probe [70].

Table 2.1 – Examples of endogenous fluorophores commonly analyzed and used on FLIM.

Fluorophores	Excitation peak (nm)	Emission peak (nm)	Fluorescent Lifetime (ns)	Reference
NAD(P)H	690-730*	425-500	2.40 (long) 0.40 (short)	[71]
FAD	890*	500-560	3.38 (long) 0.12 (short)	[71]
Collagen	700-1000*	λext/2	1.7 (long) 0.3 (short)	[72-75]
Elastin	700-1000*	400-650	1.95 (long) 0.26 (short)	[72, 76]
Tryptophan	500-580* 710-730**	340-385	3.30 (long) 0.67 (short)	[77]
Serotonin	560; 630	325-400	3.8	[78, 79]
Keratin	720-800*	360-410	2.27 (long) 0.45 (short)	[78, 80, 81]
Melanin	800*	500-700	1.08 (long) 0.14 (short)	[78, 80]
Tyrosine	565-610*	450-550	1.8	[82-84]

* corresponds to two-photon excitation, ** three-photon excitation and absence of marking is a standard 1-photon excitation. Emission wavelengths (λ_{emi}) are indicated with correspondent fluorescence lifetime (τ) for double and single fluorescence decays.

In addition to endogenous or exogenous fluorophores, there is also the possibility to employ genetically encoded fluorescent biosensors. One strategy to create these protein biosensors involves using circularly permuted fluorescent proteins derived from GFPs [85]. The circular permutation joins the original N and C terminal by a peptide linker and a specific reporter or binding protein is fused to the new coupled terminal complex originating a conformational coupling between fluorescence emission and binding to a molecule of interest [86] . This approach has been applied to probe further the glycolysis flux [87], intracellular pH [88], NADH/NAD^+ [89] and ATP/ADP ratio [90]

When performing live cell imaging it is necessary to consider possible contributions of the fluorophores described in Table 2.1. Especially where some tissues have fluorophores in abundance such as the brain (serotonin) and epidermal (keratin, melanin) tissue. Nonetheless, by careful selection of excitation wavelengths and bandpass filters is possible to ascertain the contribution of each molecule [51].

Live cell imaging using 2P-FLIM has been explored since beginning of the 2000s. This technique has been applied in vitro, in vivo and 3D cell cultures such as spheroids or biomedical constructs (Table 2.2). After the establishment of protein-bound and free NADH fluorescence lifetimes by Lakowicz et al.in 1992, and the possibility to combine FLIM with multiphoton microscopy, there was an increasing interest to apply 2P-FLIM of NAD(P)H in live cell imaging applications [46, 72]. At first, live cell imaging using 2P-FLIM focused on cancer research due to the possibility to distinguish healthy tissue and cancer tissue by differences in cellular metabolism due to the established Warburg effect [91]. Afterwards, with advances in cellular biology and metabolism, the connection between cellular metabolism with cell type and cellular behavior was established. This further increased the research interest in performing 2P-FLIM of NAD(P)H in live-cell imaging applications with spatiotemporal resolutions (Table 2.2). Recently, new metabolic trends are being observed using 2P-FLIM across multiple tissues and cell types such as brain, intestinal, stem cells, immune cells and 3D cell cultures (Table 2.2). In addition, new methods of analysis have been employed to 2P-FLIM data. In particular, unsupervised and supervised advanced statistical analysis such as PCA and machine learning models, respectively [92]. For this thesis, 2P-FLIM live cell imaging was applied to human bone-marrow derived mesenchymal stem cells and human macrophages.

Table 2.2 – Overview of 2P-FLIM live-cell imaging applications reported in the literature

Authors	Cell type	Year	Main Finding	Reference
Walsh A. et al	Human peripheral blood derived T-cells	2021	2P-FLIM and machine learning models can classify T-Cell activation	[92]
Alfonso-Garcia A. et al	Bovine pericardium scaffolds seeded with human aortic endothelial cells or human MSCs	2017	2P-FLIM can follow recellulariszation of vascular tissue constructs	[93]
Meleshina A. et al	Human bone-marrow MSCs	2016	Adipogenic differentiation triggers a shift from glycolysis to OxPhos	[94]
Ma N. et al	Chinese hamster ovary (CHO-K1) cells	2016	Measuring NAD(P)H cellular concentrations	[95]
Alfonso-Garcia A. et al	Murine macrophages	2016	2P-FLIM can measure murine macrophage polarization based on cellular metabolism	[96]
Walsh A. et al	Primary human breast tumor biopsy-derived organoids	2014	Fluorescence lifetime and fluorescence intensity ratios of NAD(P)H/FAD^+ can measure tumor response to anticancer drugs and detect drug-resistant organoids	[97]
Blacker T. et al	HEK293 cell line and murine cochlear explants	2014	NADPH is associated with higher protein-bound fluorescence lifetimes	[98]
Yaseen M. et al.	In vivo murine cerebral cortex	2013	Measuring in vivo brain metabolic transients with decreased OxPhos in anoxia conditions	[99]
Stringari C. et al	Murine small intestine tissue	2012	Lower fluorescence lifetimes are associated with glycolysis and can identify high proliferative cells	[100]
Konig K et al.,	3D human salivary gland stem cell spheroids	2011	Adipogenic differentiation increases fluorescence lifetimes and reduces fluorescence intensity	[101]
Sun Y et al.,	In vivo hamster carcinogenesis model	2009	Diagnosis of oral carcinoma in an in vivo setting with lower fluorescence lifetimes in tumor tissues	[102]
Dimitrow E. et al	Human skin tissue	2009	Melanin impacts fluorescence lifetimes and can be used to diagnose melanoma	[80]
Uchugonova A. et al	Murine and human stem cells	2008	Stem cells can be imaged together with SHG	[103]
Skala M., et al.	MCF10A human breast epithelial cell line and hamster cheek pouch model of oral cancer	2007	Cancer cells were distinguished by normal epithelial cell by decrease fluorescence lifetime	[91]

2.4.2.1. Mesenchymal stem cells

Mesenchymal stem cells (MSCs) are a non-hematopoietic subpopulation of cells with potential to differentiate into various tissues such as cartilage, fat and bone [104]. As well, MSCs induce a regenerative microenvironment by secreting bioactive molecules that inhibit tissue scarring, apoptosis, promoting angiogenesis and stimulate cellular division of tissue intrinsic or progenitor cells [105]. Due to these features, MSCs are a promising therapeutic tool for clinical applications such as tissue engineering and stem cell-based therapy. Nonetheless, MSCs need to be extensively evaluated for their properties and possible applications.

MSCs are found in various tissues in the human body, such as bone marrow, fat tissue, and muscle. However, they are mainly dormant and available in small quantities [106]. For tissue engineering and stem-cell based therapies, most strategies require adult MSCs to be isolated, expanded to large numbers or differentiated into mature cells [107]. Advances in stem cell biology have showed that cellular metabolism has an important role in dictating cellular fate [108].

Glycolysis is a specific feature of stemness and the major pathway to ensure stem cell survival and proliferation [109]. Compared with OxPhos, glycolysis has lower rates of ATP production. However, proliferating stem cells have metabolic requirements, such as biomolecules, that extend beyond ATP levels [31]. Specifically, glycolysis fuels the synthesis of amino acids and nucleotides via the pentose phosphate pathway (PPP) [30]. However, stem cell glycolysis still requires the contribution of oxidative phosphorylation with production of biosynthetic intermediates and ATP generation. Known as the Warburg effect, aerobic glycolysis in stem cells converts most of the pyruvate produced during glycolysis to lactate in the presence of oxygen [30] . Vander Heiden et al., estimated that glycolysis in proliferating cells only used 5

to 10% of the pyruvate to fuel oxidative phosphorylation while the remaining pyruvate is converted to lactate [31].

MSC differentiation promotes a metabolic switch depending on the differentiation pathway. MSCs cultured under chondrogenic conditions retain their glycolytic activity highlighted by reduced oxygen consumption and OxPhos activity [110]. The glycolytic dependence during chondrogenic differentiation is also highlighted by the increased secretion of glycosaminoglycan (GAGs) in hypoxic (4% O_2) cell culture conditions. Interestingly, higher O_2 concentrations such as normoxia negatively impact chondrogenic differentiation [111]. MSCs undergoing osteogenic or adipogenic differentiation are reliant on oxidative phosphorylation for most of their energy production. Osteogenic or adipogenic differentiation promotes a decrease in glycolytic enzymes while increasing oxygen consumption and mitochondrial biogenesis [112, 113]. Remarkably, slow-proliferating, differentiated cells can be reprogrammed to achieve pluripotency. These induced pluripotent stem cells (iPSCs) are also characterised by having a high glycolytic metabolic flux [114]. The metabolic reprogramming required to achieve pluripotency demonstrates that glycolysis is a metabolic hallmark of pluripotency (Figure 2.5).

Metabolic flexibility fuels MSCs functions, however it is important to take in account that metabolic pathways are sensitive to oxygen levels, availability of metabolic substrates such as pyruvate and glutamine, and pH levels [115]. This high sensitivity of MSCs to environmental conditions is sometimes overlooked and can mask important metabolic profiles when pursuing research in MSCs metabolism and bioenergetics. A study from Chen et al., reports activation of oxidative phosphorylation during MSCs osteogenic differentiation. Since this study did not account for contributions of mitochondrial uncoupling generating larger number of viable mitochondria or nonmitochondrial oxygen consumption by using metabolic inhibitors, it was not clear if the increase of oxygen consumption is entirely indicative of oxidative phosphorylation [112]. As a counter-point Eses et al., observed no changes in oxidative

phosphorylation when stimulating osteogenic differentiation in MSC-like stromal cell line ST2 cells by activation of the WNT signalling pathway, possibly due to a high pyruvate concentration in the cell culture medium [116]. Nonetheless, with the increasing interest in cellular metabolism, new techniques are being developed to continue to probe and highlight the metabolic shifts occurring during osteogenic differentiation. These techniques such as the usage of biorthogonal reagents in combination with cell-compatible click chemistry or improving isolation of organelles in a live cell are being currently developed to further probe cellular metabolism at a single-cell level [117, 118]. In addition, more information regarding the impact of environmental cues in MSCs differentiation is being uncovered such as the impact of oxygen, biomaterial stiffness or paracrine signalling [119-121].

With a full grasp on MSCs metabolic dependence during differentiation, it is possible to tweaks to cell culture conditions and environments to promote higher cell survival and cellular differentiation for applications in tissue engineering and stem-cell based therapies.

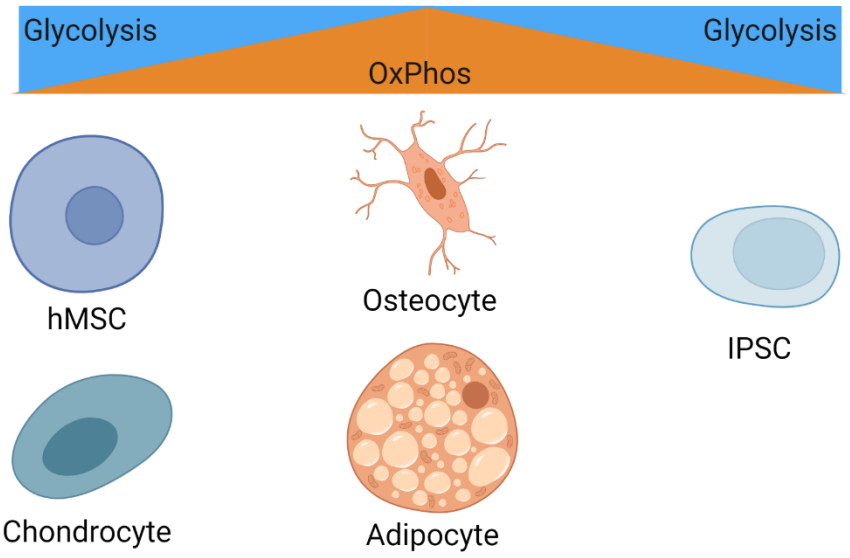

Figure 2.5 – Metabolic profile of mesenchymal stem cells, differentiated stem cells and induced pluripotent stem cells.

Metabolic 2P-FLIM has the potential to uncover non-invasively and in real-time the differentiation of stem cells in order to gain deeper understanding of the full metabolic shifts

occurring during cell differentiation. Quinn et al., followed stem cell differentiation by using only two-photon microscopy highlighting the usage of the optical redox ratio (ORR) and followed with analysing mitochondria morphology, in particular MitoTracker™ staining intensity and range of fractal clustering. A higher dependence upon oxidative phosphorylation was observed for both adipogenic and osteogenic stem cell differentiation. In addition, it was observed an increase in fractal clustering of mitochondria after 28 days in cell culture, reflecting elongation and maturation of interconnected mitochondrial networks increasing fatty acid synthesis and oxidative phosphorylation. [122]. Another study by Meleshina et al., used 2P-FLIM of NAD(P)H and FAD^+ to follow MSCs differentiation towards osteogenic or chondrogenic differentiation [123]. Here, it was observed a shift towards glycolytic metabolism during chondrogenic differentiation whilst a metabolic shift to OxPhos was observed during osteogenic differentiation. However, for the studies reported by both Quinn and Meleshina, cell culture conditions of hMSCs are not fully described. There is no description of glucose concentration pyruvate or glutamine concentrations added to the within the media and these metabolites serve as important sources of carbon for metabolic pathways.

To conclude, research in hMSCs metabolism during cell differentiation mostly shows a trend towards oxidative phosphorylation in osteogenic and adipogenic differentiation whilst chondrogenic differentiation seems to be more reliant on glycolysis. However, some reported studies do contradict this trend [124, 125]. This might be due to the differences in MSCs differentiation protocols from lab to lab, from the concentrations of metabolites to cell density. There appears to be a wide dispersion of methodologies to promote MSC differentiation which makes the understanding of cell differentiation being dependent on a specific metabolic pathway difficult to make. One way to avoid these common pitfalls is a full transparency regarding the cell culture conditions including medium formulation and validate the metabolic shifts using multiple biochemical assays.

2.4.2.2. Macrophages

Cellular metabolism is known to regulate macrophage function and polarisation with current research highlighting the role of metabolic reprogramming in macrophage activation [126]. The first described functions of macrophages were phagocytosis and microbial killing [127]. Later research demonstrated that macrophages have important roles on host defence, tissue homeostasis and tissue repair [127]. To accommodate different functions, macrophages adopt various activation states. Macrophage activation states depend on the microenvironment stimuli and amount of cytokines and chemokines produced by other immune cells [128]. Macrophage polarisation has been classically dived into two major macrophage polarisation subsets: pro-inflammatory M1 macrophages and anti-inflammatory M2 macrophages. Each polarisation subset is related to a specific immune response, in which promoting or resolving an inflammation process is a critical factor. However, macrophage polarisation in many physiology and pathologic environments is present on a continuum spectrum, involving high plasticity and heterogeneity of macrophages that do not fit the simplified M1/M2 classification [129]. Therefore, precise regulation of macrophage activation is required for disease control and to ensure tissue homeostasis. When macrophage function becomes dysregulated or the ratio between M1/M2 macrophages is unbalanced, disease complication can arise such as chronic wounds or excessive deposition of scarring tissue [130]. Due to the direct connection between cellular metabolism and macrophage function, immunometabolism has emerged recently as a focus of research in immunology associated with chronic inflammatory diseases, cancer or atherosclerosis [42, 131].

M1 macrophages *in vitro* are often polarised using potent activators such as interferon-gamma (IFNγ) and lipopolysaccharide (LPS). These activated macrophages are known as exhibiting an inflammatory phenotype [132]. This inflammatory phenotype is crucial as a first systemic response to pathogens and other viral aggressions. Pro-inflammatory macrophages

polarisation occurs in the beginning of the inflammatory response, lasting some hours. Due to the quick activation and rapid function of M1 macrophages, there is a need for fast generation of ATP and biomolecules. Immunometabolic research has demonstrated that glycolysis is upregulated in M1 macrophages to fulfil this demand of fast energy [133] with M1 macrophages are known for also having impaired OxPhos [42]. Although glycolysis produces lower amounts of ATP compared with OxPhos, its quick activation is a major advantage in response to pathogen infection [134]. Glycolysis in M1 macrophages not only produces quick ATP for phagocytosis and secretory functions but also fuels the pentose phosphate pathway [134]. The combination of glycolysis with pentose phosphate pathway supports the inflammatory phenotype of macrophages by generating amino acids for protein synthesis, nucleotides and NADPH for production of reactive oxygen species (ROS) [126]. Furthermore, glycolysis also generates pyruvate which can fuel OxPhos, in particularly the tricarboxylic acid cycle (TCA). In M1 macrophages the TCA cycle is disrupted in two ways: after the production of citrate, and after production of succinate [135]. Increased synthesis of acetyl coenzyme A (Acetyl-CoA) from citrate meets the biosynthesis demands of fatty acids, lipids and prostaglandins [136]. Fatty acid synthesis, downstream from citrate and acetyl-coA is an integral part of the inflammatory response and organizes the plasma membrane for inflammatory signalling [137]. In addition, the accumulation of succinate results in the stabilisation of HiF1-α and IL-1β [138]. HIF-1α stabilisation regulates the inflammatory response in M1 macrophages in environments with variable oxygen levels whilst IL-1β acts as a proinflammatory cytokine with pleiotropic regulation on other cells [139, 140].

M2 macrophage metabolism is in sharp contrast to inflammatory macrophages. These anti-inflammatory macrophages have longer term functions when compared with short-lived inflammatory macrophages. M2 macrophages are involved in maintaining tissue homeostasis as well to ensure tissue repair and angiogenesis [141, 142]. These roles require sustained amounts of energy for longer periods of time contrary to M1 macrophages. As a consequence,

upregulation of oxidative phosphorylation is observed since OxPhos is able to sustainably produce higher amounts of ATP and other biosynthetic metabolites compared with glycolysis [42]. Anti-inflammatory macrophages have an intact TCA cycle and enhanced mitochondrial OxPhos. In addition, increased fatty acid oxidation, fatty acid synthesis and glucose uptake has been observed in M2 macrophages and deemed necessary to fuel OxPhos [143].

Many metabolic studies of macrophages are established in *in vitro* settings. In such experiments, macrophages are cultured (often on plastic) and polarised to a desired state using different stimuli such as IFNγ, LPS or interlukin-4 (IL-4). However, the metabolic changes observed in macrophages in an *in vitro* platform remain to be fully appreciated in an *in vivo* setting [126]. One of the layers of complexity is the abundance of carbon sources in cell culture medium, whereas in contrast, nutrient competition *in vivo* can impact macrophage metabolism and therefore polarisation [144].

Current metabolomics methods have limitations to fully evaluate the metabolic profile of immune cells. Metabolomics techniques are invasive, require large cell numbers and intense sample processing [145, 146]. 2P-FLIM due to its non-invasive methodology, requires low number of cells and allows the possibility for real-time *in vivo* imaging.

2P-FLIM has been previously applied to infer on macrophage polarisation and metabolic profile *in vitro* and *in vivo* conditions. Alfonso-Garcia et al., demonstrated the use of 2P-FLIM to validate the polarisation of murine macrophages in vitro. Here, murine macrophages were polarised towards an M1 phenotype using IFNγ + LPS and to M2 macrophage using IL-4/IL-13. Macrophage polarisation was verified using immunohistochemistry to check for specific polarised macrophage markers such as iNOS for M1 macrophage and arginine for IL-4/IL-13. Using 2P-FLIM, a higher ratio of free NAD(P)H was observed for M1 macrophages, revealing a higher dependence on glycolysis when compared to M2 macrophages [147]. In addition, a study by Szulczewski et al., demonstrated the possibility to use 2P-FLIM for *in vivo* characterisation of

stromal macrophages. Here, 2P-FLIM was used combined within an intravital imaging murine model. Here, the metabolic profile of macrophages was observed concomitant with the metabolic profile of tumour cells. Interestingly, it was observed that macrophages in a tumour microenvironment have higher FAD intensity whilst tumour cells have higher NADH levels. It was also observed that macrophages have a more glycolytic profile than tumour cells [148]. Both these studies showcase the potential of 2P-FLIM to be used as a methodology for metabolic characterisation of macrophages and other immune cells in in vitro or in vivo setting.

2.5. Advanced methods of 2P-FLIM data analysis

2P-FLIM microscopy generates large amounts of experimental data. During 2P-FLIM, several experimental variables are collected at the same time. In a single data acquisition process, fluorescence intensity, fluorescence lifetimes, fraction of fluorescence lifetime are collected. Furthermore, τ_{avg} and ORR variables can be calculated using this raw data. In addition, cell type and experimental conditions are variables used to define the experimental group.

Usually, the variables that define experimental groups are common to all experimental methodologies in research. However, comparing with other common experimental tools such as confocal microscopy, colorimetric assays, PCR or flow cytometry, 2P-FLIM generates more than 1 or 2 dependent variables. 2P-FLIM of NAD(P)H to study cellular metabolism relies on the application of double exponential decay to raw data. The application of a double exponential decay to 2P-FLIM data allows the extraction of 6 dependent variables: τ_1, τ_2, α_1, α_2, τ_{avg} and NAD(P)H fluorescence intensity. In this thesis, NAD(P)H intensity values with FAD^+ fluorescence intensity to calculate the ORR. Therefore, throughout this thesis, the 2P-FLIM experimental setup derives 6 dependent variables. With this amount of variables that 2P-FLIM can generate, multivariate data analysis can be applied. These data analysis methods such as PCA and UMAP are useful to increase data interpretability without any information loss and possibly establish new correlations while determining variable importance. Furthermore, machine learning

models and application to biomedical sciences has started to gain traction. These advanced algorithms can allow the determination of important features for the outcome observed, to classify or predict experimental trends.

Multivariate data analysis techniques have been applied to large datasets in biomedical sciences. The application of multivariate data analysis techniques have been used to data mining and different “omics” approaches such as genomics, transcriptomics and metabolomics [149-151]. Consequently, the widespread and application of high-throughput techniques and the establishment of large public data bases will increase the relevance of PCA and UMAP analysis in biomedical research.

2.5.1. PCA

Principal component analysis is one of the most widely used techniques for data visualization and to reduce data dimensionality while preservation most of the information [152]. The application of PCA ranges from theoretical physics to meteorology, biology, chemistry and engineering [149, 153]. PCA analyses a dataset with multiple experimental observation described by various inter-correlated dependent variables. PCA is a descriptive tool that needs no distributional assumptions regarding original data distribution. This means the original data does not require to a Gaussian or logarithmic distribution to be able to apply PCA. The main goal of PCA is to extract information from the dataset and express this same information as a set of orthogonal variables. These orthogonal variables are known as principal components. PCA analysis plots these principal components while representing the pattern of similarity between experimental observations [154]. To ensure data visualization and reduce data dimensionality, PCA uncovers new variables which are linear functions of the original variables present in the data set. These new variables maximize variance while being uncorrelated with each other. To find these new variables, PCA, reduces data variabilities to an eigenvalue/eigenvector problem. Here, the eigenvalues are calculated between the dependent variables correlation matrix [155].

The dataset to be analysed by PCA comprises of experimental observations *I* described by *J* dependent variables generating a *I x J* matrix *A*. During the processing steps, the dependent variables are normalised so that the mean of each variable is equal to 0. In addition, if variables are measured in different units, there is a standardization processing. The standardization processes divides each variable by the square root of the sum of all the squared elements of the same variable. Afterwards, PCA components are determined by applying singular value decomposition to matrix *A* and calculated by the product of the matrix of left singular vectors by the diagonal matrix of singular values [154]. After the calculation of two principal components, these are plotted by attributing principal component 1 to *x*x axis and the second principal component analysis for *yy* axis. Principal components are uncorrelated and ordered in such way that the *kth* PC has the *kth* largest variance amongst all principal components [156] (Figure 2.6). For this thesis, a custom built python code for the calculation of PC1 and PC2 was written. This code is available in Computer Code Appendix 1.

PCA as a multivariable analysis tool has been used for data analysis in methodologies that generate a wide range of dependent variables or wide range of observations. A study by Alonso-Gutierrez et al., used PCA analysis of proteomic results to direct metabolic engineering of Escherichia coli to improve production of terpenes by upregulation of the mevalonate pathway [157]. Here Alonso-Gutierrez used as dependent variable the relative enzyme expression values of several strands of modified *E.Coli*. These relative expression values were compared with the production of terpenes and PCA was used plot the strands of *E.coli* in order to determine which enzyme expression levels promote higher production of terpenes. In addition, by analysing the multiple principle components, it was concluded that increased terpene production is associated with overexpression of terpene synthase enzyme combined with a balanced expression of the upstream enzymes in the mevalonate pathway. This methodology provides a guided method to increase the production of terpene by *E.Coli* for biotechnology applications.

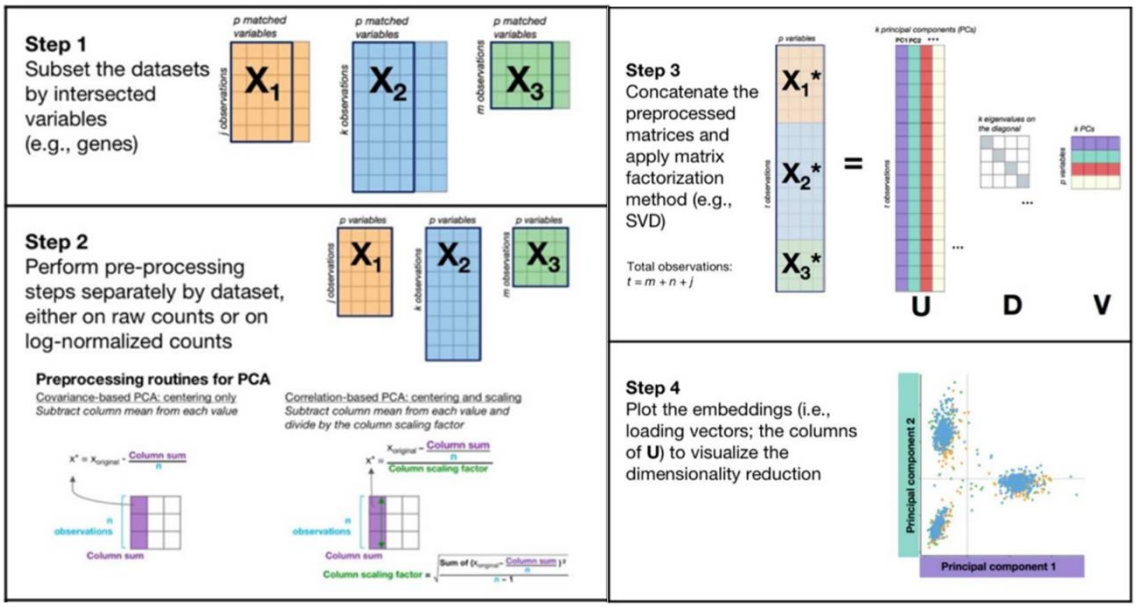

Figure 2.6 – Schematic of PCA algorithm to calculate principal components of a dataset [154]

PCA is also used to analyse genomic data. PCA analyses of genomic data, allows the discovery of a specific sample population structure or other latent effects on specific groups of data such as batch errors or variability [158]. The application of PCA to genomic data is also of high interest due to the large number of genes and the complexity of biological networks. Therefore, presenting this data visually enabling clustering for gene expression levels allows to determine the expression of certain genes required to observe a specific phenotypic outcome [159]. A study by Granucci et al., demonstrated another application of PCA analysis [160]. Here, dendritic cells were matured by exposure to gram-negative bacteria and a kinetic study of dendritic cells gene expression was performed using a microarray. During the several time-points, gene expression levels were measured and plotted in a PCA plot. In the PCA plot, the gene expression levels change after stimulation of dendritic cells reaching the biggest difference when compared with unstimulated dendritic cells at 18 hours. Afterwards, there is no changes until 48 hours after stimulation. The gene expression profile of dendritic cells is determinant of cellular phenotype and function. Using PCA revealed a pattern in a kinetic treatment study which conveyed diverse genetic profiles of dendritic cells at different time points.

PCA is an advanced statistical tool useful to be employed in large datasets or databases, as well, for samples with high numbers of dependent variables. The use of PCA allows the visualization of complex datasets and the clustering of experimental observations with similar dependent variables values. Therefore, it is possible to quickly identify samples that have higher variance or share similarities. This clustering can also promote a quick method for early classification of experimental samples, with applicability toward 2P-FLIM data.

2.5.2. UMAP

Uniform Manifold Approximation and Projection (UMAP) is a dimensionality reduction tool used to visualize complex datasets with multiple dependent variables [161, 162] (Figure 2.7). Therefore, UMAP has a similar role and application as PCA. PCA, as described before, uses linear combinations of variables to generate orthogonal variables that capture the variance present in the dataset. However, UMAP estimates a topology of datasets with large numbers of dependent variables and uses this information to produce a low dimensional (2D or 3D) orthogonal plot that preserved the relation between data points [161]. Comparing with PCA, UMAP analysis preserves better the elements of datasets. In particular, UMAP conserves local variance and global relationships between distinct experimental groups [163]. UMAP analysis has become particularly useful to define or classify different cell types in heterogeneous populations based on data from single-cell RNA-seq experiments [164, 165]. A study by Shifrut et al., demonstrated the application of UMAP analysis on RNA-seq data to screen for regulators of primary Human T-cell stimulation and immunosuppression [166]. Here, Shifrut et al., isolated primary CD8+ T-cells from Human donors. Using CRISPR-Cas9 gene editing technique, the authors were able to conduct a target screening using large single guided RNAs (sgRNAs). Due to the large numbers of data collected during the target screening, UMAP was used as a data visualization tool. By applying UMAP to the one thousand most variable genes, Shifrut et al.,

were able to observe dataclustering identifying stimulated and unstimulated T-cells in two individual Human donors [166].

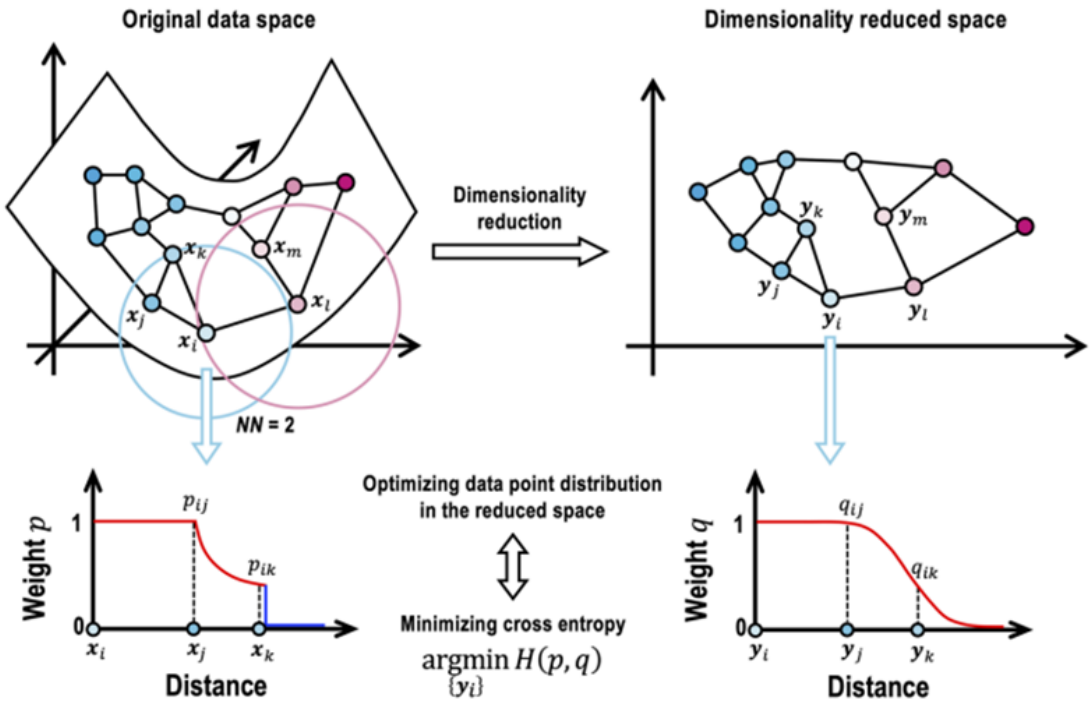

Figure 2.7 – Schematic illustration of UMAP algorithm [160].

2P-FLIM generates high numbers of dependent variables which can vary and respond to the experiment setup, there is a possibility of having large numbers of experimental observations. Walsh et al., applied UMAP as a data visualization tool to observe the distribution of activated or quiescence T-cells [92]. In this study Walsh el al., cultured human T-cells and induced an activated phenotype using anti-CD2-CD3-CD28 antibodies and applied immunofluorescence to distinguish the population of activated and quiescent T-cells. 2P-FLIM microscopy images were collected at different time points after the activation procedure. Afterwards, 2P-FLIM variables were used as a dataset to perform UMAP analysis. UMAP showed a clear trend and separation of activated and quiescent T-cell across all Human donors. The UMAP application was then the starting point to apply machine learning algorithms for T-cell

classification [92]. For this thesis, we applied UMAP analysis on 2P-FLIM variables. The python code needed to apply UMAP to 2P-FLIM variables is available on Computer Code Appendix 2.

2.5.3. Machine learning

Machine learning is defined as a field of computer science that gives computers the ability to learn without being explicitly programmed [167]. Machine learning evolved from the study of pattern recognition and computational learning theory in artificial intelligence. In particular, machine learning is established by algorithms that learn form a large dataset and makes prediction on the data [168, 169]. Recent advancements in advanced computing and imaging systems in the biomedical research field has provided a rise in new research dimension [170]. Large datasets are obtained from a single experiment whereby the degree of complexity increases with a higher number of conditions and dependent variables. The increasing size of experimental data requires precise machine learning-based data mining algorithms. Machine learning in biomedical research is usually based on deep learning-based approaches. Here, machine learning tasks are divided in two broad categories: unsupervised and supervised learning. In biomedical research, unsupervised tasks are associated to clustering of data whilst supervised machine learning algorithms are associated with the prediction of a categorical outcome (classification) [170].

Unsupervised learning algorithms are capable of detecting patterns in data without any kind of user supervision, such as, labelling. By being independent of labels or descriptions, unsupervised machine learning techniques are easier to implement and are suitable for exploratory analysis [171]. Unsupervised machine learning algorithms have already been covered in this chapter. Examples of unsupervised machine learning algorithms are PCA and UMAP. PCA and UMAP analysis use the dependent variables of experimental samples to establish relationships and orthogonal coordinates at lower dimension plots (2D or 3D).

Supervised machine learning methods are used to predict or classify an outcome of interest. These methods are used in prediction tasks were the objective is to forecast or classify a specific outcome of interest [172]. As an example, supervised machine learning algorithms can be used to determine the activation state of T-Cells or the presence of a disease [92, 173]. There are wide variety of supervised machine learning algorithms that can be applied to various types of dataset. In this chapter, there is going to be a focus on supervised machine learning algorithms that are commonly used in biomedical research and are applied later in this thesis. The three major supervised machine learning algorithms for biomedical research data are regression, support vector machines (SVM) and random forests [172].

The regression algorithm is a traditional parametric linear or logistic regression model. The regression algorithm is easily interpretable and easy to implement. However, the optimal function form of a regression algorithm and the interactions between variable must be specified before applying the algorithm. In addition, application of the regression algorithms to variables that are highly collinear makes the classification algorithm prone to over fitting. An over fitting classification algorithm occurs when the trained model does not make accurate predictions on the testing data [172].

SVM algorithm treats each predictor (dependent variable) as dimensions in a high dimensional space. Here, the algorithm identifies the best hyperplane to separate the samples into classes. SVM also tries to find the hyperplane with the maximum margin between the two closest points in space. This algorithm is adequate for highly complex data such as datasets including text, values and images or when the number of predictors is higher than the number of experimental observations. However, SVM models are prone to overfitting and the metrics for how the variables are combined to optimize the hyperplane are not provided [174]. Billah et al., applied SVM methods to gastrointestinal collected during endoscopic procedures to detect polyps [175]. In this study, Billah et al., use a computer aided method that improved the polyp

detection rate and can be used to find important regions. The images features are extracted from endoscopic images and were used to train a SVM model. After training the SVM models, public databases were used as a validation dataset and outperform state-of the-art methodologies with an accuracy of 98.23%.

Random forests use decision trees methods that automatize the detection of interaction and non-linear effects (Figure 2.8). The predictors are divided and stacked to build decision trees to be combined in a large aggregated forest. Random forests algorithm, can also build numerous trees where the dataset is re-sampled to generate an aggregate tree by averaging all re-sampled trees reducing the possibility of overfit. These decision trees are also visually interpretable, have lower risks of overfitting and the variable importance to for the classification algorithm is also provided [176] .

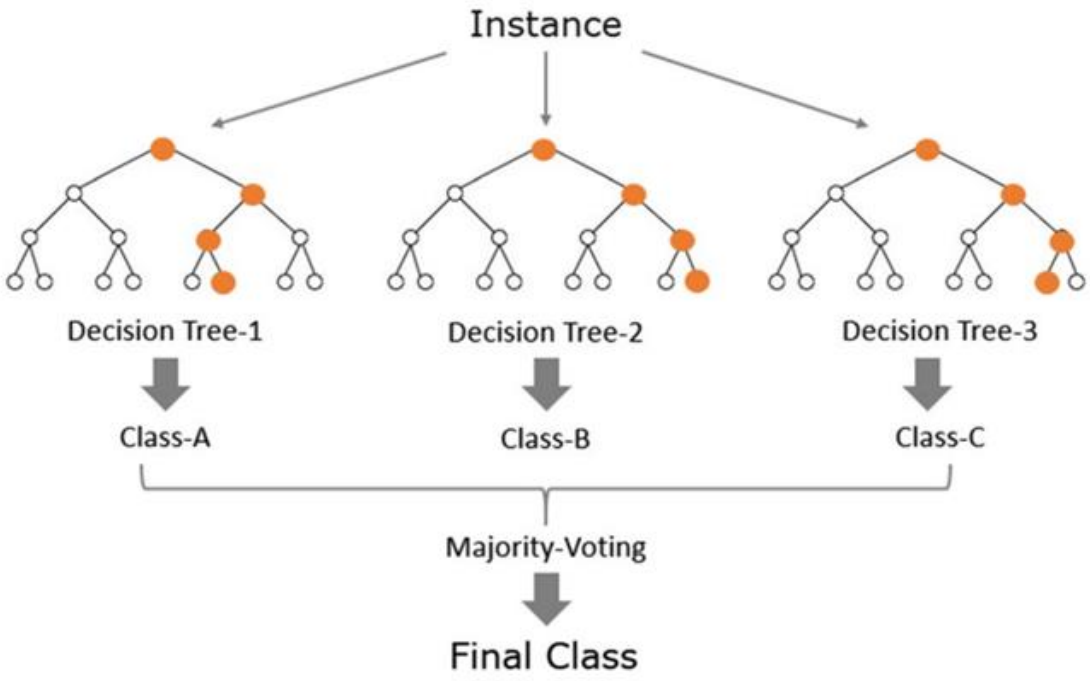

Figure 2.8 – Schematic of random forests decision trees algorithm [167].

For this thesis, regarding supervised machine learning, the random forests algorithm is the optimal choice. 2P-FLIM variables have non-linear interactions, random forests reduce overfitting of data with high prediction accuracy and variable importance can be extracted which can be useful to pinpoint a 2P-FLIM variable highly impacted during a treatment or a variable crucial for the classification process.

The predictive random forests models are non-parametric, hard to over-train, robust to outliners and fast to train. Random forests models train individual decision trees base on the dataset, both independent and dependent variables. Every tree is built using a random subset of samples and variables. For each tree, a different training set is created by random re-sampling of the original dataset. This sampled dataset is known as training set. The remaining experimental observations are described as "out-of-bag (OBB) samples. When the decision tree is being calculated, variables are randomly selected from all available variables and are evaluated by their ability to split the data. The random selection of variables for splitting data ensures a low correlation between trees and prevents over-fitting of a random forests model [176]. The variable resulting in the largest decrease in splitting error, or impurity, is chosen to separate the samples at each node. Afterwards, the remaining variables are tested again and so on until there are no more variables. In random forests the measure of impurity is known as Gini impurity. After the training dataset is used in the random forests model, the terminal nodes contain either samples belonging to the same class or contained a specified number of samples. The variables of the random forests model are also tweaked to increase prediction accuracy. This is done by tuning the parameters of *ntree* and *mtry* which comprise the number of decision trees used in the forest models as well the number of nodes used. After the model has been fully trained, the random forest models can subsequently be used to predict classes of new samples. General cross-validation procedures are unnecessary to predict the classification error of a random forests model. The cross-validation performance is already built-in as each tree has been trained by re-sampling and test OOB data. This result is usually expressed as the OOB error

rate [177]. In addition to built-in cross-validation, random forests models calculates the estimates of variable importance for classification. The importance of variables is useful to understand the relevance of a variable for a specific data set. The importance scores can be used to identify biomarkers or to remove non-informative variables [178, 179]. The variable importance scores are calculated by testing the OOB samples both with and without the variable being analysis. Another value to understand variable importance in the Gini importance variable. The gini importance value is calculated as the sum of the gini impurity decrease of each node of the model used. After random forests model training and tuning, the trained model can be used to predict its efficiency to classify random samples. The quantification of the prediction ability and the ability to classify samples is done by plotting receiving-operator characteristic curves (ROC) and calculation their respective area under the curve (ROC-AUC). For this thesis, a R code was used to tune and calculate random forests models parameters (Computer Code Appendix 3).

Lunetta et al., use random forests models to identify risk-associated single nucleotide polymorphisms (SNPs) in genome-wide analysis [180] . Here, Lunetta et al., used random forests models to screen risk-associated SNPs from a pool of irrelevant SNPs. One the main advantages of using random forests highlighted by Lunetta et al., is that there is no need to have a proposed model of genetic interactions to uncover which SNPs are correlated with diseases since all variables are screened during the model training. Qian et al., also used random forest analysis in combination with 2P-FLIM to evaluate the differentiation rates of human pluripotent stem cell derived cardiomyocyte [181]. In this study Qian et al., induced cardiomyocyte differentiation from induced pluripotent stem cells using a fifteen different protocols and cell lines with varying cell densities. After 12 days of cell culture, cardiomyocyte differentiation was measured by flow cytometry using cardiac troponin T fluorescent labelling. Afterwards, UMAP was used to plot all experimental observations and corresponding 2P-FLIM variables in a 2D plot, highlighting the metabolic shifts occurring during cardiomyocyte differentiation at different time points.

Random forests models were used to classify between high and low differentiation efficiency rate of cardiomyocytes and variable importance was also calculated. When using all 2P-FLIM variables to predict the efficacy of the classification model, Qian et al., observed a 0.91 receiver-operator characteristic area under the curve value (ROC-AUC). The application of UMAP and random forest by Qian et al., to 2P-FLIM variables showcase a non-invasive method that accurately predicts the efficiency of cardiomyocyte differentiation from human pluripotent stem cells at early differentiation stages. This early classification processes can be used to screen and validate methodologies to promote cardiomyocyte differentiation at earlier time-points instead of validating the protocol efficiency at cardiomyocyte differentiation end-point.

This thesis will focus on the use of 2P-FLIM to uncover metabolic pathways of human mesenchymal stem cells and human macrophages in response to cell behaviour, microenvironment cues or treatments, in a non-invasive and in real-time. In addition, biochemical validation of metabolic trends are performed and advanced data analysis methods employed to explore the metabolic trends measured including 2P-FLIM feature importance highlighting possible therapeutic targets.

2.6. References

[1] D. Bardell, The biologists' forum: The invention of the microscope, Bios. 75(2) (2004) 78-84.
[2] A. Zaritsky, S. Natan, J. Horev, I. Hecht, L. Wolf, E. Ben-Jacob, I. Tsarfaty, Cell motility dynamics: a novel segmentation algorithm to quantify multi-cellular bright field microscopy images, PloS One. 6(11) (2011) e27593.
[3] M.N. Gurcan, L.E. Boucheron, A. Can, A. Madabhushi, N.M. Rajpoot, B. Yener, Histopathological image analysis: a review, IEEE Reviews in Biomedical Engineering. 2 (2009) 147-171.
[4] M.M. Mariani, P. Lampen, J. Popp, B.R. Wood, V. Deckert, Impact of fixation on in vitro cell culture lines monitored with Raman spectroscopy, Analyst. 134(6) (2009) 1154-1161.
[5] K.P. Quinn, E. Bellas, N. Fourligas, K. Lee, D.L. Kaplan, I. Georgakoudi, Characterization of metabolic changes associated with the functional development of 3D engineered tissues by non-invasive, dynamic measurement of individual cell redox ratios, Biomaterials. 33(21) (2012) 5341-8.
[6] J.R. Lakowicz, Principles of fluorescence spectroscopy, 2006.
[7] M. Göppert-Mayer, Über elementarakte mit zwei quantensprüngen, Annalen der Physik. 401(3) (1931) 273-294.
[8] W. Kaiser, C.G.B. Garrett, Two-Photon excitation in CaF2:Eu2+, Physical Review Letters. 7(6) (1961) 229-231.
[9] W.R. Zipfel, R.M. Williams, W.W. Webb, Nonlinear magic: multiphoton microscopy in the biosciences, Nat Biotechnol. 21(11) (2003) 1369-77.
[10] B.A. Wilt, L.D. Burns, E.T. Wei Ho, K.K. Ghosh, E.A. Mukamel, M.J. Schnitzer, Advances in light microscopy for neuroscience, Annu Rev Neurosci. 32 (2009) 435-506.
[11] C.M. Stoscheck, Quantitation of protein, Methods in Enzymology. 182 (1990) 50-68.
[12] B.L. Diffey, Solar ultraviolet radiation effects on biological systems, Physics in Medicine and Biology. 36(3) (1991) 299-328.
[13] H.C. Ishikawa-Ankerhold, R. Ankerhold, G.P. Drummen, Advanced fluorescence microscopy techniques--FRAP, FLIP, FLAP, FRET and FLIM, Molecules. 17(4) (2012) 4047-4132.
[14] P.P. Provenzano, K.W. Eliceiri, P.J. Keely, Multiphoton microscopy and fluorescence lifetime imaging microscopy (FLIM) to monitor metastasis and the tumor microenvironment, Clin Exp Metastasis. 26(4) (2009) 357-70.
[15] E.B. van Munster, T.W.J. Gadella, Fluorescence lifetime imaging microscopy (FLIM), Microscopy Techniques2005, pp. 143-175.
[16] P.C. Schneider, R.M. Clegg, Rapid acquisition, analysis, and display of fluorescence lifetime-resolved images for real-time applications, Review of Scientific Instruments. 68(11) (1997) 4107-4119.
[17] A. Squire, P.I. Bastiaens, Three dimensional image restoration in fluorescence lifetime imaging microscopy, Journal of Microscopy. 193(Pt 1) (1999) 36-49.
[18] G. Valentini, C. D'Andrea, D. Comelli, A. Pifferi, P. Taroni, A. Torricelli, R. Cubeddu, C. Battaglia, C. Consolandi, G. Salani, L. Rossi-Bernardi, G. De Bellis, Time-resolved DNA-microarray reading by an intensified CCD for ultimate sensitivity, Optics Letters. 25(22) (2000) 1648-1650.
[19] D. Phillips, R.C. Drake, D.V. Oconnor, R.L. Christensen, Time correlated single-photon counting (TCSPC) using laser excitation, Analytical Instrumentation. 14(3-4) (1985) 267-292.
[20] Sytsma, Vroom, G. De, Gerritsen, Time-gated fluorescence lifetime imaging and microvolume spectroscopy using two-photon excitation, Journal of Microscopy. 191(1) (2008) 39-51.
[21] N. Boens, W. Qin, N. Basaric, J. Hofkens, M. Ameloot, J. Pouget, J.P. Lefevre, B. Valeur, E. Gratton, M. vandeVen, N.D. Silva, Jr., Y. Engelborghs, K. Willaert, A. Sillen, G. Rumbles, D. Phillips, A.J. Visser, A. van Hoek, J.R. Lakowicz, H. Malak, I. Gryczynski, A.G. Szabo, D.T. Krajcarski,

N. Tamai, A. Miura, Fluorescence lifetime standards for time and frequency domain fluorescence spectroscopy, Analytical Chemistry. 79(5) (2007) 2137-2149.
[22] T.W. Gadella, Jr., D.J. Arndt-Jovin, T.M. Jovin, Visualization of lipid-receptor interactions on single cells by time-resolved imaging fluorescence microscopy, J Fluoresc. 4(4) (1994) 295-8.
[23] V. Emiliani, D. Sanvitto, M. Tramier, T. Piolot, Z. Petrasek, K. Kemnitz, C. Durieux, M. Coppey-Moisan, Low-intensity two-dimensional imaging of fluorescence lifetimes in living cells, Applied Physics Letters. 83(12) (2003) 2471-2473.
[24] E.P. Buurman, R. Sanders, A. Draaijer, H.C. Gerritsen, J.J.F. van Veen, P.M. Houpt, Y.K. Levine, Fluorescence lifetime imaging using a confocal laser scanning microscope, Scanning. 14(3) (1992) 155-159.
[25] C. Buranachai, D. Kamiyama, A. Chiba, B.D. Williams, R.M. Clegg, Rapid frequency-domain FLIM spinning disk confocal microscope: lifetime resolution, image improvement and wavelet analysis, J Fluoresc. 18(5) (2008) 929-42.
[26] E. Gratton, S. Breusegem, J. Sutin, Q. Ruan, N. Barry, Fluorescence lifetime imaging for the two-photon microscope: time-domain and frequency-domain methods, J Biomed Opt. 8(3) (2003) 381-90.
[27] A.J. Walsh, R.S. Cook, H.C. Manning, D.J. Hicks, A. Lafontant, C.L. Arteaga, M.C. Skala, Optical metabolic imaging identifies glycolytic levels, subtypes, and early-treatment response in breast cancer, Cancer Res. 73(20) (2013) 6164-74.
[28] T. Funane, S.S. Hou, K.M. Zoltowska, S.J. van Veluw, O. Berezovska, A.T.N. Kumar, B.J. Bacskai, Selective plane illumination microscopy (SPIM) with time-domain fluorescence lifetime imaging microscopy (FLIM) for volumetric measurement of cleared mouse brain samples, Rev Sci Instrum. 89(5) (2018) 053705.
[29] C.A. Mitchell, S.P. Poland, J. Seyforth, J. Nedbal, T. Gelot, T. Huq, G. Holst, R.D. Knight, S.M. Ameer-Beg, Functional in vivo imaging using fluorescence lifetime light-sheet microscopy, Optics Letters. 42(7) (2017) 1269-1272.
[30] S.Y. Lunt, M.G. Vander Heiden, Aerobic glycolysis: meeting the metabolic requirements of cell proliferation, Annu Rev Cell Dev Biol. 27 (2011) 441-64.
[31] M.G. Vander Heiden, L.C. Cantley, C.B. Thompson, Understanding the Warburg effect: the metabolic requirements of cell proliferation, Science. 324(5930) (2009) 1029-33.
[32] W. McKeehan, Glycolysis, glutaminolysis and cell proliferation, Cell Biology International Reports. 6(7) (1982) 635-650.
[33] C.V. Dang, Glutaminolysis: supplying carbon or nitrogen or both for cancer cells?, Cell Cycle. 9(19) (2010) 3884-3886.
[34] M. Saraste, Oxidative phosphorylation at the fin de siecle, Science. 283(5407) (1999) 1488-1493.
[35] S.A. Mookerjee, A.A. Gerencser, D.G. Nicholls, M.D. Brand, Quantifying intracellular rates of glycolytic and oxidative ATP production and consumption using extracellular flux measurements, J Biol Chem. 292(17) (2017) 7189-7207.
[36] J. Folbergrova´, B. Ljunggren, K. Norberg, B.K. Siesjo¨, Influence of complete ischemia on glycolytic metabolites, citric acid cycle intermediates, and associated amino acids in the rat cerebral cortex, Brain Research. 80(2) (1974) 265-279.
[37] R.J. DeBerardinis, J.J. Lum, G. Hatzivassiliou, C.B. Thompson, The biology of cancer: metabolic reprogramming fuels cell growth and proliferation, Cell Metabolism. 7(1) (2008) 11-20.
[38] M. Thai, N.A. Graham, D. Braas, M. Nehil, E. Komisopoulou, S.K. Kurdistani, F. McCormick, T.G. Graeber, H.R. Christofk, Adenovirus E4ORF1-induced MYC activation promotes host cell anabolic glucose metabolism and virus replication, Cell Metabolism. 19(4) (2014) 694-701.
[39] D.E. Bauer, M.H. Harris, D.R. Plas, J.J. Lum, P.S. Hammerman, J.C. Rathmell, J.L. Riley, C.B. Thompson, Cytokine stimulation of aerobic glycolysis in hematopoietic cells exceeds

proliferative demand, Federation of American Societies for Experimental Biology Journal. 18(11) (2004) 1303-1305.
[40] J. Aldridge, E.K. Pye, Cell density dependence of oscillatory metabolism, Nature. 259(5545) (1976) 670-671.
[41] A. Daemen, D. Peterson, N. Sahu, R. McCord, X. Du, B. Liu, K. Kowanetz, R. Hong, J. Moffat, M. Gao, A. Boudreau, R. Mroue, L. Corson, T. O'Brien, J. Qing, D. Sampath, M. Merchant, R. Yauch, G. Manning, J. Settleman, G. Hatzivassiliou, M. Evangelista, Metabolite profiling stratifies pancreatic ductal adenocarcinomas into subtypes with distinct sensitivities to metabolic inhibitors, Proceedings of the National Academy of Sciences of the United States of America. 112(32) (2015) 4410-4417.
[42] L.A. O'Neill, R.J. Kishton, J. Rathmell, A guide to immunometabolism for immunologists, Nature Reviews Immunology. 16(9) (2016) 553-565.
[43] J.A. Shyer, R.A. Flavell, W. Bailis, Metabolic signaling in T cells, Cell Research. 30(8) (2020) 649-659.
[44] C. Choi, D.K. Finlay, Optimising NK cell metabolism to increase the efficacy of cancer immunotherapy, Stem Cell Res Ther. 12(1) (2021) 320.
[45] C.D. Folmes, P.P. Dzeja, T.J. Nelson, A. Terzic, Metabolic plasticity in stem cell homeostasis and differentiation, Cell Stem Cell. 11(5) (2012) 596-606.
[46] J.R. Lakowicz, H. Szmacinski, K. Nowaczyk, M.L. Johnson, Fluorescence lifetime imaging of free and protein-bound NADH, Proceedings of the National Academy of Sciences of the United States of America. 89(4) (1992) 1271-1275.
[47] M.C. Skala, K.M. Riching, A. Gendron-Fitzpatrick, J. Eickhoff, K.W. Eliceiri, J.G. White, N. Ramanujam, In vivo multiphoton microscopy of NADH and FAD redox states, fluorescence lifetimes, and cellular morphology in precancerous epithelia, Proc Natl Acad Sci U S A. 104(49) (2007) 19494-9.
[48] M.A. Yaseen, S. Sakadzic, W. Wu, W. Becker, K.A. Kasischke, D.A. Boas, In vivo imaging of cerebral energy metabolism with two-photon fluorescence lifetime microscopy of NADH, Biomed Opt Express. 4(2) (2013) 307-21.
[49] R. Niesner, B. Peker, P. Schlusche, K.H. Gericke, Noniterative biexponential fluorescence lifetime imaging in the investigation of cellular metabolism by means of NAD(P)H autofluorescence, Chemphyschem. 5(8) (2004) 1141-9.
[50] V.V. Ghukasyan, F.-J. Kao, Monitoring cellular metabolism with fluorescence lifetime of reduced nicotinamide adenine dinucleotide, The Journal of Physical Chemistry C. 113(27) (2009) 11532-11540.
[51] S. Huang, A.A. Heikal, W.W. Webb, Two-Photon Fluorescence Spectroscopy and Microscopy of NAD(P)H and Flavoprotein, Biophysical Journal. 82(5) (2002) 2811-2825.
[52] B.R. Masters, P.T. So, E. Gratton, Multiphoton excitation fluorescence microscopy and spectroscopy of in vivo human skin, Biophysical Journal. 72(6) (1997) 2405-2412.
[53] M.A. Digman, V.R. Caiolfa, M. Zamai, E. Gratton, The phasor approach to fluorescence lifetime imaging analysis, Biophys J. 94(2) (2008) L14-6.
[54] A.V. Kondrashina, R.I. Dmitriev, S.M. Borisov, I. Klimant, I. O'Brien, Y.M. Nolan, A.V. Zhdanov, D.B. Papkovsky, A phosphorescent nanoparticle-based probe for sensing and imaging of (intra)cellular oxygen in multiple detection modalities, Advanced Functional Materials. 22(23) (2012) 4931-4939.
[55] H. Wallrabe, Z. Svindrych, S.R. Alam, K.H. Siller, T. Wang, D. Kashatus, S. Hu, A. Periasamy, Segmented cell analyses to measure redox states of autofluorescent NAD(P)H, FAD & Trp in cancer cells by FLIM, Sci Rep. 8(1) (2018) 79.
[56] P.M. Schaefer, S. Kalinina, A. Rueck, C.A.F. von Arnim, B. von Einem, NADH Autofluorescence-A Marker on its Way to Boost Bioenergetic Research, Cytometry A. 95(1) (2019) 34-46.

[57] T.D. Pugh, M.W. Conklin, T.D. Evans, M.A. Polewski, H.J. Barbian, R. Pass, B.D. Anderson, R.J. Colman, K.W. Eliceiri, P.J. Keely, R. Weindruch, T.M. Beasley, R.M. Anderson, A shift in energy metabolism anticipates the onset of sarcopenia in rhesus monkeys, Aging Cell. 12(4) (2013) 672-681.
[58] T.S. Blacker, M.R. Duchen, Investigating mitochondrial redox state using NADH and NADPH autofluorescence, Free Radical Biology and Medicine. 100 (2016) 53-65.
[59] T.S. Blacker, Z.F. Mann, J.E. Gale, M. Ziegler, A.J. Bain, G. Szabadkai, M.R. Duchen, Separating NADH and NADPH fluorescence in live cells and tissues using FLIM, Nat Commun. 5 (2014) 3936.
[60] W. Ying, NAD+/NADH and NADP+/NADPH in cellular functions and cell death: regulation and biological consequences, Antioxid Redox Signal. 10(2) (2008) 179-206.
[61] N. Pollak, C. Dölle, M. Ziegler, The power to reduce: pyridine nucleotides – small molecules with a multitude of functions, Biochemical Journal. 402(2) (2007) 205-218.
[62] J.H. Ostrander, C.M. McMahon, S. Lem, S.R. Millon, J.Q. Brown, V.L. Seewaldt, N. Ramanujam, Optical redox ratio differentiates breast cancer cell lines based on estrogen receptor status, Cancer Research. 70(11) (2010) 4759-4766.
[63] A. Walsh, R.S. Cook, B. Rexer, C.L. Arteaga, M.C. Skala, Optical imaging of metabolism in HER2 overexpressing breast cancer cells, Biomedical Optics Express. 3(1) (2012) 75-85.
[64] R.I. Dmitriev, Multi-Parametric live cell microscopy of 3D tissue models, Springer2017.
[65] R. Mongeon, V. Venkatachalam, G. Yellen, Cytosolic NADH-NAD+ redox visualized in brain slices by two-photon fluorescence lifetime biosensor imaging, Antioxidants & redox signaling. 25(10) (2016) 553-563.
[66] N. O'Donnell, R.I. Dmitriev, Three-dimensional tissue models and available probes for multi-parametric live cell microscopy: a brief overview, Multi-Parametric Live Cell Microscopy of 3D Tissue Models, Springer2017, pp. 49-67.
[67] M.D. Brand, D.G. Nicholls, Assessing mitochondrial dysfunction in cells, Biochemical Journal. 435(2) (2011) 297-312.
[68] I.A. Okkelman, D.B. Papkovsky, R.I.J.C.P.A. Dmitriev, Estimation of the mitochondrial membrane potential using fluorescence lifetime imaging microscopy, Cytometry A. (2019) 471-482.
[69] R.C. Scaduto, L.W. Grotyohann, Measurement of mitochondrial membrane potential using fluorescent rhodamine derivatives, Biophysical Journal. 76(1) (1999) 469-477.
[70] I.A. Okkelman, D.B. Papkovsky, R.I. Dmitriev, Estimation of the mitochondrial membrane potential using fluorescence lifetime imaging microscopy, Cytometry A. (2019) 471-482.
[71] S.R. Alam, H. Wallrabe, Z. Svindrych, A.K. Chaudhary, K.G. Christopher, D. Chandra, A. Periasamy, Investigation of mitochondrial metabolic response to doxorubicin in prostate cancer cells: an NADH, FAD and tryptophan FLIM assay, Science Reports. 7(1) (2017) 10451-10461.
[72] K. Dowling, M.J. Dayel, M.J. Lever, P.M. French, J.D. Hares, A.K. Dymoke-Bradshaw, Fluorescence lifetime imaging with picosecond resolution for biomedical applications, Optics Letters. 23(10) (1998) 810-812.
[73] X. Chen, O. Nadiarynkh, S. Plotnikov, P.J. Campagnola, Second harmonic generation microscopy for quantitative analysis of collagen fibrillar structure, Nature Protocols. 7(4) (2012) 654-669.
[74] S. Ranjit, E. Dobrinskikh, J. Montford, A. Dvornikov, A. Lehman, D.J. Orlicky, R. Nemenoff, E. Gratton, M. Levi, S. Furgeson, Label-free fluorescence lifetime and second harmonic generation imaging microscopy improves quantification of experimental renal fibrosis, Kidney International. 90(5) (2016) 1123-1128.
[75] V. Lutz, M. Sattler, S. Gallinat, H. Wenck, R. Poertner, F. Fischer, Impact of collagen crosslinking on the second harmonic generation signal and the fluorescence lifetime of collagen autofluorescence, Skin Research Technology. 18(2) (2012) 168-179.

[76] T. Abraham, J. Hogg, Extracellular matrix remodeling of lung alveolar walls in three dimensional space identified using second harmonic generation and multiphoton excitation fluorescence, Journal of Structural Biology. 171(2) (2010) 189-196.
[77] V. Jyothikumar, Y. Sun, A. Periasamy, Investigation of tryptophan-NADH interactions in live human cells using three-photon fluorescence lifetime imaging and Forster resonance energy transfer microscopy, Journal of Biomedical Optics. 18(6) (2013) 060501-060505.
[78] L. Chunqiang, C. Pitsillides, J.M. Runnels, D. Côté, C.P. Lin, Multiphoton microscopy of live tissues with ultraviolet autofluorescence, IEEE Journal of Selected Topics in Quantum Electronics. 16(3) (2010) 516-523.
[79] S.W. Botchway, A.W. Parker, R.H. Bisby, A.G. Crisostomo, Real-time cellular uptake of serotonin using fluorescence lifetime imaging with two-photon excitation, Microscopy Research Technology. 71(4) (2008) 267-273.
[80] E. Dimitrow, I. Riemann, A. Ehlers, M.J. Koehler, J. Norgauer, P. Elsner, K. Konig, M. Kaatz, Spectral fluorescence lifetime detection and selective melanin imaging by multiphoton laser tomography for melanoma diagnosis, Experimental Dermatology. 18(6) (2009) 509-515.
[81] A. Ehlers, I. Riemann, M. Stark, K. Konig, Multiphoton fluorescence lifetime imaging of human hair, Microscopy Research Technology. 70(2) (2007) 154-161.
[82] B. Kierdaszuk, I. Gryczynski, A. Modrak-Wojcik, A. Bzowska, D. Shugar, J.R. Lakowicz, Fluorescence of tyrosine and tryptophan in proteins using one- and two-photon excitation, Photochemistry and Photobiology. 61(4) (1995) 319-324.
[83] J.B. Shear, C. Xu, W.W. Webb, Multiphoton-excited visible emission by serotonin solutions, Photochemistry and Photobiology. 65(6) (1997) 931-936.
[84] J.R. Lakowicz, B.P. Maliwal, Oxygen quenching and fluorescence depolarization of tyrosine residues in proteins, Journal of Biological Chemistry. 258(8) (1983) 4794-4801.
[85] G.S. Baird, D.A. Zacharias, R.Y. Tsien, Circular permutation and receptor insertion within green fluorescent proteins, Proceedings of the National Academy of Sciences of the United States of America. 96(20) (1999) 11241-11246.
[86] Y.P. Hung, J.G. Albeck, M. Tantama, G. Yellen, Imaging cytosolic NADH-NAD(+) redox state with a genetically encoded fluorescent biosensor, Cell Metabolism. 14(4) (2011) 545-554.
[87] A.A. Shestov, X. Liu, Z. Ser, A.A. Cluntun, Y.P. Hung, L. Huang, D. Kim, A. Le, G. Yellen, J.G. Albeck, J.W. Locasale, Quantitative determinants of aerobic glycolysis identify flux through the enzyme GAPDH as a limiting step, Elife. 3 (2014) e03342.
[88] M. Tantama, Y.P. Hung, G. Yellen, Imaging intracellular pH in live cells with a genetically encoded red fluorescent protein sensor, Journal of American Chemical Society. 133(26) (2011) 10034-10037.
[89] R. Masia, W.J. McCarty, C. Lahmann, J. Luther, R.T. Chung, M.L. Yarmush, G. Yellen, Live cell imaging of cytosolic NADH/NAD(+) ratio in hepatocytes and liver slices, American Journal of Physiology-Gastrointestinal and Liver Physiology. 314(1) (2018) 97-108.
[90] J. Berg, Y.P. Hung, G. Yellen, A genetically encoded fluorescent reporter of ATP:ADP ratio, Nature Methods. 6(2) (2009) 161-166.
[91] M.C. Skala, K.M. Riching, D.K. Bird, A. Gendron-Fitzpatrick, J. Eickhoff, K.W. Eliceiri, P.J. Keely, N. Ramanujam, In vivo multiphoton fluorescence lifetime imaging of protein-bound and free nicotinamide adenine dinucleotide in normal and precancerous epithelia, Journal of Biomedical Optics. 12(2) (2007) 024014-024024.
[92] A.J. Walsh, K.P. Mueller, K. Tweed, I. Jones, C.M. Walsh, N.J. Piscopo, N.M. Niemi, D.J. Pagliarini, K. Saha, M.C. Skala, Classification of T-cell activation via autofluorescence lifetime imaging, Nature Biomedical Engineering. 5(1) (2021) 77-88.
[93] A. Alfonso-Garcia, J. Shklover, B.E. Sherlock, A. Panitch, L.G. Griffiths, L. Marcu, Fiber-based fluorescence lifetime imaging of recellularization processes on vascular tissue constructs, Journal of Biophotonics. 11(9) (2018) e201700391.

[94] A.V. Meleshina, V.V. Dudenkova, M.V. Shirmanova, V.I. Shcheslavskiy, W. Becker, A.S. Bystrova, E.I. Cherkasova, E.V. Zagaynova, Probing metabolic states of differentiating stem cells using two-photon FLIM, Scientific Reports. 6(21853) (2016) 1-11.
[95] N. Ma, M.A. Digman, L. Malacrida, E. Gratton, Measurements of absolute concentrations of NADH in cells using the phasor FLIM method, Biomedical Optics Express. 7(7) (2016) 2441-2452.
[96] A. Alfonso-Garcia, T.D. Smith, R. Datta, T.U. Luu, E. Gratton, E.O. Potma, W.F. Liu, Label-free identification of macrophage phenotype by fluorescence lifetime imaging microscopy, Journal of Biomedical Optics. 21(4) (2016) 46005-46012.
[97] A.J. Walsh, R.S. Cook, M.E. Sanders, L. Aurisicchio, G. Ciliberto, C.L. Arteaga, M.C. Skala, Quantitative optical imaging of primary tumor organoid metabolism predicts drug response in breast cancer, Cancer Research. 74(18) (2014) 5184-5194.
[98] T.S. Blacker, Z.F. Mann, J.E. Gale, M. Ziegler, A.J. Bain, G. Szabadkai, M.R. Duchen, Separating NADH and NADPH fluorescence in live cells and tissues using FLIM, Nature Communications. 5 (2014) 3936-3945.
[99] M.A. Yaseen, S. Sakadzic, W. Wu, W. Becker, K.A. Kasischke, D.A. Boas, In vivo imaging of cerebral energy metabolism with two-photon fluorescence lifetime microscopy of NADH, Biomedical Optics Express. 4(2) (2013) 307-321.
[100] C. Stringari, R.A. Edwards, K.T. Pate, M.L. Waterman, P.J. Donovan, E. Gratton, Metabolic trajectory of cellular differentiation in small intestine by phasor fluorescence lifetime microscopy of nADH, Scientific Reports. 2 (2012) 568-577.
[101] K. Konig, A. Uchugonova, E. Gorjup, Multiphoton fluorescence lifetime imaging of 3D-stem cell spheroids during differentiation, Microscopy Research and Technique. 74(1) (2011) 9-17.
[102] Y. Sun, J. Phipps, D.S. Elson, H. Stoy, S. Tinling, J. Meier, B. Poirier, F.S. Chuang, D.G. Farwell, L. Marcu, Fluorescence lifetime imaging microscopy: in vivo application to diagnosis of oral carcinoma, Optics Letters. 34(13) (2009) 2081-2083.
[103] A. Uchugonova, K. Konig, Two-photon autofluorescence and second-harmonic imaging of adult stem cells, Journal of Biomedical Optics. 13(5) (2008) 054068-054076.
[104] A. Farini, C. Sitzia, S. Erratico, M. Meregalli, Y. Torrente, Clinical applications of mesenchymal stem cells in chronic diseases, Stem Cells International. 2014 (2014) 1-12.
[105] A.I. Caplan, Adult mesenchymal stem cells for tissue engineering versus regenerative medicine, J Cell Physiol. 213(2) (2007) 341-7.
[106] A.I. Caplan, Mesenchymal stem cells, Journal of Orthopaedic Research. 9(5) (1991) 641-650.
[107] J.E. Aubin, Bone stem cells, Journal of Cellular Biochemistry. 72(S30-31) (1998) 73-82.
[108] N. Shyh-Chang, G.Q. Daley, L.C. Cantley, Stem cell metabolism in tissue development and aging, Development. 140(12) (2013) 2535-47.
[109] G.E. Salazar-Noratto, G. Luo, C. Denoeud, M. Padrona, A. Moya, M. Bensidhoum, R. Bizios, E. Potier, D. Logeart-Avramoglou, H. Petite, Understanding and leveraging cell metabolism to enhance mesenchymal stem cell transplantation survival in tissue engineering and regenerative medicine applications, Stem Cells. 38(1) (2020) 22-33.
[110] G. Pattappa, H.K. Heywood, J.D. de Bruijn, D.A. Lee, The metabolism of human mesenchymal stem cells during proliferation and differentiation, J Cell Physiol. 226(10) (2011) 2562-70.
[111] J. Muller, K. Benz, M. Ahlers, C. Gaissmaier, J. Mollenhauer, Hypoxic conditions during expansion culture prime human mesenchymal stromal precursor cells for chondrogenic differentiation in three-dimensional cultures, Cell Transplantation. 20(10) (2011) 1589-1602.
[112] C.T. Chen, Y.R. Shih, T.K. Kuo, O.K. Lee, Y.H. Wei, Coordinated changes of mitochondrial biogenesis and antioxidant enzymes during osteogenic differentiation of human mesenchymal stem cells, Stem Cells. 26(4) (2008) 960-8.

[113] K.V. Tormos, E. Anso, R.B. Hamanaka, J. Eisenbart, J. Joseph, B. Kalyanaraman, N.S. Chandel, Mitochondrial complex III ROS regulate adipocyte differentiation, Cell Metabolism. 14(4) (2011) 537-544.
[114] K. Nishimura, A. Fukuda, K. Hisatake, Mechanisms of the metabolic shift during somatic cell reprogramming, International Journal of Molecular Sciences. 20(9) (2019) 2254-2270.
[115] Y. Liu, T. Ma, Metabolic regulation of mesenchymal stem cell in expansion and therapeutic application, Biotechnology Progress. 31(2) (2015) 468-481.
[116] E. Esen, J. Chen, C.M. Karner, A.L. Okunade, B.W. Patterson, F. Long, WNT-LRP5 signaling induces warburg effect through mTORC2 activation during osteoblast differentiation, Cell Metabolism. 17(5) (2013) 745-755.
[117] V. Ruiz-Rodado, A. Lita, M. Larion, Advances in measuring cancer cell metabolism with subcellular resolution, Nature Methods. 19(9) (2022) 1048-1063.
[118] L. Pelgrom, G. Davis, S. O'Shoughnessy, S. Van Kasteren, D. Finlay, L. Sinclair, QUAS-R: Glutamine (Q) Uptake Assay with Single cell Resolution reveals metabolic heterogeneity with immune populations, bioRxiv. (2022).
[119] K. Zha, Z. Sun, Y. Yang, M. Chen, C. Gao, L. Fu, H. Li, X. Sui, Q. Guo, S. Liu, Recent developed strategies for enhancing chondrogenic differentiation of MSC: impact on MSC-based therapy for cartilage regeneration, Stem Cells International. 2021 (2021) 1-15.
[120] H. Lui, J. Denbeigh, C. Vaquette, H.M. Tran, A.B. Dietz, S.M. Cool, A. Dudakovic, S. Kakar, A.J. van Wijnen, Fibroblastic differentiation of mesenchymal stem/stromal cells (MSCs) is enhanced by hypoxia in 3D cultures treated with bone morphogenetic protein 6 (BMP6) and growth and differentiation factor 5 (GDF5), Gene. 788 (2021) 145662-14573.
[121] Q. Gao, C. Rhee, M. Maruyama, Z. Li, H. Shen, N. Zhang, T. Utsunomiya, E.E. Huang, Z. Yao, B.A. Bunnell, H. Lin, R.S. Tuan, S.B. Goodman, The effects of macrophage phenotype on osteogenic differentiation of MSCs in the presence of polyethylene particles, Biomedicines. 9(5) (2021) 499-509.
[122] K.P. Quinn, G.V. Sridharan, R.S. Hayden, D.L. Kaplan, K. Lee, I. Georgakoudi, Quantitative metabolic imaging using endogenous fluorescence to detect stem cell differentiation, Scientific Reports. 3(3432) (2013) 1-10.
[123] A.V. Meleshina, V.V. Dudenkova, A.S. Bystrova, D.S. Kuznetsova, M.V. Shirmanova, E.V. Zagaynova, Two-photon FLIM of NAD(P)H and FAD in mesenchymal stem cells undergoing either osteogenic or chondrogenic differentiation, Stem Cell Res Ther. 8(1) (2017) 15.
[124] G. Pattappa, H.K. Heywood, J.D. de Bruijn, D.A. Lee, The metabolism of human mesenchymal stem cells during proliferation and differentiation, Journal of Cellular Physiology. 226(10) (2011) 2562-2570.
[125] L.C. Shum, N.S. White, B.N. Mills, K.L. Bentley, R.A. Eliseev, Energy metabolism in mesenchymal stem cells during osteogenic differentiation, Stem Cells and Development. 25(2) (2016) 114-122.
[126] J. Van den Bossche, L.A. O'Neill, D. Menon, Macrophage immunometabolism: where are we (Going)?, Trends in Immunology. 38(6) (2017) 395-406.
[127] S. Gordon, The macrophage: past, present and future, European Journal of Immunology. 37 Suppl 1 (2007) S9-17.
[128] C. Atri, F.Z. Guerfali, D. Laouini, Role of human macrophage polarization in inflammation during infectious diseases, International Journal Molecular Sciences. 19(6) (2018) 1801-1816.
[129] L. Parisi, E. Gini, D. Baci, M. Tremolati, M. Fanuli, B. Bassani, G. Farronato, A. Bruno, L. Mortara, Macrophage polarization in chronic inflammatory diseases: killers or builders?, Journal of Immunology Research. 2018 (2018) 1-25.
[130] K.M. Vannella, T.A. Wynn, Mechanisms of organ injury and repair by macrophages, Annual Review Physiology. 79 (2017) 593-617.

[131] P. Krzyszczyk, R. Schloss, A. Palmer, F. Berthiaume, The role of macrophages in acute and chronic wound healing and interventions to promote pro-wound healing phenotypes, Frontiers in Physiology. 9 (2018) 419-441.
[132] J. Van den Bossche, J. Baardman, N.A. Otto, S. van der Velden, A.E. Neele, S.M. van den Berg, R. Luque-Martin, H.J. Chen, M.C. Boshuizen, M. Ahmed, M.A. Hoeksema, A.F. de Vos, M.P. de Winther, Mitochondrial dysfunction prevents repolarization of inflammatory macrophages, Cell Reports. 17(3) (2016) 684-696.
[133] E.L. Pearce, E.J. Pearce, Metabolic pathways in immune cell activation and quiescence, Immunity. 38(4) (2013) 633-643.
[134] C. Nagy, A. Haschemi, Time and demand are two critical dimensions of immunometabolism: the process of macrophage activation and the pentose phosphate pathway, Frontiers in Immunology. 6 (2015) 164-172.
[135] L.A. O'Neill, A broken krebs cycle in macrophages, Immunity. 42(3) (2015) 393-394.
[136] X. Wei, H. Song, L. Yin, M.G. Rizzo, R. Sidhu, D.F. Covey, D.S. Ory, C.F. Semenkovich, Fatty acid synthesis configures the plasma membrane for inflammation in diabetes, Nature. 539(7628) (2016) 294-298.
[137] V. Infantino, V. Iacobazzi, F. Palmieri, A. Menga, ATP-citrate lyase is essential for macrophage inflammatory response, Biochemical and Biophysical Research Communications. 440(1) (2013) 105-111.
[138] G.M. Tannahill, A.M. Curtis, J. Adamik, E.M. Palsson-McDermott, A.F. McGettrick, G. Goel, C. Frezza, N.J. Bernard, B. Kelly, N.H. Foley, L. Zheng, A. Gardet, Z. Tong, S.S. Jany, S.C. Corr, M. Haneklaus, B.E. Caffrey, K. Pierce, S. Walmsley, F.C. Beasley, E. Cummins, V. Nizet, M. Whyte, C.T. Taylor, H. Lin, S.L. Masters, E. Gottlieb, V.P. Kelly, C. Clish, P.E. Auron, R.J. Xavier, L.A. O'Neill, Succinate is an inflammatory signal that induces IL-1beta through HIF-1alpha, Nature. 496(7444) (2013) 238-242.
[139] N. Dehne, B. Brune, HIF-1 in the inflammatory microenvironment, Experimental Cell Research. 315(11) (2009) 1791-1797.
[140] K. Ren, R. Torres, Role of interleukin-1beta during pain and inflammation, Brain Research Reviews. 60(1) (2009) 57-64.
[141] S. Gordon, Alternative activation of macrophages, Nature Reviews Immunology. 3(1) (2003) 23-35.
[142] S. Goerdt, O. Politz, K. Schledzewski, R. Birk, A. Gratchev, P. Guillot, N. Hakiy, C.D. Klemke, E. Dippel, V. Kodelja, C.E. Orfanos, Alternative versus classical activation of macrophages, Pathobiology. 67(5-6) (1999) 222-226.
[143] S.C. Huang, A.M. Smith, B. Everts, M. Colonna, E.L. Pearce, J.D. Schilling, E.J. Pearce, Metabolic Reprogramming Mediated by the mTORC2-IRF4 Signaling Axis Is Essential for Macrophage Alternative Activation, Immunity. 45(4) (2016) 817-830.
[144] C.H. Chang, J. Qiu, D. O'Sullivan, M.D. Buck, T. Noguchi, J.D. Curtis, Q. Chen, M. Gindin, M.M. Gubin, G.J. van der Windt, E. Tonc, R.D. Schreiber, E.J. Pearce, E.L. Pearce, Metabolic competition in the tumor microenvironment is a driver of cancer progression, Cell. 162(6) (2015) 1229-1241.
[145] A. Zhang, H. Sun, P. Wang, Y. Han, X. Wang, Modern analytical techniques in metabolomics analysis, Analyst. 137(2) (2012) 293-300.
[146] G.J.W. van der Windt, C.H. Chang, E.L. Pearce, Measuring bioenergetics in T cells using a seahorse extracellular flux analyzer, Current Protocols in Immunology. 113 (2016) 16B.1-16B.14.
[147] A. Alfonso-Garcia, T.D. Smith, R. Datta, T.U. Luu, E. Gratton, E.O. Potma, W.F. Liu, Label-free identification of macrophage phenotype by fluorescence lifetime imaging microscopy, J Biomed Opt. 21(4) (2016) 46005.

[148] J.M. Szulczewski, D.R. Inman, D. Entenberg, S.M. Ponik, J. Aguirre-Ghiso, J. Castracane, J. Condeelis, K.W. Eliceiri, P.J. Keely, In Vivo Visualization of Stromal Macrophages via label-free FLIM-based metabolite imaging, Sci Rep. 6 (2016) 25086.
[149] L. Eriksson, Tamara Byrne, E. Johansson, Johan Trygg, C. Vikström., Multi-and megavariate data analysis basic principles and applications., Umetrics Academy2013.
[150] P. Langfelder, S. Horvath, Eigengene networks for studying the relationships between co-expression modules, BMC Systems Biology. 1 (2007) 54-71.
[151] J.K. Nicholson, J. Connelly, J.C. Lindon, E. Holmes, Metabonomics: a platform for studying drug toxicity and gene function, Nature Reviews Drug Discovery. 1(2) (2002) 153-161.
[152] R.W. Preisendorfer, C.D. Mobley, Principal component analysis in meteorology and oceanography, Elsevier1988.
[153] K. Pearson, LIII. On lines and planes of closest fit to systems of points in space, The London, Edinburgh, and Dublin Philosophical Magazine and Journal of Science. 2(11) (2010) 559-572.
[154] H. Abdi, L.J. Williams, Principal component analysis, Wiley Interdisciplinary Reviews: Computational Statistics. 2(4) (2010) 433-459.
[155] A. Giuliani, The application of principal component analysis to drug discovery and biomedical data, Drug Discovey Today. 22(7) (2017) 1069-1076.
[156] L.L. Hsu, A.C. Culhane, Impact of data preprocessing on integrative matrix factorization of single cell data, Frontiers in Oncology. 10 (2020) 973-982.
[157] J. Alonso-Gutierrez, E.M. Kim, T.S. Batth, N. Cho, Q. Hu, L.J.G. Chan, C.J. Petzold, N.J. Hillson, P.D. Adams, J.D. Keasling, H. Garcia Martin, T.S. Lee, Principal component analysis of proteomics (PCAP) as a tool to direct metabolic engineering, Metabolism Engineering. 28 (2015) 123-133.
[158] G. Abraham, M. Inouye, Fast principal component analysis of large-scale genome-wide data, PloS One. 9(4) (2014) e93766.
[159] K.Y. Yeung, W.L. Ruzzo, Principal component analysis for clustering gene expression data, Bioinformatics. 17(9) (2001) 763-774.
[160] F. Granucci, C. Vizzardelli, N. Pavelka, S. Feau, M. Persico, E. Virzi, M. Rescigno, G. Moro, P. Ricciardi-Castagnoli, Inducible IL-2 production by dendritic cells revealed by global gene expression analysis, Nature Immunology. 2(9) (2001) 882-888.
[161] Leland McInnes, John Healy, J. Melville, UMAP: uniform manifold approximation and projection for dimension reduction, arXiv. (2020).
[162] M. Oide, Y. Sugita, Protein folding intermediates on the dimensionality reduced landscape with UMAP and native contact likelihood, Journal of Chemical Physics. 157(075101) (2022) 1-12.
[163] E. Becht, L. McInnes, J. Healy, C.A. Dutertre, I.W.H. Kwok, L.G. Ng, F. Ginhoux, E.W. Newell, Dimensionality reduction for visualizing single-cell data using UMAP, Nature Biotechnology. (2018).
[164] J. Cao, M. Spielmann, X. Qiu, X. Huang, D.M. Ibrahim, A.J. Hill, F. Zhang, S. Mundlos, L. Christiansen, F.J. Steemers, C. Trapnell, J. Shendure, The single-cell transcriptional landscape of mammalian organogenesis, Nature. 566(7745) (2019) 496-502.
[165] X. Wang, W.E. Allen, M.A. Wright, E.L. Sylwestrak, N. Samusik, S. Vesuna, K. Evans, C. Liu, C. Ramakrishnan, J. Liu, G.P. Nolan, F.A. Bava, K. Deisseroth, Three-dimensional intact-tissue sequencing of single-cell transcriptional states, Science. 361(6400) (2018) 1-10.
[166] E. Shifrut, J. Carnevale, V. Tobin, T.L. Roth, J.M. Woo, C.T. Bui, P.J. Li, M.E. Diolaiti, A. Ashworth, A. Marson, Genome-wide CRISPR screens in primary Human T cells reveal key regulators of immune function, Cell. 175(7) (2018) 1958-1971.
[167] A.L. Samuel, Some studies in machine learning using the game of checkers, IBM Journal of Research and Development. 3(3) (1959) 210-229.
[168] R. Kohavi, F. Provost, Glossary of terms, Machine Learning. 30(2/3) (1998) 271-274.

[169] J. Golze, S. Zourlidou, M. Sester, Traffic regulator detection using GPS trajectories, KN - Journal of Cartography and Geographic Information. 70(3) (2020) 95-105.
[170] C. Park, C.C. Took, J.K. Seong, Machine learning in biomedical engineering, Biomedical Engineering Letters. 8(1) (2018) 1-3.
[171] M. Nadif, F. Role, Unsupervised and self-supervised deep learning approaches for biomedical text mining, Briefings in Bioinformatics. 22(2) (2021) 1592-1603.
[172] T. Jiang, J.L. Gradus, A.J. Rosellini, Supervised machine learning: a brief primer, Behav Ther. 51(5) (2020) 675-687.
[173] S. Lahmiri, D.A. Dawson, A. Shmuel, Performance of machine learning methods in diagnosing parkinson's disease based on dysphonia measures, Biomedical Engineering Letters. 8(1) (2018) 29-39.
[174] Andreas Christmann, I. Steinwart, Support vector machines, 1 ed., Springer2008.
[175] M. Billah, S. Waheed, Gastrointestinal polyp detection in endoscopic images using an improved feature extraction method, Biomedical Engineering Letters. 8(1) (2018) 69-75.
[176] L. Breiman, Random forests, Machine Learning. 45(1) (2001) 5-32.
[177] W.G. Touw, J.R. Bayjanov, L. Overmars, L. Backus, J. Boekhorst, M. Wels, S.A. van Hijum, Data mining in the Life Sciences with Random Forest: a walk in the park or lost in the jungle?, Brief Bioinform. 14(3) (2013) 315-26.
[178] V.A. Fusaro, D.R. Mani, J.P. Mesirov, S.A. Carr, Prediction of high-responding peptides for targeted protein assays by mass spectrometry, Nature Biotechnology. 27(2) (2009) 190-198.
[179] R. Diaz-Uriarte, S. Alvarez de Andres, Gene selection and classification of microarray data using random forest, BMC Bioinformatics. 7 (2006) 3-16.
[180] K.L. Lunetta, L.B. Hayward, J. Segal, P. Van Eerdewegh, Screening large-scale association study data: exploiting interactions using random forests, BMC Genetics. 5 (2004) 32-45.
[181] T. Qian, T.M. Heaster, A.R. Houghtaling, K. Sun, K. Samimi, M.C. Skala, Label-free imaging for quality control of cardiomyocyte differentiation, Nat Commun. 12(1) (2021) 4580.

Chapter 3 - Intracellular label-free detection of mesenchymal stem cell metabolism within a perivascular niche-on-a-chip

The majority of the work in this chapter has been peer reviewed and published in: Perottoni. S.*, Neto G.B.N.*, Di Nitto C., Dmitriev R.I., Raimondi M.T. and Monaghan M.G. (2021). Intracellular label-free detection of mesenchymal stem cell metabolism within a perivascular niche on-a-chip . Lab on a Chip, 21, 1395-1408

3.1. Abstract

The stem cell niche at the perivascular space in human tissue plays a pivotal role in dictating the overall fate of stem cells within it. Mesenchymal stem cells (MSCs) in particular, experience influential microenvironmental conditions, which induce specific metabolic profiles that affect processes of cell differentiation and dysregulation of the immunomodulatory function. Reports focusing specifically on the metabolic status of MSCs under the effect of pathophysiological stimuli – in terms of flow velocities, shear stresses or oxygen tension – do not model heterogeneous gradients, highlighting the need for more advanced models reproducing the metabolic niche. Organ-on-a-chip technology offers the most advanced tools for stem cell niche modelling thus allowing for controlled dynamic culture conditions while profiling tuneable oxygen tension gradients. However, current systems for live cell detection of metabolic activity inside microfluidic devices require the integration of microsensors. The presence of such microsensors poses the potential to alter microfluidics and their resolution does not enable intracellular measurements but rather a global representation concerning cellular metabolism. Here, we present a metabolic toolbox coupling a miniaturised in vitro system for human-MSCs dynamic culture, which mimics microenvironmental conditions of the perivascular niche, with high-resolution imaging of cell metabolism. Using fluorescence lifetime imaging microscopy (FLIM) we monitor the spatial metabolic machinery and correlate it with experimentally validated intracellular oxygen concentration after designing the oxygen tension decay along the fluidic chamber by in silico models prediction. Our platform allows the metabolic regulation of MSCs, mimicking the physiological niche in space and time, and its real-time monitoring representing a functional tool for modelling perivascular niches, relevant diseases and metabolic-related uptake of pharmaceuticals.

3.2. Introduction

The perivascular spaces of many organs contain adult progenitor cell populations in a microenvironment called the perivascular stem cell niche, which presents specific conditions to maintain multi-lineage potential and self-renewal capacity [1, 2]. This is a

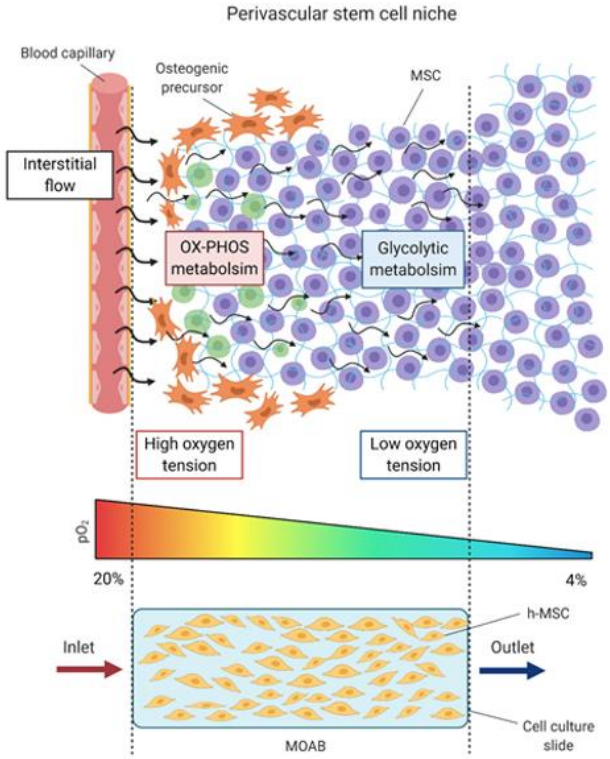

Figure 3.1 - Mesenchymal stem cells (MSCs) reside within perivascular spaces called perivascular niches, which exert regulatory control on the stem cells by interstitial flow levels and defined oxygen tension gradients leading to a specific spatial metabolic profile.

complex and dynamic milieu, where stem cells respond to specific biochemical and mechanical cues. The perivascular niche is an open system, inhabited by heterogeneous cellular populations while physicochemical factors such as oxygen concentration, nutrient availability, signalling factors as well as pH, shear stress or temperature, contribute to its homeostasis [3]. Dysregulation of the niche's microenvironment, associated with hypoxia, inflammation or metabolic reprogramming, has recently been shown to elicit niche-related pathologies [4, 5]. The influence of cellular metabolism on the overall fate of cells is eliciting

a specific interest. It has long been established that cellular metabolism is intrinsically linked to cell behaviour and phenotypic status; with one of the earliest historical reports in 1924 detailing the Warburg Effect exhibited by cancer cells when in states of aerobic and anaerobic metabolism [6]. Only recently has the appreciation of cellular metabolism begun to gather attention in stem cell biology; with a pivotal role of metabolic state in accompanying cell fate towards proliferation, quiescence or differentiation. Shifts in the balance between a glycolytic metabolic profile and the mitochondrial oxidative phosphorylation (OxPhos) define the contribution of adult progenitor and stem cells to the renewal and homeostasis of their native tissue [7-10].

Among the different cell populations involved in niche homeostasis, Mesenchymal stem cells (MSCs), which are multipotent cells present in all vascularized tissues [11]; are emerging as key players in the modulation of the overall niche response and organization [12, 13]. Moreover, due to their immunomodulatory properties, human mesenchymal stem cells (hMSCs) have been extensively applied as therapeutic agents [14, 15]. However, *in vitro* manipulation is shown to alter cell metabolism influencing hMSC's functional properties during *in vitro* expansion [16]. Several reports have examined the effect of flow, shear stress and pressure on stem cell differentiation and mineralisation, but reports specifically focusing on the metabolic status of cells in such conditions are rather lacking [17-20]. Despite efforts in improving standard 2D culture protocols [21-23], advanced tools for controlled and physiologically relevant *in vitro* cultures of hMSCs are still necessary for enhancing knowledge on their metabolic behaviour both *in vivo* and *ex vivo*. Advanced *in vitro* models of the stem cell niche offer the possibility of studying directly and manipulating human stem cell populations, within biomimetic microenvironments, with the potential of providing valid alternatives to animal models in studying tissue renewal and pathogenesis [24]. Such niche-on-a-chip (NOC) systems include fluidic devices that recapitulate relevant

feature of the *in vivo* niche microsystem within fluidic channels for dynamic cell culture [24-27]. These systems can also facilitate defined mechanical stimulation (in terms of shear forces) and spatiotemporal control of biomolecular transport by recapitulating flow velocities at interstitial levels. However, these systems do possess important limitations in their ability to reproduce the mechanical and mass transport field variables present in a native perivascular niche. 1) Microfluidic bioreactors can be utilised to generate a controlled cellular metabolism capitulating that present in the perivascular niche, by the engineering of a defined oxygen tension gradient [28-30] that mimics the spatial oxygenation at the interface between blood vessels and the stem cell niche (Figure 3.1) [31, 32]. Standard 2D cell culture methods are limited in that they typically impose uniform static normoxic or hypoxic oxygen environments. 2) Cellular metabolism in vitro is usually assessed using end-point staining assays which provide intracellular quantification but are an end-point assessment that requires culture sacrifice. 3) Microsensor integration within organ-on-chip platforms can enable continuous metabolic monitoring and recording by accessing the specific molecules involved in cellular metabolism. However, such sensors often operate via enzymatic or biochemical mechanisms which can influence the cellular microenvironment and respiration. The dimensions of currently available microsensors confines their use to extracellular readings, meaning that they are limited to indirect assessment of global cellular metabolism [33].

Advanced imaging technologies are becoming valuable tools for live label-free assessment of intracellular behaviour, and can be applied for metabolic profiling at a single-cell level [10]. Among the available fluorescence microscopy methods, Fluorescence Lifetime Imaging Microscopy (FLIM) has emerged as a key technique capture interaction of specific biomolecules in living cells. It provides high photon efficiency, lifetime accuracy, real-time measurements, high spatial resolution, and does not require staining or labelling of fluorophores. Widespread FLIM applications consist in mapping intracellular

temperature, viscosity, pH as well as measuring ions, glucose or oxygen concentration. FLIM can capture the signals emitted by endogenous fluorophores such as NAD(P)H or FAD, providing a readout of the metabolic state of the samples under investigation[34, 35]. Here, we present a metabolic toolbox that couples a micro-physiological system (MPS) for hMSCs dynamic culture capable of simultaneous imaging of intracellular metabolism at a high resolution. Predictive modelling was employed to engineer a declining gradient in oxygen tension and validated using a previously calibrated non-invasive imaging technology applicable to this miniaturised optically accessible bioreactor (MOAB). Using FLIM we were able to monitor the adaptive modes of metabolic machinery employed in addition to visualising the correlating oxygen concentrations, glucose uptake and mitochondrial membrane potential and morphology occurring at these points which were in validation with our in silico model. These results present a new method and technology to preferentially pattern an in silico-modelled metabolic gradient which will be of enormous benefit to the community in modelling perivascular niches, the relevant diseases, and also the bioavailability and metabolism-related uptake of pharmaceuticals. Additionally, the imaging toolbox presented in this perivascular niche example offer the potential to achieve multiparametric single-cell metabolic evaluation in dynamic cultures.

3.3. Materials and methods

3.3.1. Microfluidic bioreactor

The MOAB is a miniaturized bioreactor for interstitial flow perfusion and high-resolution imaging. It is fabricated by injection moulding of medical grade PC and consists in one main body and three independent lids that magnetically seal on it. In its closed configuration every lid hosts a rectangular base (3 mm x 6 mm x 0.5 mm, volume = 9 µL) cell

culture chamber with a glass surface for cell seeding and real-time imaging. Silicon tubes were perpendicularly connected to the chambers (at the inlet and outlet) allowing for perfusion of cell culture medium. The perfusion was performed by a high precision syringe pump (NE-1600, NEW ERA, Pump Systems Inc.). The MOAB was maintained at 37°C and 5% CO_2 during cell culture and fitted on a heating stage to maintain the correct temperature during image acquisition.

3.3.2. Human mesenchymal stem cells (hMSCs) culture

Bone marrow derived human MSCs (hMSCs) from Lonza® were expanded in Dulbecco's Modified Eagle's Medium (DMEM) – Low glucose (Sigma Aldrich), supplemented with 10% Foetal Bovine Serum (FBS) and 1% Penicillin Streptomycin (Pen/Strep). hMSCs at P3 were seeded in each of the three MOAB's culture chambers, after overnight pre-conditioning in complete DMEM, at a cell density of 3.5 x 10^4 cells/cm^2. The culture chambers were incubated at 37°C and 5% CO_2 for 3 hours to allow hMSCs adhering to the surface before beginning flow perfusion.

3.3.3. Mathematical modelling

A Computational Fluid Dynamic (CFD) analysis was performed to investigate the velocity profile and shear stress distribution inside the cell culture chamber at the cellular level.

A 3D, stationary model was created in COMSOL Multiphysics® 5.2 (Burlington, MA, USA). The medium flow through the micro bioreactor was simulated by implementing the Navier-Stokes equation and the continuity equation for local conservation of momentum

and mass, respectively. The flow was assumed laminar and fully developed at the entrance of the chamber with inlet velocity values computed starting from the selected flowrate range (0.5-5 µL min^{-1}). The mass transfer model assumed MM rate of uptake of oxygen by the cells (Table 2).

Table 3.1 - Model parameters and values used for the computational analysis

Oxygen diffusion coefficient				
Oxygen diffusion coefficient	DO_2	$2x10^{-9}$	$m^2\ s^{-1}$	[36]
Dynamic viscosity	η	$8.4x10^{-4}$	Pa s	[36]
Michaelis-Menten constant for oxygen uptake	Km,O	$4.05x10^{-9}$	mol cm^{-3}	[37]
Maximum uptake rate of oxygen	Vmax	100	fmol h^{-1} $cell^{-1}$	[37]

3.3.4. Quantitative intracellular O_2 imaging

We measured intracellular O_2 tension by using conjugated polymer nanoparticles for high-resolution O_2 imaging in living cells. The nanoparticle probes (bead name: SI-0.2+) are constituted by a substituted conjugated polymer (polyfluorene) covalently bounded with a phosphorescent metalloporphyrin which emits in far red wavelengths, in a low oxygen environment, due to Fluorescence Resonance Energy Transfer (FRET) mechanism. Details on the manufacturing and fluorescence properties of the copolymer complexes can be found in [38]. After seeding hMSCs inside the MOAB, the staining with nanoparticles was achieved by incubation at 8 µg/mL for 16 hours to allow for probes internalization. The culture chambers were washed twice with DMEM medium.

Imaging and related measurements were performed, after 96 hours perfusion at 0.5 µL min^{-1}, with two-photon microscope (Olympus BX61WI) in phenol red-free DMEM.

The excitation wavelength was set at 760 nm and emission wavelength signal was detected in two bandpass filters at 455-490 nm for the fluorene backbone (460 nm) and 580-638 nm for the Pt(II)-porphyrin complex [38].

In order to correlate the fluorescence intensity signal with the intracellular oxygen tension, a semi-calibration curve was obtained (Figure Appendix 4). To achieve this, stained hMSCs were imaged inside of the MOAB in static condition to ensure an oxygen homogenisation. First, the stained hMSCs were imaged in normoxia environment followed, in a separate experiment, by imaging in hypoxia conditions with the respiratory ability of the cells inhibited. To achieve this, cells were incubated at 37'C for 1 hour using 2.5 µM of Rotenone and 10 µM Antimycin A as these metabolic inhibitors act upon complex I and III of the electron transport chain, negating the cell ability to consume oxygen. Using the same excitation power, and photomultiplier (PMT) detector settings, hMSCs cells grown in a MOAB device for 3 days at 0.5 µL min^{-1} flow rate. Afterwards, they were stained and imaged using the multiphoton microscope. Imaging analysis was performed using ImageJ to select ROI areas and calculate their mean grey value.

3.3.5. 2P-FLIM analysis

2P-FLIM was performed using a custom upright (Olympus BX61WI) laser multiphoton microscopy system equipped with a pulsed (80 MHz) Titanium: sapphire laser (Chameleon Ultra, Coherent®, USA), water-immersion 25x objective (Olympus, 1.05NA) and temperature controlled stage at 37°C. During the measurements, the syringe pump was working with the flow-rate adequate to the experiment being performed (5µl min^{-1} or 0.5µl min^{-1}) or in static conditions for the O_2 probe calibration measurements.

Two photon excitation of NAD(P)H fluorescence was performed at the excitation wavelength of 760 nm. A 455/90 nm bandpass filter was used to isolate the NAD(P)H fluorescence emission. 512 x 512 pixel images were acquired with a pixel dwell time of 3.81 µs and 30 s collection time. A PicoHarp 300 TCSPC system operating in the time-tagged mode coupled with a photomultiplier detector assembly (PMA) hybrid detector (PicoQuanT GmbH, Germany) was used for fluorescence decay measurements yielding 256 time bins per pixel. TCSPC requires a defined "start", provided by the electronics steering the laser pulse or a photodiode, and a defined "stop" signal, realized by detection with single-photon sensitive detectors. The measurement of this time delay is repeated many times to account for the statistical nature of the fluorophores emission. For more detailed information on this the reader is referred elsewhere[39].

Fluorescence lifetime images with their associated decay curves for NAD(P)H were obtained and region of interest (ROI) analysis of the total cells present on the image was performed in order to remove any background artefact. The decay curved was generated and was fitted with a double-exponential decay without including the instrument response function (IRF) (Equation 3.1).

$$I(t) = I(0)[\alpha_1 e^{\frac{-t}{\tau_1}} + \alpha_2 e^{\frac{-t}{\tau_2}}] + C$$

Equation 3.1 – Fluorescence Intensity decay fitted with a double-exponential decay curve

I(t) corresponds to the fluorescence intensity measured at time t after laser excitation; α_1 and α_2 represents the fraction of the overall signal proportion of a short and long component lifetime component, respectively. τ_1 and τ_2 are the long and short lifetime components, respectively; C corresponds to background light. χ^2 statistical test was used to evaluate the goodness of multi-exponential fit to the raw fluorescence decay data. In this study all the values with $\chi 2 < 1.3$ were considered as 'good' fits.

For NAD(P)H, the double exponential decay was used to differentiate between the free (τ_1) and protein-bound (τ_2) NAD(P)H. The average fluorescence lifetime was calculated using equation 3.2.

$$\tau_{avg} = \frac{(\tau_1 \times \alpha_1 + \tau_2 \times \alpha_2)}{(\alpha_1 + \alpha_2)}$$

Equation 3.2 – Average fluorescence lifetime calculation

Images were also analysed at single-cell level to evaluate cellular heterogeneity. The z score was calculated for each cell NAD(P)H fluorescence imaging parameter starting from the mean values along the MOAB chamber for 0.5 µL min^{-1} and 5 µL min^{-1} groups respectively; then a heat map was built accordingly.

3.3.6. 2-NBDG and TMRM staining for metabolism validation

hMSCs were seeded in the MOAB following the protocol described as previously described. After 3 days of culture in static or under 0.5 µL min^{-1} or 5 µL min^{-1} flow rate the cells were stained using 100 µM of 2-NBDG or 250 nM of TMRM. Afterwards, the MOAB was incubated at 37°C for 30 minutes or 1 hour for TMRM or 2-NBDG. Then, the MOAB was washed using PBS and cell culture medium flow was restored for at least 2 hours before imaging. Fluorescence images were acquired using the same multiphoton system described before. An excitation wavelength of 850 or 860 nm was used to excite 2-NBDG or TMRM, respectively. Fluorescence emission was collected using photomultiplier tubes (PMT) with a wavelength range of 502-547nm and 580-638 nm for 2-NBDG and TMRM, respectively. Acquired images were analysed using CellProfiler™ with a custom built project pipeline [40].

3.3.7. Statistical analysis

The data obtained was evaluated for statistical significance as described in the figure legends. Results are depicted throughout this manuscript as the mean ± standard deviation. Statistical analysis was performed using PRISM (GraphPad Software, La Jolla, CA, USA). All data sets were assumed to be normally distributed which was confirmed using the Shapiro-Wilks test to test for normal distribution. Unpaired, Paired t-test or One-way ANOVA (where appropriate) were used to establish statistical differences. Statistical significance was set at $p < 0.05$.

3.4. Results

3.4.1. The microbioreactor for hMSCs culture

The culture platform employed in this study is a miniaturized optically accessible bioreactor (MOAB), recently reported for culturing hMSCs inside a dynamic MPS [41] (Figure 3.2A, B). The walls of the MOAB microchambers are fabricated from oxygen-impermeable polycarbonate (PC, with an oxygen diffusion coefficient of 8.0×10^{-8} cm^2 s^{-1}) [28] thus enabling a stable and linear gradient of the oxygen tension (Figure 3.2C).

3.4.2. Intracellular label-free investigation of hMSCs metabolism

Transparent PDMS microfluidic chips permit non-invasive optical monitoring of the MOAB microchamber for the duration of the experimentation. However, to perform high-resolution imaging, immersion objectives are necessary and the refractive index (n) of the viewing surface needs to be as close as possible to that of the objectives. PDMS (with n=1.43) generates optical aberrations on the excitation laser pathway; therefore, the overall optical quality is generally poor. Moreover, PDMS membrane thickness cannot be reduced substantially

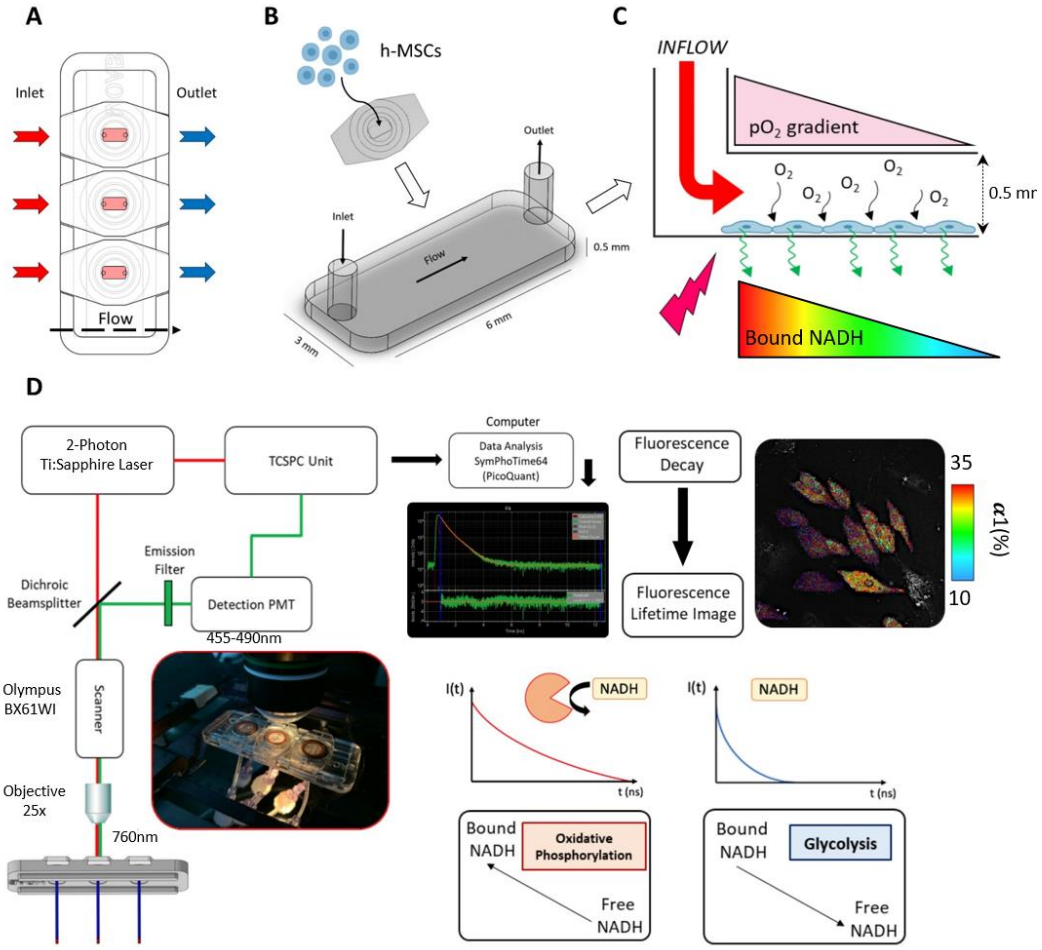

Figure 3.2 - Microfluidic bioreactor and experimental setup. (A) The Miniaturized Optically Accessible Bioreactor (MOAB) device, composed of a Polycarbonate (PC) body with three independent rectangular base flow chambers for cell culture and real-time high-resolution imaging. (B) "Plug and play" seeding of human-MSCs (hMSCs) inside the fluidic chamber for interstitial-like perfusion. (C) By using MOAB a defined oxygen tension gradient can be imposed by controlling the flow perfusion and cell density while simultaneous real-time high-resolution measurement of the metabolic activity by the detection of the bound NAD(P)H fluorescence emission can be performed. (D) Non-invasive measurement of cellular metabolism of hMSCs cultured inside MOAB, using a two-photon (2P) microscope fitted with Fluorescence Lifetime Imaging Microscopy (FLIM) detectors. The result is the NAD(P)H fluorescence decay and a colour coded picture indicating pools of free and enzyme-bound NAD(P)H quantified by their respective fluorescence lifetimes fractions. The free NAD(P)H corresponds to the short τ_1 lifetime with corresponding fraction α_1, representative of a glycolytic profile, while the protein-bound NAD(P)H is related with the long τ_2 and α_2 fraction, indicating oxidative phosphorylation (OxPhos).

without interfering with the performance of the device [42]. We integrated a rectangular glass slide (having n = 1.53 and a thickness of 0.15 mm) inside each fluidic chamber that simultaneously serves as a surface for cellular adhesion to enable high-resolution microscopy (Figure 3.2C).

3.4.3. Optimization of the MPS culture conditions

The spatial and temporal distribution of the oxygen tension across a microfluidic chamber depends on the uniformity of the flow field and on the oxygen consumption rate of cells exposed to this flow. A computational approach was employed to establish a defined perfusion regime at the inlet to create a specific oxygen gradient along the principal flow direction, while ensuring physiological physical stimulation to cells.

3.4.4. Prediction of interstitial flow velocities and shear stress

CFD analysis (COMSOL Multiphysics®) validated in previous work [26] predicted the velocity distribution profile and the levels of shear stress acting in the MOAB microchamber. Interstitial flow velocities in body tissues generate from convective transvascular flows and are reported to range within 0.1-5 μm s^{-1}, in physiological conditions, reaching up to 10 μm s^{-1} during inflammation [43]. Four flow rates (0.5, 2, 3.5 and 5 μL min^{-1}) were simulated, yielding average velocity values in the range 0.5-6 μm s^{-1} (Figure 3.3A).

The estimated wall shear stress, resulting from the flow rates applied (0.5, 2, 3.5 and 5 μL min^{-1}), ranged from an average value of 0.0005 dyne cm^{-2}, at the lowest flowrate (0.5 μL min-^{1}), to 0.005 dyne cm^{-2} at the highest (5 μL min^{-1}) (Figure 3.3A).

3.4.5. Flow-dependent oxygen concentration profile

Next, a mass transport analysis was implemented (COMSOL Multiphysics®) to predict the oxygen tension profile with consideration of hMSCs oxygen consumption across the culture chamber. The cellular consumption rate was modelled as an oxygen sink by defining a steady state flux, dependent on cell density, along the cell adhesion surface of

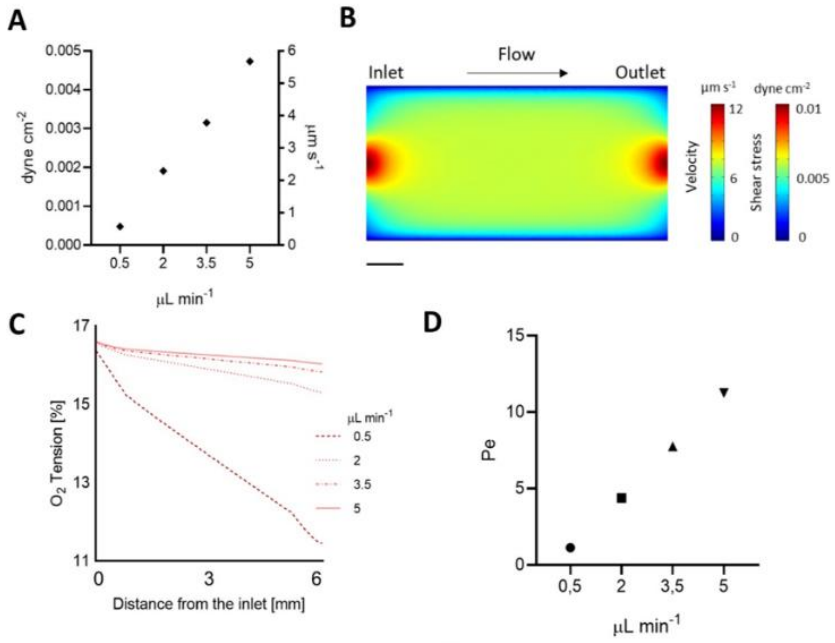

Figure 3.3 - Velocity profile, shear stress and oxygen tension inside the perivascular NOC. (A) Predicted average flow velocities and wall shear stress as function of the input flowrate. (B) Colour map of the flow velocity and wall shear stress distribution in proximity of the cell culture surface area at an inlet flowrate of 5 µL min^{-1}. Colour map in top view. (Scale bar: 1mm.) (C) Prediction of the oxygen tension depletion at a cell density of 8.3 x 104 cells cm^{-2} (corresponding to 96 hours of culture) as function of the distance from the inlet and the input flowrate. (D) Computed Pe number as a function of flowrate considering an oxygen particle at the middle height of the chamber (characteristic length L: 250 µm) in correspondence of the max velocity fillet on a section at 3 mm distance from the inlet.

the MOAB chamber while assuming a uniform distribution of cells. Single cell consumption rate was assumed to depend on both the cell type and on local oxygen availability, following the Michaelis-Menten (MM) equation [37]. As a boundary condition we imposed an oxygen partial pressure of 16.7% at the inlet of the MOAB chamber, based on experimental measurements [44].

From this simulation the oxygen concentration profile gradually decreased across the chamber given a fixed cell number, and its gradient rapidly decreased with flow velocity (Figure 3.3C). At high flow velocity, the contribution of advection prevailed on diffusion within the medium; and in this case it was represented by a 90% increase of the Peclet number (Pe) at the highest flow rate (Figure 3.3D). Moreover, at a fixed reference cell density of 6 x 10^4 cells cm^{-2}, the oxygen tension exponentially decreased with the flowrate

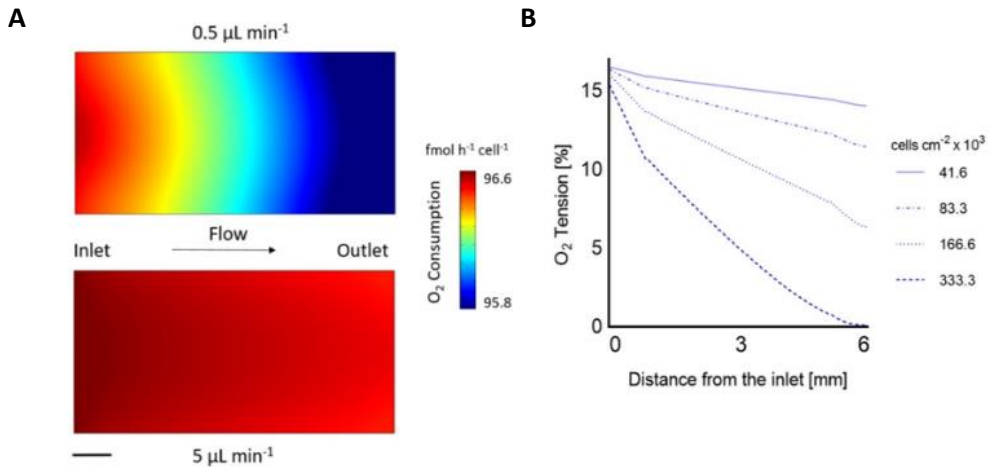

Figure 3.4 - (A) Colour maps of the single cell oxygen uptake rate spatial gradient at 0.5 µL min^{-1} (top) and 5 µL min^{-1} (bottom) at a cell density of 8.3 x 104 cells cm^{-2} (corresponding to 96 hours of culture). Colour maps in top view. (Scale bar: 1 mm.) (B) Prediction of the oxygen tension depletion at a flowrate of 5 µL min^{-1} as function of the distance from the inlet and the cell density (i.e. the day of culture).

due to the hMSCs oxygen uptake. Simulating cellular O_2 consumption decays at the two opposite flowrates (i.e. 0.5 and 5 µL min^{-1}) highlights diverse oxygenated microenvironments as function of the distance from the inlet (Figure 3.4A). Besides the flow velocity, the other element influencing the overall oxygen tension profile is the cell density. We investigated four cell density values (41.6, 83.3, 166.6 and 333.3 x 10^3 cells cm^{-2}), representing the cells doubling during the days of culture, at one fixed flowrate of 0.5 µL min^{-1}, which is the lowest in the MOAB working range. At every cell doubling, the oxygen tension gradient got steeper generating always more hypoxic conditions at the chamber outlet. After four doublings, the oxygen tension at the outlet reached 0%, representing the upper limit working condition of our system in time. This computational approach informed the preparation of the optimal experimental working conditions. The numerical results demonstrated the feasibility to simulate in vitro the varying intensities at which fluids extravasate into the stem cell interstitium, due to changes in blood vessel permeability.

3.4.6. Quantitative intracellular oxygen measurement

To assess and validate the predicted cell oxygen uptake gradient being formed inside of the MOAB, we sought to experimentally quantify intracellular oxygen. To ensure the most physiologically relevant measurements, we performed fluorescence intensity based measurements inside the MOAB using an intracellular phosphorescent probe [45]. Specifically, we used a SI-0.2^{+} nanosensor probe composed of fluorine building blocks which act as an energy donor and an antenna for platinum(II) meso-bis(pentafluorophenyl)bis(4-bromophenyl)porphyrin ($PtTFPPBr_2$) [38]. This conjugated polymer exhibits favourable properties to be used a multiphoton system due to its high intensity fluorescence emission, cell permeability and Förster resonance energy transfer (FRET) properties which is impacted in varying oxygen concentrations. At higher oxygen concentrations this probe is quenched, and lower amounts of energy are transferred from the backbone to metalloporphyrin complex resulting in a decrease of emission intensity at 640-680 nm.

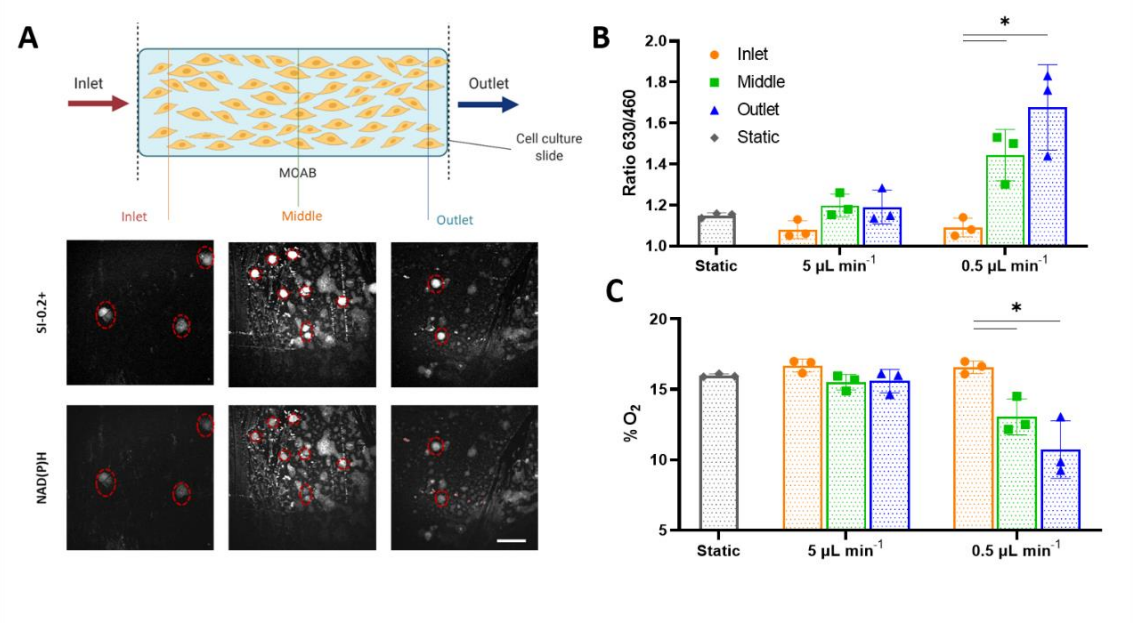

Figure 3.5 - Multiphoton quantitative intracellular oxygen imaging. (A) Representative images acquired at the inlet, middle and outlet areas for both SI-0.2+ and NAD(P)H channels and regions of interest (red) used for quantification. (B) Fluorescence intensity ratio of SI-0.2+ per NAD(P)H in the inlet, middle and outlet areas in three dynamic culture conditions (static (no flow), 0.5 µL min^{-1} and 0.5 µL min^{-1}) (n=3). Statistical analysis performed using one-way ANOVA and $p<0.05$. (C) Intracellular calculated oxygen tension in the different MOAB areas in three dynamic culture conditions (static (no flow), 0.5 µL min^{-1} and 0.5 µL min^{-1}) (n=3). One-way ANOVA was used to detect statistical differences with *$p<0.05$.

After hMSCs incubation with the probe for 16 hours, it was possible to establish a calibration curve (Figure Appendix 4) by detecting the fluorescence emission intensity in cases of uptake activity in normoxic conditions and uptake when a compromised cellular oxygen consumption rate was engineered by suppression of cells respiratory activity.

hMSCs were cultured inside the MOAB for 96 hours at a flow rate of 0.5 µL min^{-1} and 5 µL min^{-1}. Afterwards, they were stained using SI-0.2^{+} and imaged directly in the perfused chamber with a multiphoton microscope while maintaining the same flow rate. Three areas of the MOAB were analysed: inlet, middle and outlet (Figure 3.5A). Two images were acquired at the same time, one for NAD(P)H emission (as a reference signal) and another for the SI-0.2^{+} probe emission wavelength. Afterwards, the emission intensity in the cell area was calculated and a ratio of both acquisitions was performed. A statistically significant increase in the ratio 630/460 from the inlet area of 1.09 ± 0.04, to 1.44 ± 0.10 in the middle, and finally 1.68 ± 0.17 in the outlet area (Figure 3.5B) was detected in the case

of 0.5 µL min^{-1} while no detectable significant overall increase resulted in the case of 5 µL min^{-1}. As described previously [38], an increase of the 630/460 ratio is correlated with decreasing oxygen levels due to decrease of the efficiency of energy transfer from the fluorine backbone to the metalloporphyrin. By applying our semi-calibration curve (Figure Appendix 4), it was possible to correlate the intensity measurements of the 630/460 ratio to partial oxygen values and obtain an estimation of the intracellular oxygen levels. Here, we calculated that the inlet oxygen levels are on average 16.6 ± 0.4 %, 13.1 ± 1.0 % in the middle and 10.7 ± 1.7 % at the outlet when the system is perfused at 0.5 µL min^{-1} with statistically significant differences between each area (Figure 3.5C) Conversely, an increase in the flow rate to 5 µL min^{-1} leads to oxygen levels of 15.6 ± 0.7 at the outlet. Therefore, we were able to observe a direct effect on the intracellular oxygen levels by the flow rate and cell culture environment. This result agrees with the predictions of the in silico model (Figure 3.4). In this in silico model, taking as example the 0.5 µL min^{-1} group, a similar decreasing trend in oxygen distribution from the inlet (≈16.5%) to the outlet (≈11.5%) region is calculated in our model (Figure 3.3).

3.4.7. Two-photon fluorescence lifetime imaging microscopy (2P-FLIM) evaluation of cellular metabolism

2P-NAD(P)H FLIM was performed on the MOAB at specific locations (similar to the intracellular oxygen measurements): inlet, middle and outlet in order to fully delineate any metabolic heterogeneity of these cells. The MOAB was perfused at the flow rate of 0.5 µL min^{-1} and 5 µL min^{-1} and was imaged after 96 hours of culture (Figure 3.6A).

FLIM analysis of hMSCs at these locations revealed a decreasing gradient in the average fluorescence lifetime while the protein bound NAD(P)H lifetime remains stable (Figure 3.6B,C). The calculated average fluorescence lifetime for the inlet, middle and outlet are 1.545 ± 0.012 ns, 1.415 ± 0.070 ns, 1.325 ± 0.045 ns, respectively (Figure 3.6). In addition, the middle and outlet values are statistically significantly decreased when compared to inlet values. The calculated average fluorescence lifetime (τ_{avg}) has been used regularly in

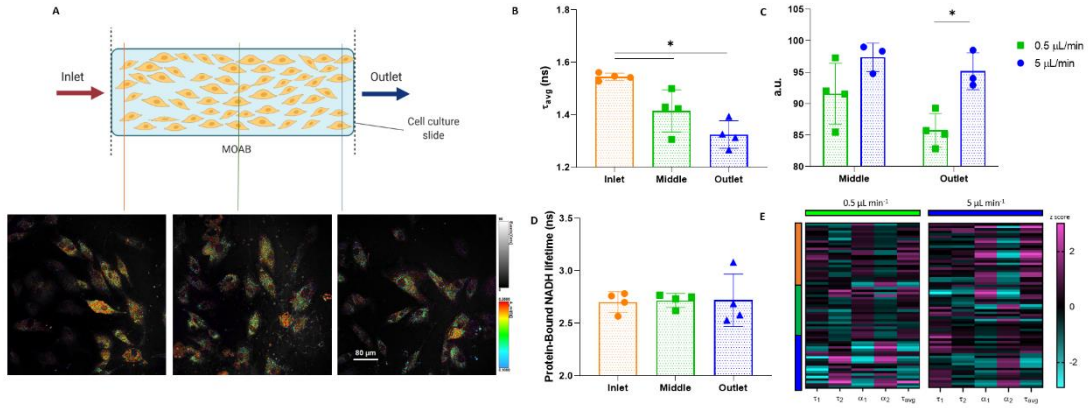

Figure 3.6 - (A) 2P-FLIM NAD(P)H imaging of hMSC cultured on the MOAB. Representative images of the areas imaged after 96 hours cell culture under 0.5 µL min^{-1} flow rate. (B) Average fluorescence lifetimes (τ_{avg}) calculated for the inlet, middle and outlet areas with n=4. One-way ANOVA was used to verify statistical difference with $p<0.05$. (C) Normalisation of middle and outlet τ_{avg} to inlet area of the MOAB at different flow rates. An unpaired t-test was used to verify statistical difference with $p<0.05$. (D) Protein-bound NAD(P)H fluorescence lifetime (τ_1) obtained with n=4 and no statistical difference between groups, verified by One-way ANOVA. (E) Heat map of z scores (normalized according to the mean of the MOAB chamber) of NADPH autofluorescence imaging parameters of hMSCs after 96 hours of perfused culture at 0.5 µL min^{-1} and 5 µL min^{-1} flow rates. Each row is a single cell. The data were clustered according the three areas: inlet, middle and outlet.

previous works as a unique and easy value to quickly discriminate between cellular metabolic states [46-48]. A higher τ_{avg} is reflective of a higher fraction and/or lifetime of the τ_2 demonstrative of a more OxPhos dependent metabolism. These observations are illustrative of a lower dependence of the cells to use OxPhos and therefore becoming more glycolytic.

However, protein-bound NAD(P)H fluorescence lifetimes (τ_2) remain stable with 2.703 ± 0.084 ns, 2.718 ± 0.058 ns, 2.719 ± 0.216 ns, for the inlet, middle and outlet, respectively (Figure 3.6C).

The same experiment was performed at a higher flow rate (5 µL min^{-1}) (Figure Appendix 5). According to our multiphysics numerical analysis (Figure 3.3, 3.4), the oxygen tension profile inside the fluidic chamber in this condition, follows a linear (R^2 = 0.97) decay, along the principal flow direction, with a higher lower slope with respect to the 0.5 µL min^{-1} condition. To better understand the changes in cellular metabolism between 5 µL min^{-1} and 0.5 µL min^{-1}, a normalisation of the middle and outlet areas to the inlet area was performed. As observed in Figure 3.6C, the average fluorescence lifetimes at 5 µL min^{-1} are higher than the 0.5 µL min^{-1} flowrate being statistically significantly higher in the outlet area. With higher values of τ_{avg}, the cells experiencing 5 µL min^{-1} flow rate results to be more spatially dependent on OxPhos than in the case of lower flow rate values. In conjugation with the computational mass transport analysis, the non-significant change of τ_{avg} at a higher flow rate can be correlated to the availability of oxygen inside the MOAB. As the cells experience higher oxygen levels in their environment, they will be less reliant on the use of glycolysis.

While the reported data in Figure 3.5B,C and D refer to average fluorescence lifetime values, the FLIM detection system was also able to detect single cell NADPH autofluorescence emission at a single-cell resolution (Figure Appendix 6). hMSCs heterogeneity inside the MOAB chamber was assessed within the inlet, middle and outlet areas. The heat-map representation (Figure 3.5E) of the z score of NADPH autofluorescence parameters confirmed metabolically similar cells clustering at the inlet, middle and outlet areas which is in strong agreement with the global observation of fluorescence lifetimes at these regions, while revealing intra-area heterogeneity. There do exist a small number of outliers per region which are starkly visible in the heatmap which do impact descriptive

statistics of Skewness, Kurtosis and coefficient of variances. This is due to the smaller number of cells used in these particular analyses.

3.4.8. Validation of metabolic changes by 2-NBDG and TMRM staining

To gain further insight into the adaptive metabolic machinery being utilised in this system and to gain spatial biochemical information about hMSCs under this declining oxygen gradient; 2-[N-(7-nitrobenz-2-oxa-1,3-diazol-4-yl)amino]-2-deoxy-d-glucose (2-NBDG) was first employed which is a commonly used fluorescence glucose analogue to estimate glucose uptake by cells [49-51]. This fluorescent compound enters the cells by the glucose transporter 1 (GLUT1) and glucose transporter 2 (GLUT2). Here, it undergoes phosphorylation by hexokinase preventing its efflux by the cell [52, 53]. 2-NBDG is a direct competitor of glucose in both glycolysis and transport which made it an interesting molecule to correlate directly glucose metabolism and uptake [54-56].

Recent literature has demonstrated that 2-NBDG staining is a non-specific cellular stain and its fluorescence intensity is not necessarily correlated with glucose transport [57]. Initial characterisation of 2-NBDG to measure glucose uptake was performed in E.Coli [58]. In particular, 2-NBDG uptake in bacteria is mediated by a mannose or a glucose/mannose transport system [59].Specifically, Yamada et al., characterised 2-NBDG mediated transport by GLUT2 in Cos1 and Min6 pancreatic beta cells. Here, the uptake of 2-NBDG by GLUT2 was highly selective, inhibited by excess glucose and blocked when using a glucose transport inhibitor [60]. Throughout this thesis, hMSCs were used. Segev et al., measured the expression levels of GLUT1-4 and concluded that GLUT1 and GLUT2 are expressed in hMSCs. However, higher expression levels of GLUT1 are observed at earlier time-points and during cell differentiation comparing with GLUT2 [61]. A study by Souza et al., have validated that inhibiting GLUT1 expression using CRISPR-Cas9 gene editing in 5TGM1 myeloma cells did

not impact 2-NBDG uptake. In addition, Souza et al., showed that 2-NBDG uptake was also independent of competing glucose concentrations [62]. Another study by Hamilton et al., used a L929 fibroblast cell line which expressed GLUT1 as its only glucose transporter, to correlate 2-NBDG fluorescence with glucose uptake. By using chemical inhibitors, overexpression of GLUT1 transporters and siRNA mediated knockdowns, Hamilton et al., were able to modulate glucose uptake in the cells but not 2-NBDG uptake [63]. To conclude, these reports demonstrate that 2-NBDG is not an accurate measurement of glucose uptake in cells expressing GLUT1. Since hMSCs mostly utilise GLUT1 as the major glucose transporter, the results obtained might not correlate directly with glucose uptake. However, currently, there are no glucose-specific fluorescence stains that allow measurements of glucose uptake that could be applied to the MOAB without compromising oxygen and nutrient gradients and achieving single-cell resolution.

In our study we used 2-NBDG to determine glucose uptake by hMSCs inside of the MOAB in static conditions or under a determined flow rate (Figure 3.7). Here we observed that the 0.5 µL min^{-1} flow rate induced a statistically significant reduction of 2-NBDG fluorescence intensity from the inlet to the outlet region of approximately 33%. When using 5 µL min^{-1} as a flow rate there was no statistical different effect on the fluorescence intensity of 2-NBDG inside of the cells (Figure 3.7B). The 0.5 µL min^{-1} results demonstrate that there is a reduction of 2-NBDG uptake from the inlet to the outlet region. Therefore, cells in the outlet are less metabolically active compared with the inlet region. Using 5 µL min^{-1} flow rate this effect is not noticeable. Although an increasing trend of 2-NBDG uptake can be

observed in the middle region, it is not enough to determine a discernable and statistically significant difference.

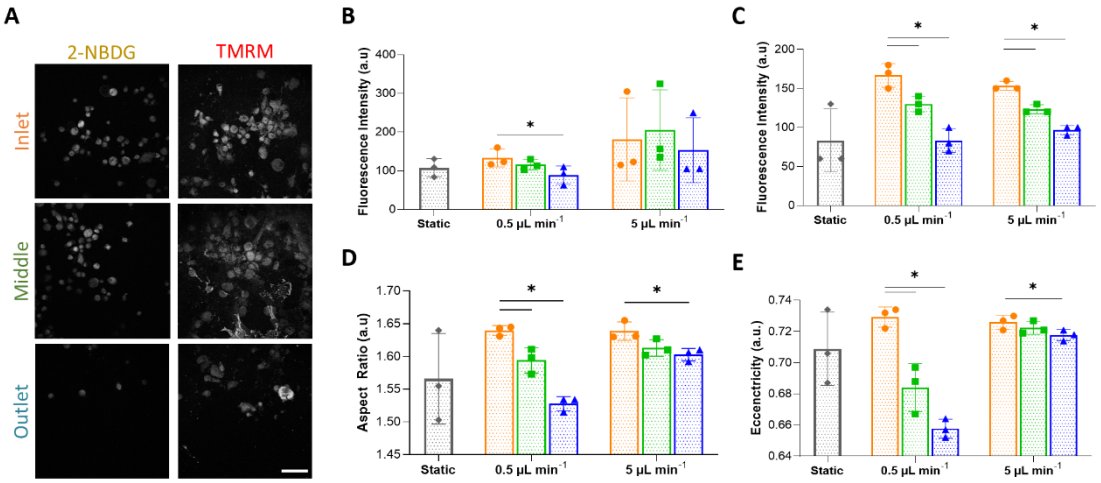

Figure 3.7 - Metabolic Validation of flow on hMSCs using 2-NBDG and TMRM. (A) Representative multiphoton images acquired at different areas of the MOAB at 0.5µl min^{-1} using 2-NBDG and TMRM, scale bar = 100µm. (B) Fluorescence intensity of 2-NBDG. (C) Fluorescence intensity of TMRM. (D, E) Aspect Ratio and Eccentricity calculated of mitochondria staining of TMRM. Paired one-way ANOVA was used to determine statistical significance with *p<0.05.

Additionally we employed Tetramethylrhodamine methyl ester (TMRM); a fluorescence compound which accumulates in the mitochondria intermembrane space in an inverse proportion manner in the same MOAB conditions.

For this study, a custom cell profiler algorithm was used to quantify TMRM staining intensity and mitochondria morphology (Figure 3.8). This script uses the raw image (Figure 3.8A) and applies a de-noising filter to highlight mitochondrial structures (Figure 3.8 B, Computer Code Appendix 7). Afterwards, the software identifies the mitochondria by taking into account the difference in fluorescence intensity of stained mitochondria and the low-intensity background. The segmentation of mitochondrial structures allows the calculation of fluorescence intensity, aspect ratio and eccentricity of individual mitochondria or merged mitochondria. These calculations are done directly in the cell profiler built-in software [40, 64].

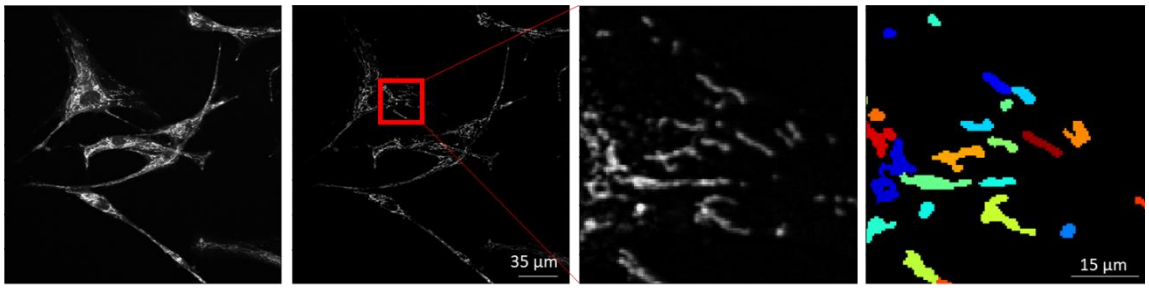

Figure 3.8 – Cell profiler segmentation and quantification analysis of TMRM staining. (A) Raw image before any processing. (B) De-noising plugin effect on raw image. (C) Zoom-in section highlighted by red-box, showing individual and connected mitochondria. (D) Segmentation color-coding of mithocondria.

Here, we stained hMSCs with TMRM and imaged in static conditions or when subject to flow. In Figure 3.7 C, there is a statistically significant decreasing trend of TMRM fluorescence intensity from the inlet to the middle and to the outlet regions in both flow rates investigated (0.5 µL min^{-1} and 5 µL min^{-1}. Using 0.5 µL min^{-1}, we detected a sharper decline in TMRM fluorescence intensity ranging at 22.2% from the inlet to the middle region and 50.3% from the inlet to the outlet region. In comparison with a flowrate of 5 µL min^{-1}, we detected a drop of 19.6% from the inlet to the middle and 36.8% from the inlet to the outlet regions.

Another parameter available from TMRM staining is observation of mitochondrial morphology. Regarding this; we used both aspect ratio and eccentricity as measurements of shape and roundness (or elongation) of mitochondria (Figure 3.7 D, E). Aspect ratio is a ratio between the major and minor axis length of the ellipse equivalent to the mitochondria and eccentricity is a measure of how much a shape deviates from being circular, with a perfect circle having 0 eccentricity [65, 66]. Figure 3.7D, we can observe a statistically significant decrease using a 0.5 µL min^{-1} flow rate from 1.640 ± 0.006 to 1.594 ± 0.016 and to 1.515 ± 0.009 from the inlet to the middle and outlet regions, respectively. Whilst for 5 µL min^{-1}, we only have a statistical significant decrease by comparing the inlet and outlet regions with 1.639 ± 0.012 and 1.603 ± 0.008, respectively. The eccentricity results present in Figure 3.7E show a similar trend. At 0.5 µL min^{-1} there is a statistically significant reduction

of eccentricity from the inlet, to middle and outlet regions from 0.729 ± 0.005, to 0.684 ± 0.013 and 0.658 ± 0.005, respectively. For 5 µL min^{-1}, the only statistical significant trend is observed from the inlet to the outlet regions corresponding to a decrease from 0.726 ± 0.004 to 0.718 ± 0.003. These results illustrate a reduction of mitochondria size and increase of its roundness particularly when using 0.5ul min^{-1} flow rate.

3.5. Discussion

Perfused in vitro cultures of hMSCs have demonstrated the influence of flow-associated shear stress on MSCs commitment to the mesengenic lineages [67, 68]. In this study, precise control enables interstitial flow velocities and low-level shear forces as well as generate a transitional oxygen concentration profile in space and time with the aim of mimicking an interface representative of the one that hMSCs experience near blood capillaries and within the stem cell niche. Due to the MOAB oxygen-impermeable polycarbonate, the only source of free oxygen to reach inside the microchamber is the oxygenated culture medium flowing from the inlet. The combination of constant flow of fresh medium with the consumption of oxygen by the cells modulates an oxygen tension in the microenvironment, leading to the establishment of a spatial oxygen gradient (Figure 3.2C). In addition, the integration of a glass slide to in the MOAB facilitates real-time visualisation of cellular metabolism by means of a two-photon (2P) microscope fitted with FLIM detectors (Figure 3.2C). Harvesting the autofluorescence properties of NAD(P)H provides an insight to the metabolic state of cells [69-71]. This is based on the presence of mixed pools of free and enzyme-bound NAD(P)H that can be individually discernible by their respective fluorescence lifetimes. Here, we focused on the use of 2P-NAD(P)H FLIM. NAD(P)H is characterised by a multi-exponential fluorescence decay, which is fitted using a double-exponential curve with an average fluorescence lifetime (τ_{avg}) obtained from the two different states fluorescence lifetimes and corresponding fractions ($\tau_{1,2}$,$\alpha_{1,2}$) [72-75]. A

representative NAD(P)H fluorescence decay, its fitting and residuals are shown in Figure 3.2D. The free NAD(P)H corresponds to the short τ1 lifetime (~0.4 ns) with corresponding fraction α_1 while the protein-bound NAD(P)H is related with the long τ_2 (>1.5 ns) and α_2 fraction [72, 76, 77]. NAD(P)H is a co-factor of important steps of the metabolic pathways, including glycolysis, OxPhos and pentose phosphate pathway [78].

CFD analysis predicts the velocity distribution profile and levels of shear stress acting in the MOAB. The highest shear stress predicted to act on cells reached 0.001 dyne cm^{-2} which is orders of magnitudes lower than the values reported for shear stress-induced MSCs differentiation [17, 67, 68]. The velocity profile together with shear stress were uniformly distributed at the bottom of the culture chamber with 75% of the surface simulating values within a 10% variation (Figure 3.3B). This simulation predicts equal mechanical stimulation (in terms of shear stress) to the cells. Afterwards, mass transport simulation analysis allowed us to predict oxygen concentration by delineating the effect of varying flowrates on oxygen diffusion and the impact of cell density on the oxygen availability thus, on the overall normoxic-hypoxic gradient within this MPS. Oxygenation levels within different body tissues and organs vary greatly. For example, the oxygen tension in lungs and liver ranges from 13% to 10% while in bone marrow or brain it reaches values from 7% down to 4% [30-32] or even lower (2%) [79]. By tuning the input flow rates of the MOAB, coupled with an appropriate cell density (relative to cellular oxygen consumption) and modelling this in silico, tuning the input flow parameters in the MOAB, we were able to recapitulate specific physiological oxygenation levels and a predefined oxygen concentration decay along the principal flow direction. This represents a functional tool that could be useful in modelling the perivascular niche present in various organs, besides the bone marrow niche modelled here, which is the one primarily investigated to elucidate its role in MSCs differentiation [11, 80, 81]. Experimental measurement of oxygen concentration in the MOAB shows a reduction of oxygen levels from the inlet to the outlet

regions. This effect of downstream depletion of oxygen levels in microfluidic platforms has been previously reported [82, 83]. Mehta et al., reported a similar approach of fluorescence intensity measurements and observed a decreasing trend of oxygen levels from the inlet to outlet areas of a flow bioreactor with a direct dependency on cellular density and a flow rate of 0.5 µl min^{-1} [83]. Other approaches have employed electrode-based or extracellular fluorescence probes to quantify dissolved oxygen in cell culture medium [84-87]. However, these approaches lack the opportunity to quantify intercellular oxygen concentrations directly and are more susceptible to experimental error [83, 88]. Moreover, our approach allows direct quantification within microfluidic cultures contained in compact system without the need of complex channels geometries, multilayered structures or modulation of gases within the culture chamber itself [28]. In order to further validated the metabolism hMSCs cultured in this system, we then employed 2P-FLIM NAD(P)H to directly evaluate the impact of this transient oxygen tension on cellular metabolism. Here, a gradient from OxPhos in the inlet to glycolysis in the outlet region was measured. This trend shows an adaptation of cellular metabolism in response to environmental conditions, specifically oxygen; which was predicted to decline along the flow chamber in response to predefine flow rates according to our computational analysis and later validated with our oxygen probe (Figure 3.3, Figure 3.5). As reported on literature, in reduced presence of oxygen the cells adapt from an aerobic to anaerobic metabolism [6].

The observed trend of decreasing τ_{avg} and its connection to an increase in glycolysis was been reported several times in literature [34, 46, 89]. Walsh et al., demonstrated a decrease in NAD(P)H τ_{avg} in aggressive types of cancer cells, known for being more reliant in glycolysis- a hallmark for their metabolic behaviour [90, 91]. The work by Meleshina et al., showed a contrast between MSCs subjected to osteogenic differentiation and undifferentiated MSCs. The latter were characterized by a lower NAD(P)H lifetimes associated with their glycolytic metabolic profile[34]. Our 2P-FLIM results clearly

demonstrate a decrease of τ_{avg} at the outlet of the MOAB chamber which is correlated with higher dependence on the glycolytic pathway by hMSCs as they are farther away from the fluidic chamber inlet. Nonetheless, NAD(P)H protein-bound lifetimes (τ_1) are constant. According to Blacker et al., τ_1 is an indicator of the ratio of NADPH and NADH [92]. These two species are difficult to separate due to spectroscopy similarities however, a longer τ_1 is associated with a higher presence of intracellular NADPH. In the results obtained, these values remain the same which is indicative of a constant ratio of NADPH/NADH pools.

NADPH is a metabolic co-factor more involved in anabolic pathways whose presence is less relevant for glycolysis and OxPhos [78]. Using our 2P-FLIM to distinguish between OxPhos and glycolysis, we can be confident that the OxPhos metabolic pathway is the one most affected by the lack of oxygen, in specific the enzymatic reactions steps that are dependent of oxygen such as the electron transport chain, as already described in literature [93]. By increasing the flow velocity from 0.5 µL min^{-1} to 5 µL min^{-1} flow rate, there is a reduction on the heterogeneity across the total area of the MOAB chamber.

Single-cell analysis was also performed revealing intra-area heterogeneity as well with some variation between single-cells. Future studies to investigate this heterogeneity further and definitively ascertain the impact of variable flow conditions are ongoing would benefit from the analysis of thousands of cells per experimental group, which is possible; necessitate the incorporation of machine learning (t-distributed stochastic neighbour embedding, t-SNE; or similar approaches) [48].

Our results strongly correlate the increase of glycolytic behaviours with the decrease of oxygen availability predicted in silico (Figure 3.4), which was validated and quantified in vitro (Figure 3.5, Figure 3.6). The relationship between oxygen availability and metabolism has been widely addressed in many studies where often the metabolic switch promoted by the lack of oxygen is majorly due to the hypoxia-inducible factors (HIFs) [94-97]. These transcription factors are composed by a stable β-subunit and two α-subunits in

which of HIF1α is oxygen-labile [98, 99]. Reducing the levels of oxygen promotes the stabilisation and inactivates the HIF prolyl hydroxylases which results in increased levels of intracellular HIFs [100, 101]. After activation, these factors can promote the expression of genes related with the glycolytic pathway such as: glucose transporter 1 (GLUT1), increasing glucose uptake; lactate dehydrogenase A, converting pyruvate to lactate; and pyruvate dehydrogenase kinase 1 (PDK1) which inhibits the role of pyruvate dehydrogenase reducing the pyruvate uptake by the mitochondria consequently reducing OxPhos and oxygen consumption[102]. Therefore, there is a correlation between the oxygen availability and cellular metabolism, validated by our oxygen measurements and 2P-FLIM.

A hypoxic environment and higher dependence of glycolysis can induce an increase of glucose uptake [103, 104]. However, our 2-NBDG results at 0.5 µL min^{-1} show a decrease in glucose uptake from the inlet to the outlet region. This might be due to an overall reduction of cellular metabolism and ATP production promoted by lower oxygen and glucose availability as low nutrient concentrations have been shown to decrease NADH and ATP levels [105, 106]. When using 2-NBDG at 5 µL min^{-1} flow rate, there is no significant trend observed. This result could be attributed to downregulated OxPhos (Figure Appendix 5) although with a higher nutrient availability compared with a 0.5 µL min^{-1} flow rate which increases glucose uptake to try to rescue ATP production levels against their oxygen limited OxPhos [107].

TMRM staining was used to connect the metabolic profiles observed with mitochondrial membrane potential and shape. As the mitochondria membrane potential (Δψm) decreases, more of TMRM accumulates originating in a higher fluorescence signal intensity. In addition, it allows one to analyse mitochondrial morphology, establishing a direct connection with cellular metabolism [108, 109]. The reduction of TMRM fluorescence intensity has been associated with an increase of Δψm, as cationic TMRM accumulates in lower amounts in a less negatively polarised mitochondria [108, 110]. Δψm is generated by

the proton pumps in the electron transport chain and functions as an energy storage during OxPhos. This potential, associated with the proton gradient, constitutes the transmembrane potential of hydrogen ions that are used to fuel ATP synthase and produce ATP[111]. The more stable the Δψm values, the higher the amount of intracellular ATP and even in hypoxia or inhibition of OxPhos, the Δψm can be rescued by ATP-consumption formed during glycolysis [112, 113]. Our results suggest that the Δψm cannot be adequately maintained in both flow rates, with reduced stability at 0.5 µL min^{-1}. This indicates that the intracellular levels of ATP in cells at the middle and outlet are lower compared with cells in the inlet region. The decreasing potential of ATP production can be due a culmination of limited availability of nutrients (for instance glucose) and the impact of reduced oxygen on metabolism. The TMRM results strongly correlates with our previous 2-NBDG experiment with lower glucose consumption and availability at 0.5 µL min^{-1}, and an attempt to rescue ATP production by the middle area cells due to higher nutrient availability at 5 µL min^{-1} (Figure 3.7A).

Furthermore, mitochondria shape and morphology are inextricably linked to metabolism and its function[109]. Mitochondria fusion (elongated) is associated with increased ATP production while fission (circular) is associated with impaired OxPhos and glycolytic dependent metabolism. Both fusion and fission processes can occur due to metabolic demands and nutrient availability[114, 115]. Our results (Figure 3.7D, E) confirm that mitochondria in outlet cells are smaller and more circular when compared with mitochondria in the inlet regions. This occurs due to the lower availability of nutrients and oxygen (Figure 3.5) in the outlet regions versus the higher nutrient and oxygen levels at the inlet. In addition, the fission process occurring in outlet cells is also indicative of a more glycolytic dependent metabolism as verified by Figure 3.6.

The results measured with 2-NBDG and TMRM validate what was implicit in Figure 3.5 and Figure 3.6. The cells in the inlet, middle and outlet regions adapt their metabolism

according to nutrient availability and oxygen levels. Here, they adjust their glucose uptake, mitochondria membrane potential and morphology in response to environmental cues promoting a glycolysis dependent metabolism and to achieve functional ATP levels.

While there are some reports of FLIM being applied to fluidic systems [116, 117], this paper demonstrates the first case of 2P-FLIM metabolic characterization of stem cells in a microfluidic bioreactor without the use of microsensors or disruptive end-point assays [33, 118]. Not only that, this study directly links and validates in silico modelling to real-time non-invasive imaging of oxygen concentration gradients followed by its impact on cellular metabolism which is validated by glucose consumption, mitochondrial membrane potential and mitochondrial morphology- all non-invasively. Recently, 2P-FLIM analysis has becoming increasing applied to microfluidic platforms due to 2P-FLIM non-invasive features. 2P-FLIM has been applied to bioreactors which mimic retinal, tumour and hepatic microenvironments [119-121]. In addition 2P-FLIM in bioreactors applications has been used to establish a single-cell sorting platform of yeast based on fluorescence lifetime [122]. In particular, an interesting application was to evaluate the role of tumour microenvironment on natural killer (NK) cells [120]. In this study by Ayuso et al., the bioreactor platform mimicked the tumour microenvironment resulting in gradually reduced NK cells cytotoxic capacity leading to compromised NK cells function. After removing NK cells from the tumour microenvironment, NK cells exhaustion persisted for an extended period of time. Here, 2P-FLIM was able to detect metabolic changes in NK cells after 1-week incubation period in the tumour bioreactor revelling lower optical redox ratios of NK cells when exposed to tumour microenvironment [120].

The focus of other future studies could be the use of 3D substrates with different morphologies in order to understand their mechanical impact on cellular metabolism and the oxygen distribution [26, 123, 124]. In addition, the real-time, label-free metabolic analysis coupled with the possibility to model oxygen distribution can be used as a more

physiological relevant cancer drug screening platform. For example, one major trigger of tumour angiogenesis is a pathological hypoxia achieved due to a decrease in blood flow, reduced vascularization and increase in oxygen consumption [125].

3.6. Conclusions

This work developed and validated a miniaturized platform for profiling stem cell metabolism in a niche-on-a-chip configuration. In this study, using in silico modelling, it was predicted that this bioreactor could sustain a microphysiological environment with transient spatial oxygen tension distribution typical of the perivascular stem cell niche. This was confirmed by microscopy-based real-time quantification of intracellular oxygenation highlighting a correlating gradient in single cell intracellular oxygen concentration. Finally, in this study high-resolution FLIM measurements of hMSCs metabolism was performed which allowed us to assess the generation of an oxygen-dependent metabolic profile. A decrease of the average fluorescence lifetime of NAD(P)H is indicative of a higher reliance on glycolysis as the chamber gets more hypoxic towards the outlet. In addition, these metabolic changes were validated by 2-NBDG and TMRM staining to account for glucose uptake, $\Delta\psi m$, and mitochondria morphology. It was demonstrated that we can tune the metabolic shift by controlling the environmental oxygen tension through perfusion flowrates and cell density. This toolbox is an innovative in vitro platform that can allow tuneable and measurable oxygen tension gradients that can achieve appreciable impacts on cellular metabolism. This advanced transient microenvironment can recapitulate aspects of intravital niches providing a reliable tool for diseases modelling and drugs screening.

3.7. References

[1] M. Crisan, M. Corselli, W.C. Chen, B. Peault, Perivascular cells for regenerative medicine, J Cell Mol Med. 16(12) (2012) 2851-60.
[2] M. Oh, J.E. Nor, The perivascular niche and self-renewal of stem cells, Frontiers in Physiology. 6 (2015) 367-373.
[3] D.E. Discher, D.J. Mooney, P.W. Zandstra, Growth factors, matrices, and forces combine and control stem cells, Science. 324(5935) (2009) 1673-7.
[4] A. Benabid, L. Peduto, Mesenchymal perivascular cells in immunity and disease, Current Opinion Immunology. 64 (2020) 50-55.
[5] S. Mendez-Ferrer, D. Bonnet, D.P. Steensma, R.P. Hasserjian, I.M. Ghobrial, J.G. Gribben, M. Andreeff, D.S. Krause, Bone marrow niches in haematological malignancies, Nature Reviews Cancer. 20(5) (2020) 285-298.
[6] M.G. Vander Heiden, L.C. Cantley, C.B. Thompson, Understanding the Warburg effect: the metabolic requirements of cell proliferation, Science. 324(5930) (2009) 1029-33.
[7] K. Ito, K. Ito, Metabolism and the control of cell fate decisions and stem cell renewal, Annual Review of Cell and Developmental Biology. 32 (2016) 399-409.
[8] C. Hu, L. Fan, P. Cen, E. Chen, Z. Jiang, L. Li, Energy metabolism plays a critical role in stem cell maintenance and differentiation, International Journal of Molecular Sciences. 17(2) (2016) 253-268.
[9] S. Palomaki, M. Pietila, S. Laitinen, J. Pesala, R. Sormunen, P. Lehenkari, P. Koivunen, HIF-1alpha is upregulated in human mesenchymal stem cells, Stem Cells. 31(9) (2013) 1902-1909.
[10] N. Shyh-Chang, G.Q. Daley, L.C. Cantley, Stem cell metabolism in tissue development and aging, Development. 140(12) (2013) 2535-47.
[11] L. da Silva Meirelles, P.C. Chagastelles, N.B. Nardi, Mesenchymal stem cells reside in virtually all post-natal organs and tissues, Journal of Cell Science. 119(Pt 11) (2006) 2204-2213.
[12] B. Fattizzo, J.A. Giannotta, W. Barcellini, Mesenchymal stem cells in aplastic anemia and myelodysplastic syndromes: the "Seed and Soil" crosstalk, International Journal Molecular Sciences. 21(15) (2020) 1-18.
[13] Y. Kfoury, D.T. Scadden, Mesenchymal cell contributions to the stem cell niche, Cell Stem Cell. 16(3) (2015) 239-53.
[14] C.M. Rivera-Cruz, J.J. Shearer, M. Figueiredo Neto, M.L. Figueiredo, The immunomodulatory effects of mesenchymal stem cell polarization within the tumor microenvironment niche, Stem Cells International. 2017 (2017) 1-18.
[15] M. Tewary, N. Shakiba, P.W. Zandstra, Stem cell bioengineering: building from stem cell biology, Nature Reviews Genetics. 19(10) (2018) 595-614.
[16] X. Yuan, T.M. Logan, T. Ma, Metabolism in Human mesenchymal stromal cells: a missing link between hMSC biomanufacturing and therapy?, Frontiers in Immunology. 10 (2019) 977-988.
[17] K.M. Kim, Y.J. Choi, J.H. Hwang, A.R. Kim, H.J. Cho, E.S. Hwang, J.Y. Park, S.H. Lee, J.H. Hong, Shear stress induced by an interstitial level of slow flow increases the osteogenic differentiation of mesenchymal stem cells through TAZ activation, PloS One. 9(3) (2014) e92427.
[18] J.K. Leach, J. Whitehead, Materials-directed differentiation of mesenchymal stem cells for tissue rngineering and regeneration, American Chemical Society Biomaterials Science and Engineering. 4(4) (2018) 1115-1127.
[19] B. Trappmann, J.E. Gautrot, J.T. Connelly, D.G. Strange, Y. Li, M.L. Oyen, M.A. Cohen Stuart, H. Boehm, B. Li, V. Vogel, J.P. Spatz, F.M. Watt, W.T. Huck, Extracellular-matrix tethering regulates stem-cell fate, Nature Materials. 11(7) (2012) 642-649.
[20] K. Bai, Y. Huang, X. Jia, Y. Fan, W. Wang, Endothelium oriented differentiation of bone marrow mesenchymal stem cells under chemical and mechanical stimulations, J Biomech. 43(6) (2010) 1176-81.

[21] K. Carter, H.J. Lee, K.S. Na, G.M. Fernandes-Cunha, I.J. Blanco, A. Djalilian, D. Myung, Characterizing the impact of 2D and 3D culture conditions on the therapeutic effects of human mesenchymal stem cell secretome on corneal wound healing in vitro and ex vivo, Acta Biomaterialia. 99 (2019) 247-257.
[22] T.J. Bartosh, J.H. Ylostalo, Efficacy of 3D culture priming is maintained in Human mesenchymal stem cells after extensive expansion of the cells, Cells. 8(9) (2019) 1031-1049.
[23] D. Mushahary, A. Spittler, C. Kasper, V. Weber, V. Charwat, Isolation, cultivation, and characterization of human mesenchymal stem cells, Cytometry A. 93(1) (2018) 19-31.
[24] Y.S. Torisawa, C.S. Spina, T. Mammoto, A. Mammoto, J.C. Weaver, T. Tat, J.J. Collins, D.E. Ingber, Bone marrow-on-a-chip replicates hematopoietic niche physiology in vitro, Nat Methods. 11(6) (2014) 663-9.
[25] C. Lin, L. Lin, S. Mao, L. Yang, L. Yi, X. Lin, J. Wang, Z.X. Lin, J.M. Lin, Reconstituting glioma perivascular niches on a chip for insights into chemoresistance of glioma, Anal Chem. 90(17) (2018) 10326-10333.
[26] A. Marturano-Kruik, M.M. Nava, K. Yeager, A. Chramiec, L. Hao, S. Robinson, E. Guo, M.T. Raimondi, G. Vunjak-Novakovic, Human bone perivascular niche-on-a-chip for studying metastatic colonization, Proceedings of the National Academy of Sciences of the United States of America. 115(6) (2018) 1256-1261.
[27] S. Sieber, L. Wirth, N. Cavak, M. Koenigsmark, U. Marx, R. Lauster, M. Rosowski, Bone marrow-on-a-chip: Long-term culture of human haematopoietic stem cells in a three-dimensional microfluidic environment, Journal of Tissue Engineering Regenerative Medicine. 12(2) (2018) 479-489.
[28] K.R. Rivera, M.A. Yokus, P.D. Erb, V.A. Pozdin, M. Daniele, Measuring and regulating oxygen levels in microphysiological systems: design, material, and sensor considerations, Analyst. 144(10) (2019) 3190-3215.
[29] A. Super, N. Jaccard, M.P. Cardoso Marques, R.J. Macown, L.D. Griffin, F.S. Veraitch, N. Szita, Real-time monitoring of specific oxygen uptake rates of embryonic stem cells in a microfluidic cell culture device, Biotechnology Journal. 11(9) (2016) 1179-1189.
[30] M.D. Brennan, M.L. Rexius-Hall, L.J. Elgass, D.T. Eddington, Oxygen control with microfluidics, Lab on a Chip. 14(22) (2014) 4305-4318.
[31] A. Mohyeldin, T. Garzon-Muvdi, A. Quinones-Hinojosa, Oxygen in stem cell biology: a critical component of the stem cell niche, Cell Stem Cell. 7(2) (2010) 150-161.
[32] A. Carreau, B. El Hafny-Rahbi, A. Matejuk, C. Grillon, C. Kieda, Why is the partial oxygen pressure of human tissues a crucial parameter? small molecules and hypoxia, Journal of Cellular and Molecular Medicine. 15(6) (2011) 1239-1253.
[33] J. Kieninger, A. Weltin, H. Flamm, G.A. Urban, Microsensor systems for cell metabolism - from 2D culture to organ-on-chip, Lab on a Chip. 18(9) (2018) 1274-1291.
[34] A.V. Meleshina, O.S. Rogovaya, V.V. Dudenkova, M.A. Sirotkina, M.M. Lukina, A.S. Bystrova, V.G. Krut, D.S. Kuznetsova, E.P. Kalabusheva, A.V. Vasiliev, E.A. Vorotelyak, E.V. Zagaynova, Multimodal label-free imaging of living dermal equivalents including dermal papilla cells, Stem Cell Research Therapy. 9(1) (2018) 84-96.
[35] K. Suhling, L.M. Hirvonen, W. Becker, S. Smietana, H. Netz, J. Milnes, T. Conneely, A.L. Marois, O. Jagutzki, F. Festy, Z. Petrasek, A. Beeby, Wide-field time-correlated single photon counting-based fluorescence lifetime imaging microscopy, Nuclear Instruments and Methods in Physics Research Section A. 942 (2019) 162365-162372.
[36] M. Lagana, M.T. Raimondi, A miniaturized, optically accessible bioreactor for systematic 3D tissue engineering research, Biomedical Microdevices. 14(1) (2012) 225-234.
[37] M.J. Osiecki, S.D.L. McElwain, W.B. Lott, Modelling mesenchymal stromal cell growth in a packed bed bioreactor with a gas permeable wall, PloS One. 13(8) (2018) e0202079.

[38] R.I. Dmitriev, S.M. Borisov, H. Dussmann, S. Sun, B.J. Muller, J. Prehn, V.P. Baklaushev, I. Klimant, D.B. Papkovsky, Versatile conjugated polymer Nanoparticles for high-Resolution O2 imaging in cells and 3D tissue models, American Chemical Society Nano. 9(5) (2015) 5275-5288.
[39] M. Wahl, T. Rohlicke, H.J. Rahn, R. Erdmann, G. Kell, A. Ahlrichs, M. Kernbach, A.W. Schell, O. Benson, Integrated multichannel photon timing instrument with very short dead time and high throughput, Rev Sci Instrum. 84(4) (2013) 043102.
[40] C. McQuin, A. Goodman, V. Chernyshev, L. Kamentsky, B.A. Cimini, K.W. Karhohs, M. Doan, L. Ding, S.M. Rafelski, D. Thirstrup, W. Wiegraebe, S. Singh, T. Becker, J.C. Caicedo, A.E. Carpenter, CellProfiler 3.0: Next-generation image processing for biology, PLoS Biol. 16(7) (2018) e2005970.
[41] L. Izzo, M. Tunesi, L. Boeri, M. Lagana, C. Giordano, M.T. Raimondi, Influence of the static magnetic field on cell response in a miniaturized optically accessible bioreactor for 3D cell culture, Biomed Microdevices. 21(1) (2019) 1-12.
[42] M. Tonin, N. Descharmes, R. Houdre, Hybrid PDMS/glass microfluidics for high resolution imaging and application to sub-wavelength particle trapping, Lab on a Chip. 16(3) (2016) 465-470.
[43] J.M. Rutkowski, M.A. Swartz, A driving force for change: interstitial flow as a morphoregulator, Trends in Cell Biology. 17(1) (2007) 44-50.
[44] H. Eghbali, M.M. Nava, G. Leonardi, D. Mohebbi-Kalhori, R. Sebastiano, A. Samimi, M.T. Raimondi, An experimental-numerical investigation on the effects of macroporous scaffold geometry on cell culture parameters, International Journal of Artificial Organs. 40(4) (2017) 185-195.
[45] D.B. Papkovsky, R.I. Dmitriev, Imaging of oxygen and hypoxia in cell and tissue samples, Cell Mol Life Sci. 75(16) (2018) 2963-2980.
[46] I.A. Okkelman, N. Neto, D.B. Papkovsky, M.G. Monaghan, R.I. Dmitriev, A deeper understanding of intestinal organoid metabolism revealed by combining fluorescence lifetime imaging microscopy (FLIM) and extracellular flux analyses, Redox Biology. 30 (2020) 101420.
[47] A. Floudas, N. Neto, V. Marzaioli, K. Murray, B. Moran, M.G. Monaghan, C. Low, R.H. Mullan, N. Rao, V. Krishna, S. Nagpal, D.J. Veale, U. Fearon, Pathogenic, glycolytic PD-1+ B cells accumulate in the hypoxic RA joint, Journal of Clinical Investigation Insight. 5(21) (2020) e139032.
[48] A.J. Walsh, K.P. Mueller, K. Tweed, I. Jones, C.M. Walsh, N.J. Piscopo, N.M. Niemi, D.J. Pagliarini, K. Saha, M.C. Skala, Classification of T-cell activation via autofluorescence lifetime imaging, Nature Biomedical Engineering. 5(1) (2021) 77-88.
[49] N. Yamamoto, M. Ueda, T. Sato, K. Kawasaki, K. Sawada, K. Kawabata, H. Ashida, Measurement of glucose uptake in cultured cells, Currents Protocols in Pharmacology. Chapter 12: Unit 12(14) (2011) 1-22.
[50] C. Zou, Y. Wang, Z. Shen, 2-NBDG as a fluorescent indicator for direct glucose uptake measurement, J Biochem Biophys Methods. 64(3) (2005) 207-15.
[51] W.H. Kim, J. Lee, D.W. Jung, D.R. Williams, Visualizing sweetness: increasingly diverse applications for fluorescent-tagged glucose bioprobes and their recent structural modifications, Sensors (Basel). 12(4) (2012) 5005-27.
[52] K. Yamada, M. Nakata, N. Horimoto, M. Saito, H. Matsuoka, N. Inagaki, Measurement of glucose uptake and intracellular calcium concentration in single, living pancreatic beta-cells, J Biol Chem. 275(29) (2000) 22278-83.
[53] K. Yoshioka, M. Saito, K.B. Oh, Y. Nemoto, H. Matsuoka, M. Natsume, H. Abe, Intracellular fate of 2-NBDG, a fluorescent probe for glucose uptake activity, in Escherichia coli cells, Biosci Biotechnol Biochem. 60(11) (1996) 1899-901.
[54] K.-B. Oh, H. Matsuoka, Rapid viability assessment of yeast cells using vital staining with 2-NBDG, a fluorescent derivative of glucose, International Journal of Food Microbiology. 76(1-2) (2002) 47-53.

[55] R.G. O'Neil, L. Wu, N. Mullani, Uptake of a fluorescent deoxyglucose analog (2-NBDG) in tumor cells, Mol Imaging Biol. 7(6) (2005) 388-92.
[56] I. Pacella, C. Procaccini, C. Focaccetti, S. Miacci, E. Timperi, D. Faicchia, M. Severa, F. Rizzo, E.M. Coccia, F. Bonacina, N. Mitro, G.D. Norata, G. Rossetti, V. Ranzani, M. Pagani, E. Giorda, Y. Wei, G. Matarese, V. Barnaba, S. Piconese, Fatty acid metabolism complements glycolysis in the selective regulatory T cell expansion during tumor growth, Proc Natl Acad Sci U S A. 115(28) (2018) E6546-E6555.
[57] L.V. Sinclair, C. Barthelemy, D.A. Cantrell, Single Cell Glucose Uptake Assays: A Cautionary Tale, Immunometabolism. 2(4) (2020) e200029.
[58] K. Yoshioka, H. Takahashi, T. Homma, M. Saito, K.-B. Oh, Y. Nemoto, H. Matsuoka, A novel fluorescent derivative of glucose applicable to the assessment of glucose uptake activity of Escherichia coli, Biochimica et Biophysica Acta (BBA) - General Subjects. 1289(1) (1996) 5-9.
[59] J. Tao, R.K. Diaz, C.R. Teixeira, T.J. Hackmann, Transport of a fluorescent analogue of glucose (2-NBDG) versus radiolabeled sugars by rumen bacteria and escherichia coli, Biochemistry. 55(18) (2016) 2578-2589.
[60] K. Yamada, M. Nakata, N. Horimoto, M. Saito, H. Matsuoka, N. Inagaki, Measurement of glucose uptake and intracellular calcium concentration in single, living pancreatic beta-cells, Journal of Biological Chemistry. 275(29) (2000) 22278-22283.
[61] H. Segev, B. Fishman, R. Schulman, J. Itskovitz-Eldor, The expression of the class 1 glucose transporter isoforms in human embryonic stem cells, and the potential use of GLUT2 as a marker for pancreatic progenitor enrichment, Stem Cells Dev. 21(10) (2012) 1653-61.
[62] L.J. D'Souza, S.H. Wright, D. Bhattacharya, Genetic evidence that uptake of the fluorescent analog 2NBDG occurs independently of known glucose transporters, PloS One. 17(8) (2022) e0261801.
[63] K.E. Hamilton, M.F. Bouwer, L.L. Louters, B.D. Looyenga, Cellular binding and uptake of fluorescent glucose analogs 2-NBDG and 6-NBDG occurs independent of membrane glucose transporters, Biochimie. 190 (2021) 1-11.
[64] D.J. Rees, L. Roberts, M. Carla Carisi, A.H. Morgan, M.R. Brown, J.S. Davies, Automated Quantification of Mitochondrial Fragmentation in an In Vitro Parkinson's Disease Model, Curr Protoc Neurosci. 94(1) (2020) e105.
[65] H. Mortiboys, K.J. Thomas, W.J. Koopman, S. Klaffke, P. Abou-Sleiman, S. Olpin, N.W. Wood, P.H. Willems, J.A. Smeitink, M.R. Cookson, O. Bandmann, Mitochondrial function and morphology are impaired in parkin-mutant fibroblasts, Ann Neurol. 64(5) (2008) 555-65.
[66] L.M. Westrate, J.A. Drocco, K.R. Martin, W.S. Hlavacek, J.P. MacKeigan, Mitochondrial morphological features are associated with fission and fusion events, PLoS One. 9(4) (2014) e95265.
[67] E. Stavenschi, M.N. Labour, D.A. Hoey, Oscillatory fluid flow induces the osteogenic lineage commitment of mesenchymal stem cells: The effect of shear stress magnitude, frequency, and duration, Journal of Biomechanics. 55 (2017) 99-106.
[68] A.B. Yeatts, D.T. Choquette, J.P. Fisher, Bioreactors to influence stem cell fate: augmentation of mesenchymal stem cell signaling pathways via dynamic culture systems, Biochimica et Biophysica Acta. 1830(2) (2013) 2470-2480.
[69] J.R. Lakowicz, H. Szmacinski, K. Nowaczyk, M.L. Johnson, Fluorescence lifetime imaging of free and protein-bound NADH, Proceedings of the National Academy of Sciences of the United States of America. 89(4) (1992) 1271-1275.
[70] J.M. Szulczewski, D.R. Inman, D. Entenberg, S.M. Ponik, J. Aguirre-Ghiso, J. Castracane, J. Condeelis, K.W. Eliceiri, P.J. Keely, In Vivo Visualization of Stromal Macrophages via label-free FLIM-based metabolite imaging, Sci Rep. 6 (2016) 25086.
[71] T.S. Blacker, M.R. Duchen, Investigating mitochondrial redox state using NADH and NADPH autofluorescence, Free Radical Biology and Medicine. 100 (2016) 53-65.

[72] I.A. Okkelman, N. Neto, D.B. Papkovsky, M.G. Monaghan, R.I. Dmitriev, A deeper understanding of intestinal organoid metabolism revealed by combining fluorescence lifetime imaging microscopy (FLIM) and extracellular flux analyses, Redox Biol. 30 (2020) 101420.
[73] P.H. Lakner, M.G. Monaghan, Y. Moller, M.A. Olayioye, K. Schenke-Layland, Applying phasor approach analysis of multiphoton FLIM measurements to probe the metabolic activity of three-dimensional in vitro cell culture models, Sci Rep. 7 (2017) 42730.
[74] A. Varone, J. Xylas, K.P. Quinn, D. Pouli, G. Sridharan, M.E. McLaughlin-Drubin, C. Alonzo, K. Lee, K. Munger, I. Georgakoudi, Endogenous two-photon fluorescence imaging elucidates metabolic changes related to enhanced glycolysis and glutamine consumption in precancerous epithelial tissues, Cancer Res. 74(11) (2014) 3067-75.
[75] K.P. Quinn, E. Bellas, N. Fourligas, K. Lee, D.L. Kaplan, I. Georgakoudi, Characterization of metabolic changes associated with the functional development of 3D engineered tissues by non-invasive, dynamic measurement of individual cell redox ratios, Biomaterials. 33(21) (2012) 5341-8.
[76] M.C. Skala, K.M. Riching, A. Gendron-Fitzpatrick, J. Eickhoff, K.W. Eliceiri, J.G. White, N. Ramanujam, In vivo multiphoton microscopy of NADH and FAD redox states, fluorescence lifetimes, and cellular morphology in precancerous epithelia, Proc Natl Acad Sci U S A. 104(49) (2007) 19494-9.
[77] M.C. Skala, K.M. Riching, D.K. Bird, A. Gendron-Fitzpatrick, J. Eickhoff, K.W. Eliceiri, P.J. Keely, N. Ramanujam, In vivo multiphoton fluorescence lifetime imaging of protein-bound and free nicotinamide adenine dinucleotide in normal and precancerous epithelia, Journal of Biomedical Optics. 12(2) (2007) 024014-024024.
[78] W. Ying, NAD+/NADH and NADP+/NADPH in cellular functions and cell death: regulation and biological consequences, Antioxid Redox Signal. 10(2) (2008) 179-206.
[79] M. Erecińska, I.A. Silver, Tissue oxygen tension and brain sensitivity to hypoxia, Respiration Physiology. 128(3) (2001) 263-276.
[80] I. Ozen, J. Boix, G. Paul, Perivascular mesenchymal stem cells in the adult human brain: a future target for neuroregeneration?, Clinical and Translational Medicine. 1(1) (2012) 30-39.
[81] M. Crisan, S. Yap, L. Casteilla, C.W. Chen, M. Corselli, T.S. Park, G. Andriolo, B. Sun, B. Zheng, L. Zhang, C. Norotte, P.N. Teng, J. Traas, R. Schugar, B.M. Deasy, S. Badylak, H.J. Buhring, J.P. Giacobino, L. Lazzari, J. Huard, B. Peault, A perivascular origin for mesenchymal stem cells in multiple human organs, Cell Stem Cell. 3(3) (2008) 301-313.
[82] J.W. Allen, S.R. Khetani, S.N. Bhatia, In vitro zonation and toxicity in a hepatocyte bioreactor, Toxicological Sciences. 84(1) (2005) 110-119.
[83] G. Mehta, K. Mehta, D. Sud, J.W. Song, T. Bersano-Begey, N. Futai, Y.S. Heo, M.A. Mycek, J.J. Linderman, S. Takayama, Quantitative measurement and control of oxygen levels in microfluidic poly(dimethylsiloxane) bioreactors during cell culture, Biomedical Microdevices. 9(2) (2007) 123-134.
[84] J. Malda, T.B. Woodfield, F. van der Vloodt, F.K. Kooy, D.E. Martens, J. Tramper, C.A. van Blitterswijk, J. Riesle, The effect of PEGT/PBT scaffold architecture on oxygen gradients in tissue engineered cartilaginous constructs, Biomaterials. 25(26) (2004) 5773-5780.
[85] T.H. Park, M.L. Shuler, Integration of cell culture and microfabrication technology, Biotechnology Progress. 19(2) (2003) 243-253.
[86] S. Andreescu, O.A. Sadik, Correlation of analyte structures with biosensor responses using the detection of phenolic estrogens as a model, Analytical Chemistry. 76(3) (2004) 552-560.
[87] W. Zhong, P. Urayama, M.A. Mycek, Imaging fluorescence lifetime modulation of a ruthenium-based dye in living cells: the potential for oxygen sensing, Journal of Physics D-Applied Physics. 36(14) (2003) 1689-1695.
[88] I.R. Sweet, G. Khalil, A.R. Wallen, M. Steedman, K.A. Schenkman, J.A. Reems, S.E. Kahn, J.B. Callis, Continuous measurement of oxygen consumption by pancreatic islets, Diabetes Technology Therapy. 4(5) (2002) 661-672.

[89] A.J. Walsh, R.S. Cook, H.C. Manning, D.J. Hicks, A. Lafontant, C.L. Arteaga, M.C. Skala, Optical metabolic imaging identifies glycolytic levels, subtypes, and early-treatment response in breast cancer, Cancer Res. 73(20) (2013) 6164-74.
[90] A. Walsh, R.S. Cook, B. Rexer, C.L. Arteaga, M.C. Skala, Optical imaging of metabolism in HER2 overexpressing breast cancer cells, Biomedical Optics Express. 3(1) (2012) 75-85.
[91] M.G. Vander Heiden, R.J. DeBerardinis, Understanding the intersections between metabolism and cancer biology, Cell. 168(4) (2017) 657-669.
[92] T.S. Blacker, Z.F. Mann, J.E. Gale, M. Ziegler, A.J. Bain, G. Szabadkai, M.R. Duchen, Separating NADH and NADPH fluorescence in live cells and tissues using FLIM, Nat Commun. 5 (2014) 3936.
[93] Y. Liu, G. Fiskum, D. Schubert, Generation of reactive oxygen species by the mitochondrial electron transport chain, Journal of Neurochemistry. 80(5) (2002) 780-787.
[94] R.D. Guzy, P.T. Schumacker, Oxygen sensing by mitochondria at complex III: the paradox of increased reactive oxygen species during hypoxia, Experimental Physiology. 91(5) (2006) 807-819.
[95] K.L. Eales, K.E. Hollinshead, D.A. Tennant, Hypoxia and metabolic adaptation of cancer cells, Oncogenesis. 5(e190) (2016) 1-8.
[96] S.Y. Lunt, M.G. Vander Heiden, Aerobic glycolysis: meeting the metabolic requirements of cell proliferation, Annu Rev Cell Dev Biol. 27 (2011) 441-64.
[97] L.A. O'Neill, R.J. Kishton, J. Rathmell, A guide to immunometabolism for immunologists, Nature Reviews Immunology. 16(9) (2016) 553-565.
[98] G.L. Wang, B.H. Jiang, E.A. Rue, G.L. Semenza, Hypoxia-inducible factor 1 is a basic-helix-loop-helix-PAS heterodimer regulated by cellular O2 tension, Proceedings of the National Academy of Sciences of the United States of America. 92(12) (1995) 5510-5514.
[99] W. Luo, H. Hu, R. Chang, J. Zhong, M. Knabel, R. O'Meally, R.N. Cole, A. Pandey, G.L. Semenza, Pyruvate kinase M2 is a PHD3-stimulated coactivator for hypoxia-inducible factor 1, Cell. 145(5) (2011) 732-744.
[100] B.H. Jiang, G.L. Semenza, C. Bauer, H.H. Marti, Hypoxia-inducible factor 1 levels vary exponentially over a physiologically relevant range of O2 tension, Am J Physiol. 271(4 Pt 1) (1996) 1172-1180.
[101] A.C.R. Epstein, J.M. Gleadle, L.A. McNeill, K.S. Hewitson, J. O'Rourke, D.R. Mole, M. Mukherji, E. Metzen, M.I. Wilson, A. Dhanda, Y.-M. Tian, N. Masson, D.L. Hamilton, P. Jaakkola, R. Barstead, J. Hodgkin, P.H. Maxwell, C.W. Pugh, C.J. Schofield, P.J. Ratcliffe, C. elegans EGL-9 and mammalian homologs define a family of dioxygenases that regulate HIF by prolyl hydroxylation, Cell. 107(1) (2001) 43-54.
[102] W.W. Wheaton, N.S. Chandel, Hypoxia regulates cellular metabolism, American Journal of Physiology-Cell Physiology. 300(3) (2011) 385-393.
[103] J.W. Allen, S.R. Khetani, R.S. Johnson, S.N. Bhatia, In vitro liver tissue model established from transgenic mice: role of HIF-1alpha on hypoxic gene expression, Tissue Eng. 12(11) (2006) 3135-47.
[104] J.T. Chi, Z. Wang, D.S. Nuyten, E.H. Rodriguez, M.E. Schaner, A. Salim, Y. Wang, G.B. Kristensen, A. Helland, A.L. Borresen-Dale, A. Giaccia, M.T. Longaker, T. Hastie, G.P. Yang, M.J. van de Vijver, P.O. Brown, Gene expression programs in response to hypoxia: cell type specificity and prognostic significance in human cancers, PLoS Med. 3(3) (2006) e47.
[105] M.L. Circu, R.E. Maloney, T.Y. Aw, Low glucose stress decreases cellular NADH and mitochondrial ATP in colonic epithelial cancer cells: Influence of mitochondrial substrates, Chem Biol Interact. 264 (2017) 16-24.
[106] C.S. Zhang, D.G. Hardie, S.C. Lin, Glucose Starvation Blocks Translation at Multiple Levels, Cell Metab. 31(2) (2020) 217-218.

[107] E.C. Vaux, E. Metzen, K.M. Yeates, P.J. Ratcliffe, Regulation of hypoxia-inducible factor is preserved in the absence of a functioning mitochondrial respiratory chain, Blood. 98(2) (2001) 296-302.
[108] S.W. Perry, J.P. Norman, J. Barbieri, E.B. Brown, H.A. Gelbard, Mitochondrial membrane potential probes and the proton gradient: a practical usage guide, Biotechniques. 50(2) (2011) 98-115.
[109] T. Wai, T. Langer, Mitochondrial Dynamics and Metabolic Regulation, Trends Endocrinol Metab. 27(2) (2016) 105-117.
[110] D.G. Nicholls, M.W. Ward, Mitochondrial membrane potential and neuronal glutamate excitotoxicity: mortality and millivolts, Trends in Neurosciences. 23(4) (2000) 166-174.
[111] L.D. Zorova, V.A. Popkov, E.Y. Plotnikov, D.N. Silachev, I.B. Pevzner, S.S. Jankauskas, V.A. Babenko, S.D. Zorov, A.V. Balakireva, M. Juhaszova, S.J. Sollott, D.B. Zorov, Mitochondrial membrane potential, Anal Biochem. 552 (2018) 50-59.
[112] J.E. Walker, The ATP synthase: the understood, the uncertain and the unknown, Biochem Soc Trans. 41(1) (2013) 1-16.
[113] F. Di Lisa, P.S. Blank, R. Colonna, G. Gambassi, H.S. Silverman, M.D. Stern, R.G. Hansford, Mitochondrial membrane potential in single living adult rat cardiac myocytes exposed to anoxia or metabolic inhibition, J Physiol. 486 (Pt 1) (1995) 1-13.
[114] M. Liesa, O.S. Shirihai, Mitochondrial dynamics in the regulation of nutrient utilization and energy expenditure, Cell Metab. 17(4) (2013) 491-506.
[115] G. Benard, N. Bellance, D. James, P. Parrone, H. Fernandez, T. Letellier, R. Rossignol, Mitochondrial bioenergetics and structural network organization, J Cell Sci. 120(Pt 5) (2007) 838-48.
[116] H.M. Wu, T.A. Lee, P.L. Ko, W.H. Liao, T.H. Hsieh, Y.C. Tung, Widefield frequency domain fluorescence lifetime imaging microscopy (FD-FLIM) for accurate measurement of oxygen gradients within microfluidic devices, Analyst. 144(11) (2019) 3494-3504.
[117] N. Shen, J.A. Riedl, D.A. Carvajal Berrio, Z. Davis, M.G. Monaghan, S.L. Layland, S. Hinderer, K. Schenke-Layland, A flow bioreactor system compatible with real-time two-photon fluorescence lifetime imaging microscopy, Biomedical Materials. 13(2) (2018) 024101-024112.
[118] M.G. Monaghan, S. Kroll, S.Y. Brucker, K. Schenke-Layland, Enabling Multiphoton and Second Harmonic Generation Imaging in Paraffin-Embedded and Histologically Stained Sections, Tissue Eng Part C Methods. 22(6) (2016) 517-23.
[119] Y. Xue, M.J. Seiler, W.C. Tang, J.Y. Wang, J. Delgado, B.T. McLelland, G. Nistor, H.S. Keirstead, A.W. Browne, Retinal organoids on-a-chip: a micro-millifluidic bioreactor for long-term organoid maintenance, Lab on a Chip. 21(17) (2021) 3361-3377.
[120] J.M. Ayuso, S. Rehman, M. Virumbrales-Munoz, P.H. McMinn, P. Geiger, C. Fitzgerald, T. Heaster, M.C. Skala, D.J. Beebe, Microfluidic tumor-on-a-chip model to evaluate the role of tumor environmental stress on NK cell exhaustion, Science Advances. 7(8) (2021) 1-14.
[121] A. Alex, T. Roh, B. Sridharan, J. Shi, P. Mukherjee, E. Chaney, J. Tunstead, J. Majer, K. Bera, D. Spillman, M. Marjanovic, J. Ekert, S. Hood, S. Boppart, Label-free multimodal multiphoton imaging of liver-on-a-chip models, SPIE2022.
[122] Y. Kong, Y. Zhao, Y. Yu, W. Su, Z. Liu, Y. Fei, J. Ma, L. Mi, Single cell sorting of young yeast based on label-free fluorescence lifetime imaging microscopy, Journal of Biophotonics. 15(4) (2022) e202100344.
[123] E. Ozaki, L. Gibbons, N.G. Neto, P. Kenna, M. Carty, M. Humphries, P. Humphries, M. Campbell, M. Monaghan, A. Bowie, S.L. Doyle, SARM1 deficiency promotes rod and cone photoreceptor cell survival in a model of retinal degeneration, Life Science Alliance. 3(5) (2020) e201900618.
[124] A. Remuzzi, B. Bonandrini, M. Tironi, L. Longaretti, M. Figliuzzi, S. Conti, T. Zandrini, R. Osellame, G. Cerullo, M.T. Raimondi, Effect of the 3D artificial nichoid on the morphology and

mechanobiological response of mesenchymal stem cells cultured in vitro, Cells. 9(8) (2020) 1873-1893.
[125] C.T. Taylor, S.P. Colgan, Regulation of immunity and inflammation by hypoxia in immunological niches, Nature Reviews Immunology. 17(12) (2017) 774-785.

Chapter 4 - 2P-FLIM unveils time-dependent metabolic shifts during osteogenic differentiation

4.1. Abstract

Tissue engineering and regenerative medicine benefits from thorough understandings of biochemical and biophysical processes involved during differentiation of human mesenchymal stem cells (hMSCs), a common source of therapeutic cells. This understanding can aid in generating large numbers of differentiated cells required for stem cell therapy and in developing tissue constructs that resemble native tissue properties. hMSCs require energy to fuel discrete biosynthetic pathways in order to multiply and to differentiate into specific cell lineages. It has been shown that hMSCs have different metabolic profiles when undergoing differentiation. In particular, undifferentiated hMSCs are reliant on glycolysis. However, when hMSCs differentiate towards an osteogenic phenotype, hMSCs rely on oxidative phosphorylation as a source of energy. In this study the metabolic profile of hMSCs was evaluated during osteogenic differentiation over 14 days using a non-invasive live-cell imaging platform- two-photon fluorescence lifetime imaging microscopy (2P-FLIM) which images and measures NADH fluorescence. During osteogenesis, we observe a higher dependence on oxidative phosphorylation for cellular energy; concomitant with an increased reliance on anabolic pathways. We validated this metabolic profile using qPCR and extracellular metabolite analysis and clarified a higher reliance of glutaminolysis in the earlier time-points of osteogenic differentiation. Based on the results obtained, we sought to promote further glutaminolysis during osteogenic differentiation. Increasing media concentrations of glutamine has been previously demonstrated to have a negative impact on cellular differentiation. Therefore, an indirect method of promoting glutaminolysis was explored so as not to impact cellular differentiation. Lactate has been shown to promote glutamine uptake via c-Myc activation triggering expression of glutamine transmembrane transporters and glutaminase 1. Therefore we chose to increase extracellular lactate concentrations to drive increased glutaminolysis rates leading to higher levels of mineral deposition, measured by alizarin red staining, and osteogenic

differentiation validated by gene expression. Lactate supplementation of osteogenic medium also promoted upregulation of lactate metabolism and increased the expression of transmembrane cellular lactate transporters, resulting in increased uptake of lactate. Higher rates of lactate dehydrogenase gene expression coupled with higher NADH fluorescence intensity demonstrate a possible conversion of lactate to pyruvate. During this conversion, NADH is formed by the reverse enzymatic reaction of lactate dehydrogenase, generating higher concentration of NADH observed by increases in NADH fluorescence intensity. In order to evaluate the importance of glutaminolysis and lactate metabolism in osteogenic differentiation, these metabolic pathways were shut down using BPTES and α-CHC respectively which led to reduced hMSC mineralisation. In summary, we showed that hMSCs osteogenic differentiation has a time-dependent metabolic profile and a metabolic shift that is observed as early as day 3 of cell culture. Osteogenic differentiation was demonstrated to be directly dependent on OxPhos and on glutaminolysis and validated using biochemical assays. Furthermore, extracellular lactate is an essential metabolite to ensure osteogenic differentiation as a metabolic fuel and signalling molecule to promote glutaminolysis. These findings have significant impact in generating potent approaches towards bone tissue engineering *in vitro* and *in vivo* by engaging directly with metabolite driven osteogenesis.

4.2. Introduction

Human mesenchymal stem cells (hMSCs) are adherent multipotent somatic cells with potential for tissue engineering and regenerative medicine due to its capacity of differentiation to, among others, osteogenic lineages [1, 2]. One facet of tissue engineering and regenerative medicine aims to develop patient-specific tissue that captures the functional properties of native tissues. Tissue engineered constructs could then be transplanted back to the patient, with minimal host rejection and superior integration [3].

Tissue engineering and regenerative medicine approaches require interaction and integration with host tissue and cells through incorporation of appropriate physical and cellular signals [4]. Appropriate physical and cellular signals of tissue engineered constructs will promote higher therapeutic potential and maximize tissue integration in host autologous transplants. Therefore, an extensive biological, biochemical, biomechanical and metabolic characterisation of hMSCs and their fully mature counterparts is required to ensure adequate development of *in situ* tissues for tissue engineering constructs. In addition, a complete hMSCs characterisation will ensure the development of a 3D cellular construct with similar features and functions as the target tissue. Matching these properties to fully mature cells and tissue is crucial for the development of functional connective tissue. Ke et al., developed 3D trachea like constructs that match native tissue properties by including separate cartilage and smooth muscle regions. To achieve this, Ke et al., used polycaprolactone and hMSCs hydrogels. Then, Ke et al., proceeded to 3D print the construct and evaluated the mechanical properties. Here, it was observed that the printed constructs had similar biological and mechanical properties compared with native trachea tissue [5]. Another study by Kim et al., demonstrates the use of a layer-by-layer fabrication of a meniscus construct combined with co-cultures of bovine MSCs and chondrocytes. Kim et al., designed the construct in order to have a three distinguishable layers: superficial, middle and deep zone with different mechanical properties and included a cross-

section hollow fibre to ensure nutrient transport for arears inside the construct [6]. Skardal el al., developed hydrogel bioinks for 3D printing of constructs that mimic both mechanical and biochemical properties of printed tissue constructs. To produce the bioinks, Skardal et al., obtained bioactive factors from decellularised tissue and controlled the mechanical properties of the bioink by using different cross-linker molecules. Skardal et al., were able to stimulate cellular development in printed bioconstructs due to the signal molecules, growth factors and cytokines included in the bioink composition [7]. These studies showcase a manipulation of cellular microenvironment by modifying mechanical, biochemical and metabolic properties which improved cell proliferation, maturation and integration with scaffolds, whilst mimicking native tissue properties.

The material properties of bone tissue are regulated by cellular activity [8]. This cellular activity encompasses the balance of resorption and deposition of bone tissue which primarily is composed of a mineralised collagen matrix. Mendez-Ferrer et al., study demonstrated that GFP-tagged MSCs directly contribute to bone remodelling by differentiating to osteoblasts [9]. Another study by Park et al., showed that bone marrow cells have all known MSCs characteristics and can migrate to the injury site to supply new osteoblasts during fracture healing [10]. Furthermore, in a murine bone fracture model, it was showed that 85% of osteoblasts were derived from MSCs with leptin-receptor ($LepR^{+}$) [11]. These cellular features and cellular behaviour are influenced by micro-environmental factors such as hormones, circulating metabolites, oxygenation and oxidative stress [12, 13]. In physiological conditions, bone is maintained by a balanced control of deposition of collagen matrix by osteoblasts and reabsorption of mineral deposits by osteoclasts. During diabetes, osteoporosis and other metabolic diseases, the continuous remodelling of bone is disrupted [14-16]. In diabetes, bone formation is hindered by the reduction of insulin levels and other pancreatic anabolic hormones such as low insulin-like growth factor 1 (IGF1). Lower IGF1 hormone levels has been showed to supress hMSCs differentiation into osteoblasts [17]. Osteoporosis is a disease characterised by

decreases in both bone quantity and quality [18]. Aging and menopause are known systemic conditions that can promote osteoporosis [18]. Aging promotes changes in cellular morphology, reduction of proliferative capacity of MSCs, reduction in telomease activity and telomere length [19]. Furthermore, MSCs capacity to differentiate into various tissue types is dependent with age. A study by Stolzing et al., demonstrated that MSC aging promotes a shift in balance of MSC differentiation towards an adipogenic lineage at the expense of osteoblast differentiation [20]. This loss in osteoblast differentiated cells promotes bone loss in both men and women by an increase of bone resorption versus bone formation. Menopause accelerates osteoclast activation and reabsorption of bone mineral due to hormonal imbalances [21, 22]. To conclude, in osteoporosis, bone resorption mechanism is not compensated by osteoblastic bone formation, generating weaker and more fragile bones. Contrastingly, for osteopetrosis, there is an increase in bone density due deficient bone reabsorption by osteoclasts. This deficiency in bone reabsorption is due to gene mutations that impair osteoclast function by interfering with proton pumps, chloride membrane channels and carbonic anhydrase II. These gene mutations reduce proton production and secretion of chloride needed to promote bone reabsorption [23].

hMSCs differentiation towards an osteogenic, adipogenic or chondrogenic lineage is accompanied by changes in phenotype, gene expression, protein secretion and cellular metabolism that occur in a time-dependent manner [24]. Metabolic regulations of hMSCs differentiation are still not fully understood [25]. Stem cells in general rely on glycolysis for energy when undifferentiated. Such a profile that is dependent on glycolysis facilitates a quick turnover of energy whilst producing biomolecules required for cellular proliferation [26]. hMSCs continue to utilize glycolysis as the main source of energy during chondrogenic differentiation [27]. However, there is a metabolic switch to oxidative phosphorylation (OxPhos) during hMSCs differentiation towards adipogenic or osteogenic lineages [28, 29]. In addition, it has been showed that an increase in oxygen consumption and increase of mitochondrial activity are important for osteogenic differentiation of hMSCs [28, 30]. Most recently, glutamine

metabolism has been shown to have an important role during hMSCs differentiation into osteogenic lineages [31].

Two-photon fluorescence lifetime imaging (2P-FLIM) is a powerful technique for non-invasive probing and monitoring of cellular metabolism. This technique is based on the fluorescence properties of nicotinamide adenine dinucleotide (NAD(P)H) and flavin adenine dinucleotide (FAD). NAD(P)H fluorescence lifetime consists of short- and long-lifetime components corresponding, respectively, to free and protein-bound forms [32]. NAD(P)H is an important metabolic co-factor that drives ATP production and other anaplerotic metabolic pathways. NAD(P)H drives glycolysis in the cytoplasm and oxidative phosphorylation (OxPhos) in the mitochondria. Therefore, longer fluorescence lifetimes are associated with higher ratios of protein-bound NAD(P)H revealing a higher dependence of OxPhos as a source of ATP. NAD(P)H fluorescence signal, specially protein-bound NAD(P)H (τ_1), can be used to infer quantitatively in NADPH concentrations[33]. NADPH has an important role in lipid, amino acid and nucleotide biosynthetic pathways as well reactive oxygen species (ROS) protection [34]. FAD^+ is also an important metabolic co-factor for OxPhos. Specifically, FAD^+ is a proton acceptor during the Krebs cycle and a proton donor on the electron transport chain (ETC) [35]. The ratios of the fluorescence intensities of FAD and NAD(P)H (FAD/NAD(P)H) are referred to as optical redox ratio and it can be used to estimate the metabolic profile of cells or tissues [36]. 2P-FLIM has been used as a technique to investigate cellular metabolism in a variety of cells, tissues and organoids [37-39]. After imaging, the sample can be still used for further metabolic, biochemical or histological validation [40]. In addition, it is possible to include machine learning models to the data analysis to further understand the impact of metabolic treatments [41].

hMSCs metabolic probing during differentiation using 2P-FLIM has been previously reported yet several of these studies have been limited to direct observation of metabolic changes at a specific time-point without other biochemical validation such as evaluation of

extracellular fluxes, measuring metabolites concentration or observing mitochondrial shape or biogenesis. In addition, considerations regarding hMSCs source and media formulation are also not made [42-44].

One study reported by Meleshina et al., applied 2P-FLIM to monitor hMSCs metabolic profile while in osteogenic differentiation culture for 21 days [42]. An increase of OxPhos was verified in hMSCs as early as day 7 of cell culture. In addition, the authors suggest that reliance on OxPhos osteogenic differentiation of hMSCs increases when cellular proliferation is less pronounced. However, Meleshina et al., work does not detail the complete media formulation used to induce osteogenic differentiation in the study. Therefore, it is difficult to determine if cells were differentiated in supraphysiological conditions impacting both hMSCs differentiation and cellular metabolism. Furthermore, Meleshina et al., study does not probe the cellular metabolic profile of differentiated hMSCs using standard techniques. Media formulation in particular, are one important consideration overlooked when investigating hMSCs bioenergetics, possibly influencing cellular metabolism due to supraphysiological levels of nutrients [28, 30, 45].

In this study, we profile hMSCs osteogenic differentiation using 2P-FLIM to uncover metabolic shifts. 2P-FLIM has non-invasive properties allowing live cell imaging during cell culture. Afterwards, the metabolic profiles observed during hMSCs osteogenic differentiation were validated using extracellular metabolite measurements and gene expression analysis (Figure 4.1). 2P-FLIM τ_{avg} parameter allowed the determination of an OxPhos profile during osteogenic differentiation. However, increased OxPhos is associated with higher ORR parameters due to a higher mitochondrial electron transport chain (ETC) activity. This increase in ETC activity, converts NADH to NAD^+ reducing NADH fluorescence intensity and increases FAD^+ concentration increasing FAD^+ fluorescence intensity. Instead, 2P-FLIM ORR results show a decrease in ORR during osteogenic differentiation. This occurs due to higher NADH

concentrations resulting in an increase of NADH fluorescence intensity. Therefore, during osteogenic differentiation, hMSCs rely on OxPhos and on metabolic pathways such as anaplerotic pathways that promote the generation of NADH.

Another aim of this study was to drive further osteogenic differentiation by promoting specific anaplerotic pathways. . We hypothesize that supplementing osteogenic differentiation medium with exogenous lactate could promote higher glutaminolysis rates and higher yields of cellular differentiation. Glutaminolysis has been shown by Yu et al., to be crucial in ensuring adequate osteogenic differentiation of hMSCs [31]. In that study, blocking glutaminolysis using a chemical inhibitor of glutamate synthase (GLS) negatively impacted osteogenic cellular differentiation by reducing mineral deposition verified by alizarin red staining. In addition, Yu et

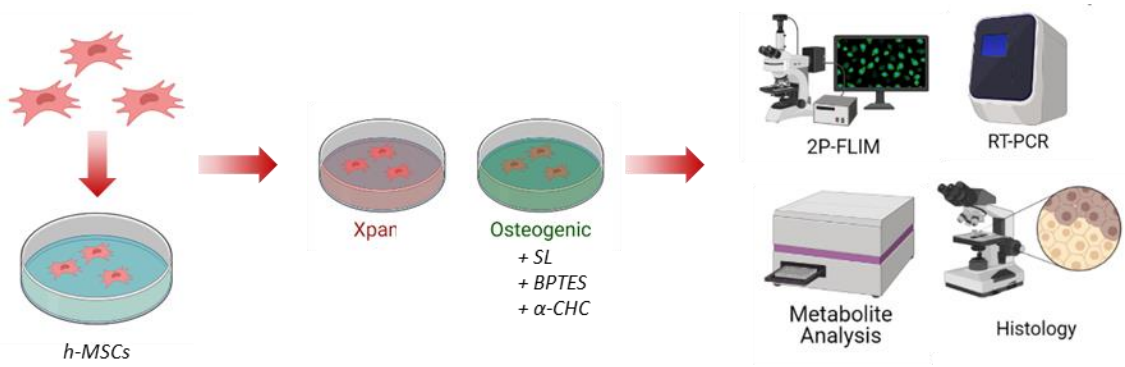

Figure 4.1 – Experimental Design. SL- sodium lactate; BPTES - Bis-2-(5-phenylacetamido-1,3,4-thiadiazol-2-yl)ethyl sulphide; α-CHC - α-Cyano-4-hydroxycinnamic. Image created using Biorender®

al., identified alpha-ketoglutarate production to be critical for proliferation and differentiation of hMSCs [31]. Due to the importance of glutamine and glutaminolysis to osteogenic differentiation, we decided to drive further osteogenic differentiation by upregulating glutaminolysis. In that manner, an increased uptake of glutamine and glutaminolysis rate culminating in alpha-ketoglutarate production will increase osteogenic cell differentiation as demosntrated by increasing mineral deposition. Perez-Escuredo et al., have demonstrated that lactate uptake by monocarboxylate transporter 1 (MCT1) promotes glutamine uptake and metabolism in oxidative cancer cells by c-Myc activation [46].

4.3. Materials and methods

4.3.1. Mesenchymal stem cell culture

Human mesenchymal stem cells (hMSCs) were purchased from Lonza® were cultured at passage 3-4 in expansion media (Xpan) prepared with Dilbecco's Modifed Eagle's Medium (DMEM), 1000 mg/L low glucose (Sigma-Aldrich) containing 10% fetal bovine serum (FBS) (Gibco® by Life Technologies) and 2% Penicilin Streptomycin (Pen-Strep) (Sigma Aldrich) at 37°C with 5% CO2. To initiate osteogenic differentiation, osteogenic media (Osteo +) was prepared by adding 0.2% (v/v) dexamethasone, 1% (v/v) β-glycerol phosphate and 0.029% (v/v) ascorbic acid as supplements to Xpan media.

For lactate supplementation of Osteo + media, 75 mM of lactate was used as a sodium salt, to avoid changes in extracellular pH (Osteo + Lact). For metabolic inhibition studies, either 5 mM of α-CHC or 10 μM BPTES were added to Osteo + media.

4.3.2. Two-photon fluorescence lifetime imaging microscopy (2P-FLIM)

2P-FLIM was performed on hMSCs seeded in 35mm petry dishes. 2P-FLIM was achieved using a custom upright (Olympus BX61WI) laser multiphoton microscopy system equipped with a pulsed (80 MHz) titanium:sapphire laser (Chameleon Ultra, Coherent®, USA), water-immersion 25× objective (Olympus, 1.05NA) and temperature-controlled stage at 37 °C. Two photon excitation of NAD(P)H and FAD^+ fluorescence was performed at the excitation wavelength of 760 and 800 nm, respectively. A 458/64 nm and 520/35 nm bandpass filter were used to isolate the NAD(P)H and FAD^+ fluorescence emissions based on their emission spectrum.

512 × 512 pixel images were acquired with a pixel dwell time of 3.81 μs and 30 s collection time. A PicoHarp 300 TCSPC system operating in the time-tagged mode coupled with a photomultiplier detector assembly (PMA) hybrid detector (PicoQuanT GmbH, Germany) was used for fluorescence decay measurements, yielding 256 time bins per pixel. TCSPC requires a defined "start", provided by the electronics steering the laser pulse or a photodiode, and a

defined “stop” signal, realized by detection with single-photon sensitive detectors. The measuring of this time delay is repeated many times to account for the statistical variance of the fluorophore’s emission. For more detailed information, the reader is referred elsewhere [47]. Fluorescence lifetime images with their associated decay curves for NAD(P)H were obtained, with a minimum of $1x10^6$ photons peak, and region of interest (ROI) analysis of the total cells present on the image was performed in order to remove any background artefact. The decay curved was generated and fitted with a double-exponential decay without including the instrument response function (IRF) (Equation 4.1).

$$I(t) = I(0)[\alpha_1 e^{\frac{-t}{\tau_1}} + \alpha_2 e^{\frac{-t}{\tau_2}}] + C$$

Equation 4.1 – Double exponential decay curve fo NAD(P)H FLIM analysis

I(t) represents the fluorescence intensity measured at time t after laser excitation; α_1 and α_2 represent the fraction of the overall signal proportion of a short and long component lifetime, respectively. τ_1 and τ_2 are the long and short lifetime components, respectively; C corresponds to background light. Chi-square statistical test was used to evaluate the goodness of multi-exponential fit to the raw fluorescence decay data. In this study, all of the fluorescence lifetime fitting values with $\chi^2 < 1.3$ were considered as ‘good’ fits. For NAD(P)H, the double exponential decay was used to differentiate between the protein-bound (τ_1) and free (τ_2) NAD(P)H. The average fluorescence lifetime was calculated using Equation 4.2.

$$\tau_{avg} = \frac{(\tau_1 \times \alpha_1 + \tau_2 \times \alpha_2)}{(\alpha_1 + \alpha_2)}$$

Equation 4.2 – Average fluorescence lifetime calculation

Intensity-based images of NAD(P)H and FAD^+ were acquired, and their ratio was calculated using Equation 4.3 to obtain the optical redox ratio (ORR).

$$ORR = \frac{FAD^{+}}{NAD(P)H}$$

Equation 4.3 – Optical redox ratio calculation

4.3.3. qPCR

hMSCs were lysed and re-suspended in 1 ml of TRIzol, briefly vortexed and 200 µL of chloroform was added. Samples were centrifuged at 12,000g for 15 minutes at 4°C to achieve phase separation. The aqueous phase was separated to a fresh RNAse free microtube. RNA precipitation was performed by adding 2 µL of glycol-blue and 500 µL of isopropanol. RNA pellets were washed using 1 mL of 70% of ethanol. RNA pellets were re-suspended in 20 µL of RNAse free water. RNA yield and purity was measured using a NanoDropTM. To estimate total RNA concentration, absorbance values obtained at 260 nm were obtained. 260/280 and 260/230 absorbance ratios were calculated to estimate RNA purity. A 260/280 ratio of ~1.8 and a 260/230 ratio of ~1.8 were deemed acceptable for RNA purity. cDNA transcription was performed with High capacity cDNA reverse transcription kit from Applied BiosystemsTM according to manufactures instructions. A mastermix solution was prepared by adding RNase inhibithor, MultiscribeTM reverse transcriptase enzyme, RT® buffer, random primers and 100 mM of dNTP Mix. RNA samples was added to the mastermix to achieve a reaction volume of 20 µL. A thermal cycle was performed with a heating step of 25 °C for 10 minutes, 37 °C for 120 min, followed by 85 °C for 5 minutes. A 100% conversion rate was assumed to determine cDNA concentration.

Gene expression was analysed using a custom PrimePCR® designed plate using SYBR® Green primers according to manufactures guidelines. Here, 10 µL of Universal SYBR® Green Supermix is added to each well of the 96-well plate to reconstitute the dried PCR primers. 4 µL of cDNA samples were added to each well and nuclease-free water was used to achieve 20 µL

of reaction volume. All primers were purchased from Bio-Rad laboratories. Accession numbers, Unique Assay ID, Amplicon Length, Gene name and symbol are present in Table Appendix 1. Primer sequences remain Bio-Rad laboratories proprietary information and are not available. PCR primers specificity are verified and guaranteed by the manufacturer. qPCR was performed on a fastPCR 96-well plate instrument (Applied Biosystems) to obtain comparative ΔΔCt values. Gene expression was compared between samples using the $2^{-\Delta\Delta Ct}$ method [43]. QPCR data was normalized to β-actin gene expression.

Z-score heatmaps of gene expression values were generated by calculating the z-score of each sample and plotted in a heatmap. Z-score values are obtained using Equation 4.4:

$$z = \frac{x - \mu}{\sigma}$$

Equation 4.4 – Z-score calculation

The z-score (z) is calculated using x the observed value, μ the mean value of the sample and σ is the standard deviation of the sample.

4.3.4. Metabolite analysis

For metabolite analysis, cell culture medium was collected at 2, 5, 8 and 11 days after being in contact with cell cultures. For extracellular measurement of glucose, the ChromaDazzle™ Glucose Assay kit from AssayGenie was used. Here, glucose standards were prepared by dissolving glucose stock solution 300 mg/dL in distilled water with concentrations ranging from 0 to 300 mg/dL to prepare a standard curve. Cell culture medium samples and standards were diluted 1/100 in o-toluidine reagent from AssayGenie. Samples were incubated in a boiling water bath for 8 minutes and cooled down in ice for 4 minutes. 200 µL were added to clear-bottom 96 well plates and absorbance values were measured in a microplate reader at 630 nm.

Extracellular measurements of lactate was performed using an L-Lactic acid colorimetric assay by AssayGenie. Here, lactate standards were obtained by sequentially diluting a 10 mM/L lacatate standard to obtain a standard curve with the concentration ranging from 0 to 7 mM/L. Samples and standards were added directly to 96 well plates and diluted 60x in chromogenic solution. For samples with increased exogenous lactate, 12x dilutions were performed. Samples were incubated at 37 °C for 5 minutes and read in a microplate reader at 530 nm.

Extracellular measurements of glutamine were performed using ChromaDazzle™ Glutamine Assay kit from AssayGenie. This kit is based on the hydrolysis of glutamine to glutamate and formation of a colorimetric product. First, a standard curve was calculated by diluting glutamine stock solution 100 mM in distilled water. Standards with concentrations from 0 to 2 mM were obtained. Enzymes A and B from the kit were reconstituted according to manufacturer's instructions. Extracellular culture medium and standards were added to clear-bottom 96-well plates and diluted 10x in assay solution containing enzymes. The enzymatic reaction was stopped at 40 min at room temperature with a stop reagent and absorbance values were measured in a plate reader at 550 nm.

In this study, there is an interest in measuring glucose and glutamine consumption. Therefore, to calculate metabolite concentration equation 4 was used. For glucose initial concentration was assumed 1000 mg/L and 2.0mM for glutamine concentration according to manufactures formulations. Extracellular lactate concentration measurements are presented directly without using Equation 4.5. In addition, for lactate measurements in lactate supplemented osteogenic medium, were corrected by taking in account the amount of lactate added exogenously.

$$\Delta[metabolite]_{consumption} = [metabolite]_{initial} - [metabolite]_{final}$$

Equation 4.5 – Calculation of hMSCs metabolite consumption.

4.3.5. PCA and UMAP

Uniform Manifold Approximate and Projection (UMAP) and Principal Components Analysis (PCA) were used as data visualisation tools to visualize clustering within 2P-FLIM data variables (Python). For this analysis, all images acquired (at least 3 per sample and condition) were used as plot points and 2P-FLIM variables or gene expression data were used as variables. Covariance error ellipses with confidence values of 99% were calculated and plotted in PCA graphs. Mahalanobis distance, two-sample Hotellings T^2 statistic, F-value, Critical F-Value and P-values were calculated to ensure statistical significant separation of PCA clusters [48]. (Table Appendix 4, Code available in Computer Code Appendix 8).

4.3.6. Alizarin red staining and DNA quantification

hMSCs were fixed with 4% paraformaldehyde (PFA) and alizarin red staining was performed for 30 minutes with a solution of 1% alizarin red in distilled water and imaged with a 10x objective using an Olympus BX41TF brightfield microscope. Alizarin red molecules bind to calcium molecules and generate a birefringent insoluble red complex [49]. Alizarin red stained cells were dissolved for 30 minutes in 10 % (v/v) acetic acid. Cells were lifted with a cell scrapper and transferred to microtubes and heated until 85 °C for 10 minutes. The tubes were centrifuge at 20,000 g for 15 minutes and 10% (v/v) ammonium hydroxide was added. Samples were pipetted in triplicate on a 96 well plate and absorbance was measured in a plate reader at 405nm.

For sample lysis, hMSCs were rinsed twice using cold phosphate buffer saline solution (PBS) and were digested using a lysis buffer containing 0.2% v/v Triton X100, 10 mM Tris pH 8, 1 mM EDTA and DNAse free water. Afterwards, the cells suspended in lysis buffer were transferred to microtubes and sonicated for 60 seconds to ensure complete cellular lysis.

DNA quantification, was performed using a Picogreen™ biochemical assay on digested samples according to manufacturer's protocol. Here, PicoGreen™ was diluted in 10 mM Tris-HCL, 1 mM EDTA with pH 7.5 (TE). A DNA stock solution (100 µg/mL) was dissolved in TE solution and serial dilution from 0 to 200 ng of DNA/mL was performed to establish a calibration curve. Afterwards, 10 µL of each standard and sample were added in triplicate to a black flat bottomed 96 well plate and further 190 ul of diluted PicoGreen™ in TE solution were added. Fluorescence emission was read at 520nm using an excitation wavelength of 480nm in a plate reader with 0.93 seconds per well of dwell time.

4.3.7. Statistics

Statistical analysis was performed using GraphPad Prism 9 (GraphPad Software, USA). Where appropriate, one-way analysis of variance (ANOVA) or two-way ANOVA were used as statistical tests followed by Tukey's multiple comparison. Results are presented as mean ± standard deviation and differences are considered as statistically significant for p-value ≤ 0.05.

4.4. Results

4.4.1. Osteogenic differentiation is dependent on oxidative phosphorylation in a time-dependent way

hMSCs were incubated in Xpan and Osteo + cell culture for 14 days. At day 7 and day 14 of incubation, hMSCs were fixed using paraformaldehyde (PFA) and stained with alizarin red to verify mineral deposition and osteogenic differentiation (Figure 4.2A). After 14 days of incubation a noticeably higher mineral deposition in Osteo + medium conditions was observed, associated with increased osteogenic differentiation (Figure 4.2A, Figure Appendix 9).

hMSCs osteogenic gene expression was quantified with qPCR, after 14 days of cell culture incubation in either Xpan or Osteo + medium (Figure 4.2 B, C, D). There is a statistically significant higher expression of (2.3-fold increase) alkaline phosphatase (ALPL) and (2.19-fold increase) prostaglandin-endoperoxide synthase 2 (PTGS2) gene expression in hMSCS when incubated in Osteo + medium (Figure 4.2B). All remaining osteogenic genes have no statistically significant expression between Osteo + and Xpan conditions. PCA visualization of osteogenic gene expression revealed a statistical significant segregation between hMSCs incubated in Xpan or Osteo + cell culture medium with p-value<0.05 and F-value higher than critical F-value (Figure 4.2C, Table Appendix 4). A z-score heatmap based on osteogenic gene expression shows similar results with a higher expression of ALPL and PTGS2 in Osteo + conditions after 14 days of incubation (Figure 4.2C).

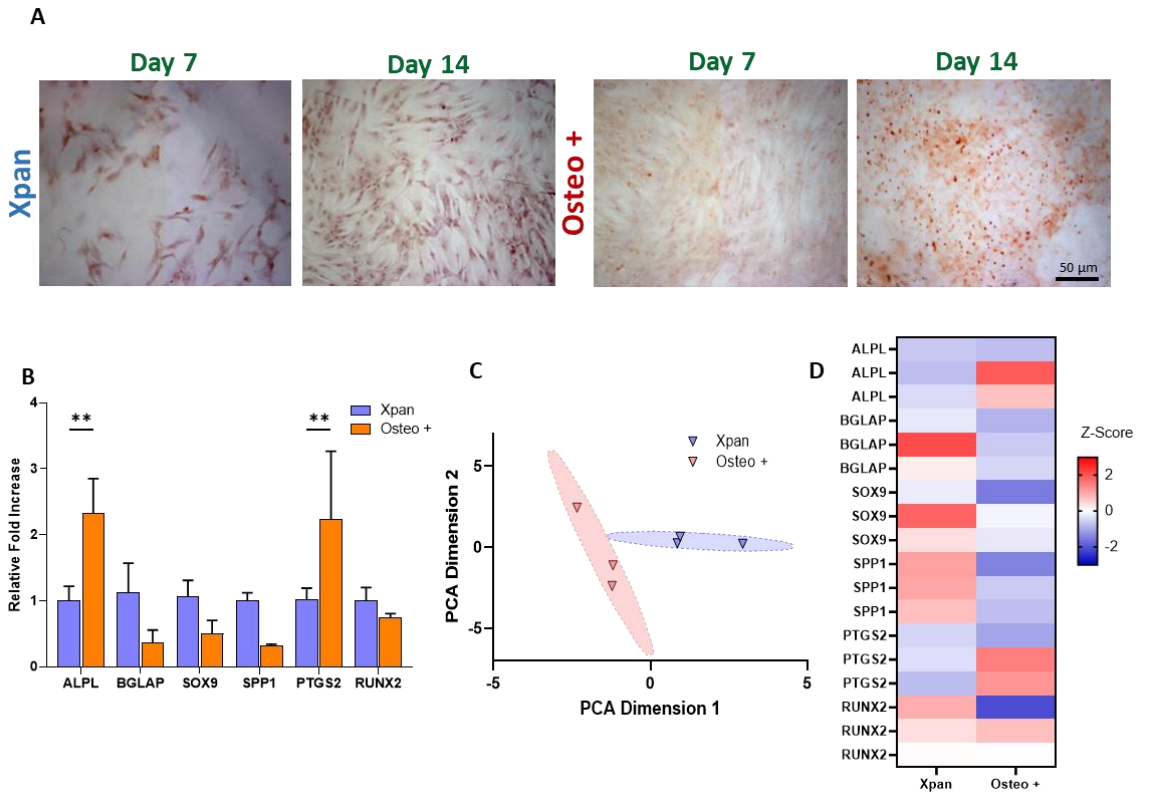

Figure 4.2 - Validation of osteogenic differentiation of hMSCs incubated in Osteo + or Xpan cell culture medium for 14 days. A) Alizarin red staining of hMSCs after 14 days in contact with Osteo + or Xpan medium. B) hMSCs gene expression of osteogenic markers after 14 days of cell culture. C) Z-score heatmap of hMSCs gene expression of osteogenic gene markers after 14 days of cell culture. D) PCA distribution and of hMSCs osteogenic gene expression after 14 days of cell culture. *p-value≤0.05, **p-value≤0.01, ***p-values≤0.001, ****p-value≤0.0001 N≥3

2P-FLIM of NAD(P)H and FAD+ revealed a time-dependent metabolic shift for hMSCs in osteogenic medium (Figure 4.3). At day 0 there is no statistically significant differences in τ_{avg}, τ_1 or ORR values between hMSCs incubated in Xpan or Osteo + media (Figure 4.3 B, C, D). On day 3 of cell culture, there is a statistically significantly higher (1.097 ± 0.04 ns versus 1.167 ± 0.004 ns) τavg and (2.683 ± 0.027 ns versus 2.800 ± 0.039 ns) τ_1 values concomitant with lower (0.724 ± 0.020 versus 0.615 ± 0.021) ORR values (Figure 4.3 B, C, D). With an increase of the incubation period, the trends observed at day 3 become more accentuated. NAD(P)H fluorescence τ_{avg} (1.167 ± 0.004 ns at day 3, versus 1.236 ± 0.010 ns at day 7 and 1.316 ± 0.011 ns at day 14) and τ_1 (2.800 ± 0.039 ns at day 3, versus 2.979 ± 0.053 ns at day 7 and 3.146 ± 0.015 ns at day 14) become higher in Osteo + treated cells while in Xpan conditions, these fluorescence variables

have constant values. Similarly, ORR values continue to decrease in Osteo + conditions after day 3 (0.615 ± 0.021 ns at day 3, versus 0.534 ± 0.029 ns at day 7 and 0.585 ± 0.012 ns at day 14)

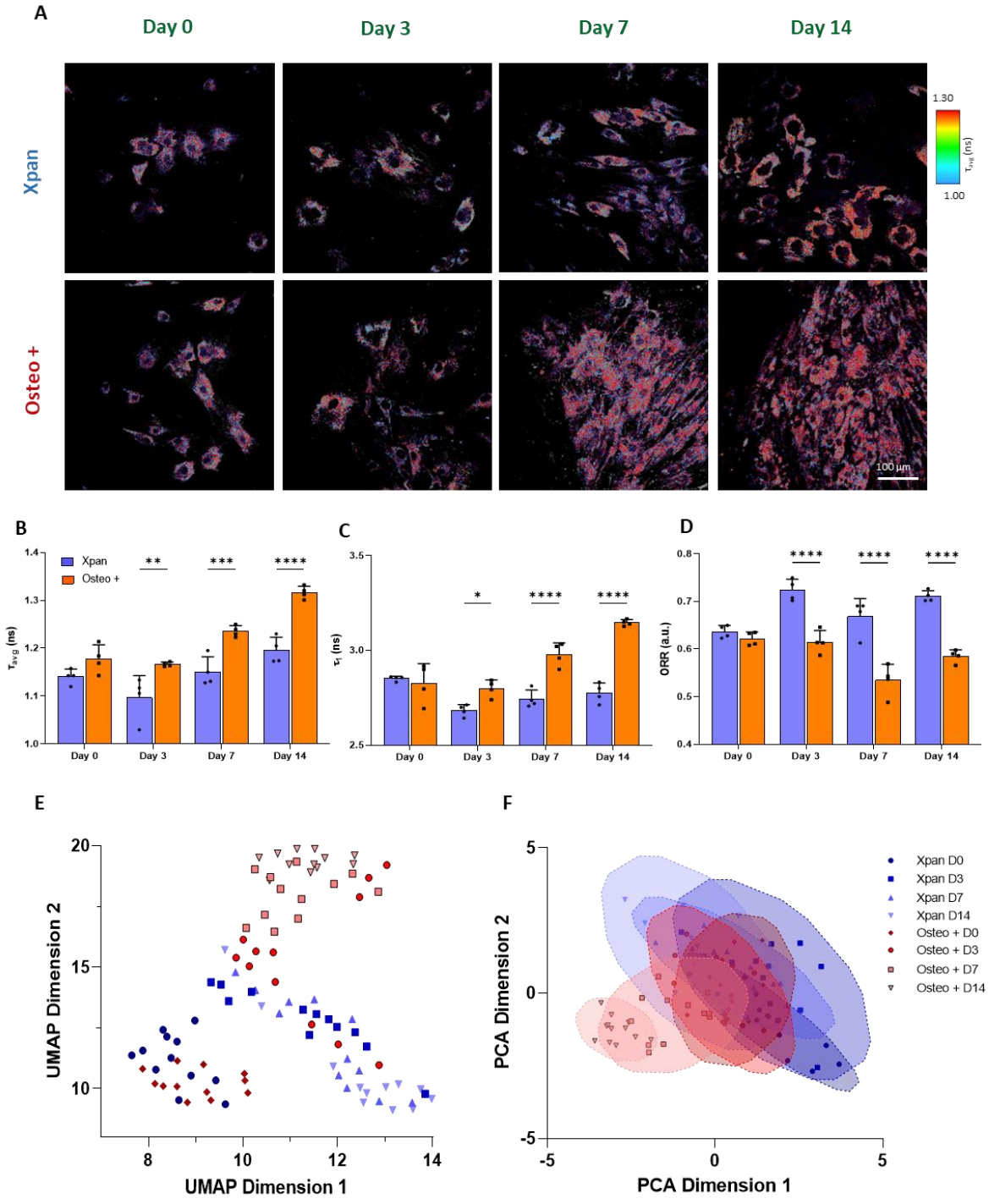

Figure 4.3 - Metabolic profiling of hMSCs incubated in Osteo + or Xpan cell culture medium for 14 days. A) 2P-FLIM imaging of hMSCs at day 0, 3, 7 and 14 of cell culture incubation. B) NAD(P)H τ_{avg} measurement of hMSCs at day 0, 3, 7 and 14 of cell culture. C) NAD(P)H protein-bound lifetime τ_1 at day 0, 3, 7 and 14 of cell culture. D) Optical Redox Ratio (ORR) of hMSCs at day 0, 3, 7 and 14 of incubation in cell culture medium. E) UMAP distribution of 2P-FLIM NAD(P)H and FAD^+ fluorescence lifetimes and intensity. F) PCA distribution of 2P-FLIM NAD(P)H and FAD^+ fluorescence lifetimes and intensity. *p-value≤0.05, **p-value≤0.01, ***p-values≤0.001, ****p-value≤0.0001 N≥3

while hMSCs in Xpan medium have stable ORR values (Figure 4.3 B, C, D).

Uniform Manifold Approximation and Projection (UMAP) and Principal Component Analysis (PCA) were used as exploratory data visualisation tools to infer the metabolic profile of hMSCs undergoing osteogenic differentiation at several time-points during cell culture (Figure 4.3 E, F). All 2P-FLIM NAD(P)H and ORR variables were used to generate the UMAP and PCA plots. UMAP revealed that for later time-points, such as day 7 and day 14, there is a strong separation between hMSCs incubated in Osteo + medium and hMSCs incubated in Xpan medium (Figure 4.3 E). For earlier time-points, there was no segregation between hMSCs incubated in both cell culture medium conditions (Figure 4.3F, Table Appendix 4). When applying PCA, there is a clear and statistically significant segregation of cells treated with Osteo + media at day 7 and day 14 compared with Xpan-treated hMSCs. (Figure 4.3 F, Table Appendix 4).

To further validate the time-dependent metabolic shifts during osteogenic differentiation, cell culture medium was collected during media exchanges at days 2, 5, 8 and 11. Glucose, lactate and glutamine concentrations were measured using colorimetric assays (Figure 4.4 A, B, C). Regarding glucose, there is statistically significant higher glucose consumption (2.42- fold increase) when cells are incubated in Xpan medium at all time-points (Figure 4.4A). For lactate, there is an increasing trend of lactate secretion in both Xpan and Osteo + treated hMSCs during the incubation period. For day 11, there is a statistically significant

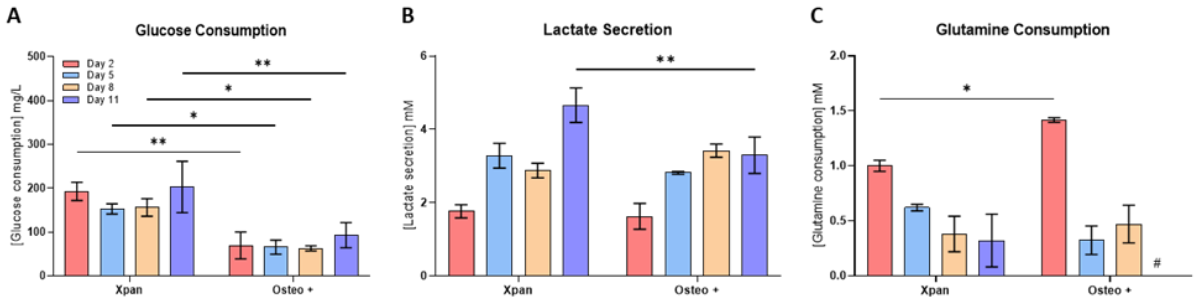

Figure 4.4 - Extracellular metabolite consumption rates of hMSCs incubated in Osteo + or Xpan cell culture medium for 14 days. A) hMSCs glucose consumption at day 2, 5, 8 and 11 of cell culture. B) Lactate secretion at day 2, 5, 8 and 11 of cell culture. C) hMSCs glutamine consumption at day 2, 5, 8 and 11 of cell culture. #no glutamine consumption, *p-value≤0.05, **p-value≤0.01, ***p-values≤0.001, ****p-value≤0.0001 N≥3.

higher lactate secretion of hMSCs incubated in Xpan medium (4.660 ± 0.384 mM) compared with hMSCs in Osteo + (3.295 ± 0.406 mM) cell culture conditions (Figure 4.4B). Lastly for glutamine, there is a statistically significant higher glutamine consumption at day 2 of hMSCs in Osteo + (1.417 ± 0.017 mM) compared with Xpan (1.000 ± 0.041 mM) cell culture conditions. For the remaining time-points there is a decreasing trend of glutamine consumption for both cell culture media conditions (0.01-fold for Osteo + and 0.32-fold for Xpan) (Figure 4.4C).

4.4.2. Lactate supplementation promotes higher mineral deposition and impacts metabolism

hMSCs osteogenic differentiation promoted a metabolic shift towards OxPhos and increased dependence on anabolic pathways such as glutaminolysis. Here, increased dependence of glutaminolysis and anabolic pathways was induced by adding exogenous lactate to osteogenic medium.

Lactate supplementation of osteogenic medium yielded a higher mineral deposition after 14 days of incubation with a higher amount of alizarin red staining when compared with Osteo + medium (Figure 4.5A,B). Osteogenic genes expression was measured by qPCR in hMSCs incubated in Osteo +, Xpan and Lactate supplemented osteogenic medium (Figure 4.5 C, D, E). There is a statistically significant increase in SRY-Box Transcription Factor 9 (SOX9) (2.7-fold increase) and Osteopontin (SPP1) gene expression (15.47-fold increase) in hMSCs when osteogenic medium is supplemented with lactate compared with Osteo + and Xpan cell culture medium (Figure 4.5C, E). RUNX2 gene expression is also slightly higher in lactate supplemented osteogenic medium compared with Xpan (1.39-fold increase) and Osteo + (1.87-fold increase) incubation medium (Figure 4.5 C, D). PCA distribution plot of cell culture conditions of hMSCs at day 14 shows a statistically significant segregation between hMSCs incubated in Osteo + Lact, Osteo + and Xpan based on the expression of their osteogenic genes with p-value<0.05 and calculated f-value higher than critical f-value (Figure 4.5D, Table Appendix 4). ALPL, BGLAP,

PTGS2 have similar gene expression values in hMSCs when incubated in osteogenic medium with and without lactate supplementation, as observed in the bar plot and the z-score heatmap (Figure 4.5 C, E).

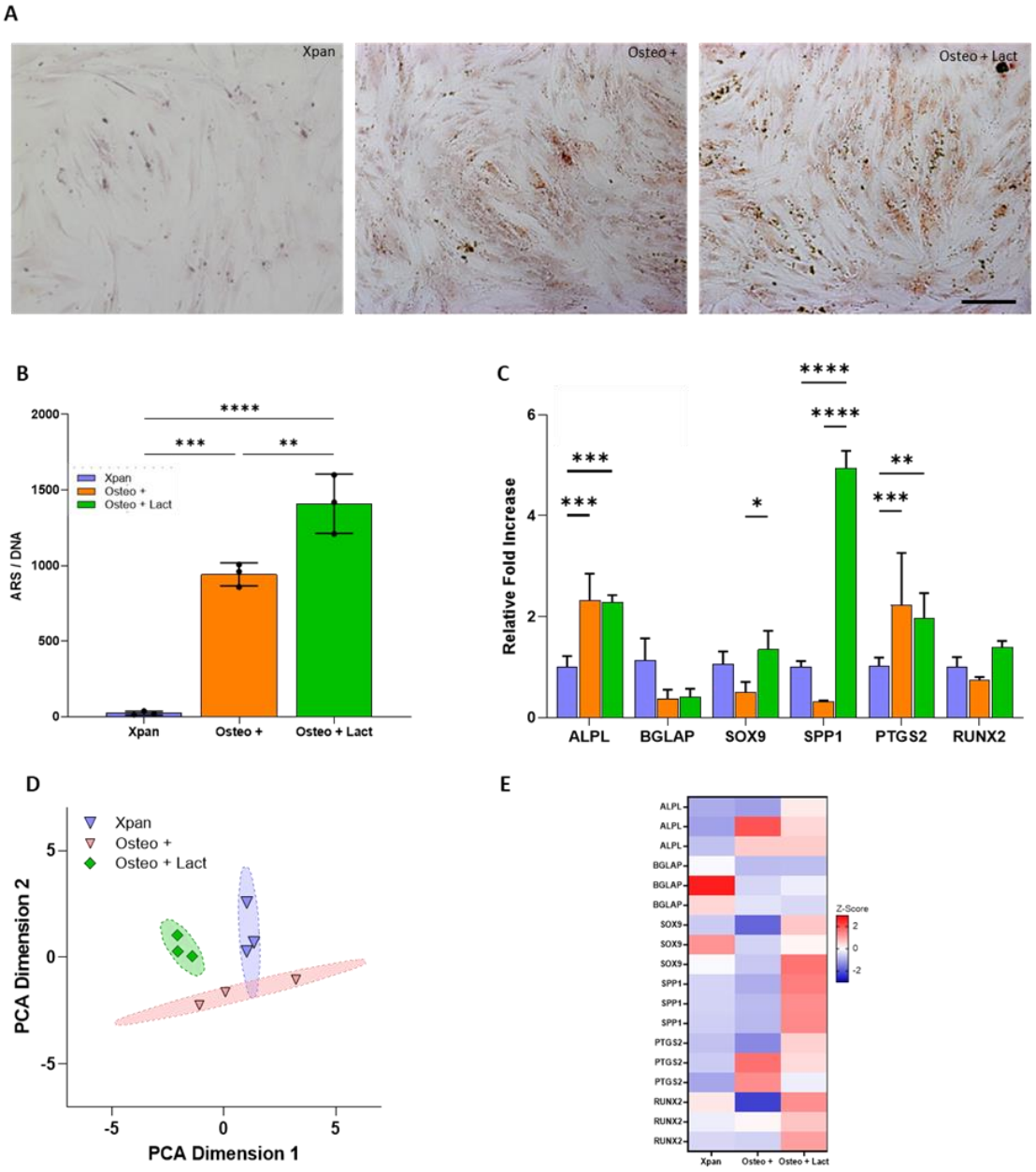

Figure 4.5 - Impact of lactate supplementation of osteogenic differentiation media. A) Alizarin red staining of hMSCs after 14 days in contact with Osteo +, Osteo + Lact or Xpan medium. B) Quantification of Alizarin red staining per amount of DNA after 14 days of hMSCs in Xpan, Osteo + and Osteo + Lact conditions. C) hMSCs gene expression of osteogenic markers after 14 days of cell culture. D) PCA distribution of hMSCs osteogenic gene expression after 14 days of cell culture. E) Z-score heatmap of hMSCs gene expression of osteogenic gene markers after 14 days of cell culture. *p-value≤0.05, **p-value≤0.01, ***p-values≤0.001, ****p-value≤0.0001 N≥3

2P-FLIM imaging of NAD(P)H was conducted at day 14 of cell culture (Figure 4.6A). 2P-FLIM revealed a statistically significant lower τ_{avg} when supplementing osteogenic medium with lactate (1.148 ± 0.005 ns) compared with non-supplemented osteogenic medium (1.187 ± 0.014 ns) (Figure 4.6B). However, τ_{avg} of Osteo + Lact (1.148 ± 0.005 ns) is statistically significantly higher compared with hMSCs incubated in Xpan medium (1.108 ± 0.002 ns) (Figure 4.6B). ORR calculations showed statistically significant lower ORR values for Osteo + Lact medium (0.547 ± 0.016 ns) compared with other cell culture medium formulations (0.779 ± 0.016 ns for Xpan and 0.668 ± 0.011 ns for Osteo +) (Figure 4.6C).

The decrease in τ_{avg} and decrease of ORR ratios demonstrates a direct metabolic impact on differentiating hMSCs when cell culture medium is supplemented with lactate when compared with non-supplemented. A decrease in τ_{avg} is associated with increased free NAD(P)H and a decrease in ORR is also related with an increase in NAD(P)H fluorescence intensity. The increase in NAD(P)H can be a direct result of increase glutaminolysis resulting in NADH regeneration in the conversion of glutamate to alpha-ketoglutarate as well with NADH production by reconversion of lactate to pyruvate [50, 51].

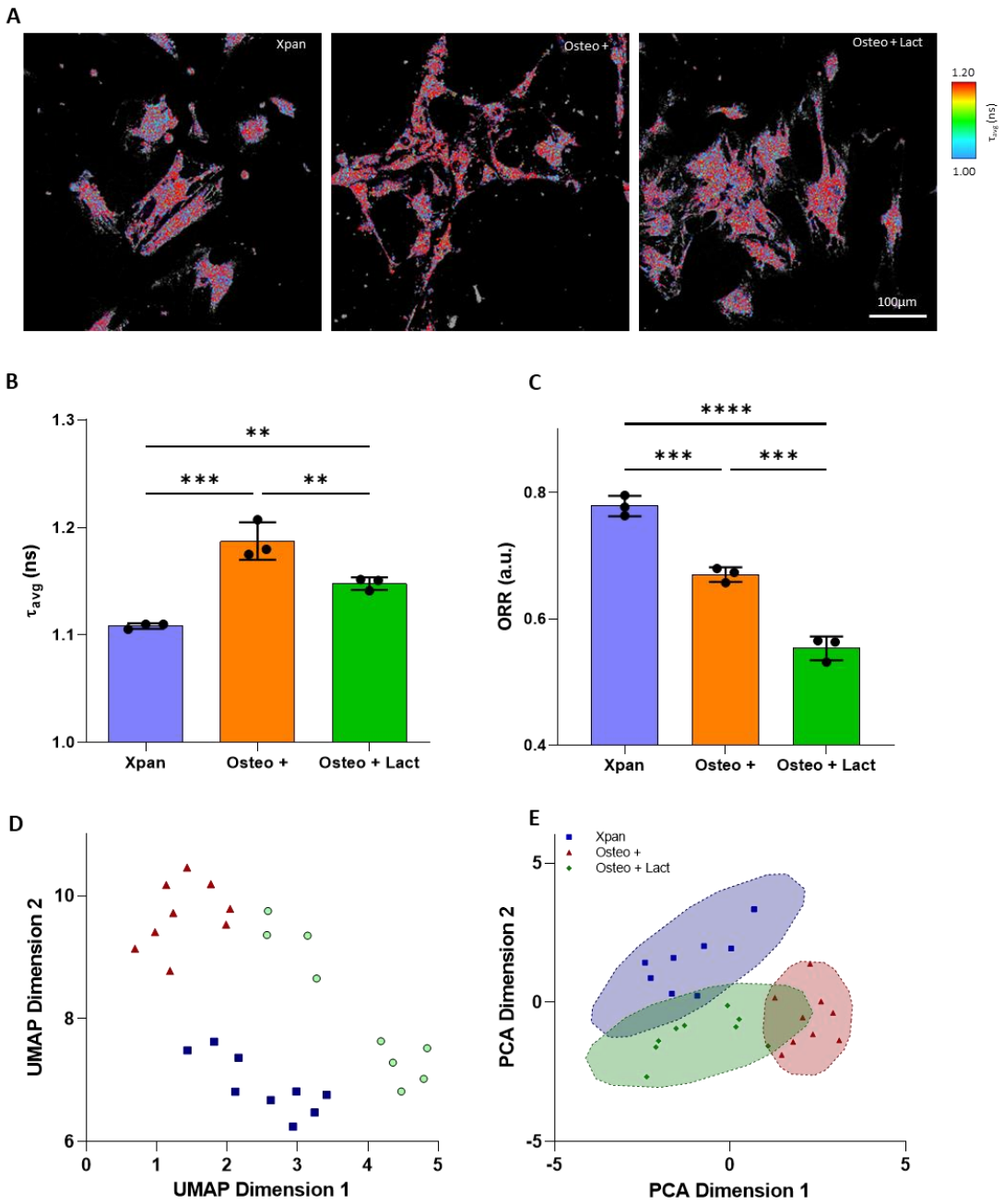

Figure 4.6 - 2P-FLIM measurement of lactate supplementation impact on hMSCs metabolism. A) 2P-FLIM imaging of hMSCs at day 14 of cell culture incubation. B) Optical Redox Ratio (ORR) of hMSCs at day 0, 3, 7 and 14 of incubation in cell culture medium. C) NAD(P)H protein-bound lifetime τ1 at day 14 of cell culture. D) UMAP distribution of 2P-FLIM NAD(P)H and FAD+ fluorescence lifetimes and intensity. E) PCA distribution of 2P-FLIM NAD(P)H and FAD+ fluorescence lifetimes and intensity. J) hMSCs glucose consumption at day 2, 5, 8 and 11 of cell culture. *p-value≤0.05, **p-value≤0.01, ***p-values≤0.001, ****p-value≤0.0001 N≥3

UMAP distribution analysis of 2P-FLIM results shows a separation between Xpan, Osteo +, Osteo + Lact (Figure 4.6 D). PCA shows a slight overlap of Osteo + lact with Osteo + and Xpan medium conditions. Nonetheless, statistical analysis of PCA clustering revealed a statistical

significant segregation with p-value<0.05 and calculated f-value higher than critical f-value (Figure 4.6 E, Table Appendix 4).

Regarding metabolite consumption and secretion, lactate supplementation promotes statistically significant lower glucose consumption compared with Xpan medium at early time-points. At day 5 and 8, lactate supplementation of osteogenic medium slightly increases (2.26-fold change) with statistical significance the amount of glucose consumption compared with Osteo + medium (Figure 4.7 A). At day 11, lactate supplementation promotes a decrease of hMSCs glucose consumption (Figure 4.7 A). For lactate secretion measurements of lactate supplemented osteogenic medium, exogenous lactate medium contribution was taken in account and the values were corrected. hMSCs incubated in Osteo + Lact conditions have an increasing trend of lactate secretion until day 11 (Figure 4.7 B). Here, there is a statistically significant higher secretion of lactate when hMSCs are present in Xpan media (202.67 ± 47.84 mM) when compared with the other cell culture conditions (59.33 ± 12.47 mM for Osteo + Lact and 92.67 ± 23.57 mM) (Figure 4.8B). When hMSCs are incubated in Osteo + Lact medium, there is a higher consumption of glutamine at day 2 (1.827 ± 0.009 mM) compared with other cell culture medium (1.417 ± 0.017 for Osteo + and 1.000 ± 0.041 for Xpan) (Figure 4.7 C). For the remaining time-points there is a sharp decrease in glutamine consumption for lactate supplemented osteogenic medium (Figure 4.7 C).

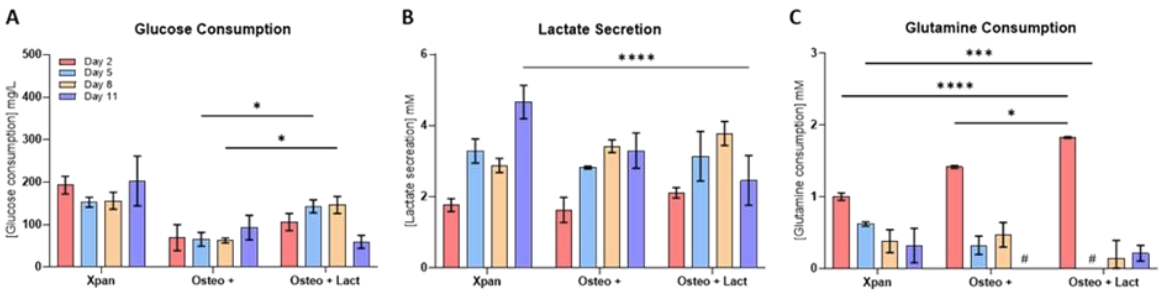

Figure 4.7 - Extracellular metabolite quantification of hMSCs after 14 days in cell culture. A) hMSCs glucose consumption at day 2, 5, 8 and 11 of cell culture. B) Lactate secretion at day 2, 5, 8 and 11 of cell culture. C) hMSCs glutamine consumption at day 2, 5, 8 and 11 of cell culture. #no glutamine consumption, *p-value≤0.05, **p-value≤0.01, ***p-values≤0.001, ****p-value≤0.0001 N≥3

4.4.3. Lactate supplementation promotes higher glutaminolysis, lactate metabolism and poly-hydrolases gene expression

hMSCs were incubated for 14 days in Xpan, Osteo +, and Osteo + Lact cell culture conditions. Afterwards, the expression of genes related with glutaminolysis, poly-hydrolases, lactate metabolism, lactate transport was measured using qPCR (Figure 4.8). Osteo + Lact cell culture medium promoted an increase in expression of glutaminolysis related genes such as GOT1 (2.17- fold), GOT2 (1.461-fold), GLS (2.73-fold) and GLUD1 (1.64-fold) when compared with non-supplemented osteogenic medium (Figure 4.8 A, B). Osteo + Lact induced an increase expression of P4HA1 (2.15-fold), P4HA2 (3.12-fold) and specially P4HA3 (1.97-fold) poly-hydrolases when compared with Osteo + medium (Figure 4.8 C, D).

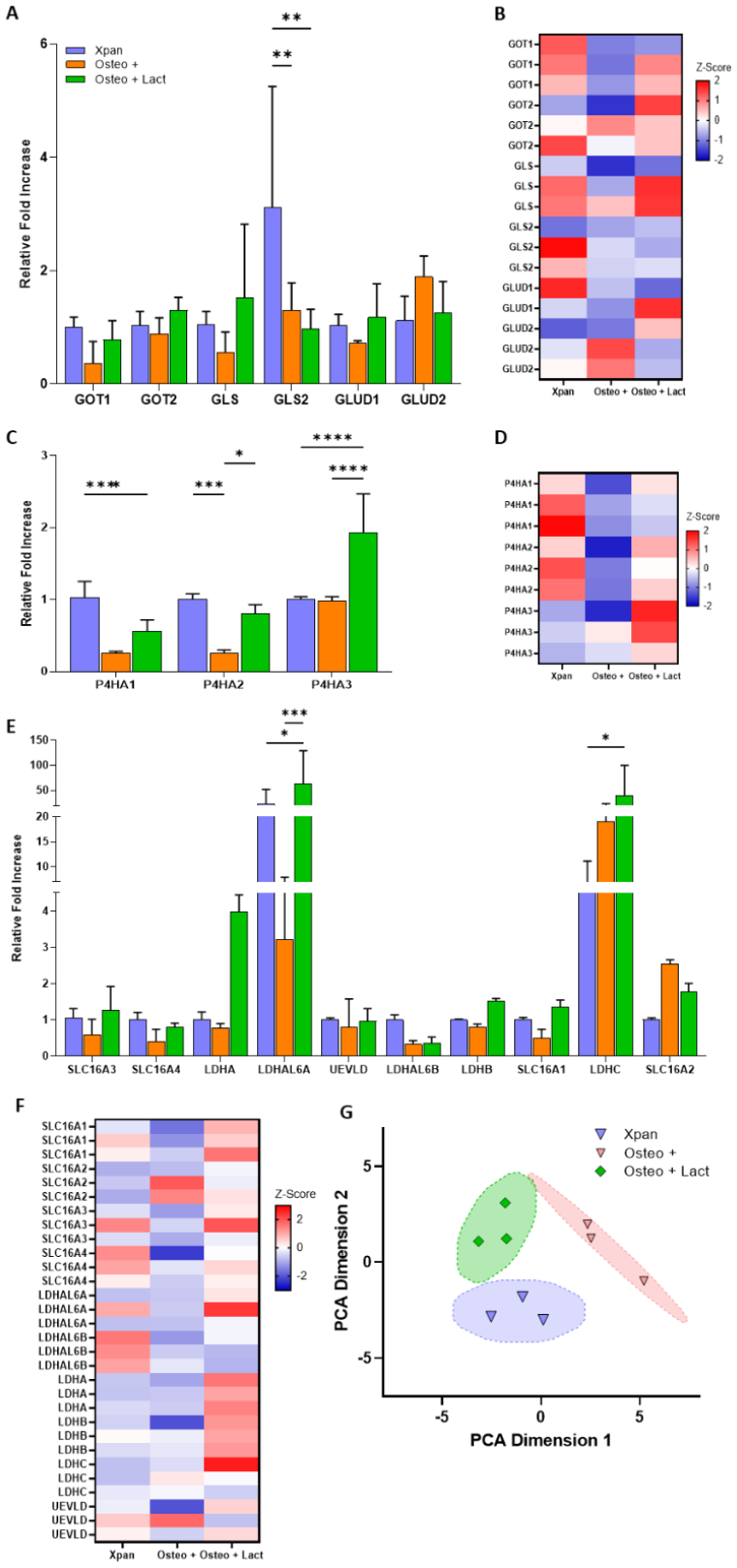

Figure 4.8 - Impact of lactate supplementation of osteogenic differentiation media on the expression of metabolic genes. A) hMSCs relative fold variation of glutaminolysis genes. B) Z-score heatmap of genes expression related with glutaminolysis. C) hMSCs relative fold variation of poly-hydrolases genes. D) Z-score heatmap of genes expression of poly-hydrolases. E) hMSCs relative fold variation of lactate transport and metabolism genes. F) Z-score heatmap of genes expression related with lactate transport and metabolism G) PCA distributions of cell culture conditions at day 14 based on glutaminolysis, lactate metabolism and poly-hydrolase gene expression. *p-value≤0.05, **p-value≤0.01, ***p-values≤0.001, ****p-value≤0.0001 N≥3

Furthermore, Osteo + Lact medium also promoted the increase expression of lactate transporter genes such as SLC16A1 (2.78-fold), SLC16A3 (2.15-fold), SLC16A4 (2.00-fold) and lactate metabolic genes LDHAL6A (19.89-fold), LDHAL6B (1.09-fold), LDHA (5.16-fold), LDHB (1.89-fold), LDHC (2.12-fold) (Figure 4.8 E, F). Finally, PCA distribution of cell culture conditions calculated based on the expression of metabolism related genes showed a statistical significant segregation between Osteo +, Osteo + Lact and Xpan cell culture conditions with p-value<0.05 and calculated F-value higher than critical F-value (Figure 4.8 G).

4.4.4. Blocking glutaminolysis and lactate absorption impacts osteogenic differentiation

Lactate supplementation of osteogenic medium promoted higher hMSCs mineral deposition and upregulation of glutaminolysis and the reconversion from lactate to pyruvate as measured by τ_{avg}, ORR, metabolites consumption and gene expression. To validate an osteogenic differentiation dependent on glutaminolysis and lactate transport/metabolism, these metabolic pathways were blocked using chemical inhibitors. To inhibit glutaminolysis BPTES; a chemical competitor of glutamate synthase enzyme, the first step of the glutaminolysis pathway was used. Inhibiting this enzyme has showed to inhibit the glutaminolysis pathway [52]. Regarding lactate transport, α-CHC was used. This chemical component inhibits the uptake of lactate by blocking SLC16A1 transported [53]. This transmembrane transporter was showed to be the main entry point of lactate in hMSCs cells [54] (Figure 4.9 A).

When treating hMSCs during 14 days with Osteo + medium supplemented with α-CHC, BPTES or no glutamine added (No Glu), there is a reduction of alizarin red staining demonstrating lower mineral deposition (Figure 4.9 B). We further validated this result by calculating the amount of alizarin red stain per amount of DNA. Here, we noticed a statistically

significant reduction of ARS when hMSCs are incubated in Osteo + medium supplemented with either α-CHC or BPTES (Figure 4.9 C).

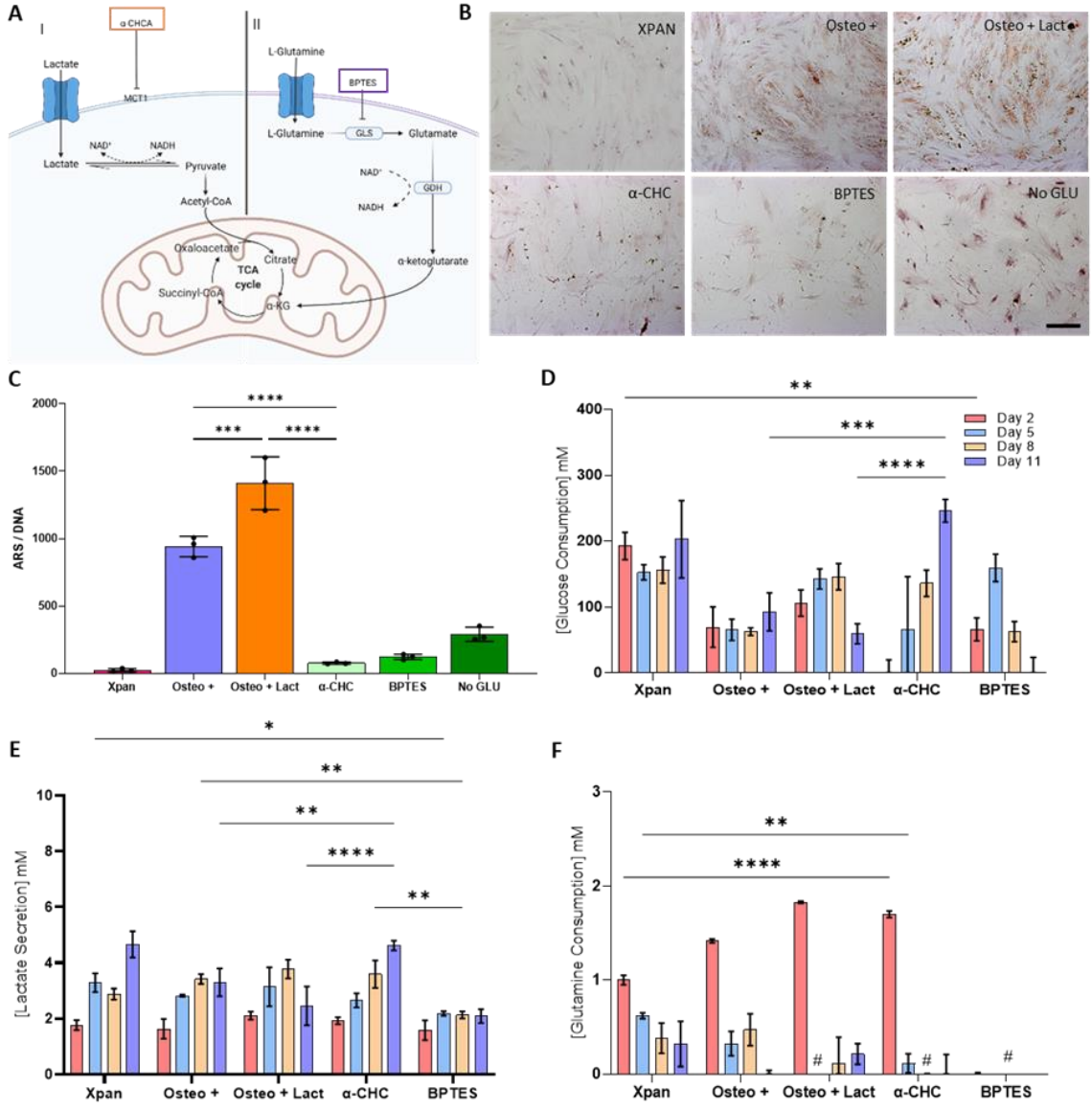

Figure 4.9 - Inhibition of osteogenic differentiation using osteogenic medium supplemented with BPTES or α-CHC during 14 days of cell culture. A) Schematic detailing the inhibition target. B) Alizarin red staining of hMSCs after 14 days in contact with Osteo +, Osteo + Lact, α-CHC or BPTES supplemented osteogenic medium, Osteo + medium without glutamine (No Glu) or Xpan medium. C) Quantification of Alizarin red staining per amount of DNA after 14 days of hMSCs in various cell culture conditions. D) hMSCs glucose consumption at day 2, 5, 8 and 11 of cell culture. E) Lactate secretion at day 2, 5, 8 and 11 of cell culture. F) hMSCs glutamine consumption at day 2, 5, 8 and 11 of cell culture. #no glutamine consumption, *p-value≤0.05, **p-value≤0.01, ***p-values≤0.001, ****p-value≤0.0001 N≥3

α-CHC treatment promotes an increasing trend of glucose consumption being statistically significantly higher at day 11 when compared with Osteo + medium and Lactate supplemented Osteo + medium. BPTES has an increasing trend of glucose consumption until day

5. Afterwards, there is a decrease of glucose consumption until day 11 (Figure 4.9D). α-CHC treated hMSCs have an increasing trend of lactate secretion during the period of incubation. At day 11, there is a statistically significant higher lactate secretion when compared with Osteo + or Lactate supplemented Osteo + medium. For BPTES, there is a stable lactate secretion during the incubation period. In addition, BPTES treatment promotes a statistically significant decrease of lactate when compared with all of the other cell culture medium conditions (Figure 4.9E).

α-CHC supplemented osteogenic medium promotes a decreasing trend of glutamine consumption whilst being statistically significantly higher when compared with Xpan at day 2.

At later time-points, a-CHC treated hMSCs have a decreasing trend of glutamine consumption (Figure 4.9F). As expected, BPTES supplementation of osteogenic medium has a negative impact on glutamine consumption. With BPTES treatment hMSCs did not consume any glutamine during cell culture (Figure 4.9F).

2P-FLIM of NAD(P)H was performed to assess the impact of α-CHC and BPTES on hMSCs metabolism after 24 hours treatment (Figure 4.10A). hMSCs τ_{avg} and ORR measurements are not directly impacted by α-CHC treatment, resulting in no statistical significance in all cell culture conditions for both τ_{avg} and ORR parameters (Figure 4.10B, C). For BPTES, the presence or removal of glutamine resulted in distinct metabolic profiles and impacted τ_{avg} and ORR measurements. The removal of glutamine from osteogenic medium statistically significantly decreased τ_{avg} (0.90-fold decrease) of hMSCs compared with Xpan, Osteo+ and Osteo+ Lact cell culture medium condition (Figure 4.10D). Regarding ORR, BPTES treatment of osteogenic medium and the removal of glutamine from osteogenic medium resulted in an increase of 1.10-fold and 1.17-fold of ORR, respectively, when compared with other cell culture medium conditions (Figure 4.10 E).

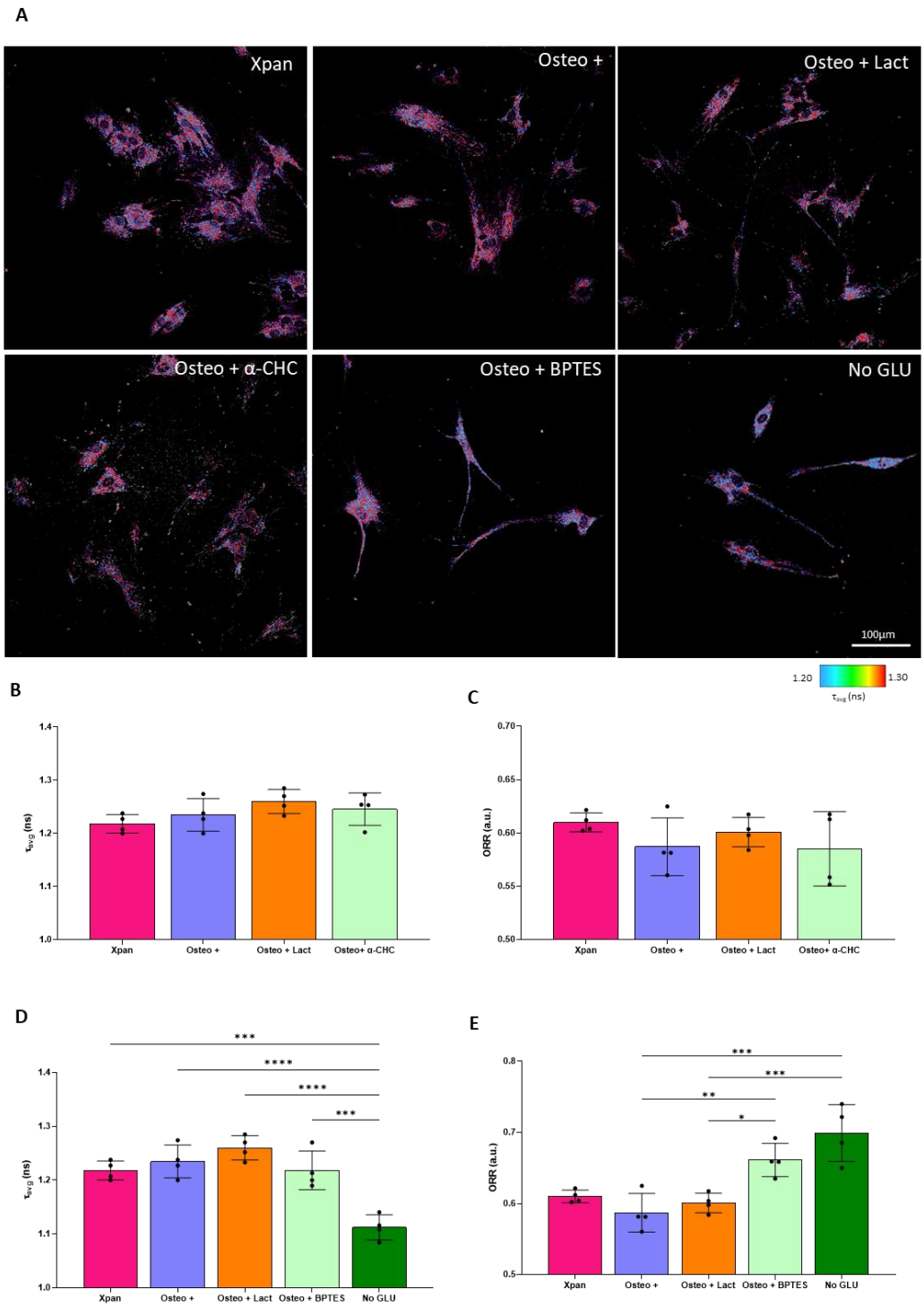

Figure 4.10 – 2P-FLIM validation of metabolic inhibition by α-CHC and BPTES after 24 hours. A) 2P-FLIM imaging of hMSCs in different cell culture conditions B) NAD(P)H τ_{avg} measurement of hMSCs after 24 hours of α-CHC treatment. C) Optical Redox Ratio (ORR) of hMSCs after 24 hours of α-CHC treatment. D) NAD(P)H τ_{avg} measurement of hMSCs after 24 hours of BPTES treatment. E) Optical Redox Ratio (ORR) of hMSCs after 24 hours of BPTES treatment. *p-value≤0.05, **p-value≤0.01, ***p-values≤0.001, ****p-value≤0.0001 N≥3

4.5. Discussion

In this study, hMSCs osteogenic differentiation was achieved using osteogenic medium and validated by mineral deposition and osteogenic gene expression. During the osteogenic differentiation, 2P-FLIM was used to monitor the metabolic profile of hMSCs. This technique showed that hMSCs in osteogenic medium are more dependent on OxPhos as a source of energy than hMSCs in Xpan medium. Also, 2P-FLIM highlighted a higher dependence on glutaminolysis and anabolic pathways verified by increased glutamine consumption. Osteogenic medium was supplemented with lactate to upregulate glutaminolysis and other anabolic pathways. Here, lactate supplementation of osteogenic medium drove increased mineral deposition and higher osteogenic gene expression when compared with non-supplemented osteogenic medium. Again, 2P-FLIM revealed a higher dependence of anabolic pathways and higher ratio of free NAD(P)H. The higher ratio of free NAD(P)H is a consequence of glutaminolysis and re-conversion of lactate into pyruvate. Osteogenic differentiation dependence on glutaminolysis and lactate re-conversion to pyruvate was validated by inhibiting glutaminolysis using BPTES and lactate uptake using α-CHC. The use of each metabolic inhibitor resulted in a decrease in mineral deposition and metabolite uptake. Furthermore, it was demonstrated that inhibiting glutaminolysis resulted in higher ORR ratios, validating that lower ORR ratios can result from higher glutaminolysis rates.

As expected Osteo + cell culture medium promotoed osteogenic differentiation of hMSCs (Figure 4.2A, B, C, D). We observed increased mineral deposition measured by the higher amount of alizarin red staining. In addition, a higher fold of expression of osteogenic genes such as alkaline phosphatase (ALPL) and prostaglandin-endoperoxide synthase 2 (PTGS2) were measured compared with hMSCs in growth medium. Nakamura et al., demonstrated that ALPL inhibition supressed osteogenic differentiation and overexpression of ALPL resulted in increased osteogenic differentiation in murine MSCs. Nakamura et al., results demonstrate that ALPL is an

important marker to establish differentiation of MSCs [55]. Another study by Beheshtizadeh et al., using a in silico approach, determined that increased PTGS2 expression upregulates osteogenesis and its regulatory pathways [56]. In this study, we verified increased levels of osteogenic differentiation observed by increased mineral deposition and increased gene expression levels of ALPL and PTGS2. Therefore, higher mineral deposition and increased levels of ALPL and PTGS2 gene expression are associated with higher osteogenic differentiation.

To profile hMSCs metabolism undergoing differentiation, we imaged hMSCs at several time-points during cell culture, using non-invasive 2P-FLIM (Figure 4.3A). hMSCs treated with osteogenic medium showed a higher τ_{avg}, as early as day 3, reflective of a metabolic shift towards OxPhos as a consequence of a higher proportion of longer lifetime and protein-bound NAD(P)H [32, 57] (Figure 4.3B). Also, τ_1 lifetimes are higher in osteogenic conditions, highlighting higher amounts of NADPH and anabolic activity [33, 58] (Figure 4.3C).

Varying interpretations of ORR are reported in previous studies [41, 59] and for this study, we adopt a lower ORR reflecting a higher fraction of NAD(P)H and a lower FAD^+ associated with upregulation of Krebs cycle. This ORR interpretation allows for easier and quicker analysis of impact of NADH-dependent metabolic pathways. An increased generation of NADH will result in a decreased ORR (Equation 4.3)[60, 61]. Osteogenic medium induced lower ORR possibly to fuel both OxPhos and anabolic pathways (Figure 4.3D). These metabolic results are in agreement with the literature; higher OxPhos and anabolic pathways dependence during osteogenic differentiation [28, 42, 62]. However, we are the first to uncover a metabolic switch as early as day 3.

UMAP and PCA distribution analysis of 2P-FLIM variables confirmed a time-dependent metabolic switch during osteogenic differentiation. Taking into account 2P-FLIM variables in the UMAP analysis, there is noticeable a separation between Xpan and Osteo + treated cells at day 7 and day 14 (Figure 4.3E). PCA analysis revealed also a separation at day 7 and 14 between

these culture conditions (Figure 4.3F). Overall, the statistical significance and the distance between PCA and UMAP clusters of both cell culture conditions increases with longer incubation periods. The usage of PCA and UMAP as data-visualisation tools allows to quickly analyse the gene expression and metabolic difference of hMSCs in different cell culture conditions [41, 63]. Mahalanobis distance, Two-sample Hotellings T2 test, F-value, F-critical and P-values were calculated to ensure statistical significance between PCA cluster groups (Table Appendix 4). The clear and statistically valid segregation of cell culture and hMSCs profiles demonstrate the possibility to use PCA and UMAP not only as data-visualisation tools but to possibly be used as classification tools.

Extracellular metabolite analysis confirms 2P-FLIM metabolic results. Osteo + treated hMSCs have lower glucose consumption compared with Xpan treated hMSCs cultures demonstrating a lower reliance on glycolysis when treated osteogenic medium [58]. Regarding lactate production, there is no statistically significant differences between Xpan and Osteo + media except for at day 14. Glucose consumption and lactate secretion results demonstrate that during osteogenic differentiation hMSCs continue to produce lactate in spite of decreasing glucose consumption. Since lactate secretion values are not impacted by lower glycolytic rates other metabolites are being used to fuel OxPhos. With presence of glutamine and pyruvate in cell culture medium, these metabolites are used as metabolic fuel in anaplerotic pathways [64, 65]. Interestingly, the peak of glutamine consumption occurs at earlier time-points followed by a decreasing trend, demonstrating a time-dependence of the glutaminolysis pathway. Nonetheless, for Osteo +, glutamine is used at a higher rate when comparing with Xpan cultures

The trends observed with 2P-FLIM and extracellular metabolite quantification, confirm a metabolic switch towards OxPhos by reduction of glucose consumption while showing a higher dependence of glutaminolysis at earlier time-points. The metabolic switch towards a more OxPhos dependence is a known feature of differentiated cells and it has been demonstrated to

occur also during osteogenic differentiation [28, 66]. Interestingly, glutamine has been shown to be a critical metabolite to achieve osteogenic differentiation [31]. One study by Yu et al., demonstrated that glutamine is an important metabolite to achieve osteogenic differentiation by its anaplerotic role in feeding the Krebs cycle by proxy of alpha-ketoglutarate. In addition, this study demonstrated that glutamine removal impacts osteogenic differentiation by decrease of alizarin red staining [31]. Interestingly, Gayatri et al., demonstrated that increasing glutamine concentrations 10-fold supresses osteogenic differentiation of human and murine MSCs [67]. Therefore, to promote glutaminolysis and anaplerotic pathways and consequently promote earlier osteogenesis, the glutaminolysis pathway rate needs to be increased without increasing extracellular concentrations of glutamine.

To achieve a higher rate of glutaminolysis, we decided to upregulate the glutaminolysis pathway by modifying the Osteo + cell culture medium formulation. Pérez-Escuredo et al., showcase the upregulation of glutamine uptake and glutaminolysis promoted by increased lactate concentration on oxidative tumour cells. In this study, extracellular lactate secreted by tumour cells acts as a signalling molecule that increase the expression of glutaminolysis-specific enzymes such as glutamine transporter ASCT2 and glutaminase 1 (GLS1) by c-Myc activation. Pérez-Escuredo et al., study demonstrates how extracellular lactate can promote increased glutaminolysis [46]. Following this approach, we decided to increase exogenous lactate levels in the Osteo + medium to promote higher glutaminolysis and hMSCs osteogenic differentiation and mineral deposition. To account for pH changes due to increased lactate concentration, exogenous lactate in the form of sodium lactate was used to stabilize pH values [46].

Lactate supplementation of osteogenic media yielded a higher mineral deposition and osteogenic differentiation (Figure 4.4A, B, C, D). Regarding osteogenic gene expression, an increased expression of ALPL, SOX9, SPP1 and RUNX2 genes was observed in osteogenic medium supplemented with lactate. Works in literature demonstrated that gene expression of

ALPL, SOX9, SPP1 and RUNX2 genes is related with higher osteogenic differentiation levels [68, 69]. Fernandez-Moure et al., verified that MSC from the cortical fraction of the bone had higher osteogenic differentiation potential correlated by increase gene expression levels of ALPL and SPP1 [68]. In addition, a study by Friedl et al., demonstrated that hMSCs osteogenic differentiation promoted by mechanical strain results in increase ALPL, SOX9 and RUNX2 gene expression [69]. However, lactate supplementation of osteogenic medium did not translate to increased gene expression of BGLAP and PTGS2. Wang et al., analysed the dynamic and temporal expression profiles of osteogenic differentiation gene markers of hMSCs. In Wang et al., study, hMSCs were grown in osteogenic differentiation medium during 28 days and alizarin red staining was used to verify osteogenic differentiation. Here, increased BGLAP gene expression due to osteogenic differentiation was only verified at day 21 of cell cultures and not at earlier time-points [70]. While PTGS2 gene expression is required for osteogenic differentiation as it was verified in Figure 4.2, we do not observe that increased levels of osteogenic differentiation are associated with increased expression levels of PTGS2. Huang et al., analysed the spatiotemporal expression of PTGS2 and targeting the expression of PTGS2 in monolayer cultures, negatively impacts osteogenic differentiation [71]. In addition, another study by Yoon et al., used PTGS2 inhibitors during osteogenic differentiation of hMSCs. In this study by Yoon et al., following hMSCs differentiation, the inhibition of PTGS2 negatively impacted ALPL and calcium contents in inflammatory environments. However, in non-inflammatory conditions, ALPL expression and calcium contents were not impacted by PTGS2 inhibition, suggesting a non-specific role in osteogenic differentiation [72]. Huang et al., and Yoon et al., work demonstrates that PTGS2 is essential for earlier bone formation especially in inflammatory environments but is not required to be continuously expressed for later time-points osteogenic differentiation. In this study, the increased gene expression of ALPL, SOX9, SPP1 and RUNX2 is associated with hMSCs osteogenesis and follows the trend observed in literature. In addition, the non-upregulation of BGLAP and PTGS2 are not synonymous of poor

osteogenic differentiation. BGLAP and PTGS2 upregulation is not observed at the time-points of this study experiments or critical to ensure osteogenic differentiation in non-inflammatory environments.

Using 2P-FLIM, we observed a shift in metabolism when supplementing osteogenic medium with lactate (Figure 4.6A). A lower τ_{avg} shows an increase in free NAD(P)H fraction in the cytoplasm concomitant with a reduction of protein bound-NADH. This shift in NAD(P) fraction is associated with higher metabolic dependence on glycolysis (Figure 4.6 B). Simultaneously, there is a decrease in ORR associated with OxPhos and anaplerotic metabolic pathways such as glutaminolysis (Figure 4.6 C). UMAP and PCA distribution analysis of 2P-FLIM data revealed a segregation between the hMSCs treated with Osteo + SL, Osteo + and Xpan medium (Figure 4.6 D, E). This shows that the three cell culture formulations promote distinct metabolic properties in hMSCs.

Extracellular metabolic secretion of lactate supplemented osteogenic medium treated hMSCs increased slightly glucose consumption, maintained similar levels of lactate secretion and increased glutamine consumption at earlier time points (Figure 4.7 A, B, C). To account for exogenous lactate supplementation, lactate secretion measurements were corrected when measuring extracellular lactate. This trend shows similar glucose consumption and lactate secretion to Osteo + medium whilst showing higher glutaminolysis level at early time points.

Metabolic gene expression revealed for most genes, higher expression levels when hMSCs are incubated for 14 days in osteogenic lactate supplemented cell culture medium (Figure 4.8). Glutaminase (GLS) (1.73-fold), glutamate dehydrogenase 1 (GLUD1) (0.63-fold), glutamic-oxaloacetic transaminase 1 (GOT1) (1.16-fold) and glutamic-oxaloacetic transaminase 2 (GOT2) (0.46-fold) are glutaminolysis related genes and are highly expressed when hMSCs are incubated in Osteo + cell culture medium (Figure 4.8 A, B). These glutaminolysis genes are responsible for the conversion of glutamine to glutamate and the conversion of glutamate to

alpha-ketoglutarate in the cytoplasm and the mitochondrial matrix [73, 74]. Alpha-ketoglutarate can then be used to fuel the Krebs cycle and OxPhos in hMSCs [75]. Furthermore, P4HA1 (1.15-fold), PAHA2 (2.11-fold) and P4HA3 (0.97-fold) are highly expressed in Osteo + Lact cell culture conditions (Figure 4.8 C, D). These poly-hydrolases are located within the endoplasmic reticulum, are activated by the presence of alpha-ketoglutarate and are crucial for the formation of the collagen triple helix. The incomplete hydroxylation of proline residues impacts collagen triple helix formation reducing collagen secretion to the cytoplasm and lastly reducing extracellular secretion of collagen [76]. The ability to secrete high amounts of extracellular matrix such as collagen I is a known feature of osteoblasts and important during bone formation [77]. Lactate metabolic genes are also highly expressed in lactate supplemented osteogenic medium when compared with non-supplemented osteogenic medium. SLC16A1 (1.78-fold), SLC16A3 (1.15-fold), SLC16A4 (1.00-fold) gene expression levels increase in lactate osteogenic supplemented medium compared with osteogenic medium. SLC16A1, SLC16A2, SLC16A3, SLC16A4 are responsible for the transport of lactate across the plasmatic membrane (Figure 4.8 E, F). SL16A1 in particular has been showed to express MCT1 one of the main membrane transporter of lactate in hMSCs [78] . LDH (4.16-fold for isoform A, 0.88-fold for isoform B, and 1.12-fold for isoform C) is also highly expressed in all isoforms when treating hMSCs with Osteo+ cell culture medium. LDH is responsible for conversion of pyruvate to lactate and is capable of performing the reverse enzymatic reaction [79]. The upregulation of LDH gene expression without an increase in extracellular lactate concentrations demonstrates that LDH has a higher ratio of reverse enzymatic reaction compared with the forward reaction. Glutaminolysis and lactate gene expression demonstrate that exogenous lactate supplementation of lactate medium promotes upregulation of glutaminolysis while increasing lactate uptake and re-conversion to pyruvate in hMSCs.

PCA metabolic gene expression analysis revealed a statistically significant segregation between all cell culture conditions (Figure 4.8 G). This confirms that lactate supplementation of

osteogenic medium is having a direct impact on hMSCs metabolism. hMSCs when treated with Osteo + Lact medium have higher level of glutaminolysis rate, higher uptake of lactate, higher rates of lactate conversion to pyruvate and higher secretion levels of collagen. These metabolic shifts can be therefore responsible for higher levels of osteogenic differentiation.

The gene expression panel used in Figure 4.6, Figure 4.7 and Figure 4.8 demonstrate differentiating and metabolic pathways trends. Using the qPCR data obtained with hMSCs at day 14 of cell culture, a search for RNAseq libraries was conducted to establish a relationship between the upregulation observed in some gene and known signalling pathways. During this search, there was a focus on finding the expression of common genes at similar time points. A RNAseq study by Liu et al., focussed on comparing transcriptomic profile of hMSCs at day 7 of cellular differentiation towards a osteogenic or adipogenic lineages. In Liu et al., RNAseq library there is an upregulation of the valine, leucine and isoleucine amino acid pathway . This pathway according to Kyoto Encyclopedia of Genes and Genomes (KEGG) is highly dependent on pyruvate metabolite [80]. In addition, focal adhesion, protein digestion and absorption and ECM receptor interaction are upregulated. Another upregulated cellular pathway matched in Gene Ontology database is the metabolic processes pathway, including extracellular matrix organization, cell matrix interaction and cell adhesion [80]. One separate study has demonstrated that PTGS2 and RUNX2 have increased pathway upregulation with multiple binding sites associated with cellular growth and proliferation. RUNX2 and PTGS2 were showed to interact with the GTF2I promotor which upregulates ALPL and BGLAP gene expression [81]. Unfortunately, there were no findings pertaining the regulation of metabolic genes during osteogenic differentiation published in RNAseq libraries.

After showing the importance of glutaminolysis and lactate in osteogenic differentiation we decided to block glutaminolysis using BPTES or removing glutamine (No Glu) from the osteogenic medium, as well as blocking the uptake of lactate using α-CHC (Figure 4.9 A). BPTES

impacts directly the GLS enzyme whilst α-CHC inhibits the SLC16A1 transporter, responsible for lactate uptake. Aliziran red staining and extracellular metabolic analysis shows that inhibiting lactate uptake and glutaminolysis impacts negatively osteogenic differentiation.

2P-FLIM NAD(P) measurements of the metabolic profile of hMSCs after 24 hours treatment demonstrated that α-CHC does not impact either τ_{avg} or ORR redox ratio at earlier treatments times. Since α-CHC directly inhibits a transmembrane transporter responsible for lactate uptake, the impact on metabolism might not be pronounced in short culture times probably due to the pyruvate available on the medium which can evade lactate uptake to be converted back to pyruvate while generating NADH. However, BPTES treatment or removal of glutamine significantly impacted hMSCs metabolism after 24 hours. Removal of glutamine produced a statistically significant decrease of τ_{avg} possibly generated by the cell compensating the absence of an essential metabolite by increasing glycolysis to fuel the Krebs cycle for cellular differentiation. ORR measurements show a statically significant increase in BPTES and no glutamine osteogenic medium. This trend is a direct opposite from what is observed experimentally with upregulated glutaminolysis in this study. Increased ORR due to BPTES or removal of glutamine results from a reduction of NADH availability due to not being regenerated during glutamate conversion to alpha-ketoglutarate [41].

Lactate was added to osteogenic medium in the presence of BPTES and α-CHC in order to complement glutaminolysis and lactate transport inhibition studies in hMSCs. Lactate supplementation of osteogenic medium with BPTES was not able to rescue osteogenic differentiation. In addition, lactate supplementation of osteogenic medium with α-CHC was also not able to promote osteogenic differentiation (Figure Appendix 10). This results demonstrates that osteogenic differentiation supplemented with lactate impacts directly both metabolic pathways: glutaminolysis and lactate uptake.

Lactate supplementation was able to promote further osteogenic differentiation. This was validated by increased mineral deposition and gene expression of osteogenic markers. The metabolic shifts promoted by the exogenous lactate drove increased glutaminolysis and lactate uptake. Glutaminolysis upregulation was validated by increased gene expression of glutaminolysis-related genes, decreased τ_{avg} and ORR and increased glutamine consumption in early time-points of differentiation. In particular, 2P-FLIM NADH results showcase an impact of increased glutaminolysis in real-time with increased the fraction of free NADH and increased NADH concentration. Lactate role in metabolism was also observed to be upregulated with extracellular lactate supplementation. The impact on lactate metabolic upregulation occurs concurrently with glutaminolysis upregulation. 2P-FLIM of NAD(P)H have similar trend by intracellular formation of pyruvate by lactate re-conversion generating free NADH. Increased gene expression of SL16A1, the major transmembrane transport of lactate, shows cells adaptability to exogenous lactate concentrations, followed by LDH upregulation which translates to LDH enzyme responsible for converting lactate to pyruvate. Furthermore, inhibition of any isolated pathways negatively impacted osteogenic differentiation and was not able to be rescued by lactate supplementation. The conjugation of these results validate the role of glutaminolysis in hMSCs osteogenic differentiation following the trend observed by Yu et al. in which blocking glutaminolysis with BPTES negatively impacted osteogenic differentiation [31]. It seems that both metabolic pathways are essential for osteogenic differentiation, glutaminolysis metabolic pathway and the direct and indirect role of lactate in hMSCs metabolism. In this study, a new role for lactate in osteogenic differentiation of hMSCs was uncovered. Here, lactate can act indirectly on osteogenic differentiation as a signalling to upregulate glutaminolysis and directly by being used as metabolic fuel to regenerate pyruvate. In particular, this study demonstrates for the first time the importance of lactate for hMSCs differentiation. Only recently, has lactate started to be understood as a fuel source and a distinct signalling molecule instead of just a metabolic by-product. Lactate is becoming an interesting

metabolite and has been showed to contribute to reduce inflammatory cell signalling [82]. Furthermore, the only study demonstrating the impact of extracellular lactate on stem cells was a study by Gatie et al. In this study, Gatie et al., observed that increasing extracellular lactate stimulates murine embryonic stem cells differentiation towards extraembryonic endoderm cells in vitro [83].

This study demonstrates the possibility to modulate hMSCs differentiation using extracellular metabolites. The importance of glutaminolysis in osteogenic differentiation was verified. As well, new roles for lactate metabolite were uncovered while promoting increased hMSCs osteogenic differentiation. This work demonstrates not only the importance of essential metabolites in osteogenic differentiation but also showcases 2P-FLIM as a method to uncover and validate metabolic profiles of hMSCs non-invasively in real-time. This new metabolic viewpoint in stem cell differentiation should be taken in account when promoting stem cell differentiation in vitro. Importantly, the metabolic environment during cell culture or cell maturation should be established to either promote higher differentiation rates of hMSCs or to simulate metabolic properties of native tissue. Furthermore, for tissue engineered constructs the use of lactate as a coating or as a biocompatible material in the form of lactic acid can promote further stem cell differentiation and diminish inflammation in the implantation site. The metabolic role of lactate as fuel and signalling molecule is still a new approach to a metabolite that is traditionally considered as a metabolic by-product and established as a cellular metabolism endpoint. Current research is now shining a new light on the impact of exogenous lactate impact on cellular function. However, research in various cell types using numerous methodologies is still require to establish the various roles and potential impact of lactate.

4.6. Conclusion

In this study, we uncovered a time-dependent metabolic shift during osteogenic differentiation highlighted by 2P-FLIM, histology and extracellular metabolite measurements. Here, we showed that osteogenic differentiation is a phenotypic and metabolic process that occurs in a time-dependent manner reliant on glutaminolsysis and lactate. The inhibition of these pathways using BPTES and α-CHC and removal of metabolites impacts negatively osteogenic differentiation. We manage to modulate the metabolism of differentiating hMSCs by increasing extracellular concentration of lactate in order to increase mineral deposition and osteogenic differentiation. The supplementation of osteogenic medium with lactate promoted higher osteogenic differentiation, glutaminolysis, lactate metabolism and end-point poly-hydrolises gene expression. At latter time-points, lactate supplemented osteogenic cells have already separate metabolism compared with cells in non-supplemented osteogenic medium and Xpan growth medium. We believe this study provides further information on the metabolic shifts occurring during hMSCs differentiation as well the role of glutaminolysis and extracellular lactate in osteogenic differentiation. Furthermore, lactate supplementation of osteogenic medium can improve tissue engineering applications by increasing osteogenic differentiation of hMSCs seeded in biomimetic scaffolds. This study approach to use non-invasive 2P-FLIM combined with UMAP and PCA can further uncover and modulate cellular metabolism in order to promote higher differentiation rates in hMSCs.

4.7. References

[1] S.E. Haynesworth, D. Reuben, A.I. Caplan, Cell-based tissue engineering therapies: the influence of whole body physiology, Advanced Drug Delivery Reviews. 33(1-2) (1998) 3-14.
[2] A.I. Caplan, Adult mesenchymal stem cells for tissue engineering versus regenerative medicine, J Cell Physiol. 213(2) (2007) 341-7.
[3] D. Rana, H. Zreiqat, N. Benkirane-Jessel, S. Ramakrishna, M. Ramalingam, Development of decellularized scaffolds for stem cell-driven tissue engineering, Journal of Tissue Engineering and Regenerative Medicine. 11(4) (2017) 942-965.
[4] D. Howard, L.D. Buttery, K.M. Shakesheff, S.J. Roberts, Tissue engineering: strategies, stem cells and scaffolds, Journal of Anatomy. 213(1) (2008) 66-72.
[5] D. Ke, H. Yi, S. Est-Witte, S. George, C. Kengla, S.J. Lee, A. Atala, S.V. Murphy, Bioprinted trachea constructs with patient-matched design, mechanical and biological properties, Biofabrication. 12(1) (2019) 1-12.
[6] M. Kim, M.J. Farrell, D.R. Steinberg, J.A. Burdick, R.L. Mauck, Enhanced nutrient transport improves the depth-dependent properties of tri-layered engineered cartilage constructs with zonal co-culture of chondrocytes and MSCs, Acta Biomaterialia. 58 (2017) 1-11.
[7] A. Skardal, M. Devarasetty, H.W. Kang, I. Mead, C. Bishop, T. Shupe, S.J. Lee, J. Jackson, J. Yoo, S. Soker, A. Atala, A hydrogel bioink toolkit for mimicking native tissue biochemical and mechanical properties in bioprinted tissue constructs, Acta Biomaterialia. 25 (2015) 24-34.
[8] E. Seeman, P.D. Delmas, Bone quality--the material and structural basis of bone strength and fragility, New England Journal of Medicine. 354(21) (2006) 2250-2261.
[9] S. Mendez-Ferrer, T.V. Michurina, F. Ferraro, A.R. Mazloom, B.D. Macarthur, S.A. Lira, D.T. Scadden, A. Ma'ayan, G.N. Enikolopov, P.S. Frenette, Mesenchymal and haematopoietic stem cells form a unique bone marrow niche, Nature. 466(7308) (2010) 829-834.
[10] D. Park, J.A. Spencer, B.I. Koh, T. Kobayashi, J. Fujisaki, T.L. Clemens, C.P. Lin, H.M. Kronenberg, D.T. Scadden, Endogenous bone marrow MSCs are dynamic, fate-restricted participants in bone maintenance and regeneration, Cell Stem Cell. 10(3) (2012) 259-272.
[11] C.K. Chan, E.Y. Seo, J.Y. Chen, D. Lo, A. McArdle, R. Sinha, R. Tevlin, J. Seita, J. Vincent-Tompkins, T. Wearda, W.J. Lu, K. Senarath-Yapa, M.T. Chung, O. Marecic, M. Tran, K.S. Yan, R. Upton, G.G. Walmsley, A.S. Lee, D. Sahoo, C.J. Kuo, I.L. Weissman, M.T. Longaker, Identification and specification of the mouse skeletal stem cell, Cell. 160(1-2) (2015) 285-298.
[12] L.C. Hofbauer, C.C. Brueck, S.K. Singh, H. Dobnig, Osteoporosis in patients with diabetes mellitus, Journal of Bone Mineral Research. 22(9) (2007) 1317-1728.
[13] H. Nojiri, Y. Saita, D. Morikawa, K. Kobayashi, C. Tsuda, T. Miyazaki, M. Saito, K. Marumo, I. Yonezawa, K. Kaneko, T. Shirasawa, T. Shimizu, Cytoplasmic superoxide causes bone fragility owing to low-turnover osteoporosis and impaired collagen cross-linking, Journal of Bone and Mineral Research. 26(11) (2011) 2682-2694.
[14] C.E. Murray, C.M. Coleman, Impact of diabetes mellitus on bone health, International Journal Molecular Sciences. 20(19) (2019) 1-23.
[15] U. Foger-Samwald, P. Dovjak, U. Azizi-Semrad, K. Kerschan-Schindl, P. Pietschmann, Osteoporosis: pathophysiology and therapeutic options, Experimental and Clinical Sciences Journal. 19 (2020) 1017-1037.
[16] P. Su, Y. Tian, C. Yang, X. Ma, X. Wang, J. Pei, A. Qian, Mesenchymal stem cell migration during bone formation and bone diseases therapy, International Journal Molecular Sciences. 19(8) (2018) 2343-2361.
[17] J.L. Crane, L. Zhao, J.S. Frye, L. Xian, T. Qiu, X. Cao, IGF-1 signaling is essential for differentiation of mesenchymal stem cells for peak bone mass, Bone Research. 1(2) (2013) 186-194.

[18] C.J. Rosen, M.L. Bouxsein, Mechanisms of disease: is osteoporosis the obesity of bone?, Nature Clinical Practices Rheumatology. 2(1) (2006) 35-43.
[19] M. Kim, C. Kim, Y.S. Choi, M. Kim, C. Park, Y. Suh, Age-related alterations in mesenchymal stem cells related to shift in differentiation from osteogenic to adipogenic potential: implication to age-associated bone diseases and defects, Mechanisms of Ageing and Development. 133(5) (2012) 215-225.
[20] A. Stolzing, E. Jones, D. McGonagle, A. Scutt, Age-related changes in human bone marrow-derived mesenchymal stem cells: consequences for cell therapies, Mechanisms of Ageing and Development. 129(3) (2008) 163-173.
[21] S.A. Brown, C.J. Rosen, Osteoporosis, Medical Clinics of North America. 87(5) (2003) 1039-1063.
[22] M. Kveiborg, A. Flyvbjerg, S.I.S. Rattan, M. Kassem, Changes in the insulin-like growth factor-system may contribute to in vitro age-related impaired osteoblast functions, Experimental Gerontology. 35(8) (2000) 1061-1074.
[23] X. Feng, J.M. McDonald, Disorders of bone remodeling, Annual Review of Pathology: Mechanisms of Disease. 6 (2011) 121-145.
[24] S.G. Almalki, D.K. Agrawal, Key transcription factors in the differentiation of mesenchymal stem cells, Differentiation. 92(1-2) (2016) 41-51.
[25] X. Yuan, T.M. Logan, T. Ma, Metabolism in Human mesenchymal stromal cells: a missing link between hMSC biomanufacturing and therapy?, Frontiers in Immunology. 10 (2019) 977-988.
[26] S.Y. Lunt, M.G. Vander Heiden, Aerobic glycolysis: meeting the metabolic requirements of cell proliferation, Annu Rev Cell Dev Biol. 27 (2011) 441-64.
[27] B. Rocha, V. Calamia, J. Mateos, P. Fernandez-Puente, F.J. Blanco, C. Ruiz-Romero, Metabolic labeling of human bone marrow mesenchymal stem cells for the quantitative analysis of their chondrogenic differentiation, Journal of Proteome Research. 11(11) (2012) 5350-5361.
[28] L.C. Shum, N.S. White, B.N. Mills, K.L. Bentley, R.A. Eliseev, Energy Metabolism in Mesenchymal Stem Cells During Osteogenic Differentiation, Stem Cells Dev. 25(2) (2016) 114-22.
[29] A.D. Hofmann, M. Beyer, U. Krause-Buchholz, M. Wobus, M. Bornhauser, G. Rodel, OXPHOS supercomplexes as a hallmark of the mitochondrial phenotype of adipogenic differentiated human MSCs, PloS One. 7(4) (2012) e35160.
[30] C.T. Chen, Y.R. Shih, T.K. Kuo, O.K. Lee, Y.H. Wei, Coordinated changes of mitochondrial biogenesis and antioxidant enzymes during osteogenic differentiation of human mesenchymal stem cells, Stem Cells. 26(4) (2008) 960-8.
[31] Y. Yu, H. Newman, L. Shen, D. Sharma, G. Hu, A.J. Mirando, H. Zhang, E. Knudsen, G.F. Zhang, M.J. Hilton, C.M. Karner, Glutamine Metabolism Regulates Proliferation and Lineage Allocation in Skeletal Stem Cells, Cell Metab. 29(4) (2019) 966-978 e4.
[32] J.R. Lakowicz, H. Szmacinski, K. Nowaczyk, M.L. Johnson, Fluorescence lifetime imaging of free and protein-bound NADH, Proceedings of the National Academy of Sciences of the United States of America. 89(4) (1992) 1271-1275.
[33] T.S. Blacker, Z.F. Mann, J.E. Gale, M. Ziegler, A.J. Bain, G. Szabadkai, M.R. Duchen, Separating NADH and NADPH fluorescence in live cells and tissues using FLIM, Nat Commun. 5 (2014) 3936.
[34] W. Ying, NAD+/NADH and NADP+/NADPH in cellular functions and cell death: regulation and biological consequences, Antioxid Redox Signal. 10(2) (2008) 179-206.
[35] A.A. Heikal, Intracellular coenzymes as natural biomarkers for metabolic activities and mitochondrial anomalies, Biomarkers in Medicine. 4(2) (2010) 241-263.
[36] I. Georgakoudi, K.P. Quinn, Optical imaging using endogenous contrast to assess metabolic state, Annual Review of Biomedical Engineering. 14 (2012) 351-367.

[37] A. Floudas, N. Neto, V. Marzaioli, K. Murray, B. Moran, M.G. Monaghan, C. Low, R.H. Mullan, N. Rao, V. Krishna, S. Nagpal, D.J. Veale, U. Fearon, Pathogenic, glycolytic PD-1+ B cells accumulate in the hypoxic RA joint, Journal of Clinical Investigation Insight. 5(21) (2020) e139032.
[38] A.J. Walsh, R.S. Cook, M.E. Sanders, L. Aurisicchio, G. Ciliberto, C.L. Arteaga, M.C. Skala, Quantitative optical imaging of primary tumor organoid metabolism predicts drug response in breast cancer, Cancer Research. 74(18) (2014) 5184-5194.
[39] I.A. Okkelman, N. Neto, D.B. Papkovsky, M.G. Monaghan, R.I. Dmitriev, A deeper understanding of intestinal organoid metabolism revealed by combining fluorescence lifetime imaging microscopy (FLIM) and extracellular flux analyses, Redox Biology. 30 (2020) 101420.
[40] S. Perottoni, N.G.B. Neto, C. Di Nitto, R.I. Dmitriev, M.T. Raimondi, M.G. Monaghan, Intracellular label-free detection of mesenchymal stem cell metabolism within a perivascular niche-on-a-chip, Lab on a Chip. 21(7) (2021) 1395-1408.
[41] A.J. Walsh, K.P. Mueller, K. Tweed, I. Jones, C.M. Walsh, N.J. Piscopo, N.M. Niemi, D.J. Pagliarini, K. Saha, M.C. Skala, Classification of T-cell activation via autofluorescence lifetime imaging, Nature Biomedical Engineering. 5(1) (2021) 77-88.
[42] A.V. Meleshina, V.V. Dudenkova, A.S. Bystrova, D.S. Kuznetsova, M.V. Shirmanova, E.V. Zagaynova, Two-photon FLIM of NAD(P)H and FAD in mesenchymal stem cells undergoing either osteogenic or chondrogenic differentiation, Stem Cell Res Ther. 8(1) (2017) 15.
[43] A.V. Meleshina, V.V. Dudenkova, M.V. Shirmanova, V.I. Shcheslavskiy, W. Becker, A.S. Bystrova, E.I. Cherkasova, E.V. Zagaynova, Probing metabolic states of differentiating stem cells using two-photon FLIM, Scientific Reports. 6(21853) (2016) 1-11.
[44] K. Konig, A. Uchugonova, E. Gorjup, Multiphoton fluorescence lifetime imaging of 3D-stem cell spheroids during differentiation, Microscopy Research Technology. 74(1) (2011) 9-17.
[45] G. Pattappa, H.K. Heywood, J.D. de Bruijn, D.A. Lee, The metabolism of human mesenchymal stem cells during proliferation and differentiation, J Cell Physiol. 226(10) (2011) 2562-70.
[46] J. Perez-Escuredo, R.K. Dadhich, S. Dhup, A. Cacace, V.F. Van Hee, C.J. De Saedeleer, M. Sboarina, F. Rodriguez, M.J. Fontenille, L. Brisson, P.E. Porporato, P. Sonveaux, Lactate promotes glutamine uptake and metabolism in oxidative cancer cells, Cell Cycle. 15(1) (2016) 72-83.
[47] M. Wahl, T. Rohlicke, H.J. Rahn, R. Erdmann, G. Kell, A. Ahlrichs, M. Kernbach, A.W. Schell, O. Benson, Integrated multichannel photon timing instrument with very short dead time and high throughput, Rev Sci Instrum. 84(4) (2013) 043102.
[48] A.M. Goodpaster, M.A. Kennedy, Quantification and statistical significance analysis of group separation in NMR-based metabonomics studies, Chemometrics and Intelligent Laboratory Systems. 109(2) (2011) 162-170.
[49] H. Puchtler, S.N. Meloan, M.S. Terry, On the history and mechanism of alizarin and alizarin red S stains for calcium, Journal of Histochemistry and Cytochemistry. 17(2) (1969) 110-124.
[50] O. Feron, Pyruvate into lactate and back: from the warburg effect to symbiotic energy fuel exchange in cancer cells, Radiotherapy and Oncology. 92(3) (2009) 329-333.
[51] L. Häggström, Energetics of glutaminolysis - a theoretical evaluation, Production of Biologicals from Animal Cells in Culture1991, pp. 79-81.
[52] G.A. Nagana Gowda, G.A. Barding, Jr., J. Dai, H. Gu, D.H. Margineantu, D.M. Hockenbery, D. Raftery, A metabolomics study of BPTES altered metabolism in human breast cancer cell lines, Frontiers in Molecular Biosciences. 5 (2018) 49-62.
[53] V. Miranda-Goncalves, S. Granja, O. Martinho, M. Honavar, M. Pojo, B.M. Costa, M.M. Pires, C. Pinheiro, M. Cordeiro, G. Bebiano, P. Costa, R.M. Reis, F. Baltazar, Hypoxia-mediated upregulation of MCT1 expression supports the glycolytic phenotype of glioblastomas, Oncotarget. 7(29) (2016) 46335-46353.
[54] K.J. McCullagh, R.C. Poole, A.P. Halestrap, M. O'Brien, A. Bonen, Role of the lactate transporter (MCT1) in skeletal muscles, American Journal of Physiology. 271(1) (1996) 143-150.

[55] T. Nakamura, A. Nakamura-Takahashi, M. Kasahara, A. Yamaguchi, T. Azuma, Tissue-nonspecific alkaline phosphatase promotes the osteogenic differentiation of osteoprogenitor cells, Biochemical and Biophysical Research Communications. 524(3) (2020) 702-709.
[56] N. Beheshtizadeh, Y. Asgari, N. Nasiri, A. Farzin, M. Ghorbani, N. Lotfibakhshaiesh, M. Azami, A network analysis of angiogenesis/osteogenesis-related growth factors in bone tissue engineering based on in-vitro and in-vivo data: A systems biology approach, Tissue Cell. 72 (2021) 101553.
[57] M.C. Skala, K.M. Riching, D.K. Bird, A. Gendron-Fitzpatrick, J. Eickhoff, K.W. Eliceiri, P.J. Keely, N. Ramanujam, In vivo multiphoton fluorescence lifetime imaging of protein-bound and free nicotinamide adenine dinucleotide in normal and precancerous epithelia, Journal of Biomedical Optics. 12(2) (2007) 024014-024024.
[58] M.G. Vander Heiden, L.C. Cantley, C.B. Thompson, Understanding the Warburg effect: the metabolic requirements of cell proliferation, Science. 324(5930) (2009) 1029-33.
[59] A. Varone, J. Xylas, K.P. Quinn, D. Pouli, G. Sridharan, M.E. McLaughlin-Drubin, C. Alonzo, K. Lee, K. Munger, I. Georgakoudi, Endogenous two-photon fluorescence imaging elucidates metabolic changes related to enhanced glycolysis and glutamine consumption in precancerous epithelial tissues, Cancer Res. 74(11) (2014) 3067-75.
[60] N. Neto, R.I. Dmitriev, M.G. Monaghan, Seeing Is Believing: Noninvasive Microscopic Imaging Modalities for Tissue Engineering and Regenerative Medicine, Cell Engineering and Regeneration, Springer, Cham2020, pp. 599-638.
[61] H. Wallrabe, Z. Svindrych, S.R. Alam, K.H. Siller, T. Wang, D. Kashatus, S. Hu, A. Periasamy, Segmented cell analyses to measure redox states of autofluorescent NAD(P)H, FAD & Trp in cancer cells by FLIM, Sci Rep. 8(1) (2018) 79.
[62] K. Schilling, E. Brown, X. Zhang, NAD(P)H autofluorescence lifetime imaging enables single cell analyses of cellular metabolism of osteoblasts in vitro and in vivo via two-photon microscopy, Bone. 154 (2022) 116257-116268.
[63] L. McInnes, J. Healy, N. Saul, L. Großberger, UMAP: uniform manifold approximation and projection, Journal of Open Source Software. 3(29) (2018).
[64] H. Brunengraber, C.R. Roe, Anaplerotic molecules: current and future, Journal of Inherited Metabolic Disease. 29(2-3) (2006) 327-331.
[65] S. Jitrapakdee, A. Vidal-Puig, J.C. Wallace, Anaplerotic roles of pyruvate carboxylase in mammalian tissues, Cellular and Molecular Life Sciences. 63(7-8) (2006) 843-854.
[66] W. Gu, X. Gaeta, A. Sahakyan, A.B. Chan, C.S. Hong, R. Kim, D. Braas, K. Plath, W.E. Lowry, H.R. Christofk, Glycolytic Metabolism Plays a Functional Role in Regulating Human Pluripotent Stem Cell State, Cell Stem Cell. 19(4) (2016) 476-490.
[67] M.B. Gayatri, N.N. Gajula, S. Chava, A.B.M. Reddy, High glutamine suppresses osteogenesis through mTORC1-mediated inhibition of the mTORC2/AKT-473/RUNX2 axis, Cell Death Discovery. 8(1) (2022) 277-289.
[68] J.S. Fernandez-Moure, B. Corradetti, P. Chan, J.L. Van Eps, T. Janecek, P. Rameshwar, B.K. Weiner, E. Tasciotti, Enhanced osteogenic potential of mesenchymal stem cells from cortical bone: a comparative analysis, Stem Cell Research Therapy. 6 (2015) 203-216.
[69] G. Friedl, H. Schmidt, I. Rehak, G. Kostner, K. Schauenstein, R. Windhager, Undifferentiated human mesenchymal stem cells (hMSCs) are highly sensitive to mechanical strain: transcriptionally controlled early osteo-chondrogenic response in vitro, Osteoarthritis Cartilage. 15(11) (2007) 1293-300.
[70] L. Wang, Z.-y. Li, Y.-p. Wang, Z.-h. Wu, B. Yu, Dynamic expression profiles of marker genes in osteogenic differentiation of Human bone marrow-derived mesenchymal stem cells, Chinese Medical Sciences Journal. 30(2) (2015) 108-113.
[71] C. Huang, M. Xue, H. Chen, J. Jiao, H.R. Herschman, R.J. O'Keefe, X. Zhang, The spatiotemporal role of COX-2 in osteogenic and chondrogenic differentiation of periosteum-derived mesenchymal progenitors in fracture repair, PloS One. 9(7) (2014) e100079.

[72] D.S. Yoon, J.H. Yoo, Y.H. Kim, S. Paik, C.D. Han, J.W. Lee, The effects of COX-2 inhibitor during osteogenic differentiation of bone marrow-derived human mesenchymal stem cells, Stem Cells Dev. 19(10) (2010) 1523-33.
[73] V.H. Villar, F. Merhi, M. Djavaheri-Mergny, R.V. Duran, Glutaminolysis and autophagy in cancer, Autophagy. 11(8) (2015) 1198-1208.
[74] Y. Ortiz-Pedraza, J.O. Munoz-Bello, L. Olmedo-Nieva, A. Contreras-Paredes, I. Martinez-Ramirez, E. Langley, M. Lizano, Non-Coding RNAs as key regulators of glutaminolysis in cancer, International Journal of Molecular Sciences. 21(8) (2020) 2872-2898.
[75] A.A. Starkov, An update on the role of mitochondrial alpha-ketoglutarate dehydrogenase in oxidative stress, Molecular and Cellular Neuroscience. 55 (2013) 13-16.
[76] J. Myllyharju, Prolyl 4-hydroxylases, the key enzymes of collagen biosynthesis, Matrix Biology. 22(1) (2003) 15-24.
[77] H.C. Blair, Q.C. Larrouture, Y. Li, H. Lin, D. Beer-Stoltz, L. Liu, R.S. Tuan, L.J. Robinson, P.H. Schlesinger, D.J. Nelson, Osteoblast differentiation and bone matrix formation in vivo and in vitro, Tissue Engineering Part B Reviews. 23(3) (2017) 268-280.
[78] Y.I. Rattigan, B.B. Patel, E. Ackerstaff, G. Sukenick, J.A. Koutcher, J.W. Glod, D. Banerjee, Lactate is a mediator of metabolic cooperation between stromal carcinoma associated fibroblasts and glycolytic tumor cells in the tumor microenvironment, Experimental Cell Research. 318(4) (2012) 326-335.
[79] C.J. Valvona, H.L. Fillmore, P.B. Nunn, G.J. Pilkington, The regulation and function of lactate dehydrogenase A: therapeutic potential in brain tumor, Brain Pathology. 26(1) (2016) 3-17.
[80] J. Liu, L. Gan, B. Ma, S. He, P. Wu, H. Li, J. Xiong, Alterations in chromatin accessibility during osteoblast and adipocyte differentiation in human mesenchymal stem cells, BMC Med Genomics. 15(1) (2022) 17.
[81] K. Jaager, S. Islam, P. Zajac, S. Linnarsson, T. Neuman, RNA-seq analysis reveals different dynamics of differentiation of human dermis- and adipose-derived stromal stem cells, PloS One. 7(6) (2012) e38833.
[82] H.L. Caslin, D. Abebayehu, J.A. Pinette, J.J. Ryan, Lactate is a metabolic mediator that shapes immune cell fate and function, Frontiers in Physiology. 12 (2021) 1-14.
[83] M.I. Gatie, T.T. Cooper, R. Khazaee, G.A. Lajoie, G.M. Kelly, Lactate enhances mouse es cell differentiation toward XEN cells in vitro, Stem Cells. 40(3) (2022) 239-259.

Chapter 5 - Non-Invasive classification of macrophage polarisation by 2P-FLIM and machine learning

The majority of the work in this chapter has been peer reviewed and published in: Neto G.B.N., O'Rourke S.A., Zhang M., Fitzgerald H.K., Dunne A. and Monaghan M.G. (2022). Non-Invasive classification of macrophage polarisation by 2P-FLIM and machine learning. eLife 11:e77373

5.1. Abstract

In this study, fluorescence lifetime imaging of NAD(P)H-based cellular autofluorescence is applied as a non-invasive modality to classify two contrasting states of human macrophages by proxy of their governing metabolic state. Macrophages were obtained from human blood-circulating monocytes, polarised using established treatments, and metabolically challenged using small molecules to validate their responding metabolic actions in extracellular acidification and oxygen consumption. Fluorescence lifetime imaging microscopy (FLIM) quantified variations in NAD(P)H-derived fluorescent lifetimes in large field-of-view images of individual polarised macrophages also challenged, in real-time with small molecule perturbations of metabolism during imaging. We uncover FLIM parameters that are pronounced under the action of carbonyl cyanide-p-trifluoromethoxyphenylhydrazone (FCCP) which strongly stratifies the phenotype of polarised human macrophages. This stratification and parameters emanating from a FLIM approach, served as the basis for machine learning models. Applying a random forest model, identified three strongly governing FLIM parameters, achieving a ROC AUC value of 0.944 when classifying human macrophages.

5.2. Introduction

Two-photon fluorescence lifetime imaging microscopy (2P-FLIM) is a non-destructive modality that can interrogate exogenous and endogenous fluorophores. 2P-FLIM provides high spatial and temporal resolution to image murine and human cell types, 2D and 3D cell cultures, and biopsies in vitro and in vivo [1-3]. 2P-FLIM allows reduced nicotinamide adenine dinucleotide (NAD(P)H) and flavin adenine dinucleotide (FAD^+) to be studied and quantified using 2P-FLIM, giving insight into cellular metabolism [2-4]. The average time for a fluorophore to return to the ground state from the excited state while emitting fluorescence is known as the fluorescence lifetime. NADH and NADPH fluorescence properties are identical, and hence NAD(P)H refers to these intracellular pools combined [5]. NAD(P)H is noted as having a long

fluorescence lifetime when enzyme-bound and a short fluorescence lifetime when free in the cytoplasm. NAD(P)H fluorescence properties offer extended information into NAD(P)H protein/enzyme binding [4]. 2P-FLIM facilitates quantification of NAD(P)H fluorescence lifetimes and its respective proportions. In addition, 2P-FLIM can be used as microscopy-based spatial approach and applied to limited cell numbers, which is beneficial in assessing limited sample numbers or validating metabolism-based therapies [6, 7].

Macrophages are essential components of the host immune response and key regulators of homeostatic function. In addition to host defence, macrophages are intimately involved in tissue homeostasis and play a key role in pathologies including heart failure, diabetes and cancer [8]. Macrophages adopt specific polarisation states, ranging in a spectrum, to accomplish various functions and mechanisms of action. Here, classically activated (M1) and alternatively activated (M2) macrophages occupy opposite ends [8, 9]. In vitro, M1-macrophage behaviour can be evoked using IFNγ and/or microbial products such as LPS. M1-macrophage phenotype is defined by secretion of significant amount of pro-inflammatory cytokines; TNFα and IL-1β, enhanced endocytosis and ability to kill intracellular pathogens. [10, 11].

M2-macrophage behaviour exists more heterogeneously and can be triggered by IL-4 or IL-13, IL1-β, TGF-β, IL-6, phagocytosis of apoptotic cells or association with a tumour microenvironment, respectively generating M2a, M2b, M2c, M2f and tumour-associated (TAM) macrophages. [12-14]. M2 macrophages exhibit decreased expression of protein membrane markers, such as CD14 and CCR5, and increased fibronectin-1 production. In addition, M2 macrophages are also characterised by downregulation of pro-inflammatory cytokines [11, 15, 16]. Most often, macrophage behaviour is assessed by end-point assays using cytokine measurements, gene analysis and staining of surface markers. However, there is a gathering shift towards non-invasive modalities to speed up this process and obtain spatio-temporal analysis. Two recent examples of this include the use of raman microscopy to map the lipidomic

spatial signature of polarised macrophages [17], and the use of average fluorescent lifetime parameters to discern murine macrophage phenotype [18].

We use an imaging-based approach, primarily focusing on metabolic machinery characteristically employed by polarised human macrophages. Macrophage metabolism poses a huge potential in the next generation of therapeutics for inflammatory disease. Human macrophage function and metabolism are inextricably linked [19]. IFNγ activated human macrophages (IFNγ-M1) are primed for enhanced inflammatory responses by stabilising HIF1α levels, activation of the JAK-STAT pathway, and increased production of IL-1β, all of which are dependent on enhanced levels of glycolysis [20]. Alternatively activated human anti-inflammatory macrophages, most often observed in vitro through stimulation with IL-4 (IL-4-M2), are defined by an intact tricarboxylic acid cycle (TCA), enhanced OxPhos, increased fatty acid synthesis (FAS), and fatty acid oxidation (FAO) [19, 21]. In a nutshell, IFNγ-M1 macrophages are more active in glycolysis, while IL-4-M2 macrophages are more dependent on oxidative phosphorylation for their energy production. When assessing metabolism and bioenergetics, most methods are based on extracellular flux assays, measurement of cellular oxygen consumption, exogenous staining, radio-labelling nutrients and gas chromatography – mass spectrometry (GC-MS). Metabolism probing methods require a substantial amount of sample processing yet still pose limitations due to short lived oxidative metabolites [22-25].

2P-FLIM imaging of NAD(P)H acquires five fluorescence lifetime variables (τ_1, τ_2, α_1, α_2, τ_{avg}) and one fluorescence intensity-based variable (ORR) descriptive of the polarisation linked-metabolic state of IFNγ-M1 and IL-4-M2 macrophage phenotypes. Furthermore, additional information can be obtained from these measurements by real-time perturbation of basal metabolism and metabolic capacity. To achieve this, sequential knockdown of intercellular pathways and uncomplexing of mitochondrial coupling is performed via metabolic inhibitors.

For data visualisation purposes, we applied the Uniform Manifold Approximate and Projection (UMAP) technique, instead of principal component analysis (PCA), due to its processing speed, capability to preserve the global and local structures of the data, and ability to use non-metric distance functions [26]. For in-depth statistical analysis, machine learning algorithms are employed for classification/supervised pattern recognition. Machine learning algorithms have been used to characterise DNA- and RNA-binding proteins, determine genetic and epigenetic contributions of antibody repertoire diversity, and to classify chronic periodontitis patients based on their immune cell response to ex-vivo stimulation with ligands [27-29]. In addition, machine learning algorithms can be used to group samples into different classes (for example, in this study, IFNγ-M1 vs IL-4-M2, based on 2P-FLIM variables) whilst determining which variables are the most important for this task [30]. For our work, we employed the random forests algorithm for the classification task due to random forests high prediction accuracy, robustness to outliers, and possibility to obtain the relative importance of each variable [31, 32].

Another advantage of the random forests model is that we can use the OOB (out-of-bag) error estimate to determine the values of the hyper-parameters. OOB error makes random forests especially suitable for small datasets, where we do not have additional data for validating the model. The hyper-parameters of the random forests model are the number of trees (*ntree*) and number of variables selected for the best split at each node (*mtry*). The OOB error of the final optimal random forests model serves as the estimate of the model's prediction error.

The trained random forests model can be used to distinguish between the different populations of macrophages and to measure which 2P-FLIM variables are the most important for this differentiation. In our study, we used all data points obtained from both full field-of-view (FoV) and donor-specific single cell images for training and validating the random forests

model. Thus, there is no extra data available for testing our trained model. Therefore, to demonstrate the predictive ability and efficiency of the trained model, we calculated the area under the receiver operating characteristics curve (ROC-AUC), in which the specificity and sensitivity of the trained model are plotted. The ROC curve is an evaluation metric for binary classification problems. ROC curves plot the true positive rate against false positive rate at various threshold values. The AUC is the measure of the ability of a classifier to distinguish between classes and is used as a summary of the ROC curve. An ROC-AUC value smaller than 0.5 suggests no discrimination, 0.7 to 0.8 is considered acceptable, 0.8 to 0.9 is considered excellent, and more than 0.9 is considered outstanding [33]. Similar applications of machine learning methods have been explored by Walsh et al., for classification of activated t-cells and Qian et al., for quality control of cardiomyocyte differentiation [34, 35].

We hypothesise that 2P-FLIM of NAD(P)H and FAD^+ provides quantitative information to evaluate and identify human-derived macrophage polarisation by proxy of their metabolism. 2P-FLIM of NAD(P)H and FAD^+ has strong clinical potential fuelled by the emergence of metabolic approaches to treat disease and inflammation. To test our hypothesis, we derived human macrophages from blood-circulating monocytes and polarised them into IFNγ-M1 or IL-4-M2 macrophages. We confirmed human macrophage cytokine and gene expression-related polarisation, while human macrophage metabolic behaviour was assessed via traditional extracellular flux assays. Finally, 2P-FLIM was applied during which real-time responses of photonic variables to metabolism-challenging small molecules were measured. This study establishes 2P-FLIM as a method to discriminate IFNγ-M1 and IL-4-M2 macrophages, which is most pronounced by macrophages differential responses when treated with FCCP. This allows the accurate classification of macrophage polarisation using machine learning methods, e.g., the random forests model, and to evaluate single-cell heterogeneity. Our work reports, for the first time, the classification of human macrophages by random forests using data obtained from real-time metabolic perturbations triggered during 2P-FLIM.

5.3. Materials and methods

5.3.1. Human blood monocyte-derived macrophage isolation

This study was approved by the research ethics committee of the School of Biochemistry and Immunology, Trinity College Dublin and was conducted in accordance with the Declaration of Helsinki. Leucocyte-enriched buffy coats from anonymous healthy donors were obtained with permission from the Irish Blood Transfusion Board (IBTS), St. James's Hospital, Dublin. Donors provided informed written consent to the IBTS for their blood to be used for research purposes. PBMC were isolated and differentiated into macrophages as described previously [36]. The purity of $CD14^{+}CD11b^{+}$ macrophages was assessed by flow cytometry and was routinely >95% (Figure Appendix 11).

5.3.2. Cytokine measurements

Macrophages (1 x 10^6 cells/ml) were treated with IFNγ (20 ng/ml) or IL-4 (20 ng/ml) for 24 hours. Supernatants were harvested, and cytokine concentrations of TNFα and IL-10 were quantified by ELISA (eBioscience) according to the manufacturer's protocol.

5.3.3. Real-time PCR

Macrophages (1 x 10^6 cells/ml) were treated with IFNγ (20 ng/ml) or IL-4 (20 ng/ml) for 24 hours. RNA was extracted using High-Pure RNA Isolation Kits (Roche) and assessed for concentration and purity using the NanoDrop 2000c – UV- Vis spectrophotometer. RNA was equalised and reverse transcribed using the Applied Biosystems High-Capacity cDNA reverse transcription kit. Real-Time PCR Detection System (Bio-Rad Laboratories, California) was used to detect mRNA expression of target genes. PCR reactions included iTaq Universal SYBR Green Supermix (Bio-rad Laboratories), cDNA Taqman fast universal PCR Master Mix and pre-designed TaqMan gene expression probes (Applied Biosystems) for CXCL9, CXCL10, MRC1, CCL13, and the

housekeeping gene, 18S ribosomal RNA. The $2^{-\Delta\Delta CT}$ method was used to analyse relative gene expression.

5.3.4. Seahorse analyser

Macrophages were cultured at 1 x 10^6 cells/ml for six days prior to re-seeding at 2 x 10^5 cells/well in a Seahorse 96-well microplate and allowed to rest for five hours prior to stimulation with IFNγ (20 ng/ml) and IL-4 (20 ng/ml) for 24 hours. The Seahorse cartridge plate was hydrated with XF calibrant fluid and incubated in a non-CO_2 incubator at 37°C for a minimum of eight hours prior to use. Thirty minutes prior to placement into the Seahorse XF/XFe analyser, cell culture medium was replaced with complete XF assay medium (Seahorse Biosciences, supplemented with 10 mM glucose, 1 mM sodium pyruvate, 2 mM L-glutamine, and pH adjusted to 7.4) and incubated in a non-CO_2 incubator at 37°C. Blank wells (XF assay medium only) were prepared without cells for subtracting the background oxygen consumption rate (OCR) and extracellular acidification rate (ECAR) during analysis. Oligomycin (1 mM, Cayman Chemicals), carbonyl cyanide-p-trifluoromethoxyphenylhydrazone (FCCP) (1 mM, Santa Cruz biotechnology), rotenone (Rot) (500 nM), and antimycin A (AA) (500 nM) and 2-deoxy-D-glucose (2-DG) (25 mM, all Sigma-Aldrich) were prepared in XF assay medium and loaded into the appropriate injection ports on the cartridge plate and incubated for ten minutes in a non-CO_2 incubator at 37°C. OCR and ECAR were measured over time with sequential injections of oligomycin, FCCP, rotenone and antimycin A and 2-DG. Analysis of results was performed using Wave software (Agilent Technologies). The rates of basal glycolysis, maximal glycolysis, basal respiration and maximal respiration were calculated as detailed in the manufacturer's protocol and supplied in Table 5.1.

Table 5.1 - Calculation of basal glysolysis, max glycolycic, basal respiration, max rate

Rate	Calculation
Basal	Average ECAR values prior to oligomycin treatment – non-
Max	Average ECAR values after oligomycin and before FCCP
Basal	Average OCR values prior to oligomycin treatment –
Max	Average OCR values after FCCP and before

ECAR- extracellular acidification rate; OCR- oxygen consumption rate; FCCP- carbonyl cyanide-p-

5.3.5. Two-photon fluorescence lifetime imaging microscopy (2P-FLIM)

2P-FLIM was performed on 24 hours-polarised macrophages seeded in *ibidi®* Luer µ-slides with a 0.8 mm channel height. 2P-FLIM was achieved using a custom upright (Olympus BX61WI) laser multiphoton microscopy system equipped with a pulsed (80 MHz) titanium:sapphire laser (Chameleon Ultra, Coherent®, USA), water-immersion 25× objective (Olympus, 1.05NA) and temperature-controlled stage at 37 °C. Two photon excitation of NAD(P)H and FAD^+ fluorescence was performed at the excitation wavelength of 760 and 800 nm, respectively. Several studies have reported that two-photon excitation in the range of 720-760nm can be used to selectively excite NAD(P)H, while for FAD^+ a excitation wavelength above 900nm is commonly used [5, 37].A 458/64 nm and 520/35 nm bandpass filter were used to isolate the NAD(P)H and FAD^+ fluorescence emissions based on their emission spectra[5].

512 × 512 pixel images were acquired with a pixel dwell time of 3.81 µs and 30 s collection time. A PicoHarp 300 TCSPC system operating in the time-tagged mode coupled with a photomultiplier detector assembly (PMA) hybrid detector (PicoQuanT GmbH, Germany) was used for fluorescence decay measurements, yielding 256 time bins per pixel. TCSPC requires a defined “start”, provided by the electronics steering the laser pulse or a photodiode, and a defined “stop” signal, realized by detection with single-photon sensitive detectors. The measuring of this time delay is repeated many times to account for the statistical variance of

the fluorophore's emission. For more detailed information, the reader is referred elsewhere [38].

Fluorescence lifetime images with their associated decay curves for NAD(P)H were obtained with a minimum of $1x10^6$ photons peak. After imaging, the background noise was removed. This was performed by defining regions of interest (ROI) of the cells on the 2P-FLIM image. Consequently, lower values of photons/pixel are removed from analysis improving the signal-to-noise ratio (Figure Appendix 12).

The decay curved was generated and fitted with a double-exponential decay without including the instrument response function (IRF) (

Equation 5.1)

$$I(t) = I(0)[\alpha_1 e^{\frac{-t}{\tau_1}} + \alpha_2 e^{\frac{-t}{\tau_2}}] + C$$

Equation 5.1 - Fluorescence Intensity decay fitted with a double-exponential decay curve

I(t) represents the fluorescence intensity measured at time t after laser excitation; α_1 and α_2 represent the fraction of the overall signal proportion of a short and long component lifetime, respectively. τ_1 and τ_2 are the long and short lifetime components, respectively; C corresponds to background light. Chi-square statistical test was used to evaluate the goodness of multi-exponential fit to the raw fluorescence decay data. In this study, all of the fluorescence lifetime fitting values with $\chi^2 < 1.3$ were considered as 'good' fits. For NAD(P)H, the double exponential decay was used to differentiate between the protein-bound (τ_1) and free (τ_2) NAD(P)H. The average fluorescence lifetime was calculated using Equation 5.2

$$\tau_{avg} = \frac{(\tau_1 \times \alpha_1 + \tau_2 \times \alpha_2)}{(\alpha_1 + \alpha_2)}$$

Equation 5.2 - Average fluorescence lifetime calculation

Intensity-based images of NAD(P)H and FAD^+ were acquired, and their ratio was calculated using Equation 5.3 to obtain the optical redox ratio (ORR).

$$ORR = \frac{FAD^+}{NAD(P)H}$$

Equation 5.3 - Optical redox ratio calculation

From the images acquired using 2P-FLIM, single-cell - analysis was performed using a custom-made script on Cell Profiler® [39]. The single-cell analysis was conducted in a similar way as the global 2P-FLIM analysis.

5.3.6. Macrophage classification and machine learning

Uniform Manifold Approximate and Projection (UMAP) was used for data visualisation, in order to determine the clustering of 2P-FLIM imaging datasets in global- and single-cell analysis[26]. UMAP was implemented in Python, and the plots obtained in Graphpad. Random forests were applied to classify IFNγ-M1 and IL-4-M2 macrophages in both full FoV and single-cell donor-specific approaches. Random forests classification was implemented in R. Random forests hyperparameters include the number of decision trees in the forests, the number of features considered by each tree when splitting a node, and the maximal depth of each tree; the best hyperparameters were determined through grid search with the highest accuracy and by determining the lowest OBB error rates (Table 4, 5). α_1 variable was removed from the random forests model due to its deterministic relationship with α_2 variable (Figure Appendix 13). Receiver-operating curves (ROC) were plotted, and areas under the curves (AUC) values were calculated without the employment of a testing dataset. In addition, random forests feature selection was utilised to evaluate the weight of each 2P-FLIM variable to determine its relative importance in macrophage classification for both overall and single cell datasets.

Support vector machine (SVM) and logistic regression models were compared with random forests model and yielded similar performance on the experimental data split to 80% training and 20% testing

5.3.7. Statistics

Each experiment was performed in at least four healthy donors (defined by N) with 3-4 technical replicates run for each experiment (defined by n), depending on the assay type. Normality tests were performed to determine the normal distribution of the data. For ELISA and PCR data, one-way ANOVA and Tukey's test were used for comparing more than two groups. For Seahorse data, repeated-measures one way ANOVA was used to account for the variance in basal metabolism across donors. All statistical analysis was performed on GraphPad Prism™ 9.00 (GraphPad Software).

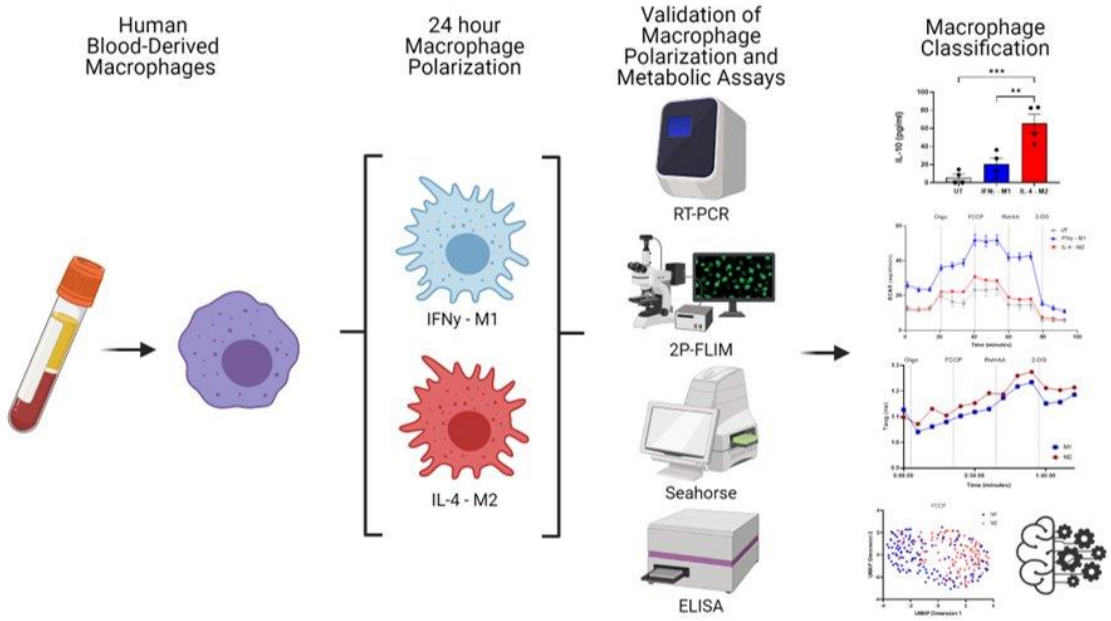

Figure 5.1 - Overview of experimental work. Image created using biorender.com

5.4. Results

5.4.1. Macrophage polarisation with IFNγ and IL-4 induces metabolic reprograming

Human blood-derived macrophages were polarised by incubating in cell culture media containing IFNγ (M1) or IL-4 (M2) for 24 hours. Polarisation was confirmed using ELISA and RT-PCR. Cellular metabolic activity was analysed using a sequence of metabolic enzyme inhibitors, and the inhibitors effect was measured by extracellular acidification ratio (ECAR), oxygen consumption ratio (OCR) and 2P-FLIM (Figure 5.1).

A slightly higher amount of TNFα production was obtained for IFNγ-M1 when compared with IL-4-M2 macrophages. Regarding IL-10, a statistically higher production was measured in IL-4-M2 when compared with IFNγ-M1 and untreated macrophages (Figure 5.2A, D). For gene expression, a higher amount of CXCL9 and a statistically significant increase in CXCL10 in IFNγ-M1 macrophages were observed (Figure 5.2B, C). In addition, MRC1 and CCL13 were further expressed in IL-4-M2 macrophages when compared with untreated and IFNγ – M1 macrophages

(Figure 5.2, F). IFNγ-M1 macrophages have a higher dependence on aerobic glycolysis, whilst IL-4-M2 macrophages are more reliant on oxidative phosphorylation.

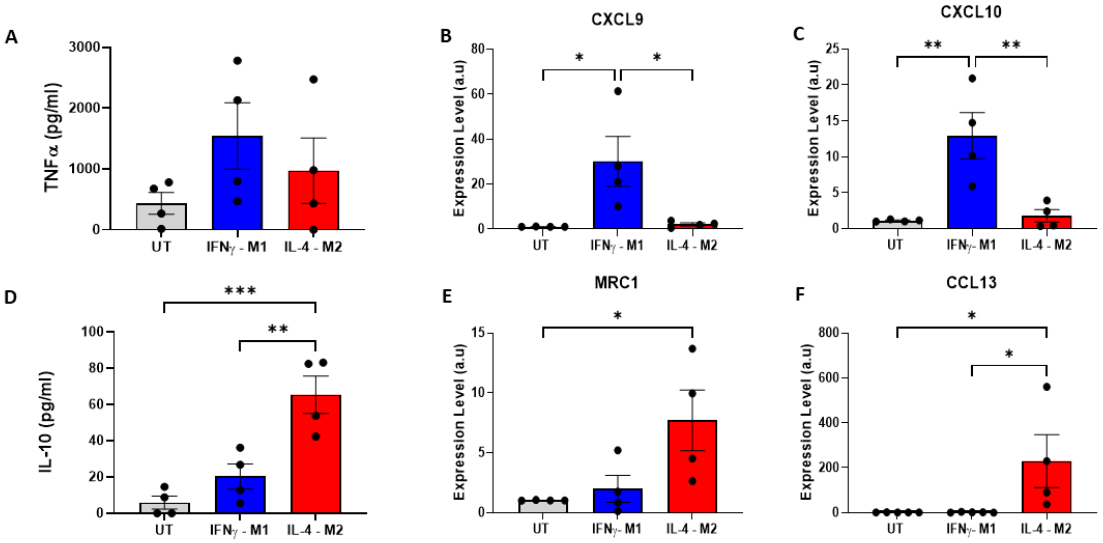

Figure 5.2 - Validation of macrophage polarisation of IFNγ-M1, IL-4-M2, and untreated (UT) macrophages. (A,B) ELISA of inflammatory cytokine TNFα and anti-inflammatory IL-10 in IFNγ-M1, IL-4-M2, and untreated (UT) macrophages. (C,D,E,F) Evaluation of CXCL9, MRC1, CXCL10, and CCL13 gene expression in IFNγ-M1, IL-4-M2, and untreated (UT) macrophages. *p<0.05, **p<0.01, ***p<0.001, N= 6 donors.

We used extracellular acidification (ECAR) and oxygen consumption ratios (OCR) to certify this metabolic behaviour which is linked to macrophage polarisation. For ECAR and OCR, we used four different metabolic modulators in succession: oligomycin, FCCP, Rot+AA and 2-DG, to evaluate cellular metabolism (Figure 5.3). IFNγ-M1 macrophages exhibited a higher ECAR and lower OCR in response to the treatments added, whilst IL-4-M2 and untreated macrophages had lower ECAR and higher OCR (Figure 5.3 A,D). After plotting ECAR and OCR curves, the areas under the curves (AUC) were measured to reflect basal glycolysis, maximal glycolysis, basal respiration and maximal respiration.

IFNγ-M1 macrophages have a statistically significant increase of basal and max glycolysis when compared with untreated macrophages (Figure 5.3 B,C). In addition, all

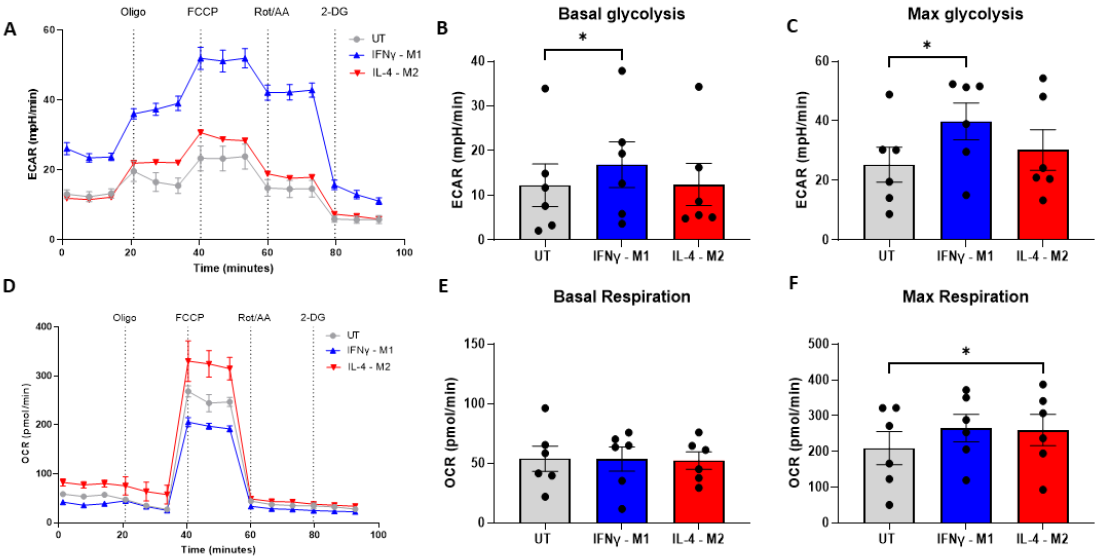

Figure 5.3 – Macrophage metabolic profiling of IFNγ-M1, IL-4-M2, and untreated (UT) macrophages. (A,D) Extracellular acidification ratio (ECAR) and Oxygen consumption ratio (OCR) profile of IFNγ-M1, IL-4-M2, and untreated (UT) macrophages when treated sequentially with oligomycin, FCCP, rotenone + antimycin A and 2-DG. (B,C,E,F) Area under the curve (AUC) values calculated from ECAR and OCR between each treatment. *p<0.05, **p<0.01, ***p<0.001, N= 6 donors.

macrophage types have similar basal respiration, whilst IL-4-M2 macrophages have a statistically significant increase in max respiration when compared with untreated macrophages (Figure 5.3E, F).

5.4.2. 2P-FLIM captures metabolic shifts on IFNγ and IL-4 treated macrophages

2P-FLIM harvests NAD(P)H and FAD^+ autofluorescence to infer cellular metabolism. NAD(P)H enzyme-bound state is characterised by a longer fluorescence lifetime, whilst NAD(P)H free-state has a shorter fluorescence lifetime. NAD(P)H and FAD^+ fluorescence intensity is measured in order to calculate the ORR (Equation 4). These fluorescence features enable the distinction between an OxPhos or glycolytic-dependent metabolism [1, 2, 34, 40-43].

For this experiment, we seeded unpolarised macrophages in *ibidi®* Luer µ-slides in static conditions, and polarised the macrophages using IFNγ or IL-4 for 24 hours. These macrophages are derived from the same donors as per those presented in Figure 5.2, Figure 5.3. Afterwards, we followed the same subjection of metabolic enzymatic inhibitors applied in the ECAR/OCR experiment in which we treated the macrophages with oligomycin, FCCP, Rot+AA and 2-DG. During the time-course of the experiments the field of view was maintained so as to record single-cell metabolic variations (Figure Appendix 14, Figure Appendix 15).

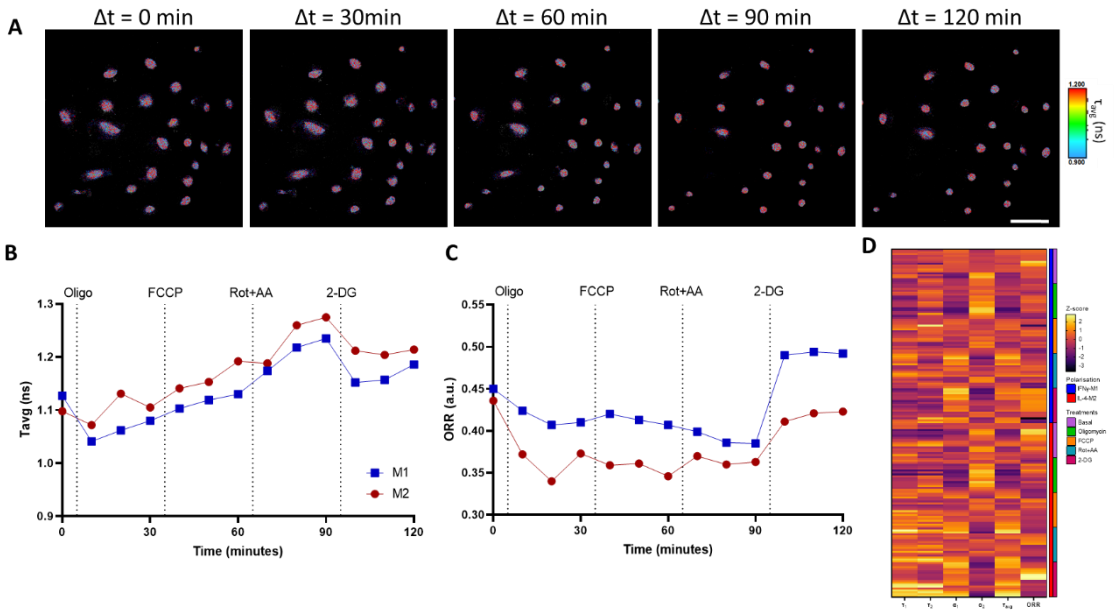

Figure 5.4 - 2P-FLIM Metabolimaging analysis. (A) Time-course imaging of representative (same field of view throughout) IFNγ-M1 macrophages, scale bar:100µm (B,C) Average fluorescence lifetime (τ_{avg}) and optical redox ratio (ORR) values for IFNγ-M1 and IL-4-M2 when treated sequentially with oligomycin, FCCP, rotenone + antimycin A and 2-DG of a representative donor. (D) z-score heatmap of 2P-FLIM acquired data for 6 donors separated by macrophage polarisation and metabolic inhibitor, each individual row corresponds to an imaging field.

We derived the average fluorescence lifetime (τ_{avg}) and optical redox ratio (ORR) of IFNγ-M1 and IL-4-M2 macrophages from the full FoV of 2P-FLIM data and observed an increasing trend of τ_{avg} in response to the application metabolic enzymatic inhibitors. With the exception of 2-DG, in which a decrease of τ_{avg} was observed for both macrophage phenotypes (Figure 5.4B). Regarding ORR, there is a slight decreasing trend of ORR, followed by a raise in ORR with the 2-DG treatment for IFNγ-M1 macrophages. For IL-4-M2 macrophages, there is a decrease in ORR with the oligomycin treatment, followed by stabilisation with FCCP and Rot+AA, and finally an increase elicited by 2-DG (Figure 5.4C). We compiled all the full FoV 2P-FLIM variables: τ_1, τ_2, α_1, α_2, τ_{avg} and ORR into a representative z-score heatmap, stratified according to macrophage

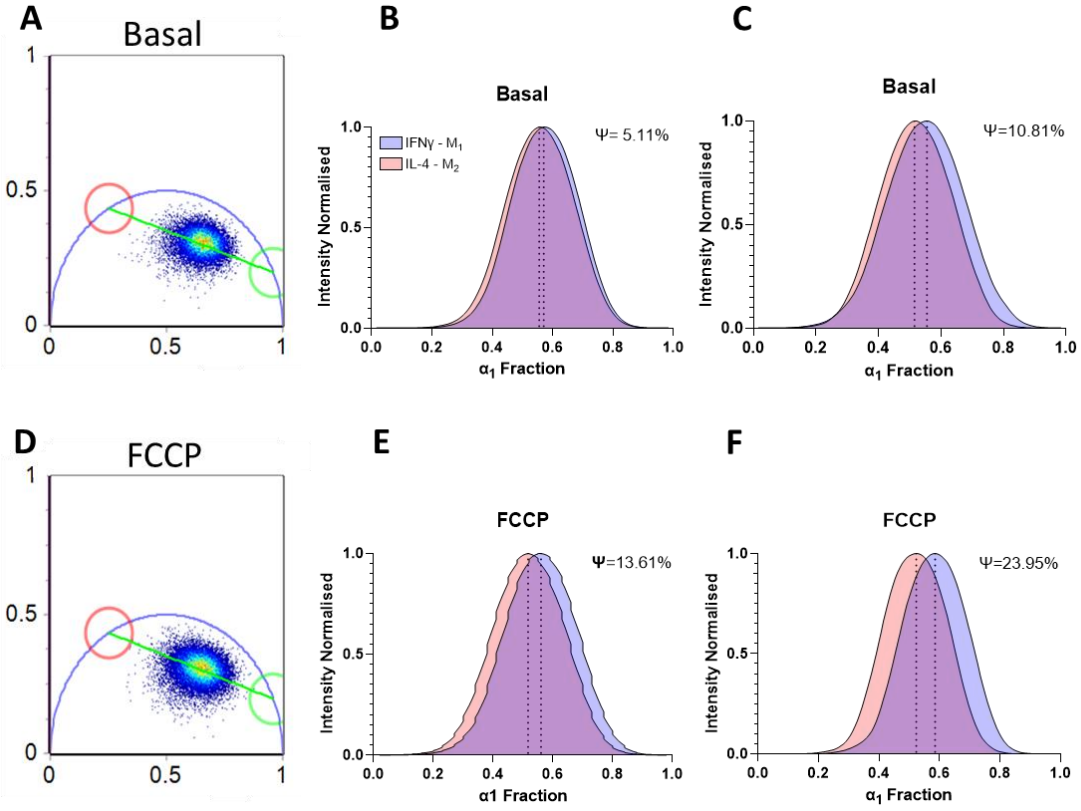

Figure 5.5 – Phasor Analysis of NADH FLIM variables in Basal and FCCP conditions. A) Basal Phasor with values set at 3.4 ns (red) and 0.4 ns (green) and all donors basal FLIM data distribution , B) Histogram of all donors normalised to pixel intensity in basal conditions, C) Histogram distribution of a representative donor normalised to pixel intensity in basal conditions, D) FCCP Phasor with values set at 3.4 ns (red) and 0.4 ns (green) and all donors FCCP FLIM data distribution, E) Histogram of all donors (N=6) normalised to pixel intensity in FCCP conditions and F) Histogram distribution of a representative donor normalised to pixel intensity in FCCP conditions. Ψ value is the non-overlapped area for both curves in each plot when compared with the total area occupied by both curves. A higher Ψ value determines a better segregation between data sets.

type and metabolic inhibitors across all donors. IFNγ-M1 macrophages have lower τ_1, τ_2, τ_{avg} and ORR values when compared with IL-4-M2 macrophages (Figure 5.3D).

Phasor analysis was applied to the raw FLIM data (Figure 5.5). Here, we plotted the phasor maps while fixing the lifetimes at 3.4 ns and 0.4 ns as indicated in literature [44]. Furthermore, we generated histogram plots that showcase the distribution of the data in the phasor plot as well as the difference between IFNγ-M1 and IL-4-M2 macrophages (Figure 5.5). Phasor analysis of 2P-FLIM data determined a higher segregation between FCCP treated IFNγ-M1 macrophages and IL-4-M2 macrophages compared with basal IFNγ-M1 macrophages and IL-4-M2 macrophages distributions of fluorescence lifetimes. During this measure, percentage of separation, Ψ, between both distribution lifetimes was calculated. Ψ values show that FCPP treatment promote an increase of 13% in the separation of IFNγ-M1 macrophages and IL-4-M2 macrophages fluorescence lifetime distributions.

5.4.3. 2P-FLIM variables allow the classification of IFNγ-M1 and IL-4-M2 macrophages

Uniform Manifold Approximate and Projection (UMAP) was applied to full FoV 2P-FLIM variables associated with IFNγ-M1 and IL-4-M2 macrophages as a data visualisation tool. The coordinates for each image were defined using a cosine distance function computed using the 2P-FLIM variables: τ_{avg}, τ_1, τ_2, α_1, α_2 and ORR (Figure 5.6A). UMAP representation of 2P-FLIM variables acquired during FCCP treatment provides a separation between IFNγ-M1 and IL-4-M2 macrophages (Figure 5.6B).

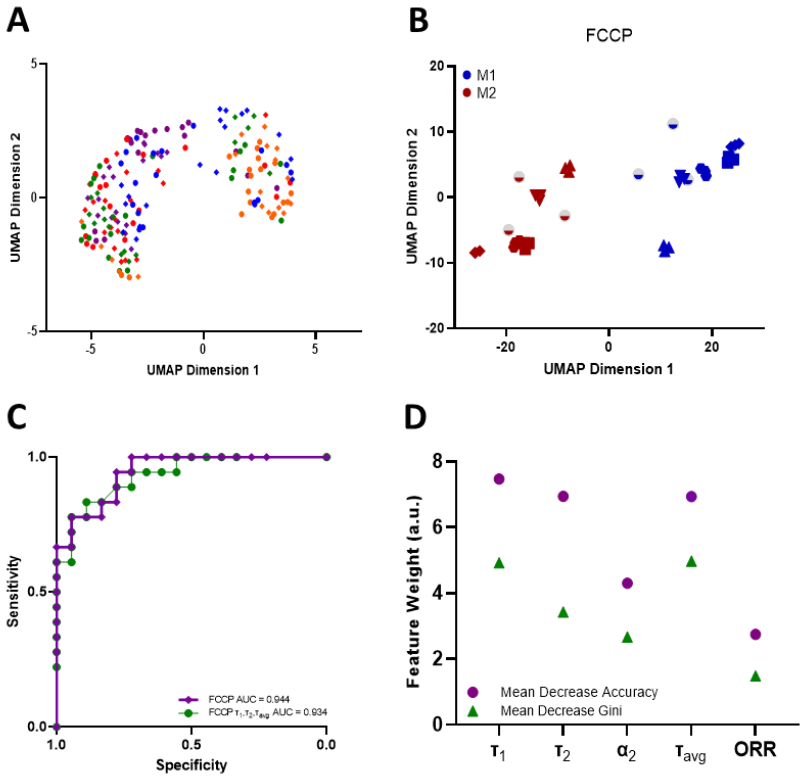

Figure 5.6 – UMAP and Machine learning analysis of 2P-FLIM data. (A) UMAP plot of 2P-FLIM variables after each treatment each dot corresponds to an individual imaging field. (B) UMAP plot of 2P-FLIM variables after FCCP treatment, each dot corresponds to an individual imaging field. (C) Receiver-operator curve and area under curve values of random forests machine learning model applied to 2P-FLIM data after FCCP treatment. (D) 2P-FLIM weight features determined by mean decrease accuracy and mean decrease Gini of random forests model used to classify macrophages.

Random forests classification models were established to classify macrophage polarisation from 2P-FLIM variables when treated with FCCP (Table 5.2). To adequately train the random forests model, we removed α_1 2P-FLIM variable as it exhibit a negative correlation with α_2 variable (Figure Appendix 13). Receiver operator characteristic (ROC) curves of our dataset reveal high accuracy for predicting macrophage polarisation in the full field of view during FCCP (AUC=0.944), when using 2P-FLIM variables as predictors (Figure 5.6C). When using τ_1, τ_2 and τ_{avg}, as the only 2P-FLIM variables in the same trained random forests a high prediction accuracy was still achieved (AUC=0.934) (Figure 5.6C). Next, the mean decrease accuracy and mean decrease Gini returned by the random forests model reveal that τ_1, τ_2 and τ_{avg} are the most important 2P-FLIM variables for macrophage classification and data segregation (Figure 5.6D).

Table 5.2 – Hyper-parameters, OBB, ROC-AUC and confusion matrix of full FoV random forests model.

Donor (No. of data	ntree	mtry	OOB	ROC-AUC	TP	FP	FN	TN
All Donors – Full FoV (36)	100	2	16.67	0.944	16	2	4	14

ntree –number of trees; mtry- number of variables selected for the best split at each node; OBB- out-of-bag error; ROC-AUC – area under receiver operating characteristics curve; TP – true positive; FP – false positive; FN – false negative; TN – true negative

PCA and t-SNE analysis were applied to full FoV 2P-FLIM variables associated with IFNγ-M1 and IL-4-M2 macrophages as complementary data visualisation tools (Figure 5.7). PCA analysis, when focusing only on FCCP treatments showed a segregation between IFNγ-M1 and IL-4-M2 macrophages, however there is a slight overlap of the confidence ellipses (Figure 5.7 C). t-SNE analysis, did not revealed any segregation between IFNγ-M1 and IL-4-M2 macrophages 2P-FLIm variables profile (Figure 5.7 D).

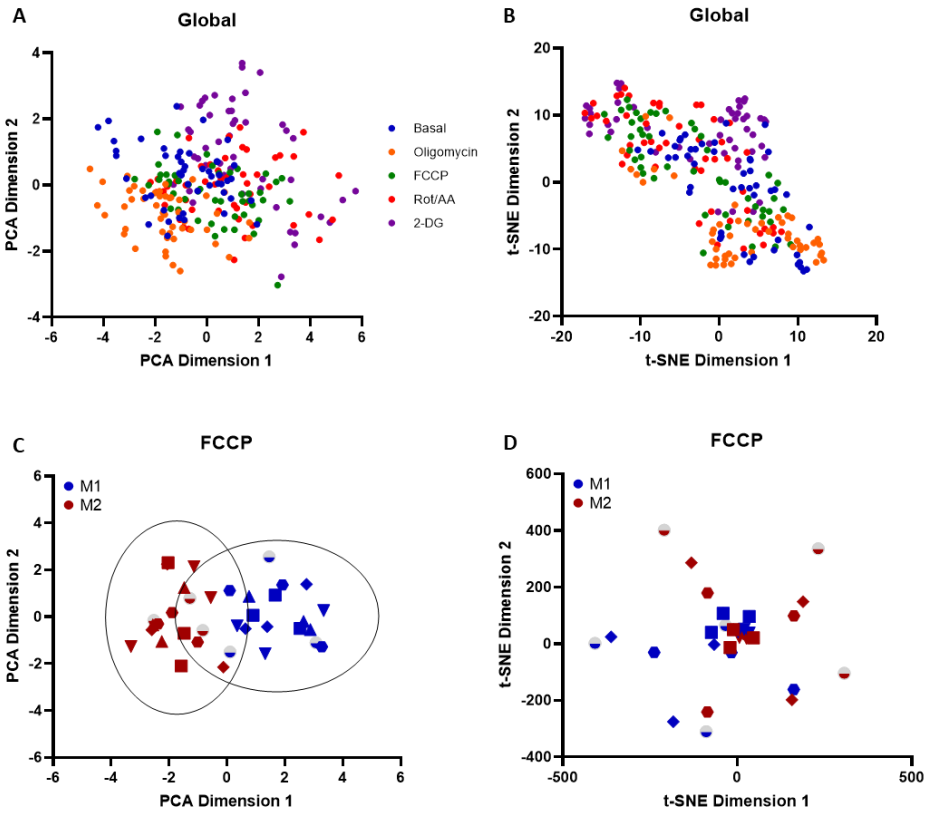

Figure 5.7 – PCA and t-SNE data visualization of 2P-FLIM variables obtained from full FoV collected during the course of metabolic treatments (A, B). PCA data visualization of 2P-FLIM variables obtained from full FoV collected during FCCP treatments and representation of 99.9% confidence ellipses derived from 3 standard deviations of the data presented for each group of samples (C). t-SNE data visualization of 2P-FLIM variables obtained from full FoV collected during FCCP treatments (D)

5.4.4. 2P-FLIM classification models are sensitive to cell heterogeneity

Macrophage polarisation heterogeneity at a single-cell level was evaluated within each donor in response to the FCCP treatment (Figure 5.8). Here, we utilised Cell Profiler® to evaluate and track single-cell metabolic shifts (Figure 5.8A). A representative donor UMAP reveals two clusters, one majorly occupied by IFNγ-M1 macrophages and the other occupied by IL-4-M2 macrophages (Figure 5.8B).

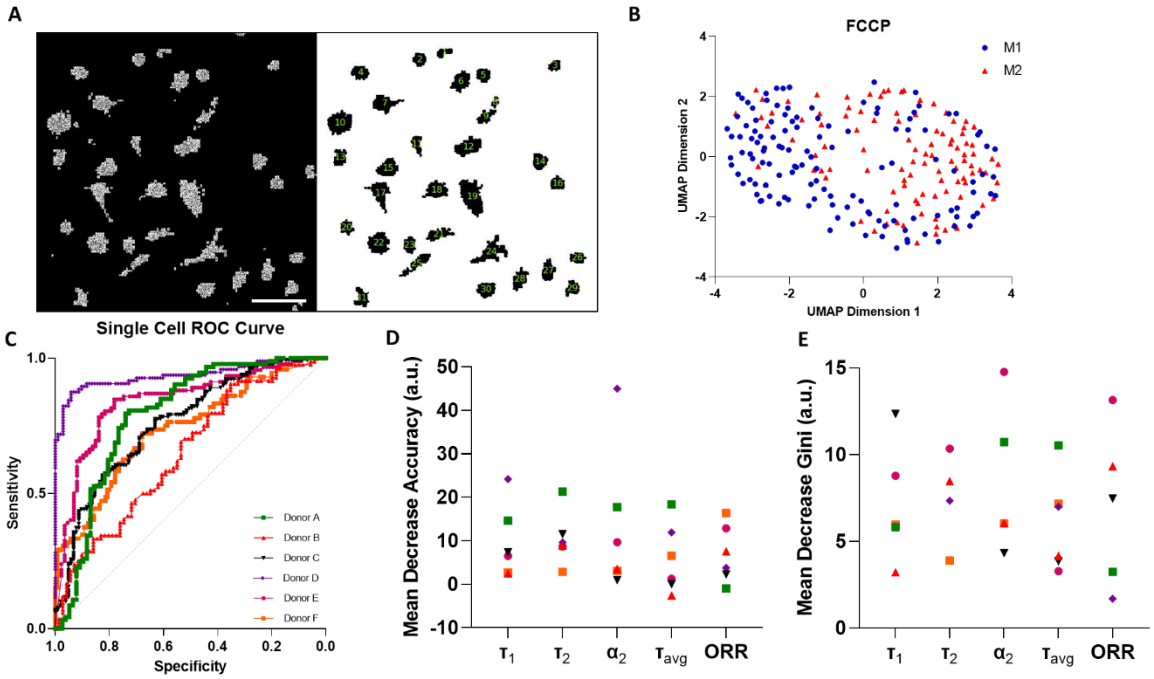

Figure 5.8 - Single-cell 2P-FLIM imaging analysis. (A) Single-cell analysis using a custom-built Cell Profiler® script, scale bar=100µm. (B) Single-cell UMAP clustering of a representative donor after FCCP treatment using 2P-FLIM variables. (C) Receiver-operating curves (ROC) of random forests model for classification of macrophages of all human donors used in this study. (D) Mean decrease in accuracy and (E) mean decrease in Gini of each 2P-FLIM variable returned by the random forests model.

Afterwards, we established new random forests models trained with single-donor 2P-FLIM variables. The new random forests models were trained using τ_{avg}, τ_1, τ_2, α_2 and ORR as predictors, obtained from single-cells. The random forests hyper-parameters were tuned based on the lower OBB estimate (Table 5). Subsequently, we evaluated trained random forests models accuracy by plotting ROC-AUC curves (Figure 5.8 C, Table 5.3). From Figure 5.8 C and table 5 it is noticeable that single-cell classification performance is affected by donor variability during the FCCP treatment. Donors D, E and A have the highest ROC-AUC values and lowest OOB errors. Finally, we measured the weighting of each 2P-FLIM variable via the random forests classification model for higher ROC AUC donors, and found that τ_1, τ_2, τ_{avg} and α_2 are the most important variables for classifying macrophage type at a single-cell level (Figure 5.8 D,E).

Table 5.3- Hyper-parameters, OBB, ROC-AUC and confusion matrix of single-cell donor-specific random forests models.

Donor (No. of data points)	ntree	mtry	OOB (%)	ROC-AUC	TP	FP	FN	TN
A (170)	400	5	23.53	0.791	55	22	18	75
B (155)	200	3	38.06	0.650	29	42	17	67
C (232)	100	2	30.17	0.760	93	36	34	69
D (199)	300	4	10.05	0.937	98	5	15	81
E (179)	150	2	19.55	0.843	69	18	17	75
F (212)	150	3	28.77	0.735	127	13	48	24

ntree –number of trees; mtry- number of variables selected for the best split at each node; OBB- out-of-bag error; ROC-AUC – area under receiver operating characteristics curve; TP – true positive; FP – false positive; FN – false negative; TN – true negative

5.5. Discussion

In this study, we use macrophage polarisation as a model system to demonstrate the effectiveness of random forests, applied to 2P-FLIM parameters influenced by metabolic perturbations (Figure 5.1). The polarisation of human macrophages is often crudely described as two opposite phenotypes: classical activation (IFNγ-M1-Macrophages) and alternative activation (IL-4-M2-macrophages). The higher production of TNFα in IFNγ-treated human macrophages and low IL-10 production are evidence of a macrophage classical activation [45] (Figure 5.2 A, B). In contrast, treating human macrophages with IL-4, an increase in IL-10 production and higher expression of MRC1 and CCL13, are characteristic of an alternative activation of macrophages [46, 47] (Figure 5.2 D, E and F). Furthermore, we performed flow cytometry of polarised macrophages using antibodies to detect CD80, CD86, CD163 and CD206 surface markers, further validating the intended macrophage polarisation (Figure Appendix 11). Extending from this, extracellular flux analysis was performed. Extracellular flux measurements revealed a higher acidification ratio (ECAR) and a lower oxygen consumption ratio (OCR) for IFNγ-M1-macrophages during the different stages of metabolic inhibition when compared with IL-4-M2 macrophages (Figure 5.3 A, D). By calculating the basal glycolysis rate and maximum

glycolysis, IFNγ-M1-macrophages presented higher glycolytic rates (Figure 5.3 B, C). The acidification (from ECAR) is linked with the production of lactate as a by-product of glycolysis, which reduces extracellular pH [20]. Regarding IL-4-M2 macrophages, a reduced ECAR and increased OCR during the extracellular flux treatments (Figure 5.3 A, D) together with a higher max respiration potential was observed when compared with untreated macrophages. However, no difference was observed at the basal respiration measures (Figure 5.3 E, F). ECAR and OCR calculated results are associated with a higher dependence of OxPhos as a more active metabolic machinery in IL-4-M2 macrophages. In order to fuel the upregulation of the TCA cycle and the ETC, the mitochondria need to consume more oxygen at the complex IV site of the electron transport chain [21, 48].

We next sought to underline 2P-FLIM as a complimentary and more advantageously, a non-invasive spatial evaluation of macrophage metabolism reflecting macrophage induced polarisation. Recapitulating the sequence of metabolic enzyme inhibition which formed a basis of the extracellular flux analysis, sequential 2P-FLIM micrographs of IFNγ- or IL-4-polarised macrophages were acquired (Figure 5.4 A). A reduced τ_{avg}, observed with IFNγ-M1 macrophages reflects a higher relative amount of free NAD(P)H (which has characteristic short fluorescence lifetimes), indicative with glycolysis [41, 49]. In contrast IL-4-M2 macrophages had higher τ_{avg} - reflective of OxPhos, due to increased proportion of longer lifetime, protein-bound NAD(P)H [1, 34] (Figure 5.4 B). Varying interpretations of ORR are reported in previous studies [34, 50] and for this study, we adopt a lower ORR reflecting a higher fraction of NAD(P)H and a lower FAD^+ associated with upregulation of OxPhos (Equation 4)[2]. IL-4-M2 macrophages exhibited a lower ORR across the treatments in contrast with IFNγ-M1 macrophages, validating a higher dependency of IL-4-M2 macrophages on OxPhos when compared with IFNγ-M1 macrophages. A heatmap overviewing the 2P-FLIM output variables was compiled showcasing the shifts promoted by the different treatments in both phenotype-directed human macrophages (Figure 5.4 D). With IL-4-M2 macrophages, there is a noticeable increase in τ_1, τ_2 and τ_{avg} and an

appreciable decrease in ORR when compared with IFNγ-M1 treated macrophages. The trending increase of NAD(P)H fluorescence lifetimes is further exacerbated after treatment with FCCP in IL-4-M2 macrophages. Indeed, given the ability of FLIM to imaging and measure NAD(P)H and FAD^+ others have employed small molecules to gain further information about the dynamics of metabolic machinery in states of disease and differentiation. For instance, during stem cell osteogenic differentiation, Guo et al., tested oligomycin A (mitochondrial respiration inhibitor) as an experimental treatment in parallel to standard osteogenic media. A decrease in NAD(P)H average lifetime was calculated (therefore reduced oxidative phosphorylation), increased lactate production, lower oxygen consumption and osteogenic differentiation [51]. The heterogeneous response towards metabolic inhibitors by IFNγ-M1 or IL-4-M2 macrophages yields clustering patterns in the two-dimensional projected space via the UMAP method (Figure 5.6 A). When analysing each treatment individually, measurements emanating from the FCCP treatment yielded the highest segregation across all donors between IFNγ-M1 and IL-4-M2 macrophages (Figure 5.6 B). In addition, our phasor analysis also demonstrates a higher segregation of IFNγ-M1 and IL-4-M2 macrophages when using FFCP treatment (Figure 5.5). Albeit, the limitation in pre-defining values for the fluorescence lifetime variables such as τ_1 and τ_2 can mask important predictors for random forests.

Higher NAD(P)H fluorescence lifetimes such as τ_1, τ_2 and τ_{avg} are attributable to two major factors: increases in NADPH concentrations and microenvironmental shifts [42, 52]. FCCP functions as an uncoupler of mitochondria inner membrane allowing unhinged proton flux to the mitochondria matrix causing a reduction of mitochondrial pH, increasing effectively the fluorescence lifetime of NAD(P)H. The unhinged proton flux due to FCCP compliments existing studies whereby Schaefer et al., reported an increased NAD(P)H fluorescence lifetime due to reduced mitochondria pH elicited by FCCP treatment [53, 54]. Another consequence of FCCP treatment is an increase in ETC activity indicated by increased oxygen consumption of IL-4-M2 macrophages (Figure 5.3 D). Increased ETC activity promotes an increase of NADH and FAD^+

directly impacting the ORR. One would have expected the ORR to increase after the FCCP treatment as observed in IFNγ macrophages. However, for IL-4-M2 macrophages, the ORR begins to decrease. FCCP induction of maximal ETC activity increases the demand for NADH and $FADH_2$ causing a concomitant increase of the FAO and TCA cycle activity already upregulated in IL-4-M2 macrophages [55] . This demand results in a reduced pool of FAD^+ and an increase of NADH, effectively reducing ORR [55-57]. The higher heterogeneity in FCCP response is due to the effect of FCCP on the mitochondrial membrane and the higher dependence of FAS/FAO of IL-4-M2 macrophages basally [21]. Blacker et al. reported the FCCP impact in great detail where, when seeking to separate NADH and NADPH fluorescence in live cells and tissues using FLIM, inhibiting mitochondrial oxidative phosphorylation in wild-type HEK293 cells using rotenone (10 μM) or uncoupling using FCCP (1 μM) [58]. Blacker et al., study provides excellent insight into NADH and NADPH dynamics and separation, and the treatment of FCCP has a similar effect on HEK293 cells as the IFNγ-M1 macrophages reported in our study. Whereby FCCP has less a significant impact on our IL-4-M2 macrophages. Here, FCCP uncoupling promotes higher ETC, higher TCA activity impacting the ORR and, at the same time, a decreased mitochondrial pH increases the fluorescence lifetimes of NAD(P)H [53, 54]. Regarding IFNγ-M1 macrophages, their lower dependence on ETC, TCA, FAO and lower mitochondria membrane potential while producing most of ATP by glycolysis, makes the impact of FCCP on the mitochondria and fluorescence lifetimes less pronounced.

Random forests models were applied to study the endpoint variables of the 2P-FLIM obtained during the FCCP treatment of IFNγ-M1 macrophages and IL-4-M2 macrophages. 2P-FLIM measurements contain a minimum of 24 cells per field-of-view and culminate in total of 36 data points used for random forests training. For random forests training, a low OBB error rate and a high ROC-AUC of 0.944 was achieved when classifying a population of IFNγ-M1 and IL-4-M2 macrophages (Figure 5.6 C, D, Table 5.2). When random forests classification was performed using only three predictors: τ_1, τ_2 and τ_{avg}, the ROC-AUC classification accuracy

decreased slightly to 0.934 (Figure 5.6 C). When applying random forests for feature importance based on mean decrease in accuracy and mean decrease in Gini, τ_1, τ_2 and τ_{avg} are the best performing 2P-FLIM variables for classifying an IFNγ-M1 or an IL-4-M2 macrophage when subjected to the FCCP treatment (Figure 5.6 D). Determining the best 2P-FLIM variables as τ_1, τ_2 and τ_{avg} implies that these FLIM features are divergent in IFNγ-M1 and IL-4-M2 macrophages. This outcome agrees with our previous results showing that FCCP highly impacts the NAD(P)H fluorescence lifetimes in IFNγ-M1 and IL-4-M2 macrophages (Figure 5.4D). This accuracy of 2P-FLIM to classify cell phenotype compliments the random forests machine learning models approach of Walsh et al., classifying $CD3^+$ and $CD3^+CD8^+$ T-cell activation [34].

Precise regulation of macrophage activation state is key to understanding disease control, tissue homeostasis and implant response, with this regulation shown to be directly related with macrophage intracellular metabolism [21]. Therefore, impaired macrophage metabolism results in compromised homeostasis such as the case of diabetes, the foreign body response to biomaterials, obesity or cancer [59, 60]. Depending on the investigation being applied, shifts observed in cellular metabolism, cytokine production or gene expression are typically a cumulative output from a broad population. We investigated the clustering pattern of IFNγ-M1 macrophages and IL-4-M2 macrophages using single-cell data within individual donors (Figure 5.8 A, B), and found that the IFNγ-M1 macrophage and IL-4-M2 macrophage appeared as separate clusters within a donor. Classifying IFNγ-M1 and IL-4-M2 macrophages at a single-cell level yielded some varied results, with four donors providing acceptable predicting performance (OOB<31%; ROC AUC>0.75) (Figure 5.8C, D). There is some cell-to-cell variability which could stem from the uptake capacity of FCCP and other treatments in our experiments as well the underlying health of the donors which is not available [61, 62]. Nonetheless, for the four donors with the most superior performance during classification, τ_1, τ_2, τ_{avg} and α_2 are the most potent variables highlighted by the random forests model, which agrees with the case of full FoV analysis. Future efforts to improve single-cell classification include increasing the overall

number of cells analysed to ensure a stronger classification. In addition, by observing phenotypic IFNγ-M1 and IL-4-M2 macrophage cell surface markers (examples include CD80, CD86, CD163 and CD206, respectively) during the imaging process by immunofluorescence or other modes of tagging, it would be possible to improve the classification efficiency. [63].

2P-FLIM imaging has several advantages when compared with traditional metabolic assays and methods to classify and validate macrophage metabolism. 2P-FLIM enables spatial and temporal resolution in a non-invasive manner, allowing single-cell and cell-to-cell evaluations into cellular heterogeneity in a basal and interrogated mode. 2P-FLIM requires no fixation nor staining of cells and can be performed in real-time with only a small number of cells. In this work, we demonstrated the feasibility of using 2P-FLIM as a tool to distinguish and classify opposing human macrophage polarisation states based on cellular metabolism and fluorescence lifetimes variables. Visualisation of the data showed a clear classification of IFNγ-M1 and IL-4-M2 macrophages in response to FCCP during real-time imaging in a full FoV. The excellent performance of machine learning models, applied on the data extracted from the non-invasive technique, underlines further the efficiency of this workflow. This workflow can be easily adopted to non-invasively characterise macrophage polarisation in in vivo models and in vitro multicellular organoid models. These organoid models can be developed to study foreign body interactions, biomaterial assessment, pharmaceutical research and screening and clinical applications such as disease diagnosis.

5.6. Conclusion

In this study, we employed 2P-FLIM microscopy and random forests models to classify polarised IFNγ-M1 and IL-4-M2 macrophages. Here, we promoted macrophage polarisation using IFNγ and IL-4 cytokine to drive M1 and M2 macrophages like phenotype. Macrophage polarisation was validated using PCR, ELISA, extracellular flux assay and measuring oxygen consumption. After obtaining polarised macrophages from 6 human donors, 2P-FLIM was

performed in a static chamber in which multiple metabolic challengers were added following a time-course. UMAP was applied to 2P-FLIM acquired variables and showed a higher segregation of 2P-FLIM variables acquired from of IFNγ-M1 and IL-4-M2 macrophages during FCCP treatment. Random forests analysis of the FoV revealed a low OOB error of 16.67 and a high 0.944 ROC-AUC curve value determining a high efficiency on classifying macrophage polarisation in a FoV 2P-FLIM image. Single-cell 2P-FLIM measurements of FCCP treatment response of IFNγ-M1 and IL-4-M2 macrophages revealed sing-cell heterogeneity as well as donor-to-donor variability revealed by varying OOB error and ROC-AUC values. This study showcases 2P-FLIM of NAD(P)H as a methodology to classify macrophages based on their response to a metabolic challenger. This promotes the possibility of using 2P-FLIM to classify cells or macrophage polarisation in samples with low cell numbers or in diseased tissues. This approach can be used further to classify multiple types of immune cells based on their metabolic profile.

5.7. References

[1] I.A. Okkelman, N. Neto, D.B. Papkovsky, M.G. Monaghan, R.I. Dmitriev, A deeper understanding of intestinal organoid metabolism revealed by combining fluorescence lifetime imaging microscopy (FLIM) and extracellular flux analyses, Redox Biology. 30 (2020) 101420.
[2] N. Neto, R.I. Dmitriev, M.G. Monaghan, Seeing Is Believing: Noninvasive Microscopic Imaging Modalities for Tissue Engineering and Regenerative Medicine, Cell Engineering and Regeneration, Springer, Cham2020, pp. 599-638.
[3] M.C. Skala, K.M. Riching, A. Gendron-Fitzpatrick, J. Eickhoff, K.W. Eliceiri, J.G. White, N. Ramanujam, In vivo multiphoton microscopy of NADH and FAD redox states, fluorescence lifetimes, and cellular morphology in precancerous epithelia, Proc Natl Acad Sci U S A. 104(49) (2007) 19494-9.
[4] J.R. Lakowicz, H. Szmacinski, K. Nowaczyk, M.L. Johnson, Fluorescence lifetime imaging of free and protein-bound NADH, Proceedings of the National Academy of Sciences of the United States of America. 89(4) (1992) 1271-1275.
[5] S. Huang, A.A. Heikal, W.W. Webb, Two-Photon Fluorescence Spectroscopy and Microscopy of NAD(P)H and Flavoprotein, Biophysical Journal. 82(5) (2002) 2811-2825.
[6] K.R. Peterson, M.A. Cottam, A.J. Kennedy, A.H. Hasty, Macrophage-targeted therapeutics for metabolic disease, Trends in Pharmacological Sciences. 39(6) (2018) 536-546.
[7] C.W.t. Shields, M.A. Evans, L.L. Wang, N. Baugh, S. Iyer, D. Wu, Z. Zhao, A. Pusuluri, A. Ukidve, D.C. Pan, S. Mitragotri, Cellular backpacks for macrophage immunotherapy, Science Advances. 6(18) (2020).
[8] D.M. Mosser, J.P. Edwards, Exploring the full spectrum of macrophage activation, Nat Rev Immunol. 8(12) (2008) 958-69.
[9] S. Gordon, Alternative activation of macrophages, Nature Reviews Immunology. 3(1) (2003) 23-35.
[10] D.O. Adams, Molecular interactions in macrophage activation, Immunology Today. 10(2) (1989) 33-35.
[11] F.O. Martinez, A. Sica, A. Mantovani, M. Locati, Macrophage activation and polarization, Frontiers in Bioscience. 13 (2008) 453-461.
[12] A. Mantovani, S. Sozzani, M. Locati, P. Allavena, A. Sica, Macrophage polarization: tumor-associated macrophages as a paradigm for polarized M2 mononuclear phagocytes, Trends in Immunology. 23(11) (2002) 549-555.
[13] P.L. Graney, S. Ben-Shaul, S. Landau, A. Bajpai, B. Singh, J. Eager, A. Cohen, S. Levenberg, K.L. Spiller, Macrophages of diverse phenotypes drive vascularization of engineered tissues, Science Advances. 6(18) (2020) 1-15.
[14] A. Mantovani, F. Marchesi, A. Malesci, L. Laghi, P. Allavena, Tumour-associated macrophages as treatment targets in oncology, Nature Reviews Clinical Oncology. 14(7) (2017) 399-416.
[15] J. Wang, G. Roderiquez, T. Oravecz, M.A. Norcross, Cytokine regulation of human immunodeficiency virus type 1 entry and replication in human monocytes/macrophages through modulation of CCR5 expression, Journal of Virology. 72(9) (1998) 7642-7647.
[16] A. Gratchev, P. Guillot, N. Hakiy, O. Politz, C.E. Orfanos, K. Schledzewski, S. Goerdt, Alternatively activated macrophages differentially express fibronectin and its splice variants and the extracellular matrix protein betaIG-H3, Scandinavian Journal of Immunology. 53(4) (2001) 386-392.
[17] N. Feuerer, J. Marzi, E.M. Brauchle, D.A. Carvajal Berrio, F. Billing, M. Weiss, M. Jakobi, N. Schneiderhan-Marra, C. Shipp, K. Schenke-Layland, Lipidome profiling with Raman microspectroscopy identifies macrophage response to surface topographies of implant

materials, Proceedings of the National Academy of Sciences of the United States of America. 118(52) (2021) e2113694118.
[18] M. Kröger, J. Scheffel, E.A. Shirshin, J. Schleusener, M.C. Meinke, J. Lademann, M. Maurer, M.E. Darvin, Label-free imaging of macrophage phenotypes and phagocytic activity in the human dermis in vivo using two-photon excited FLIM, bioRxiv. (2021).
[19] J. Van den Bossche, L.A. O'Neill, D. Menon, Macrophage immunometabolism: where are we (Going)?, Trends in Immunology. 38(6) (2017) 395-406.
[20] F. Wang, S. Zhang, R. Jeon, I. Vuckovic, X. Jiang, A. Lerman, C.D. Folmes, P.D. Dzeja, J. Herrmann, Interferon gamma induces reversible metabolic reprogramming of M1 macrophages to sustain cell viability and pro-inflammatory activity, EBioMedicine. 30 (2018) 303-316.
[21] L.A. O'Neill, R.J. Kishton, J. Rathmell, A guide to immunometabolism for immunologists, Nature Reviews Immunology. 16(9) (2016) 553-565.
[22] J. Ma, K. Wei, J. Liu, K. Tang, H. Zhang, L. Zhu, J. Chen, F. Li, P. Xu, J. Chen, J. Liu, H. Fang, L. Tang, D. Wang, L. Zeng, W. Sun, J. Xie, Y. Liu, B. Huang, Glycogen metabolism regulates macrophage-mediated acute inflammatory responses, Nature Communications. 11(1) (2020) 1769-1775.
[23] S.J. Koo, I.H. Chowdhury, B. Szczesny, X. Wan, N.J. Garg, Macrophages promote oxidative metabolism to drive nitric oxide generation in response to trypanosoma cruzi, Infection and Immunity. 84(12) (2016) 3527-3541.
[24] A. Vivekanandan-Giri, J. Byun, S. Pennathur, Quantitative analysis of amino acid oxidation markers by tandem mass spectrometry, Methods in Enzymology. 491 (2011) 73-89.
[25] F. Fall, E. Lamy, M. Brollo, E. Naline, N. Lenuzza, E. Thevenot, P. Devillier, S. Grassin-Delyle, Metabolic reprograming of LPS-stimulated human lung macrophages involves tryptophan metabolism and the aspartate-arginosuccinate shunt, PloS One. 15(4) (2020) e0230813.
[26] L. McInnes, J. Healy, N. Saul, L. Großberger, UMAP: uniform manifold approximation and projection, Journal of Open Source Software. 3(29) (2018).
[27] A. Culos, A.S. Tsai, N. Stanley, M. Becker, M.S. Ghaemi, D.R. McIlwain, R. Fallahzadeh, A. Tanada, H. Nassar, C. Espinosa, M. Xenochristou, E. Ganio, L. Peterson, X. Han, I.A. Stelzer, K. Ando, D. Gaudilliere, T. Phongpreecha, I. Maric, A.L. Chang, G.M. Shaw, D.K. Stevenson, S. Bendall, K.L. Davis, W. Fantl, G.P. Nolan, T. Hastie, R. Tibshirani, M.S. Angst, B. Gaudilliere, N. Aghaeepour, Integration of mechanistic immunological knowledge into a machine learning pipeline improves predictions, Nature Machine Intelligence. 2(10) (2020) 619-628.
[28] B. Alipanahi, A. Delong, M.T. Weirauch, B.J. Frey, Predicting the sequence specificities of DNA- and RNA-binding proteins by deep learning, Nature Biotechnology. 33(8) (2015) 831-838.
[29] D.J. Bolland, H. Koohy, A.L. Wood, L.S. Matheson, F. Krueger, M.J. Stubbington, A. Baizan-Edge, P. Chovanec, B.A. Stubbs, K. Tabbada, S.R. Andrews, M. Spivakov, A.E. Corcoran, Two mutually exclusive local chromatin states drive efficient V(D)J recombination, Cell Reports. 15(11) (2016) 2475-2487.
[30] W.G. Touw, J.R. Bayjanov, L. Overmars, L. Backus, J. Boekhorst, M. Wels, S.A. van Hijum, Data mining in the Life Sciences with Random Forest: a walk in the park or lost in the jungle?, Brief Bioinform. 14(3) (2013) 315-26.
[31] L. Breiman, Random Forests, Machine Learning. 45(1) (2001) 5-32.
[32] A. Verikas, A. Gelzinis, M. Bacauskiene, Mining data with random forests: A survey and results of new tests, Pattern Recognition. 44(2) (2011) 330-349.
[33] J.N. Mandrekar, Receiver operating characteristic curve in diagnostic test assessment, Journal of Thoracic Oncology. 5(9) (2010) 1315-1316.
[34] A.J. Walsh, K.P. Mueller, K. Tweed, I. Jones, C.M. Walsh, N.J. Piscopo, N.M. Niemi, D.J. Pagliarini, K. Saha, M.C. Skala, Classification of T-cell activation via autofluorescence lifetime imaging, Nature Biomedical Engineering. 5(1) (2021) 77-88.
[35] T. Qian, T.M. Heaster, A.R. Houghtaling, K. Sun, K. Samimi, M.C. Skala, Label-free imaging for quality control of cardiomyocyte differentiation, Nat Commun. 12(1) (2021) 4580.

[36] O.R. Mahon, D.J. Kelly, G.M. McCarthy, A. Dunne, Osteoarthritis-associated basic calcium phosphate crystals alter immune cell metabolism and promote M1 macrophage polarization, Osteoarthritis Cartilage. 28(5) (2020) 603-612.
[37] J.M. Levitt, M.E. McLaughlin-Drubin, K. Munger, I. Georgakoudi, Automated biochemical, morphological, and organizational assessment of precancerous changes from endogenous two-photon fluorescence images, PloS One. 6(9) (2011) e24765.
[38] M. Wahl, T. Rohlicke, H.J. Rahn, R. Erdmann, G. Kell, A. Ahlrichs, M. Kernbach, A.W. Schell, O. Benson, Integrated multichannel photon timing instrument with very short dead time and high throughput, Rev Sci Instrum. 84(4) (2013) 043102.
[39] C. McQuin, A. Goodman, V. Chernyshev, L. Kamentsky, B.A. Cimini, K.W. Karhohs, M. Doan, L. Ding, S.M. Rafelski, D. Thirstrup, W. Wiegraebe, S. Singh, T. Becker, J.C. Caicedo, A.E. Carpenter, CellProfiler 3.0: Next-generation image processing for biology, PLoS Biol. 16(7) (2018) e2005970.
[40] A. Floudas, N. Neto, V. Marzaioli, K. Murray, B. Moran, M.G. Monaghan, C. Low, R.H. Mullan, N. Rao, V. Krishna, S. Nagpal, D.J. Veale, U. Fearon, Pathogenic, glycolytic PD-1+ B cells accumulate in the hypoxic RA joint, Journal of Clinical Investigation Insight. 5(21) (2020) e139032.
[41] S. Perottoni, N.G.B. Neto, C. Di Nitto, R.I. Dmitriev, M.T. Raimondi, M.G. Monaghan, Intracellular label-free detection of mesenchymal stem cell metabolism within a perivascular niche-on-a-chip, Lab on a Chip. 21(7) (2021) 1395-1408.
[42] P.M. Schaefer, S. Kalinina, A. Rueck, C.A.F. von Arnim, B. von Einem, NADH Autofluorescence-A Marker on its Way to Boost Bioenergetic Research, Cytometry A. 95(1) (2019) 34-46.
[43] M.C. Skala, K.M. Riching, D.K. Bird, A. Gendron-Fitzpatrick, J. Eickhoff, K.W. Eliceiri, P.J. Keely, N. Ramanujam, In vivo multiphoton fluorescence lifetime imaging of protein-bound and free nicotinamide adenine dinucleotide in normal and precancerous epithelia, Journal of Biomedical Optics. 12(2) (2007) 024014-024024.
[44] S. Ranjit, L. Malacrida, D.M. Jameson, E. Gratton, Fit-free analysis of fluorescence lifetime imaging data using the phasor approach, Nature Protocols. 13(9) (2018) 1979-2004.
[45] R. Tokunaga, W. Zhang, M. Naseem, A. Puccini, M.D. Berger, S. Soni, M. McSkane, H. Baba, H.J. Lenz, CXCL9, CXCL10, CXCL11/CXCR3 axis for immune activation - A target for novel cancer therapy, Cancer Treatment Reviews. 63 (2018) 40-47.
[46] M.N. Artyomov, A. Sergushichev, J.D. Schilling, Integrating immunometabolism and macrophage diversity, Seminars in Immunology. 28(5) (2016) 417-424.
[47] F.O. Martinez, S. Gordon, M. Locati, A. Mantovani, Transcriptional profiling of the human monocyte-to-macrophage differentiation and polarization: new molecules and patterns of gene expression, Journal of Immunology. 177(10) (2006) 7303-7311.
[48] J. Van den Bossche, J. Baardman, M.P. de Winther, Metabolic Characterization of Polarized M1 and M2 Bone Marrow-derived Macrophages Using Real-time Extracellular Flux Analysis, J Vis Exp. (105) (2015).
[49] A.J. Walsh, R.S. Cook, H.C. Manning, D.J. Hicks, A. Lafontant, C.L. Arteaga, M.C. Skala, Optical metabolic imaging identifies glycolytic levels, subtypes, and early-treatment response in breast cancer, Cancer Res. 73(20) (2013) 6164-74.
[50] A. Varone, J. Xylas, K.P. Quinn, D. Pouli, G. Sridharan, M.E. McLaughlin-Drubin, C. Alonzo, K. Lee, K. Munger, I. Georgakoudi, Endogenous two-photon fluorescence imaging elucidates metabolic changes related to enhanced glycolysis and glutamine consumption in precancerous epithelial tissues, Cancer Res. 74(11) (2014) 3067-75.
[51] H.W. Guo, J.S. Yu, S.H. Hsu, Y.H. Wei, O.K. Lee, C.Y. Dong, H.W. Wang, Correlation of NADH fluorescence lifetime and oxidative phosphorylation metabolism in the osteogenic differentiation of human mesenchymal stem cell, Journal of Biomedical Optics. 20(1) (2015) 017004-017012.

[52] T.S. Blacker, Z.F. Mann, J.E. Gale, M. Ziegler, A.J. Bain, G. Szabadkai, M.R. Duchen, Separating NADH and NADPH fluorescence in live cells and tissues using FLIM, Nat Commun. 5 (2014) 3936.
[53] P.M. Schaefer, D. Hilpert, M. Niederschweiberer, L. Neuhauser, S. Kalinina, E. Calzia, A. Rueck, B. von Einem, C.A.F. von Arnim, Mitochondrial matrix pH as a decisive factor in neurometabolic imaging, Neurophotonics. 4(4) (2017) 045004-045022.
[54] K. Blinova, S. Carroll, S. Bose, A.V. Smirnov, J.J. Harvey, J.R. Knutson, R.S. Balaban, Distribution of mitochondrial NADH fluorescence lifetimes: steady-state kinetics of matrix NADH interactions, Biochemistry. 44(7) (2005) 2585-2594.
[55] M.H. Ludtmann, P.R. Angelova, Y. Zhang, A.Y. Abramov, A.T. Dinkova-Kostova, Nrf2 affects the efficiency of mitochondrial fatty acid oxidation, Biochemical Journal. 457(3) (2014) 415-424.
[56] A. Viola, F. Munari, R. Sanchez-Rodriguez, T. Scolaro, A. Castegna, The metabolic signature of macrophage responses, Frontiers in Immunology. 10 (2019) 1462-1478.
[57] T.E. Akie, M.P. Cooper, Determination of fatty acid oxidation and lipogenesis in mouse primary hepatocytes, Journal of Visualized Experiments. (102) (2015) e52982.
[58] T.S. Blacker, M.R. Duchen, Investigating mitochondrial redox state using NADH and NADPH autofluorescence, Free Radical Biology and Medicine. 100 (2016) 53-65.
[59] J.C. McNelis, J.M. Olefsky, Macrophages, immunity, and metabolic disease, Immunity. 41(1) (2014) 36-48.
[60] A. Mantovani, A. Sica, Macrophages, innate immunity and cancer: balance, tolerance, and diversity, Current Opinions in Immunology. 22(2) (2010) 231-237.
[61] S.T. Smiley, M. Reers, C. Mottola-Hartshorn, M. Lin, A. Chen, T.W. Smith, G.D. Steele, Jr., L.B. Chen, Intracellular heterogeneity in mitochondrial membrane potentials revealed by a J-aggregate-forming lipophilic cation JC-1, Proceedings of the National Academy of Sciences of the United States of America. 88(9) (1991) 3671-3675.
[62] C. Stiebing, T. Meyer, I. Rimke, C. Matthaus, M. Schmitt, S. Lorkowski, J. Popp, Real-time Raman and SRS imaging of living human macrophages reveals cell-to-cell heterogeneity and dynamics of lipid uptake, Journal of Biophotonics. 10(9) (2017) 1217-1226.
[63] P.J. Murray, J.E. Allen, S.K. Biswas, E.A. Fisher, D.W. Gilroy, S. Goerdt, S. Gordon, J.A. Hamilton, L.B. Ivashkiv, T. Lawrence, M. Locati, A. Mantovani, F.O. Martinez, J.L. Mege, D.M. Mosser, G. Natoli, J.P. Saeij, J.L. Schultze, K.A. Shirey, A. Sica, J. Suttles, I. Udalova, J.A. van Ginderachter, S.N. Vogel, T.A. Wynn, Macrophage activation and polarization: nomenclature and experimental guidelines, Immunity. 41(1) (2014) 14-20.

Chapter 6 - Discussion and Conclusions

6.1. Summary

With the rising interest in cellular metabolism to fully characterise diseases, either as a diagnostic tool or as a target of therapy, new methodologies are welcomed to fully appreciate the metabolic profile of cells, tissues or organoids. Current metabolomics techniques lack real-time analysis, spatial distribution and require a high amount of cells and samples. The objective of this thesis was to broaden and expand the applications of 2P-FLIM to monitor and modulate cellular metabolism as well to apply machine learning models to 2P-FLIM fluorescence variables. 2P-FLIM will be an important tool to explore cellular metabolism in cells, tissues and organoids with both non-invasive and spatial capability that other methodologies do not possess. Furthermore, 2P-FLIM allows continuous monitoring of cellular metabolism which open the door to ongoing time-dependent evaluation of metabolism. During the course of this thesis, the advantages of using 2P-FLIM were explored. In particular, 2P-FLIM was applied in limited cell numbers experiments, measuring of NAD(P)H intensities and metabolic cell profiles of 3D cell culture models agreeing with biochemical validation and literature [1-3].

In chapter 3 it was established that flow velocity in bioreactors can directly impact cellular metabolism due to oxygen and nutrient availability, and this is detectable by 2P-FLIM. This was verified by using an oxygen fluorescence label to measure the oxygen gradient being formed by cellular respiration from the inlet to the outlet region of the bioreactor. Then, 2P-FLIM was used to evaluate cellular metabolism from the inlet to the outlet region due to 2P-FLIM spatial capabilities. Here, a metabolic gradient from the inlet region to the outlet region was observed. hMSCs in the inlet region have a metabolic profile more dependent on OxPhos while hMSCs in the outlet region are more dependent on glycolysis as a course of energy. This metabolic trend fits with the availability of oxygen in the cell cultures. As OxPhos requires oxygen to produce ATP, the reduction of oxygen availability forced the hMSCs to adapt to a metabolic profile reliant on glycolysis. This chapter showcases the important non-invasive and

spatial property of 2P-FLIM, as with current methodologies it would be experimentally challenging to study different regions of the same bioreactor in a non-invasive way. Not only could 2P-FLIM infer the metabolic profile of hMSCs, it was possible to validate the metabolic shifts occurring using fluorescent labels of mitochondria and glucose uptake validating the metabolic shifts occurring.

Chapter 4 describes the metabolic shifts occurring during osteogenic stem cell differentiation using 2P-FLIM. A gradient of increased oxidative phosphorylation and anabolic pathways including glutaminolysis was observed when human stem cells undergo osteogenic differentiation using 2P-FLIM. In addition, gene expression and extracellular metabolite measurements validated the metabolic trends being observed. The trend observed during osteogenic differentiation of hMSCs gave rise to the hypothesis to drive anabolic pathways and glutaminolysis using non-invasive methods. To achieve this goal, lactate was added to promote higher glutaminolysis levels as observed in literature. Lactate promoted higher levels of mineral deposition, osteogenic differentiation and upregulated anaplerotic pathways including glutaminolysis culminating in higher expression of collagen producing genes. The chemical inhibition of glutaminolysis or re-absorption of lactate impacted negatively the osteogenic differentiation of stem cells validated by alizarin red staining. As a final result of chapter 5, not only was osteogenic differentiation upregulated using an extracellular metabolite upregulating anabolic pathways, it was shown that lactate could be act as a signalling molecule and source of energy to promote osteogenic differentiation.

Finally, for chapter 5, human macrophages were polarised towards a M1 or M2 state using IFNy or IL-4, respectively. Then, 2P-FLIM was used to monitor macrophage response to a selection of inhibitors while maintaining the same field-of-view. The selection of inhibitors, in specific FCCP, allowed to unlock the different metabolic profiles of human macrophages by ensuing different metabolic responses measured by 2P-FLIM. The collected 2P-FLIM variables

were then used to train random forests models to classify human macrophages polarisation in a full field-of-view or single-cell level. Random forest models were able to classify human macrophages accurately and with lower error when encompassing all of the human donors used in the experiment. For single-cells analysis in single donors, random forests were able to classify single-cell macrophages according to their polarisation state albeit with higher donor-dependent error rates. This chapter showcased the ability to separate human macrophages polarisation based on their metabolism, to follow short term impacts of inhibitors on cells as well to apply machine learning models to 2P-FLIM variables as a future research or diagnosis tool requiring lower amounts of human cells, especially important for tissue biopsies.

6.2. Limitations

While these studies and this thesis showcase 2P-FLIM application in cellular metabolism is important to be cognisant of some 2P-FLIM limitations. 2P-FLIM technique is limited regarding the long-lifetime of NAD(P)H. Noticeably, the longer lifetime is only referred to as protein-bound NAD(P)H. While there is no doubt regarding the conformational changes that promote this fluorescence lifetime shift, there is a contribution of NADPH directly on the observed values [4]. This means that effects of higher metabolic dependence on glycolysis could possibly be masked by higher NADPH values due to ROS production or upregulation of NADPH dependent pathways [5]. These results can attenuate fluorescence lifetime values and can make post-analysis complicated, especially if there is a known contribution of ROS production. Nonetheless, during this thesis, there was always an effort to validate 2P-FLIM findings using other approaches such as fluorescence labelling, qPCR and measuring extracellular metabolite concentrations to avoid simplistic analysis of metabolic profiles.

Regarding chapter 3, there is the limitation of using 2-NBDG as a glucose uptake fluorescence molecule. In particular, it has been demonstrated that 2-NBDG experiments are limited and might not translate to a direct measure of glucose uptake [6]. Initial characterisation

of 2-NBDG as measure of glucose uptake was performed in E.Coli [7]. In particular, it has been shown that 2-NBDG uptake in bacteria is mediated by a mannose or a glucose/mannose transporter system [8]. Later studies, evaluated the possibility to use 2-NBDG to monitor glucose transport in mammalian cells [9]. Specifically, the work by Yamada et al., characterised GLUT2 mediated 2-NBDG transport in Cos1 and MIN6 pancreatic beta cells. Here, the uptake of 2-NBDG in these cells was highly selective and competitively inhibited by excess D-glucose and blocked when using a glucose transport inhibitor. In addition, high 2-NBDG staining and fluorescence emission is often correlated with high glycolytic activity in activated CD8+ T-Cells [10, 11]. However, a study by Sinclair et al., compared 2-NBDG quantification with a well-established radiolabelled ^{3}H-2DG assay and inhibited glucose transporters using Cytochalasin B, 4,6-O-ethylidene-α-D-glucose and 2-DG as a direct substrate competitor for ^{3}H-DG. Here, there was no impact on 2-NBDG staining when treating T-cells with glucose transporter inhibitors, excess 2-DG or glucose, contrary to what was observed with 3H-2DG treatment. The data presented by Sinclair et al., demonstrate that there is a different transport pathway between radiolabelled 2-DG and 2-NBDG in T-Cells therefore, concluding that glucose transport and 2-NBDG are not mediated by a common transporter. Despite this conclusion, 2-NBDG is still used in some research, such as biomedical research using mesenchymal stem cells and also T-cells as a glucose uptake assay [12, 13]. As alternatives, to measure glucose uptake, radiolabelled glucose such as 3H-2DG is a well-established methodology. However, ^{3}H-2DG experiments require specific equipment, training and are limited to whole populations without mixture of cells or single-cell resolution [6].

For the specific bioreactor application of chapter 3, there was a need to use a fluorescence label with single-cell resolution to not compromise the metabolic microenvironment occurring in the closed bioreactor. However, no well-established alternatives of fluorescence labelling to 2-NBDG with single-cell resolution have been developed. Some companies have started to produce colorimetric assays to measure glucose uptake by blocking

cellular metabolism using 2-DG and oxidising 2-DG6P to generate NADPH to generate a fluorescent signal with a working enzyme. Nonetheless, this alternative would not be adequate for bioreactor live-cell imaging.

Regarding chapter 3 application of 2-NBDG, there were other experimental methodologies such as 2P-FLIM, O2-sensitive fluorescence molecules and TMRM staining that can validate the metabolic profile of hMSCs in the MOAB environment. The culmination of these results points towards an increase of glycolytic activity from the inlet to the outlet region of the MOAB. Therefore, it would still be appropriate to assume that increased glycolytic activity could be connected with increased glucose uptake. Nonetheless, future experiments using novel fluorescent labels of glucose could be performed to validate the results obtained using 2-NBDG.

In chapter 4, there is a limitation of only using one biological donor of hMSCs, therefore, there is an overall homogeneity of the data observed. To further improve the validity of this study, the results obtained should be validated using more biological donors. Another small limitation is regarding the cell culture medium used. For hMSCs cell culture, low glucose concentration DMEM medium was used. This medium formulation aligns better with *in vivo* conditions. However, the tissue engineering field usually uses high glucose medium promoting supraphysiological levels of glucose but elevated levels of osteogenic differentiation [14, 15]. In this study, the goal was to uncover metabolic trends, modulate them and unexpectedly, a new role of lactate as an important metabolite for osteogenic differentiation was uncovered. Nonetheless, this lactate importance for osteogenic differentiation can also be tested in high glucose conditions. However, high glucose cell culture conditions have a lower clinical relevancy and can be detrimental for stem cell proliferation and differentiation [16-18].

Regarding chapter 5, there is clearly the presence of donor heterogeneity at a single-cell level since some random forest models achieved lower error values in some donors. In order to improve this algorithm access to additional identifiers of donors (such as sex, general health,

age) would be required, as well to increase immensely the number of donor to generate a database of 2P-FLIM variables acquired from polarised macrophages [19]. In addition, the use of FACS-sorting conjugated with 2P-FLIM of NAD(P)H or immunostaining could be done to exclude non-polarised macrophages to ensure the quality of the data acquired and to be used in training and validating the random forests models. [20, 21]. However, special attention would be required to not overlap and influence the spectral properties of NAD(P)H and the immunofluorescence molecule at the time of 2P-FLIM data acquisition.

6.3. Future work

In this thesis, the importance of cellular metabolism in various fields has been reemphasized with 2P-FLIM as a powerful modality to uncover this. Ranging from cancer, stem cell biology and immunology there is a huge potential to uncover new cellular processes dependent on metabolism as well as new therapeutic targets. To properly investigate cellular metabolism in real-time without cell numbers limitations and with spatial resolution there is a need to use 2P-FLIM as an exploratory tool. 2P-FLIM as an exploratory tool for cellular metabolism can be applied in a wide range of cells, organoids and tissues. However, it seems the best application of 2P-FLIM to explore metabolism *in vitro* would be in samples with low cells number such as human tissue biopsies or to study tissue-resident macrophages.

Regarding the thesis, additional studies are need to validate lactate as a trigger of osteogenesis. We explored its usefulness in low glucose conditions. Since high glucose conditions are usually used in a tissue engineering setting it would be interesting to observe the impact of lactate in such conditions.

Another future study to follow would be the usage of different macrophages polarisation cytokines such as LPS. Since macrophage polarisation works as a spectrum it would interesting to follow up the results using different types of macrophage polarisation. However,

machine learning models for classification are limited to only two classes. So, machine learning application for multiple types of macrophage polarisation simultaneously would be limited.

The development of new optical instruments and analysis methods broaden the applications of 2P-FLIM for metabolic probing in various research fields as well for medical applications. In particular for cancer therapeutics, 2P-FLIM can be used to follow extracellular vesicles (EVs) based treatment [22]. By following EVs with particular RNA sequences associated with fluorescence probes, 2P-FLIM can be used as high-throughput sequencing methods to detect specific oncogene expression. In addition, using these EVs to deliver anti-tumour RNA sequences can not only detect cancer but also to treat cells while being tracked using 2P-FLIM [22, 23]. Ongoing technological advancements can also broaden the applications of 2P-FLIM. Slepkov et al., have integrated simultaneous FLIM and coherent anti-Stokes Raman scattering (CARS) microscopy to provide another layer of information to metabolic imaging [24]. Using such equipment would allow to collect FLIM data to elucidate NAD(P)H microenvironment as well to probe directly certain metabolites and lipid presence at a cellular level. Furthermore, improved resolution achieved by sub-diffraction-limited resolution can provide improved information regarding NAD(P)H microenvironment and explore mitochondrial heterogeneity [25, 26]. Towards a medical setting, FLIM can be used combined with endoscopy. Sun et al., developed a clinically compatible FLIM endoscopic system to allow for in vivo imaging during surgical procedures [27]. In particular, this system was tested in intraoperative setting for imaging of head and neck squamous cell carcinoma. Nonetheless, other similar applications such as colonoscopy or esophagogastroduodenoscopy (EGD) can be combined with FLIM and machine learning algorithms to provide early and fast detection of tumour tissues [28].

FLIM or 2P-FLIM can also help to expand current experimental techniques. Usually, in biomedical research there mostly interest in fluorescence intensity or detection of fluorescence at a particular wavelength. FLIM brings fluorescence lifetime, a unique optical parameter to be

used in methodologies that are already using fluorescence emission as an experimental variable. Specifically, fluorescence lifetime is a useful parameter to unmix fluorescence emissions allowing for current imaging or detection methodologies to not be limited to the number of wavelength-specific sensor panels [29]. Therefore, an interesting application of FLIM to a known experimental technology is to combine with flow cytometry or other high-throughput methods [30]. Here, faster and improved single-cell analysis is achieved and possible spectral overlaps due to fluorescence emission or unavailability of appropriate targeting fluorescence probes are resolved [31].

Machine learning models continue to be developed and applied in the biomedical field [32]. These new algorithms are currently being employed in biomedical research but also at the point of care testing and clinical trials [33]. These models allows build predictions of long-term disease progressions and outcomes, to diagnose patients based on medical methodologies as well to evaluate therapeutic efficiency paving the way to a more personalised medicine [34]. Improving the accuracy of each machine learning model is dependent on: developing new models applied to particular types of datasets; improving or increasing the size of datasets. To tackle the first issue, developing new machine learning models requires interdisciplinary collaborations and it might be difficult to develop a one-size-fits-all machine learning model. Therefore, some research fields have resorted to used tailored machine learning models such as engineering and biomedical fields [35, 36].

The improvement of datasets will allow better predictions and classifications of the experimental classes. To improve datasets, experimental setups must be carefully planned and allow the full characterisation of an experimental group using other methodologies before using the data as a training or validation data set [37, 38]. Another possibility to improve machine learning models would be to use large datasets such as medical information databases. In particular, medical information databases are rapidly growing experimental datasets and

machine learning application can highlight risk factors, important variables or identify therapeutics. However, most medical databases are yet not available electronically and the usage of such sensitive databases can put the privacy of patients at risk and currently, new privacy protection strategies are being developed [39, 40].

6.4. Conclusions

The studies in this thesis have yielded impactful insight into cellular metabolism, specifically in the case of mesenchymal stem cells and macrophages. In addition, they demystify examples of usage and methodology that can be applied to 2P-FLIM showcasing its strength as a metabolic exploratory tool in different settings. These findings contribute to the overall 2P-FLIM metabolic field as these new ways to improve and apply 2P-FLIM in research are a go-to for researchers through the use of biochemical validations, machine learning algorithms and metabolic modulation. Ultimately, the key findings from this thesis are summarised below:

- 2P-FLIM successfully determined spatial metabolic variations in a flow bioreactor. Here, a metabolic gradient from the inlet to the outlet region was measured. Specifically, hMSCs in the inlet region had a higher dependence on oxidative phosphorylation while stem cells closer to the outlet regions had higher glycolytic dependence. In addition, it was shown that this metabolic gradient was promoted by decreased intracellular oxygen as cells were consuming it in the inlet regions. This information can be used to modulate complex gradient environments in bioreactors and are also important for research that utilises low flow in their bioreactors.

- 2P-FLIM can measure metabolic shifts during cell culture incubation. Here, 2P-FLIM was mapped and measured the metabolic profiles of hMSCs in cell culture during osteogenic differentiation showing that 2P-FLIM can explore not only quick metabolic changes but also to follow long term metabolic profiles

- Lactate is an important metabolite for osteogenic cell differentiation. Lactate supplementation of osteogenic medium promoted higher levels of osteogenic differentiation validated by increased expression of osteogenic genes and higher mineral deposition

- Human macrophage polarisation can be classified using machine learning methods by proxy of their metabolism. 2P-FLIM was used to explore the metabolic profiles of polarised human macrophages. It was noticed that due to the metabolic profile of polarised macrophages the differences between M1 and M2 macrophages become accentuated when treating the macrophages with FCCP. Afterwards, using 2P-FLIM variables to observe this difference, these variables were then used as predictors in machine learning algorithms, obtaining high rating of classification.

Collectively these finding exemplify the potential of 2P-FLIM as an exploratory metabolic tool. It can be used as a non-invasive tool, with spatial translation and to generate variables for machine learning models. Afterwards, this data can then be used to classify cell type based on metabolism, uncover new metabolic pathway dependence and identify new therapeutic targets.

6.5. References

[1] E. Ozaki, L. Gibbons, N.G. Neto, P. Kenna, M. Carty, M. Humphries, P. Humphries, M. Campbell, M. Monaghan, A. Bowie, S.L. Doyle, SARM1 deficiency promotes rod and cone photoreceptor cell survival in a model of retinal degeneration, Life Science Alliance. 3(5) (2020) e201900618.
[2] I.A. Okkelman, N. Neto, D.B. Papkovsky, M.G. Monaghan, R.I. Dmitriev, A deeper understanding of intestinal organoid metabolism revealed by combining fluorescence lifetime imaging microscopy (FLIM) and extracellular flux analyses, Redox Biology. 30 (2020) 101420.
[3] A. Floudas, N. Neto, V. Marzaioli, K. Murray, B. Moran, M.G. Monaghan, C. Low, R.H. Mullan, N. Rao, V. Krishna, S. Nagpal, D.J. Veale, U. Fearon, Pathogenic, glycolytic PD-1+ B cells accumulate in the hypoxic RA joint, Journal of Clinical Investigation Insight. 5(21) (2020) e139032.
[4] T.S. Blacker, Z.F. Mann, J.E. Gale, M. Ziegler, A.J. Bain, G. Szabadkai, M.R. Duchen, Separating NADH and NADPH fluorescence in live cells and tissues using FLIM, Nature Communications. 5 (2014) 3936-3945.
[5] T.S. Blacker, M.R. Duchen, Investigating mitochondrial redox state using NADH and NADPH autofluorescence, Free Radical Biology and Medicine. 100 (2016) 53-65.
[6] L.V. Sinclair, C. Barthelemy, D.A. Cantrell, Single cell glucose uptake assays: a cautionary tale, Immunometabolism. 2(4) (2020) e200029.
[7] K. Yoshioka, H. Takahashi, T. Homma, M. Saito, K.-B. Oh, Y. Nemoto, H. Matsuoka, A novel fluorescent derivative of glucose applicable to the assessment of glucose uptake activity of Escherichia coli, Biochimica et Biophysica Acta (BBA) - General Subjects. 1289(1) (1996) 5-9.
[8] J. Tao, R.K. Diaz, C.R. Teixeira, T.J. Hackmann, Transport of a fluorescent analogue of glucose (2-NBDG) versus radiolabeled sugars by rumen bacteria and escherichia coli, Biochemistry. 55(18) (2016) 2578-2589.
[9] K. Yamada, M. Nakata, N. Horimoto, M. Saito, H. Matsuoka, N. Inagaki, Measurement of glucose uptake and intracellular calcium concentration in single, living pancreatic beta-cells, Journal of Biological Chemistry. 275(29) (2000) 22278-22283.
[10] M. Sukumar, J. Liu, Y. Ji, M. Subramanian, J.G. Crompton, Z. Yu, R. Roychoudhuri, D.C. Palmer, P. Muranski, E.D. Karoly, R.P. Mohney, C.A. Klebanoff, A. Lal, T. Finkel, N.P. Restifo, L. Gattinoni, Inhibiting glycolytic metabolism enhances CD8+ T cell memory and antitumor function, Journal of Clinical Investigation. 123(10) (2013) 4479-4488.
[11] N.E. Scharping, A.V. Menk, R.S. Moreci, R.D. Whetstone, R.E. Dadey, S.C. Watkins, R.L. Ferris, G.M. Delgoffe, The tumor microenvironment represses T cell mitochondrial biogenesis to drive intratumoral T cell metabolic insufficiency and dysfunction, Immunity. 45(2) (2016) 374-388.
[12] Y. Kawasaki, K. Sato, K. Mashima, H. Nakano, T. Ikeda, K. Umino, K. Morita, J. Izawa, N. Takayama, H. Hayakawa, K. Tominaga, H. Endo, Y. Kanda, Mesenchymal stromal cells inhibit aerobic glycolysis in activated T Cells by negatively regulating Hexokinase II activity through PD-1/PD-L1 interaction, Transplant Cell Therapy. 27(3) (2021) 231-239.
[13] C. Xu, C. Feng, P. Huang, Y. Li, R. Liu, C. Liu, Y. Han, L. Chen, Y. Ding, C. Shao, Y. Shi, TNFalpha and IFNgamma rapidly activate PI3K-AKT signaling to drive glycolysis that confers mesenchymal stem cells enhanced anti-inflammatory property, Stem Cell Research Therapy. 13(1) (2022) 491-505.
[14] J. Nulty, R. Burdis, D.J. Kelly, Biofabrication of prevascularised hypertrophic cartilage microtissues for bone tissue engineering, Frontiers in Bioengineering and Biotechnology. 9 (2021) 661989-661205.

[15] Y. Wang, Y. Wang, Y. Lu, J. Yu, High glucose enhances the odonto/osteogenic differentiation of stem cells from apical papilla via NF-KappaB signaling pathway, BioMed Research International. 2019 (2019) 1-11.
[16] P.A. Sotiropoulou, S.A. Perez, M. Salagianni, C.N. Baxevanis, M. Papamichail, Characterization of the optimal culture conditions for clinical scale production of human mesenchymal stem cells, Stem Cells. 24(2) (2006) 462-471.
[17] A. Stolzing, N. Coleman, A. Scutt, Glucose-induced replicative senescence in mesenchymal stem cells, Rejuvenation Research. 9(1) (2006) 31-35.
[18] N. Saki, M.A. Jalalifar, M. Soleimani, S. Hajizamani, F. Rahim, Adverse effect of high glucose concentration on stem cell therapy, Internation Journal Hematology - Oncology and Stem Cell Research. 7(3) (2013) 34-40.
[19] M. Garelnabi, L.M. Taylor-Smith, E. Bielska, R.A. Hall, D. Stones, R.C. May, Quantifying donor-to-donor variation in macrophage responses to the human fungal pathogen cryptococcus neoformans, PloS One. 13(3) (2018) e0194615.
[20] S. Shakya, K. Asosingh, J.A. Mack, E.V. Maytin, Optimized protocol for the preparation of single cells from cutaneous wounds for flow cytometric cell sorting and analysis of macrophages, MethodsX. 7(101027) (2020) 1-17.
[21] S.D. Jayasingam, M. Citartan, T.H. Thang, A.A. Mat Zin, K.C. Ang, E.S. Ch'ng, Evaluating the polarization of tumor-associated macrophages into M1 and M2 phenotypes in Human cancer tissue: technicalities and challenges in routine clinical practice, Frontiers in Oncology. 9 (2019) 1512-1521.
[22] Y. Ouyang, Y. Liu, Z.M. Wang, Z. Liu, M. Wu, FLIM as a promising tool for cancer diagnosis and treatment monitoring, Nano-Micro Letters. 13(1) (2021) 133-160.
[23] K. O'Brien, K. Breyne, S. Ughetto, L.C. Laurent, X.O. Breakefield, RNA delivery by extracellular vesicles in mammalian cells and its applications, Nature Reviews Molecullar Cell Biology. 21(10) (2020) 585-606.
[24] A.D. Slepkov, A. Ridsdale, H.N. Wan, M.H. Wang, A.F. Pegoraro, D.J. Moffatt, J.P. Pezacki, F.J. Kao, A. Stolow, Forward-collected simultaneous fluorescence lifetime imaging and coherent anti-Stokes Raman scattering microscopy, Journal of Biomedical Optics. 16(2) (2011) 021103-021110.
[25] J. Aryaman, I.G. Johnston, N.S. Jones, Mitochondrial heterogeneity, Frontiers in Genetics. 9 (2018) 718-734.
[26] P.-Y. Lin, Y.-C. Lin, C.-S. Chang, F.-J. Kao, Fluorescence lifetime imaging microscopy with subdiffraction-limited resolution, Japanese Journal of Applied Physics. 52(2R) (2013) 1-4.
[27] Y. Sun, J.E. Phipps, J. Meier, N. Hatami, B. Poirier, D.S. Elson, D.G. Farwell, L. Marcu, Endoscopic fluorescence lifetime imaging for in vivo intraoperative diagnosis of oral carcinoma, Microscopy Microanalysis. 19(4) (2013) 791-798.
[28] M. Billah, S. Waheed, Gastrointestinal polyp detection in endoscopic images using an improved feature extraction method, Biomedical Engineering Letters. 8(1) (2018) 69-75.
[29] G.J. Kremers, E.B. van Munster, J. Goedhart, T.W. Gadella, Jr., Quantitative lifetime unmixing of multiexponentially decaying fluorophores using single-frequency fluorescence lifetime imaging microscopy, Biophysical Journal. 95(1) (2008) 378-389.
[30] A. Bitton, J. Sambrano, S. Valentino, J.P. Houston, A review of new high-throughput methods designed for fluorescence lifetime sensing from cells and tissues, Frontiers in Physics. 9 (2021) 1-13.
[31] J. Houston, M. Naivar, J. Martin, G. Goddard, S. Carpenter, J. Mourant, J. Freyer, Endogenous fluorescence lifetime of viable cells by flow cytometry, SPIE2008.
[32] P. Hamet, J. Tremblay, Artificial intelligence in medicine, Metabolism. 69S (2017) S36-S40.
[33] I. Danciu, G. Agasthya, J.P. Tate, M. Chandra-Shekar, I. Goethert, O.S. Ovchinnikova, B.H. McMahon, A.C. Justice, In with the old, in with the new: machine learning for time to event

biomedical research, Journal of American Medical Information Association. 29(10) (2022) 1737-1743.
[34] M. Strzelecki, P. Badura, Machine learning for biomedical application, Applied Sciences. 12(4) (2022) 1-5.
[35] H. Majidifard, B. Jahangiri, W.G. Buttlar, A.H. Alavi, New machine learning-based prediction models for fracture energy of asphalt mixtures, Measurement. 135 (2019) 438-451.
[36] L. Liu, S. Zhao, H. Chen, A. Wang, A new machine learning method for identifying Alzheimer's disease, Simulation Modelling Practice and Theory. 99 (2020).
[37] A. Kazeminejad, R.C. Sotero, Topological properties of resting-state fMRI functional networks improve machine learning-based autism classification, Frontiers in Neuroscience. 12 (2018) 1018-1028.
[38] A.J. Walsh, K.P. Mueller, K. Tweed, I. Jones, C.M. Walsh, N.J. Piscopo, N.M. Niemi, D.J. Pagliarini, K. Saha, M.C. Skala, Classification of T-cell activation via autofluorescence lifetime imaging, Nature Biomedical Engineering. 5(1) (2021) 77-88.
[39] C. Castaneda, K. Nalley, C. Mannion, P. Bhattacharyya, P. Blake, A. Pecora, A. Goy, K.S. Suh, Clinical decision support systems for improving diagnostic accuracy and achieving precision medicine, Journal of Clinical Bioinformatics. 5 (2015) 4-20.
[40] W. Kim, J. Seok, Privacy-preserving collaborative machine learning in biomedical applications, 2022 International Conference on Artificial Intelligence in Information and Communication (ICAIIC), 2022, pp. 179-183.

Chapter 7 - Appendices

Computer Code Appendix 1 – PCA python code for PCA analysis. PCA python code was run in Spyder version 5.0 running internal Python version 3.8.10

```
import pandas as pd
from sklearn.preprocessing import StandardScaler
import matplotlib.pyplot as plt
from sklearn.decomposition import PCA
digits =pd.read_csv("C:\\Users\\...\\csv")
print (digits)
FLIM_data = digits[
   [
     't1',
     't2',
     'a1',
     'a2',
     'tavg',
     'orr',
                     ]
    ].values
scaled_FLIM_data = StandardScaler().fit_transform(FLIM_data)
pca = PCA(n_components=2)
principalComponents = pca.fit_transform(scaled_FLIM_data)
plt.scatter(
    principalComponents[:,0],
    principalComponents[:,1],
    )
plt.gca().set_aspect('auto')
plt.xlabel('PCA dimension 1')
plt.ylabel('PCA dimension 2')
plt.title('PCA projection of M1 vs M2', fontsize=18)
exit()
```

Computer Code Appendix 2 – UMAP python code for PCA analysis. UMAP python code was run in Spyder version 5.0 running internal Python version 3.8.10

```
import pandas as pd
import umap
import seaborn as sns
from sklearn.preprocessing import StandardScaler
import matplotlib.pyplot as plt
import matplotlib.patches as mpatches
digits =pd.read_csv("C:\\Users\\...\\.csv")
print (digits)
FLIM_data = digits[
   [
     't1',
     't2',
     'a1',
     'a2',
     'tavg',
     'orr'
      ]
    ].values
scaled_FLIM_data = StandardScaler().fit_transform(FLIM_data)
embedding = reducer.fit_transform(scaled_FLIM_data)
embedding.shape
plt.scatter(
    embedding[:,0],
    embedding[:,1],
    )
plt.gca().set_aspect('auto')
plt.xlabel('PCA dimension 1')
plt.ylabel('PCA dimension 2')
blue_color= mpatches.Patch(color="blue",hatch="/", label= "Basal")
orange_color= mpatches.Patch(color="darkorange", label="Olygomycin")
green_color= mpatches.Patch(color="green", label="FCCP")
```

```
red_color= mpatches.Patch(color="red", label= "Rot/AA")

purple_color=mpatches.Patch(color="mediumorchid", label="2-DG")

plt.legend(handles=[blue_color,orange_color,green_color,red_color,purp
le_color],loc="best")

plt.title('UMAP projection of M1 vs M2', fontsize=18)

exit()
```

Computer Code Appendix 3 – Random forests model R code. Random forests R code was run in Rstudio with R version 4.1.1

```
Data<-read.csv("C:/Users/.../….csv",
               header=TRUE, stringsAsFactors=TRUE)[ ,-4]
head(Data)
train<-sample(nrow(Data), 0.75*nrow(Data), replace=FALSE)
TrainSet<-Data[train, ]
ValidSet<-Data[-train, ]
library("randomForest")
library("caret")
library('pROC')
#step 0 create a RF model with randomly chosen values for mtry and
ntree#
control<-trainControl(method="repeatedcv", number=10, repeats=3)
tunegrid<-expand.grid(.mtry=4)
set.seed(123)
RF0<-train(x=TrainSet[ ,-1], y=TrainSet[ ,1], method="rf", ntree=150,
maxnodes=8, trControl=control, tuneGrid=tunegrid)
print(RF0)
#step 1-tune the parameters mtry and ntree#
control<-trainControl(method="repeatedcv", number=10, repeats=3,
search="grid")
tunegrid<-expand.grid(.mtry=c(1:5))
RFlist<-list()
for (ntree in c(100, 150, 200, 250, 300, 350, 400)) {
  set.seed(123)
  RFi<-train(x=TrainSet[ ,-1], y=TrainSet[ ,1], method="rf",
ntree=ntree, maxnodes=8, trControl=control, tuneGrid=tunegrid)
  key<-toString(ntree)
  RFlist[[key]]<-RFi
}
results<-resamples(RFlist)
summary(results)
dotplot(results)
#step 2-get the optimal value of mtry when ntree is 100#
```

```
control<-trainControl(method="repeatedcv", number=10, repeats=3,
search="grid")

tunegrid<-expand.grid(.mtry=c(1:5))

set.seed(123)

RFj<-train(x=TrainSet[ ,-1], y=TrainSet[ ,1], method="rf", ntree=250,
maxnodes=8, trControl=control, tuneGrid=tunegrid)

print(RFj)

plot(RFj)

#step 3-compare#

control<-trainControl(method="repeatedcv", number=10, repeats=3)

tunegrid<-expand.grid(.mtry=1)

set.seed(123)

RF1<-train(x=TrainSet[ ,-1], y=TrainSet[ ,1], method="rf", ntree=250,
maxnodes=8, trControl=control, tuneGrid=tunegrid)

print(RF1)

sink(file="OOB+Confusion_DonorH.txt")

#step 4-fit the data with the optimal combination of mtry and ntree#

set.seed(123)

RFfinal<-randomForest(x=TrainSet[ ,-1], y=TrainSet[ ,1], ntree=250,
mtry=1, maxnodes=8, importance=TRUE, proximity=TRUE)

print(RFfinal)

plot(RFfinal)

sink(file = NULL)

sink(file="VariableImportanteGlobal_DonorH.txt")

#variable importance -- top 4#

varImpPlot(RFfinal, sort=T, n.var=4, main="Top 4 important variables")

var.imp<-varImpPlot(RFfinal)

var.imp<-as.data.frame(var.imp)

var.imp

sink(file = NULL)

sink(file="ROC+AUC_DonorH.txt")

#ROC curves + AUC

pred_test <- predict(RFfinal, ValidSet, type="prob", norm.votes=TRUE,
predict.all=FALSE, proximity=FALSE, nodes=FALSE)

head(pred_test)

pred_test <- data.frame(pred_test)
```

```
pred_test_roc <- roc(ValidSet$Row_Labels, pred_test$M1)
textdata<-as.data.frame(pred_test_roc[["sensitivities"]])
textdataB<-as.data.frame(pred_test_roc[["specificities"]])
textdata
textdataB
auc(pred_test_roc)
plot(pred_test_roc)
sink(file=NULL)
exit ()
```

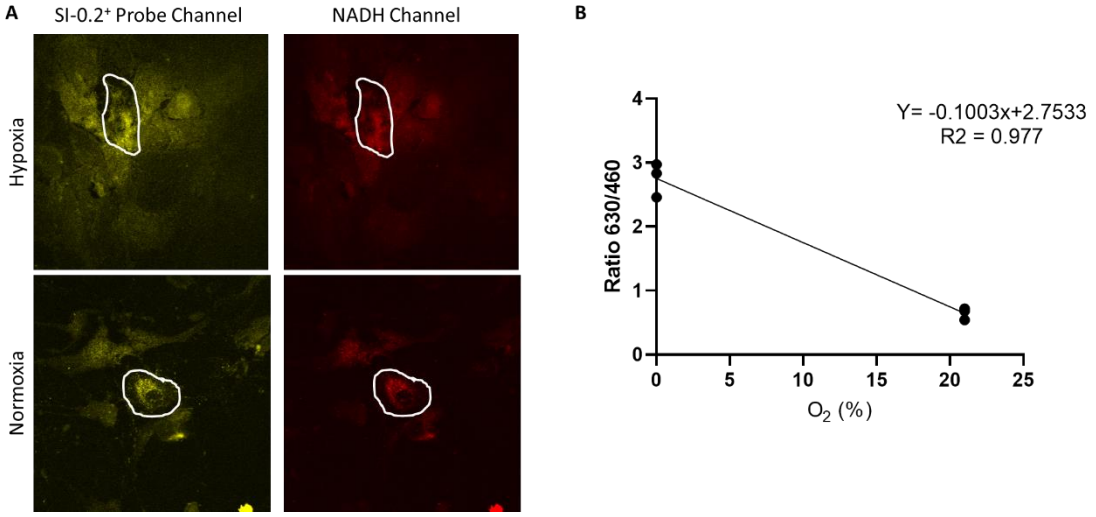

Figure Appendix 4 - Fluorescence intensity measurements of intracellular oxygen. A) Representative images of hMSC acquired in Normoxia (21%) and Hypoxia (0%) conditions. B) Linear regression and coefficient of determination calculated for the 630/460 ratio measured from ROI areas (n=3). At least 3 images for each n-value were obtained.

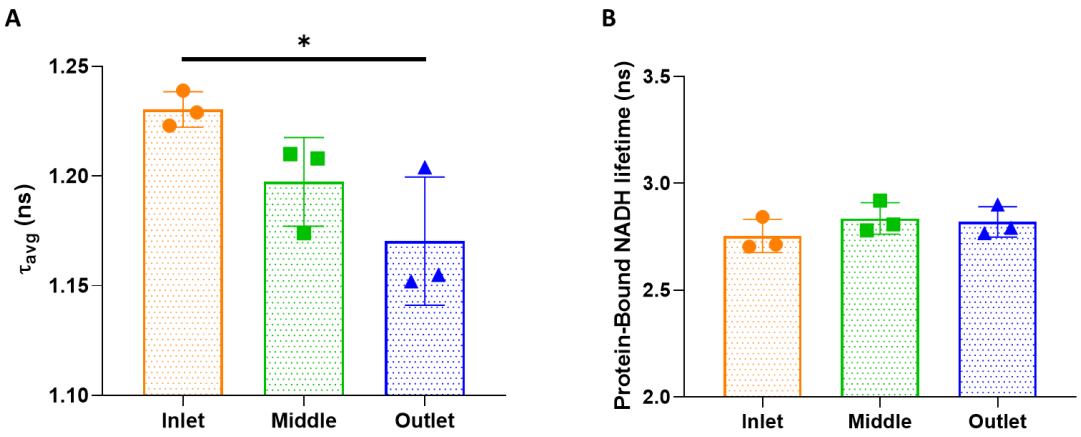

Figure Appendix 5 - 2P-Photon FLIM of NAD(P)H of hMSC cultured in the MOAB with 5µL min^{-1} . A) Calculated average fluorescence lifetimes for the inlet, middle and outlet region. B) Protein-bound lifetimes measured for the inlet, middle and outlet region. n=3. One-Way ANOVA was used for to verify statistical difference with p-value < 0.05

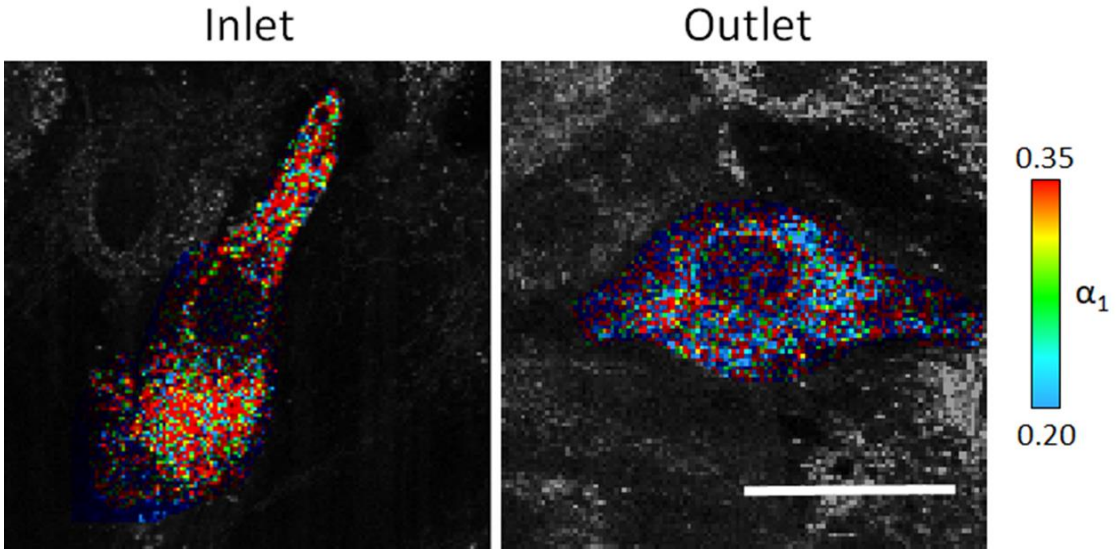

Figure Appendix 6 - Single-cell 2P-Photon FLIM of NAD(P)H of hMSC cultured in the MOAB with 5µL min^{-1}. Representative comparison between the α_1 parameter in single cells analysed at the inlet (right) and outlet (left) respectively. Scale bar: 50 µm

.

Computer Code Appendix 7 – Cell profiler code used to calculate mitochondria morphology and fluorescence intensity. Cell profiler version 4.0

[1] [Images]

To begin creating your project, use the Images module to compile a list of files and/or folders that you want to analyze. You can also specify a set of rules to include only the desired files in your selected folders.

[2] [Metadata]

The Metadata module optionally allows you to extract information describing your images (i.e, metadata) which will be stored along with your measurements. This information can be contained in the file name and/or location, or in an external file.

[3] [NamesAndTypes]

The NamesAndTypes module allows you to assign a meaningful name to each image by which other modules will refer to it.

[4] [Groups]

The Groups module optionally allows you to split your list of images into image subsets (groups) which will be processed independently of each other. Examples of groupings include screening batches, microtiter plates, time-lapse movies, etc.

[5] [EnhanceOrSuppressFeatures]

The de-noising filter. Should use “Enhance” function, with Feature “Speckles” and Feature size 10

[6] [IdentifyPrimaryObjects]

[7] [MeasureObjectSizeShape]

[8] [MeasureObjectIntensity]

[9] [ExportToSpreadsheet]

Table Appendix 1 – Gene symbol, name, accession number, unique assay ID and amplicon length of genes used for qPCR

Gene Symbol	Gene Name	RefSeq Accession No	Unique Assay Id	Amplicon Length
ALPL	alkaline phosphatase,	NC_000001.10,NG_008940.1,NT_004610.19	qHsaCID0010031	99
GOT1	glutamic-oxaloacetic transaminase 1	NC_000010.10,NT_030059.13	qHsaCID0006686	140
SLC16A3	monocarboxylic acid transporter 4	NC_000017.10,NT_010663.15	qHsaCID0014322	180
BGLAP	bone gamma-carboxyglutamate (gla) protein	NC_000001.10,NT_004487.19	qHsaCED0038437	69
GOT2	glutamic-oxaloacetic transaminase 2, mitochondrial	NC_000016.9,NT_010498.15	qHsaCID0013583	152
P4HA1	prolyl 4-hydroxylase	NC_000010.10,NT_030059.13	qHsaCID0009945	148
SLC16A4	monocarboxylic acid transporter 5	NC_000001.10,NT_032977.9	qHsaCED0036763	78
P4HA2	prolyl 4-hydroxylase	NC_000005.9,NT_034772.6	qHsaCID0012216	79
SOX9	SRY (sex determining region Y)-box 9	NC_000017.10,NG_012490.1,NT_010783.15	qHsaCED0021217	77
LDHA	lactate dehydrogenase A	NC_000011.9,NG_011816.1,NT_009237.18,NG_008185.1	qHsaCED0056429	68
P4HA3	prolyl 4-hydroxylase,	NC_000011.9,NT_167190.1	qHsaCID0009995	104
SPP1	secreted phosphoprotein 1	NC_000004.11,NT_016354.19	qHsaCID0012060	99
GLS	glutaminase	NC_000002.11,NT_005403.17	qHsaCID0007574	120
PTGS2	prostaglandin-endoperoxide synthase 2	NC_000001.10,NT_004487.19	qHsaCID0020933	148
UEVLD	UEV and lactate/malate dehyrogenase domains	NC_000011.9,NG_012138.1,NT_009237.18	qHsaCED0036634	75
GLS2	glutaminase 2 mitochondrial	NC_000012.11,NT_029419.12	qHsaCED0002029	72
RUNX2	runt-related transcription factor 2	NC_000006.11,NT_007592.15,NG_008020.1	qHsaCID0006726	80
GLUD1	glutamate dehydrogenase 1	NC_000010.10,NG_013010.1,NT_030059.13	qHsaCED0038578	73
LDHB	lactate dehydrogenase B	NC_000012.11,NT_009714.17,NG_017038.1	qHsaCID0012068	60
SLC16A1	monocarboxylic acid transporter 1	NC_000001.10,NT_032977.9,NG_015880.1	qHsaCID0008777	64
GLUD2	glutamate dehydrogenase 2	NC_000023.10,NG_016456.1,NT_011786.16	qHsaCED0038220	102
LDHC	lactate dehydrogenase C	NC_000011.9,NG_011816.1,NT_009237.18	qHsaCID0018614	130
SLC16A2	monocarboxylic acid transporter 8	NC_000023.10,NG_011641.1,NT_011669.17	qHsaCID0015666	149

Table Appendix 4 – Mahalanobis distance, Hotelling T^2 stats, F-value, Critical F-Values, P-value and significance results of PCA statistical significance analysis

Figure 4.2	Mahalanobis Distance	Two-Sample T2 Stats	F-Value	Critical F-Value	P-value	Significance
Osteo vs Xpan	4.121	25.478	9.554	9.552	0.025	YES
Figure 4.3						
Osteo vs Xpan (D0)	1.165	8.151	3.89	3.467	0.2063	NO
Osteo vs Xpan (D3)	1.986	23.665	11.295	3.467	0.105	NO
Osteo vs Xpan (D7)	3.223	62.314	29.748	3.467	0.044	YES
Osteo vs Xpan (D14)	5.32	169.823	81.052	3.467	0.012	YES
Figure 4.5						
Osteo vs Xpan	3.105	49.152	11.264	9.552	0.048	YES
Xpan vs Lact	11.06	183.472	68.802	9.552	0.0005	YES
Lact vs Osteo	6.4905	63.19	23.696	9.552	0.006	YES
Figure 4.6						
Xpan vs Osteo	5.569	139.584	65.431	3.682	0.01	YES
Osteo vs Lact	3.127	43.992	20.621	3.682	0.0472	YES
Lact vs Xpan	3.888	68.019	31.884	3.682	0.0289	YES
Figure 4.8						
Osteo vs Xpan	7.513	84.666	31.75	9.552	0.0034	YES
Xpan vs Lact	5.232	41.059	15.397	9.552	0.0127	YES
Lact vs Osteo	4.942	36.641	13.74	9.552	0.0151	YES

Computer Code Appendix 8 – PCA statistical analyses code. PCA statistical analysis code was run in Spyder version 5.0 with internal python version 3.8.10

```
import numpy as np
import pandas as pd
from scipy.stats import chi2

#Euclidian Difference Vector between Centroids - Excel
digits4 =pd.read_csv("C:\\Users\\...\\r.csv")
print (digits4)
#number of variables
numbvar=2
##pooled covariance##
dataGp1=digits[['x','y']]
dataGp2=digits2[['x','y']]
##Centroid values##
y_mu = digits4
cov1 = np.cov(dataGp1.values.T)
inv_covmat1 = np.linalg.inv(cov1)
cov2 = np.cov(dataGp2.values.T)
inv_covmat2 = np.linalg.inv(cov2)
#pooled variance-covariance matrix
size1=digits.shape[0]
size2=digits2.shape[0]
Sp= (((size1-1)*cov1)+((size2-1)*cov2))/((size1+size2-2))
inv_covSp = np.linalg.inv(Sp)
## Calculate Mahalanobis ##
left = np.dot(y_mu, inv_covSp)
CalcMahal = np.dot(left, y_mu.T)
mahal=np.sqrt(CalcMahal)
mahal.diagonal()
  print ('mahal=',mahal)
```

```
###End Mahalabonis###

###Start Hotelling two-sample T2 stats######

T2=(size1*size2)/(size1+size2)*(CalcMahal)

print('T2 Stats=',T2)

###End T2 Hotelling Statistic###

###Starts F-Critical####

T2F=((size1+size2-numbvar-1)/(numbvar*(size1+size2-2)))*T2

print ('F-value=',T2F)

##End T2H F-Value##

Fcritical  = (numbvar,size1+size2-numbvar-1)

#From Fcritical matrix - first number is number of fredom
degress numerator

#From Fcritical matrix - second number is number of fredom
degress denominator

# alpha - always use 0.05

# use degrees of freedom and alpha to calculate the critical F-
Value#

##https://www.danielsoper.com/statcalc/calculator.aspx?id=4##

##Check Critical F- Value calculator if T2F is higher than
Critical F, then

#data is signifcative#

##Calculation of P-value##

df=numbvar-1

pvalue = chi2.pdf(mahal,df=df)

print ('pvalue=',pvalue)


##FinishedStats##

Exit()
```

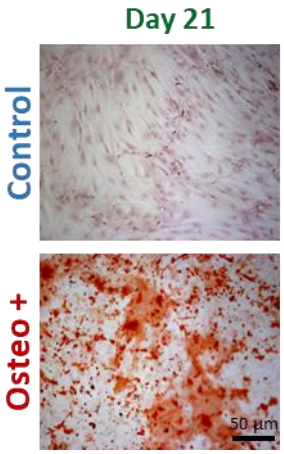

Figure Appendix 9 - Alizarin red staining of hMSCs after 21 days of incubation in either Xpan or Osteo+ cell culture media.

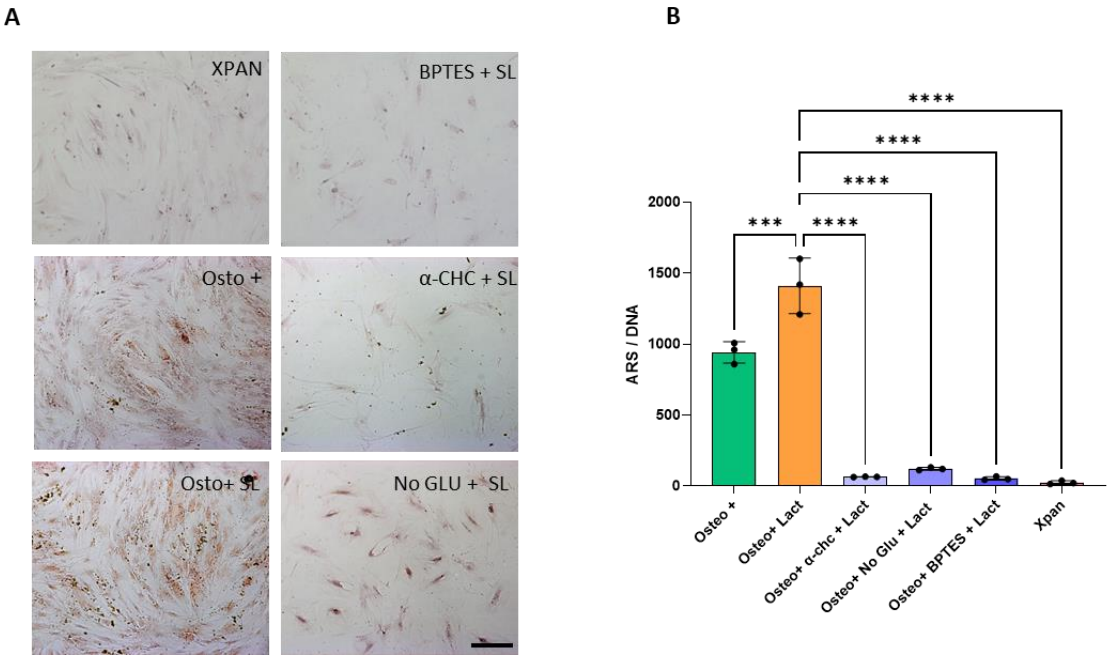

Figure Appendix 10 – Supplementation of Osteo + cell culture medium with lactate and metabolic inhibitors. (A) Alizarin red staining of hMSCs after 14 days of cell culture in several cell culture medium formulations. (B) Alizarin red quantification per DNA of hMSCs after 14 days of cell culture

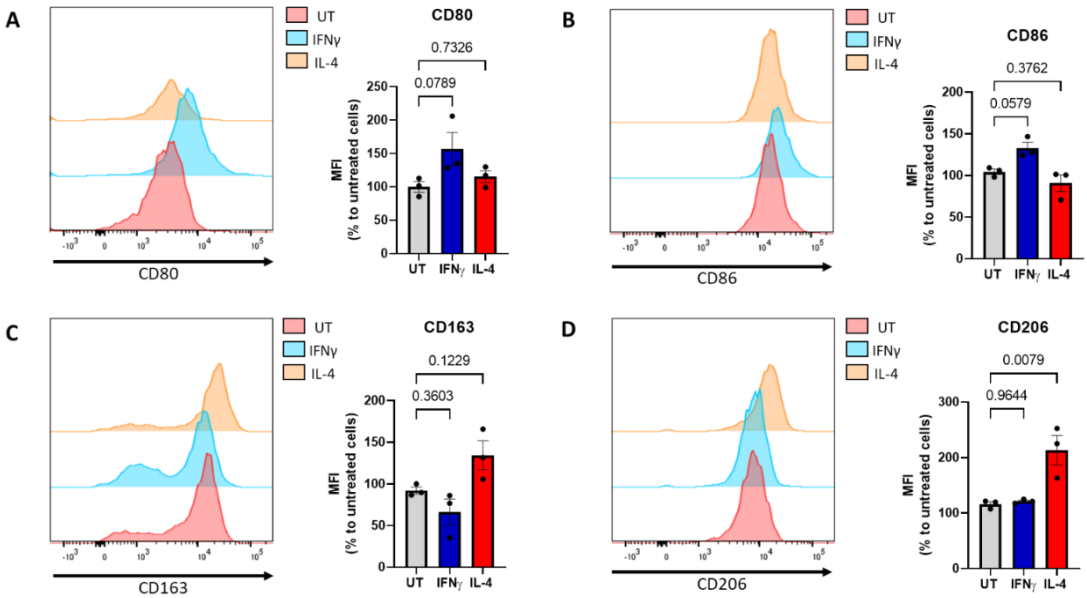

Figure Appendix 11 - Validation of macrophage polarisation using Flow Cytometry. Primary human macrophages were left untreated (UT), treated with IFNγ (20 ng/ml) or IL-4 (20 ng/ml) for 24 hours. Cells were stained for M1 maturation surface markers CD80, CD86, and M2 surface markers CD163, CD206, and analysed by flow cytometry. (A-D) Representative histograms depicting median fluorescence intensity (MFI) of surface markers. Bar graphs depict MFI as a percentage to the control (untreated cells) (N = 3). All data is represented as Mean ± SEM and analysed by One Way Anova with Dunnett's multiple comparisons test.

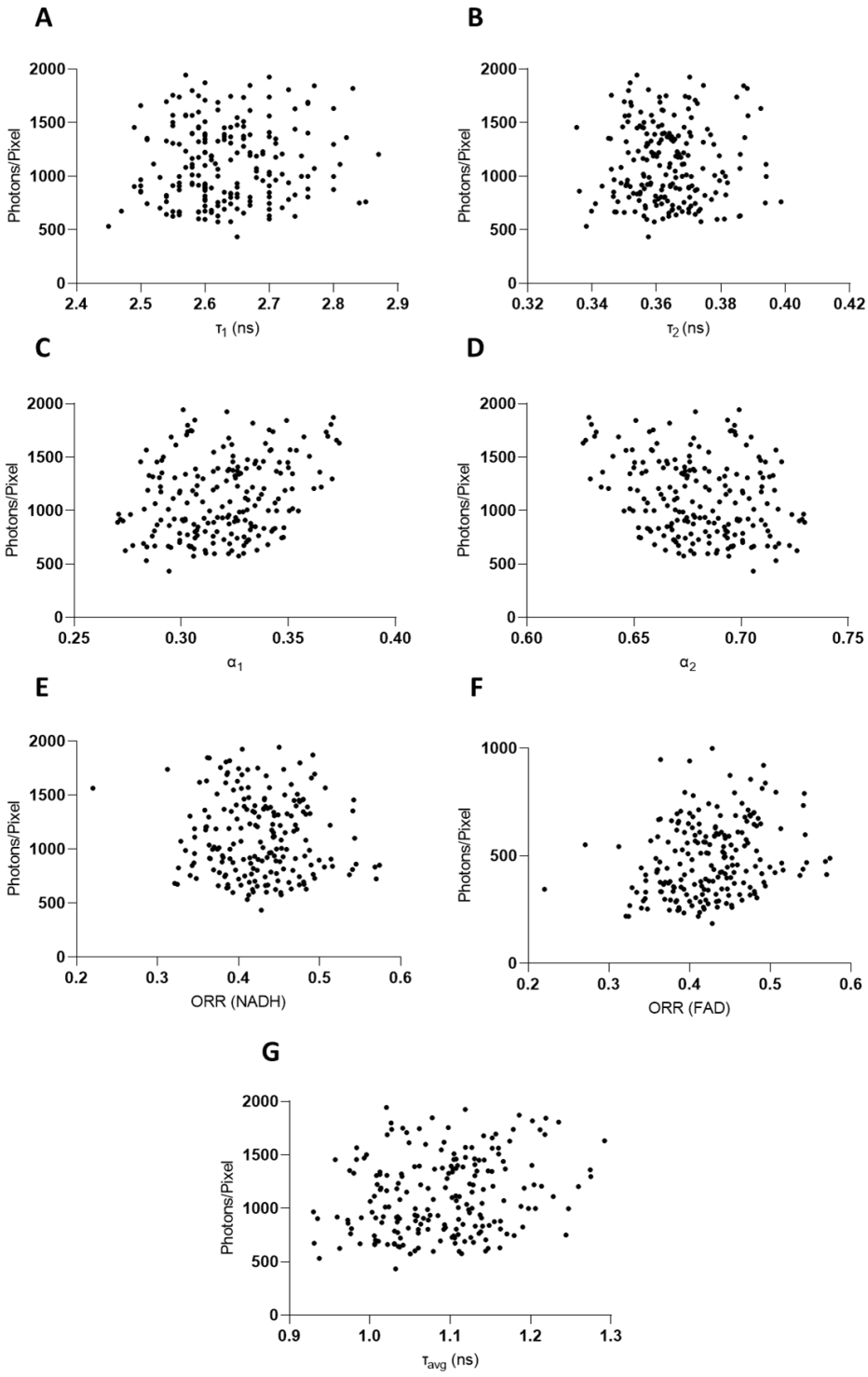

Figure Appendix 12 - Dispersion plot distribution of photons/pixel per fluorescence lifetime variable value. A) τ_1, B) τ_2, C) α_1, D) α_2, E) ORR distribution based on NADH results, F) ORR distribution based on FAD results and G) τ_{avg},. These values are obtained after background removal

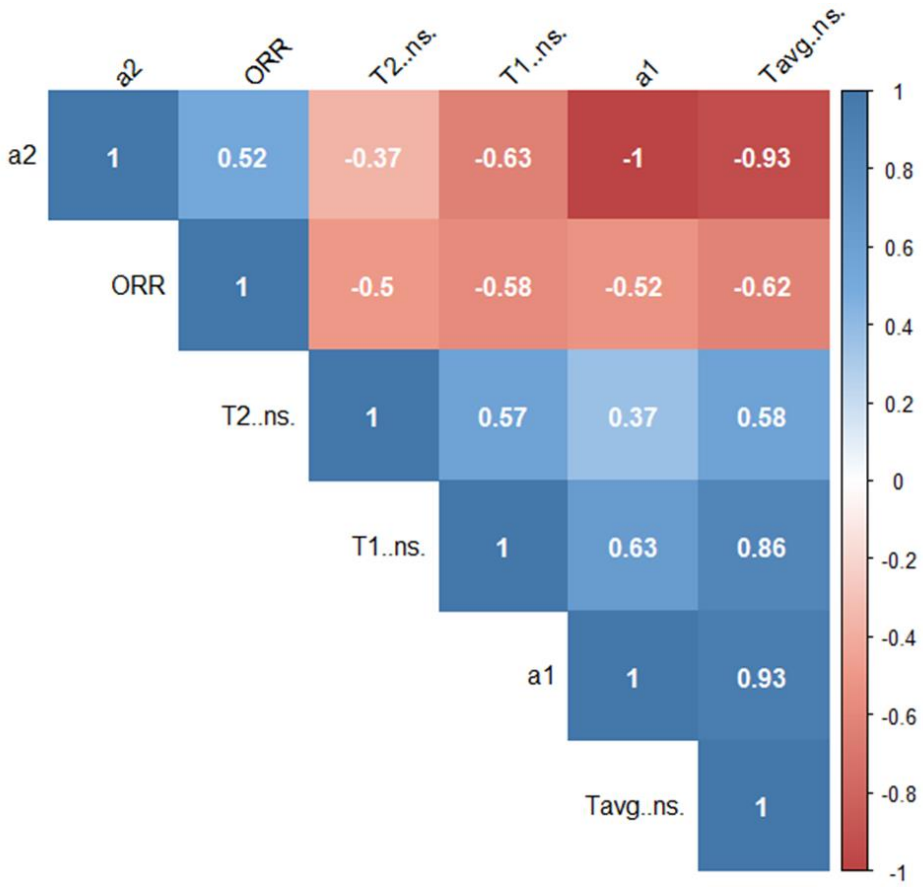

Figure Appendix 13 - Correlation matrix of 2P-FLIM NAD(P)H variables with correlation values displayed

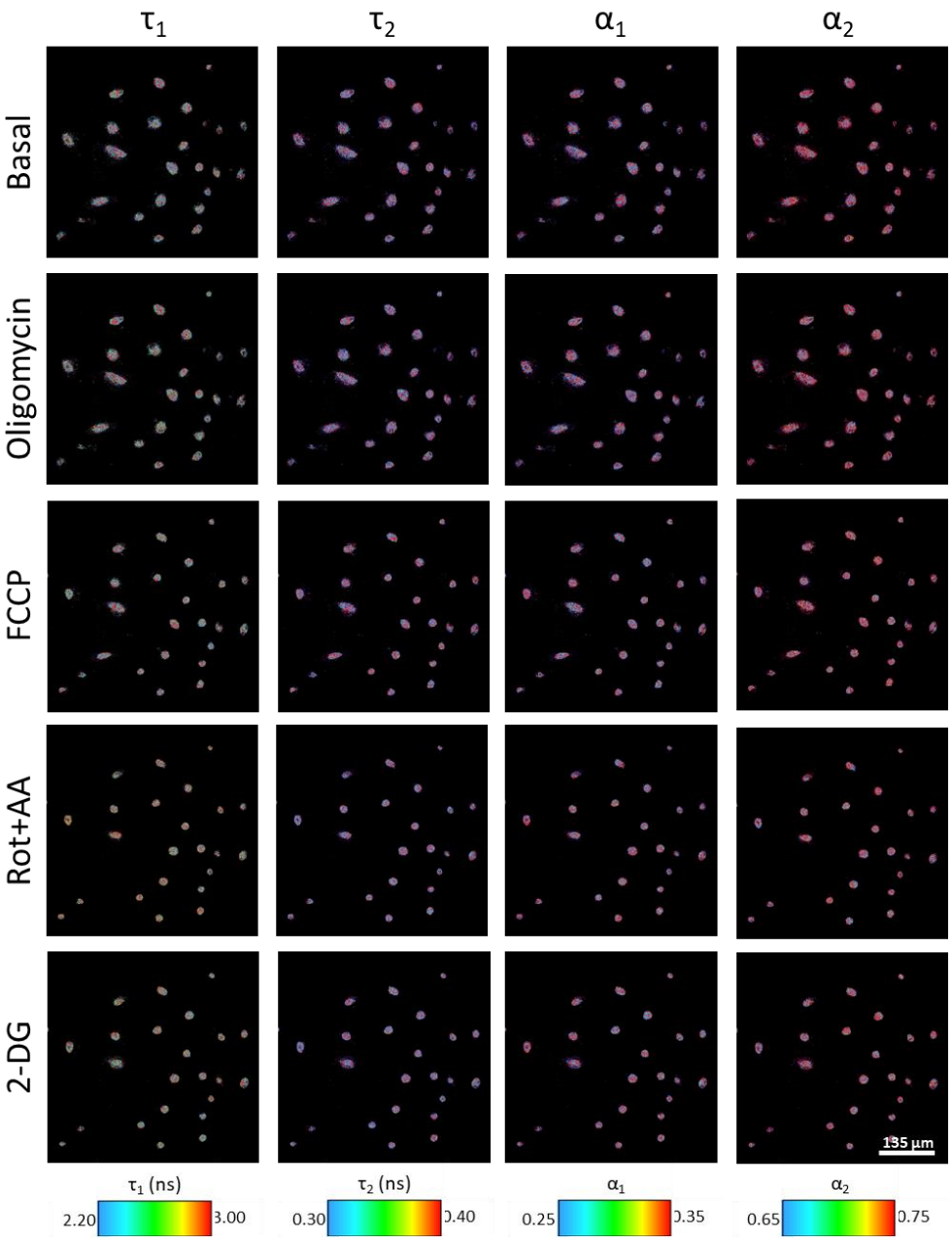

Figure Appendix 14 - 2P-FLIM of IFNγ-M1 macrophages for basal conditions, Oligomycin, Carbonyl cyanide-p-trifluoromethoxyphenylhydrazone (FCCP), Rotenone with Antimycin A and 2- Deoxy-D-glucose treatments with the concentrations detailed in the main manuscript. All treatment images collected at the 30 mins of treatment and color-coded for different NADH FLIM variables

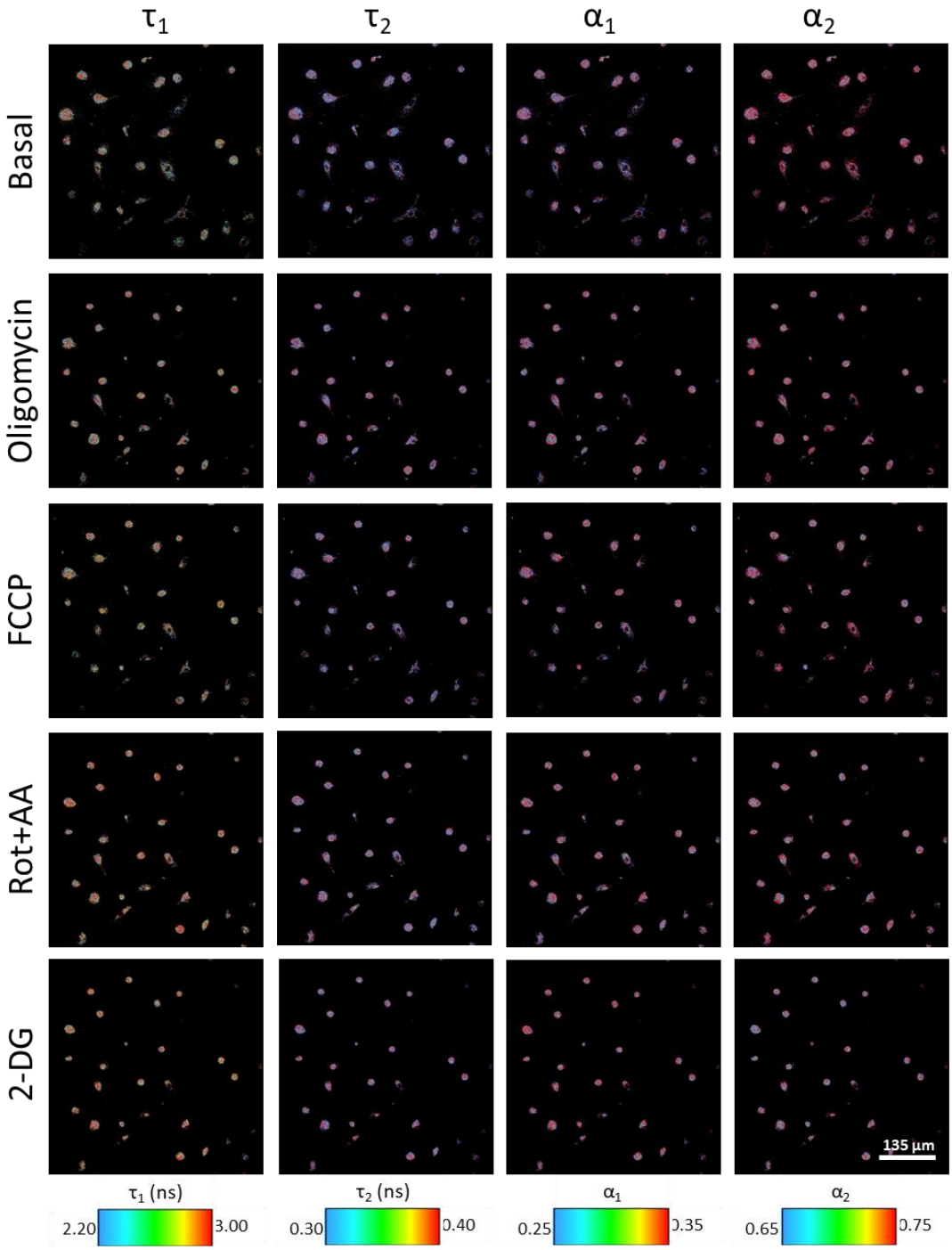

Figure Appendix 15 - 2P-FLIM of IFNγ-M2 macrophages for basal conditions, Oligomycin, Carbonyl cyanide-p-trifluoromethoxyphenylhydrazone (FCCP), Rotenone with Antimycin A and 2- Deoxy-D-glucose treatments with the concentrations detailed in the main manuscript. All treatment images collected at the 30 mins of treatment and color-coded for different NADH FLIM variables.